

HYDROTHERMAL SYNTHESSES, STRUCTURES, AND PROPERTIES OF NEW
IODATE AND SELENITE COMPOUNDS OF TRANSITION METALS,
LANTHANIDES, AND ACTINIDES

Except where reference is made to the work of others, the work described in this dissertation is my own or was done in collaboration with my advisory committee. This dissertation does not include proprietary or classified information.

Jie Ling

Certificate of Approval:

Thomas R. Webb
Associate Professor
Chemistry and Biochemistry

Thomas E. Albrecht-Schmitt, Chair
Professor
Chemistry and Biochemistry

Curtis G. Shannon
Professor
Chemistry and Biochemistry

Anne E. V. Gorden
Assistant Professor
Chemistry and Biochemistry

George T. Flowers
Interim Dean
Graduate School

HYDROTHERMAL SYNTHESSES, STRUCTURES, AND PROPERTIES OF NEW
IODATE AND SELENITE COMPOUNDS OF TRANSITION METALS,
LANTHANIDES, AND ACTINIDES

Jie Ling

A Dissertation

Submitted to

the Graduate Faculty of

Auburn University

in Partial Fulfillment of the

Requirements for the

Degree of

Doctor of Philosophy

Auburn, Alabama
December 17, 2007

HYDROTHERMAL SYNTHESSES, STRUCTURES, AND PROPERTIES OF NEW
IODATE AND SELENITE COMPOUNDS OF TRANSITION METALS,
LANTHANIDES, AND ACTINIDES

Jie Ling

Permission is granted to Auburn University to make copies of this dissertation at its discretion, upon request of individuals or institutions and at their expense. The author reserves all publication rights.

Signature of Author

Date of Graduation

VITA

Jie Ling, son of Yinwen Ling and Xilian Zhang, was born on September 1, 1977, in Hunan, China. After graduated from Longhui No.1 High School in 1994, he went to Wuhan University where he obtained a Bachelor degree of Engineering in Instrumental Analysis in 1998 and a Master degree of science in Materials Chemistry in 2002. In the fall of 2003, he entered Graduate School at Auburn University to pursue a Doctoral degree in Chemistry under the guidance of Dr. Thomas E. Albrecht-Schmitt.

DISSERTATION ABSTRACT

HYDROTHERMAL SYNTHESSES, STRUCTURES, AND PROPERTIES OF NEW
IODATE AND SELENITE COMPOUNDS OF TRANSITION METALS,
LANTHANIDES, AND ACTINIDES

Jie Ling

Doctor of Philosophy, December 17, 2007
(B. Eng., Wuhan University, 1998)
(M. S., Wuhan University, 2002)

252 Typed Pages

Directed by Thomas E. Albrecht-Schmitt

Iodate and selenite anions possessing a nonbonding, but stereochemically active lone pair of electrons, were selected as building blocks to produce new compounds with noncentrosymmetric structures, which is a prerequisite for nonlinear optics (NLO). A broad range of other elements, including transition metals, lanthanides, and even actinides, were utilized to synthesize new compounds and new structures under mild hydrothermal or supercritical conditions. Another important reason for investigating iodate chemistry of actinides is to gain a better understanding of the chemistry involving spent nuclear fuel. The success of intercalating iodic acid molecules into an existing uranyl phase provides a great example of the immobilization of ^{129}I which is a key

long-lived radionuclide in spent nuclear fuel. Single crystal X-ray diffraction measurements were carried out to determine the structures of prepared new compounds. Spectroscopic, second harmonic generation, thermal, and magnetic characterizations are additionally utilized to investigate structure-property relationships.

ACKNOWLEDGMENT

There is a long list of people I wish to express my sincerest gratitude. At first, I would like to thank my research advisor, Professor Thomas E. Albrecht-Schmitt, a erudite and kindly person. He opened the door of actinide chemistry for me, and led me into this mysterious and exciting field. During the four years working with him, I was deeply impressed by his meticulous and aggressive attitude to research. Following the interest in actinide chemistry, I decided to take the cherished chance to work with Dr. Peter C. Burns, a big name in actinide chemistry, as a postdoctoral fellow.

I would also like to thank my committee members, Dr. T. Webb, Dr. C. Shannon, and Dr. A. E. V. Gordon for their precious advice and help within this dissertation.

I would like to thank the group members, Phil, Tyler, Shehee, Tanya, Jin, Travis, Noel, Yaqin, Anna, and Andrea, for their friendship and useful discussions. Dr. John Gordon, thank you for giving me so much help. Mr. T. Carrington, Ms. Julie Arriaga, and Ms. Hongxia Zhang, thank you for your help in the IR, TGA, and Raman measurements.

In addition, I would like to express my appreciation to Dr. Susan M. Kauzlarich (UC-Davis) and Dr. Thomas E. Mallouk (PSU) for their kindness of answering my questions I had in my research.

Finally, I would like to thank my parents for their support and love along my life. And Nan Ye, my girl friend, thanks a lot for your love and company during my time at Auburn.

Style manual or journal used:

American Chemical Society Style

Computer software used:

Microsoft Word 2000, Microsoft Excel, Atoms v.5.0, & 6.0, CorelDRAW 10, Microcal
Origin 6.0

TABLE OF CONTENTS

LIST OF FIGURES	xvi
LIST OF TABLES	xxiii
CHAPTER 1. INTRODUCTION	1
Hydrothermal Synthesis.....	1
Supercritical Reactions	2
Nonlinear Optical Materials.....	5
Chemistry of Iodates and Selenites.....	12
Chemistry of Actinide Elements.....	20
Iodate Chemistry of Spent Nuclear Fuel.....	22
References.....	26
CHAPTER 2. SYNTHESSES, STRUCTURES, AND PROPERTIES OF NOVEL GOLD AND PALLADIUM IODATES	30
Abstract.....	32
Introduction.....	33
Experimental.....	33
Synthesis of $\text{NaAu}(\text{IO}_3)_4$	33
Synthesis of $\text{KAu}(\text{IO}_3)_4$	34
Synthesis of $\text{RbAu}(\text{IO}_3)_4$	34

Synthesis of $K_{2.5}Pd(IO_3)_4 \cdot H_{0.5}IO_3$	34
Synthesis of $Pd(IO_3)_2$	35
Crystallographic Studies	35
Powder X-Ray Diffraction	36
Vibrational Spectroscopy	36
Thermal Analysis	37
UV-Vis Diffuse Reflectance Spectroscopy	37
Results and Discussion	45
Synthesis	45
Crystal Structures of $M^I Au(IO_3)_4$ ($M^I = Na, K, Rb$)	45
Crystal Structure of $K_{2.5}Pd(IO_3)_4 \cdot H_{0.5}IO_3$	53
Crystal Structure of $Pd(IO_3)_2$	53
Vibrational Spectrum of $KAu(IO_3)_4$	61
Vibrational Spectra of $K_{2.5}Pd(IO_3)_4 \cdot H_{0.5}IO_3$ and $Pd(IO_3)_2$	61
Thermal Spectra of $KAu(IO_3)_4$ and $Pd(IO_3)_2$	62
UV-Vis Diffuse Reflectance Spectroscopy of $KAu(IO_3)_4$	62
Conclusions	63
References	71

CHAPTER 3. SYNTHESSES, STRUCTURES, AND PROPERTIES OF THREE

PALLADIUM SELENITES AND SELENATE, $PdSeO_3$, $PdSe_2O_5$, AND $Na_2Pd(SeO_4)_2$

.....	74
Abstract	74
Introduction	76

Experimental	77
Synthesis of PdSeO ₃	78
Synthesis of PdSe ₂ O ₅	78
Synthesis of Na ₂ Pd(SeO ₄) ₂	78
Crystallographic Studies	79
Powder X-Ray Diffraction	81
Vibrational Spectroscopy	81
Thermal Analysis	81
Results and Discussion	81
Syntheses of PdSeO ₃ , PdSe ₂ O ₅ , and Na ₂ Pd(SeO ₄) ₂	81
Crystal Structures of PdSeO ₃	85
Crystal Structures of PdSe ₂ O ₅	85
Crystal Structures of Na ₂ Pd(SeO ₄) ₂	86
Vibrational Spectroscopy	93
Thermal Analysis	93
Conclusions	94
References	95

CHAPTER 4. SYNTHESSES, STRUCTURE, AND PROPERTIES OF NEW TRANSITION METAL SELENITES, Ag ₄ (Mo ₂ O ₅)(SeO ₃)(SeO ₄), Ag ₂ (MoO ₃)SeO ₃ , AND AgNbO(SeO ₃) ₂	99
Abstract	99
Introduction	101
Experimental	102

Synthesis of $\text{Ag}_4(\text{Mo}_2\text{O}_5)(\text{SeO}_3)(\text{SeO}_4)$	103
Synthesis of $\text{Ag}_2(\text{MoO}_3)\text{SeO}_3$	103
Synthesis of $\text{AgNbO}(\text{SeO}_3)_2$	103
Crystallographic Studies	104
Powder X-Ray Diffraction.....	104
Vibrational Spectroscopy.....	105
Thermal Analysis	105
Results and Discussion	116
Syntheses.....	116
Crystal Structure of $\text{Ag}_4(\text{Mo}_2\text{O}_5)(\text{SeO}_3)(\text{SeO}_4)$	117
Crystal Structure of $\text{Ag}_2(\text{MoO}_3)\text{SeO}_3$	118
Crystal Structure of $\text{AgNbO}(\text{SeO}_3)_2$	119
Vibrational Spectra of $\text{Ag}_4(\text{Mo}_2\text{O}_5)(\text{SeO}_4)_2(\text{SeO}_3)$, $\text{Ag}_2(\text{MoO}_3)_3\text{SeO}_3$, and $\text{AgNbO}(\text{SeO}_3)_2$	130
Thermal Analysis of $\text{Ag}_4(\text{Mo}_2\text{O}_5)(\text{SeO}_4)_2(\text{SeO}_3)$ and $\text{Ag}_2(\text{MoO}_3)_3\text{SeO}_3$	131
Conclusions.....	132
References.....	133

CHAPTER 5. HYDROTHERMAL SYNTHESSES AND STRUCTURE

CHARACTERIZATION OF LATE LANTHANIDE IODATES, $\text{Ln}(\text{IO}_3)_3$ AND

$\text{Ln}(\text{IO}_3)_3(\text{H}_2\text{O})$ ($\text{Ln} = \text{Yb}, \text{Lu}$)	136
Abstract.....	136
Introduction.....	138

Experimental	139
Synthesis of $\text{Yb}(\text{IO}_3)_3$	139
Synthesis of $\text{Lu}(\text{IO}_3)_3$	139
Synthesis of $\text{Yb}(\text{IO}_3)_3(\text{H}_2\text{O})$ and $\text{Lu}(\text{IO}_3)_3(\text{H}_2\text{O})$	140
Crystallographic Studies	140
Raman Spectroscopy	141
Results and Discussion	149
Syntheses	149
Crystal Structures of $\text{Yb}(\text{IO}_3)_3$ and $\text{Lu}(\text{IO}_3)_3$	149
Crystal Structures of $\text{Yb}(\text{IO}_3)_3(\text{H}_2\text{O})$ and $\text{Lu}(\text{IO}_3)_3(\text{H}_2\text{O})$	150
Raman Spectra of $\text{Yb}(\text{IO}_3)_3$ and $\text{Lu}(\text{IO}_3)_3$	152
Raman Spectra of $\text{Yb}(\text{IO}_3)_3(\text{H}_2\text{O})$ and $\text{Lu}(\text{IO}_3)_3(\text{H}_2\text{O})$	154
Conclusions	170
References	171
 CHAPTER 6. INTERCALATION OF IODIC ACID INTO THE LAYERED URANYL	
IODATE, $\text{UO}_2(\text{IO}_3)_2(\text{H}_2\text{O})$	174
Abstract	174
Introduction	175
Experimental	176
Synthesis of $\text{UO}_2(\text{IO}_3)_2(\text{H}_2\text{O}) \cdot 2\text{HIO}_3$	176
Crystallographic Studies	176
Powder X-Ray Diffraction	177
Vibrational Spectroscopy	177

Thermal Analysis	177
Results and Discussion	181
Syntheses.....	181
Crystal Structure of $\text{UO}_2(\text{IO}_3)_2(\text{H}_2\text{O})\cdot 2\text{HIO}_3$	181
Vibrational Spectrum of $\text{UO}_2(\text{IO}_3)_2(\text{H}_2\text{O})\cdot 2\text{HIO}_3$	187
Thermal Analysis of $\text{UO}_2(\text{IO}_3)_2(\text{H}_2\text{O})\cdot 2\text{HIO}_3$	187
Conclusions.....	188
References.....	189
CHAPTER 7. CRITICAL ROLE OF WATER CONTENT IN THE FORMATION AND REACTIVITY OF URANIUM AND NEPTUNIUM IODATES UNDER HYDROTHERMAL CONDITIONS: IMPLICATIONS FOR THE OXIDATIVE DISSOLUTION OF SPENT NUCLEAR FUEL.....	
	191
Abstract.....	191
Introduction.....	193
Experimental.....	193
Syntheses.....	194
Crystallographic Studies	195
Magnetic Susceptibility Measurement.....	195
Nonlinear Optical Measurement.....	196
Results and Discussion	197
Syntheses.....	197
Crystal Structure of $\text{Np}(\text{IO}_3)_4$	206
Crystal Structure of $\text{Np}(\text{IO}_3)_4\cdot n\text{H}_2\text{O}\cdot n\text{HIO}_3$	207

Magnetic Property of $\text{Np}(\text{IO}_3)_4$	208
Conclusions.....	209
References.....	214
CHAPTER 8. SUMMARY.....	217
References.....	226

LIST OF FIGURES

- Figure 1.1. The pressure-temperature phase diagram of water. The dotted line gives the anomalous behaviour of water. The green lines mark the freezing point and the blue line the boiling point, showing how they vary with pressure4
- Figure 1.2. The non-centrosymmetric crystal schematic6
- Figure 1.3. A modified Kurtz powder NLO instrument used to measure SHG activity.....7
- Figure 1.4. (top) A phase-matchable curve for a SHG material. (bottom) A non-phase matchable curve for a SHG material.....8
- Figure 1.5. The various binding modes of the iodate, IO_3^- , anion to the metal center14
- Figure 1.6. The radial probability of finding an electron from the nucleus of Sm^{3+} and Pu^{3+} . The broken lines demonstrate the nonrelativistic effect on the electrons15
- Figure 1.7. The oxidation states of the early actinide series. The environmentally important actinides are in bold.....16
- Figure 1.8. The redox potentials for Np, Pu and U in acidic media, demonstrating the close potential differences between oxidation states17

Figure 1.9. The UO_2^{2+} cation in tetragonal bipyramidal, pentagonal bipyramidal, and hexagonal bipyramidal environments as common building units for uranyl structure formation. They can be interconnected by corner-, edge-, or face-sharing with each other or other building units in order to construct different structure types	18
Figure 1.10. The wide variety of fission products of U235 in spent nuclear fuel	23
Figure 2.1. A photograph showing yellow crystals of $\text{K}[\text{Au}(\text{IO}_3)_4]$ that have grown directly on the surface of elemental gold under hydrothermal conditions. Crystals typically have maximum dimensions of several millimeters.....	47
Figure 2.2. Two views of the $[\text{Au}(\text{IO}_3)_4]^{1-}$ anion in the structure of $\text{K}[\text{Au}(\text{IO}_3)_4]$. Gold is shown in yellow, iodine in magenta, and oxygen in red.....	48
Figure 2.3. A view down the c axis of the structure of $\text{KAu}(\text{IO}_3)_4$ showing the polar stacking of the $[\text{Au}(\text{IO}_3)_4]^{1-}$ anions. K^+ cations have been omitted for clarity. Gold is shown in yellow, iodine in magenta, and oxygen in red.....	49
Figure 2.4. Two depictions of the $[\text{Pd}(\text{IO}_3)_4]^{2-}$ anion in the structure of $\text{K}_{2.5}\text{Pd}(\text{IO}_3)_4 \cdot \text{H}_{0.5}\text{IO}_3$. Palladium is shown in orange, iodine in magenta, and oxygen in red.....	54
Figure 2.5. An illustration of the centrosymmetric packing of the $[\text{Pd}(\text{IO}_3)_4]^{2-}$ anions in $\text{K}_{2.5}\text{Pd}(\text{IO}_3)_4 \cdot \text{H}_{0.5}\text{IO}_3$. K^+ cations and iodate/iodic acid units have been omitted for clarity. Palladium is shown in orange, iodine in magenta, and oxygen in red.....	55

Figure 2.6. The depiction of the coordination environment of Pd ²⁺ cations with iodate ligands in the structure of Pd(IO ₃) ₃ . Palladium is shown in orange, iodine in magenta, and oxygen in red	56
Figure 2.7. The depiction of the layer structure of Pd(IO ₃) ₃ in the [ab] plane. Palladium square planes are shown in orange, iodine atoms in magenta, and oxygen atoms in red.....	57
Figure 2.8. The depiction of stacking mode of layer structure of Pd(IO ₃) ₂ along c axis. Palladium square planes are shown in orange, iodine atoms in magenta, and oxygen atoms in red	58
Figure 2.9. The IR spectrum of KAu(IO ₃) ₄	64
Figure 2.10. The Raman spectrum of KAu(IO ₃) ₄	65
Figure 2.11. The IR spectrum of Pd(IO ₃) ₂	66
Figure 2.12. The Raman spectrum of Pd(IO ₃) ₂	67
Figure 2.13. The TGA spectrum of KAu(IO ₃) ₄	68
Figure 2.14. The TGA spectrum of Pd(IO ₃) ₂	69
Figure 2.15. The UV-Vis Diffuse Reflectance spectrum of KAu(IO ₃) ₄	70
Figure 3.1. (A) View of the structure of PdSeO ₃ showing [PdO ₄] units joined together through corner-sharing to form a chain that extends down the b axis. The palladium chains are further connected by tridentate SeO ₃ ²⁻ anions. (B) A depiction of the neutral layers in PdSeO ₃ . Orange (large), yellow (medium) and red (small) balls represent Pd, Se and O atoms, respectively	87

- Figure 3.2. Illustration of the one-dimensional chains formed from $[\text{PdO}_4]$ units and $\text{Se}_2\text{O}_5^{2-}$ anions in the structure of PdSe_2O_5 . Orange (large), yellow (medium) and red (small) balls represent Pd, Se and O atoms, respectively88
- Figure 3.3. View of the one-dimensional $[\text{Pd}(\text{SeO}_4)_2]^{2-}$ chains in $\text{Na}_2\text{Pd}(\text{SeO}_4)_2$. Orange (large), yellow (medium), blue (medium), and red (small) balls represent Pd, Se, Na and O atoms, respectively89
- Figure 4.1. A view of the one-dimensional $[(\text{Mo}_2\text{O}_5)(\text{SeO}_4)_2(\text{SeO}_3)]^{4-}$ chains that extend down the *c*-axis in the structure of $\text{Ag}_4(\text{Mo}_2\text{O}_5)(\text{SeO}_4)_2(\text{SeO}_3)$. Green polyhedra represent the MoO_6 building blocks, yellow (medium) and red (small) balls stand for selenium and oxygen atoms, respectively. Silver atoms are deleted for the purpose of clarification121
- Figure 4.2. A depiction of individual polar $[(\text{Mo}_2\text{O}_5)(\text{SeO}_4)_2(\text{SeO}_3)]^{4-}$ chains with the C_2 distortion of the Mo(VI) octahedra aligning on one side of each chain in $\text{Ag}_4(\text{Mo}_2\text{O}_5)(\text{SeO}_4)_2(\text{SeO}_3)$. Green polyhedra represent the MoO_6 building blocks, yellow (medium) and red (small) balls stand for selenium and oxygen atoms, respectively. Silver atoms are deleted for the purpose of clarification122
- Figure 4.3. A view of the two-dimensional $[(\text{MoO}_3)_3\text{SeO}_3]^{2-}$ layer in $\text{Ag}_2(\text{MoO}_3)_3\text{SeO}_3$ that extends in the $[bc]$ plane. Green (large), yellow (medium) and red (small) balls stand for selenium and oxygen atoms, respectively. Silver atoms are deleted for the purpose of clarification123
- Figure 4.4. An illustration of the stacking of the $[(\text{MoO}_3)_3\text{SeO}_3]^{2-}$ layers in $\text{Ag}_2(\text{MoO}_3)_3\text{SeO}_3$. Green (large), yellow (medium) and red (small) balls

	stand for selenium and oxygen atoms, respectively. Silver atoms are deleted for the purpose of clarification.....	124
Figure 4.5.	An illustration of two one-dimensional chains formed by corner-sharing connection of Nb(1) (top) and Nb(2) (below) octahera along <i>c</i> axis in the structure of AgNbO(SeO ₃) ₂ . Green (large), yellow (medium) and red (small) balls stand for selenium and oxygen atoms, respectively. Silver atoms are deleted for the purpose of clarification	125
Figure 4.6.	A view of the structure of AgNbO(SeO ₃) ₂ along <i>c</i> aixs. Green (large), purple (large), yellow (medium) and red (small) balls stand for niobium, silver, selenium and oxygen atoms, respectively.....	126
Figure 4.7.	IR and Raman spectra of Ag ₄ (Mo ₂ O ₅)(SeO ₄) ₂ (SeO ₃).....	127
Figure 4.8.	IR and Raman spectra of Ag ₂ (MoO ₃) ₃ SeO ₃	128
Figure 4.9.	A TGA thermogram for Ag ₄ (Mo ₂ O ₅)(SeO ₄) ₂ (SeO ₃)	129
Figure 5.1.	The coordination environment of the Lu site in Lu(IO ₃) ₃ (50% probability ellipsoids are shown). Operations used to generate symmetry equivalent atoms: (a) 1.5- <i>x</i> , 0.5+ <i>y</i> , 1.5- <i>z</i> ; (b) 1- <i>x</i> , 1- <i>y</i> , 2- <i>z</i> ; (e) <i>x</i> , 1+ <i>y</i> , <i>z</i>	157
Figure 5.2.	A packing diagram viewed along the <i>b</i> -axis showing the stacking of the two-dimensional layers in Ln(IO ₃) ₃ (<i>Ln</i> = Yb, Lu)	158
Figure 5.3.	The coordination environment of the Yb site in Yb(IO ₃) ₃ (H ₂ O) (50% probability ellipsoids are shown). Operations used to generate symmetry equivalent atoms: (a) <i>x</i> , <i>y</i> -1, <i>z</i> ; (b) <i>x</i> , 1- <i>y</i> , 1/2+ <i>z</i>	161
Figure 5.4.	A ball and stick plot of a two-dimensional layer in Ln(IO ₃) ₃ (H ₂ O) (<i>Ln</i> = Yb, Lu) viewed (a) perpendicular to the layer or (b) parallel to the layer.....	162

Figure 5.5. A packing diagram showing the stacking of the two-dimensional layers in $Ln(\text{IO}_3)_3(\text{H}_2\text{O})$ ($Ln = \text{Yb}, \text{Lu}$).....	163
Figure 5.6. Raman spectrum of (a) $\text{Lu}(\text{IO}_3)_3$, and (b) $\text{Yb}(\text{IO}_3)_3$ at room temperature in the I–O stretching frequency region	166
Figure 5.7. Raman spectrum of (a) $\text{Lu}(\text{IO}_3)_3$, and (b) $\text{Yb}(\text{IO}_3)_3$ at room temperature covering the iodate bending and lattice vibrational regions; (c) Raman spectrum of $\text{Yb}(\text{IO}_3)_3$ collected at liquid N_2 temperature. A highly resolved spectrum was obtained at low temperature.....	167
Figure 5.8. Raman spectrum of (a) $\text{Lu}(\text{IO}_3)_3(\text{H}_2\text{O})$, and (b) $\text{Yb}(\text{IO}_3)_3(\text{H}_2\text{O})$ at room temperature in the I–O stretching region	168
Figure 5.9. Raman spectrum of (a) $\text{Lu}(\text{IO}_3)_3(\text{H}_2\text{O})$, and (b) $\text{Yb}(\text{IO}_3)_3(\text{H}_2\text{O})$ at room temperature in the iodate bending and lattice vibrational regions	169
Figure 6.1. Depiction of the intercalation of iodic acid into $\text{UO}_2(\text{IO}_3)_2(\text{H}_2\text{O})$ (A) to yield $\text{UO}_2(\text{IO}_3)_2(\text{H}_2\text{O}) \cdot 2\text{HIO}_3$ (B) UO_7 pentagonal bipyramids are shown in green, I atoms in purple, and O atoms in red	183
Figure 6.2. (top) View down the c axis of the $[\text{UO}_2(\text{IO}_3)_2(\text{H}_2\text{O})]$ layers in $\text{UO}_2(\text{IO}_3)_2(\text{H}_2\text{O})$. (bottom) Packing of the highly corrugated $[\text{UO}_2(\text{IO}_3)_2(\text{H}_2\text{O})]$ layers in $\text{UO}_2(\text{IO}_3)_2(\text{H}_2\text{O})$ viewed down the b axis.....	184
Figure 6.3. IR spectrum of $\text{UO}_2(\text{IO}_3)_2(\text{H}_2\text{O}) \cdot 2\text{HIO}_3$	185
Figure 6.4. DSC spectrum of $\text{UO}_2(\text{IO}_3)_2(\text{H}_2\text{O}) \cdot 2\text{HIO}_3$	186
Figure 7.1. Photograph showing the hydrothermal reduction of the neptunium(VI) iodate $\text{NpO}_2(\text{IO}_3)_2(\text{H}_2\text{O})$ to the neptunium(IV) iodates $\text{Np}(\text{IO}_3)_4$ and $\text{Np}(\text{IO}_3)_4 \cdot n\text{H}_2\text{O} \cdot n\text{HIO}_3$	210

Figure 7.2. (a) View of the one-dimensional chains in $\text{Np}(\text{IO}_3)_4$ consisting of eight-coordinate, dodecahedral $\text{Np}(\text{IV})$ centers bridged by iodate. (b) Depiction of the pinwheel packing of the $\text{Np}(\text{IO}_3)_4$ chains211

Figure 7.3. Depiction of the structure of $\text{Np}(\text{IO}_3)_4 \cdot n\text{H}_2\text{O} \cdot n\text{HIO}_3$. This structure consists of a three-dimensional network constructed from nine-coordinate tricapped trigonal prismatic $\text{Np}(\text{IV})$ that are bridged by iodate anions to create the channels that extend along the c axis. The channels are partially filled by iodate anions or water molecules212

Figure 7.4. Temperature dependence of the inverse magnetic susceptibility of a $\text{Np}(\text{IO}_3)_4$ single crystal. The Curie-Weiss fitting curve is shown as a solid line213

LIST OF TABLES

Table 2.1. Crystallographic Data for NaAu(IO ₃) ₄ , KAu(IO ₃) ₄ , and RbAu(IO ₃) ₄	38
Table 2.2. Crystallographic Data for K _{2.5} Pd(IO ₃) ₄ ·H _{0.5} IO ₃ and Pd(IO ₃) ₂	39
Table 2.3. Atomic Coordinates and Equivalent Isotropic Displacement Parameters for NaAu(IO ₃) ₄	40
Table 2.4. Atomic Coordinates and Equivalent Isotropic Displacement Parameters for KAu(IO ₃) ₄	41
Table 2.5. Atomic Coordinates and Equivalent Isotropic Displacement Parameters for RbAu(IO ₃) ₄	42
Table 2.6. Atomic Coordinates and Equivalent Isotropic Displacement Parameters for K _{2.5} Pd(IO ₃) ₄ ·H _{0.5} IO ₃	43
Table 2.7. Atomic Coordinates and Equivalent Isotropic Displacement Parameters for Pd(IO ₃) ₂	44
Table 2.8. Selected Bond Distances (Å) and Angles (°) for NaAu(IO ₃) ₄	50
Table 2.9. Selected Bond Distances (Å) and Angles (°) for KAu(IO ₃) ₄	51
Table 2.10. Selected Bond Distances (Å) and Angles (°) for RbAu(IO ₃) ₄	52
Table 2.11. Selected Bond Distances (Å) and Angles (°) for K _{2.5} Pd(IO ₃) ₄ ·H _{0.5} IO ₃	59
Table 2.12. Selected Bond Distances (Å) and Angles (°) for Pd(IO ₃) ₂	60

Table 3.1. Crystallographic Data for PdSeO ₃ , PdSe ₂ O ₅ , and Na ₂ Pd(SeO ₄) ₂	80
Table 3.2. Atomic Coordinates and Equivalent Isotropic Displacement Parameters for PdSeO ₃	82
Table 3.3. Atomic Coordinates and Equivalent Isotropic Displacement Parameters for PdSe ₂ O ₅	83
Table 3.4. Atomic coordinates and equivalent isotropic displacement parameters for Na ₂ Pd(SeO ₄) ₂	84
Table 3.5. Selected Bond Distances (Å) and Angles (°) for PdSeO ₃	90
Table 3.6. Selected Bond Distances (Å) and Angles (°) for PdSe ₂ O ₅	91
Table 3.7. Selected Bond Distances (Å) and Angles (°) for Na ₂ Pd(SeO ₄) ₂	92
Table 4.1. Crystallographic Data for Ag ₄ (Mo ₂ O ₅)(SeO ₄) ₂ (SeO ₃) and Ag ₂ (MoO ₃) ₃ SeO ₃	106
Table 4.2. Crystallographic Data for AgNbO(SeO ₃) ₂	107
Table 4.3. Atomic Coordinates and Equivalent Isotropic Displacement Parameters for Ag ₄ (Mo ₂ O ₅)(SeO ₄) ₂ (SeO ₃)	108
Table 4.4. Atomic Coordinates and Equivalent Isotropic Displacement Parameters for Ag ₂ (MoO ₃) ₃ SeO ₃	109
Table 4.5. Atomic Coordinates and Equivalent Isotropic Displacement Parameters for AgNbO(SeO ₃) ₂	110
Table 4.6. Selected Bond Distances (Å) and Angles (°) for Ag ₄ (Mo ₂ O ₅)(SeO ₄) ₂ (SeO ₃)	111
Table 4.7. Selected Bond Distances (Å) and Angles (°) for Ag ₂ (MoO ₃) ₃ SeO ₃	112
Table 4.8. Selected Bond Distances (Å) and Angles (°) for AgNbO(SeO ₃) ₂	114

Table 5.1. Crystallographic Data for $\text{Yb}(\text{IO}_3)_3$ and $\text{Lu}(\text{IO}_3)_3$	143
Table 5.2. Crystallographic Data for $\text{Yb}(\text{IO}_3)_3(\text{H}_2\text{O})$ and $\text{Lu}(\text{IO}_3)_3(\text{H}_2\text{O})$	144
Table 5.3. Atomic Coordinates and Equivalent Isotropic Displacement Parameters for $\text{Yb}(\text{IO}_3)_3$	145
Table 5.4. Atomic Coordinates and Equivalent Isotropic Displacement Parameters for $\text{Lu}(\text{IO}_3)_3$	146
Table 5.5. Atomic Coordinates and Equivalent Isotropic Displacement Parameters for $\text{Yb}(\text{IO}_3)_3(\text{H}_2\text{O})$	147
Table 5.6. Atomic Coordinates and Equivalent Isotropic Displacement Parameters for $\text{Lu}(\text{IO}_3)_3(\text{H}_2\text{O})$	148
Table 5.7. Selected Bond Distances (\AA) and Angles ($^\circ$) for $\text{Yb}(\text{IO}_3)_3$	159
Table 5.8. Selected Bond Distances (\AA) and Angles ($^\circ$) for $\text{Lu}(\text{IO}_3)_3$	160
Table 5.9. Selected Bond Distances (\AA) and Angles ($^\circ$) for $\text{Yb}(\text{IO}_3)_3(\text{H}_2\text{O})$	164
Table 5.10. Selected Bond Distances (\AA) and Angles ($^\circ$) for $\text{Lu}(\text{IO}_3)_3(\text{H}_2\text{O})$	165
Table 6.1. Crystallographic Data for $\text{UO}_2(\text{IO}_3)_2(\text{H}_2\text{O}) \cdot 2\text{HIO}_3$ and $\text{UO}_2(\text{IO}_3)(\text{H}_2\text{O})$	178
Table 6.2. Atomic Coordinates and Equivalent Isotropic Displacement Parameters for $\text{UO}_2(\text{IO}_3)_2(\text{H}_2\text{O}) \cdot 2\text{HIO}_3$	179
Table 6.3. Selected Bond Distances (\AA) and Angles ($^\circ$) for $\text{UO}_2(\text{IO}_3)_2(\text{H}_2\text{O}) \cdot 2\text{HIO}_3$	180
Table 7.1. Crystallographic Data for $\text{Np}(\text{IO}_3)_4$ and $\text{Np}(\text{IO}_3)_4 \cdot n\text{H}_2\text{O} \cdot n\text{HIO}_3$	198
Table 7.2. Atomic Coordinates and Equivalent Isotropic Displacement Parameters for $\text{Np}(\text{IO}_3)_4$	199
Table 7.3. Atomic Coordinates and Equivalent Isotropic Displacement Parameters for $\text{Np}(\text{IO}_3)_4 \cdot n\text{H}_2\text{O} \cdot n\text{HIO}_3$	200

Table 7.4. Selected Bond Distances (Å) and Angles (°) for $\text{Np}(\text{IO}_3)_4$	201
Table 7.5. Selected Bond Distances (Å) and Angles (°) for $\text{Np}(\text{IO}_3)_4 \cdot n\text{H}_2\text{O} \cdot n\text{HIO}_3$	202
Table 8.1. A list of new compounds and some of their properties reported in this dissertation	224

CHAPTER 1

INTRODUCTION

Hydrothermal Synthesis

Hydrothermal synthesis, as an important branch of inorganic synthetic chemistry, includes various techniques of crystallizing substances from high temperature aqueous solutions at high pressure.^{1,2} The term “hydrothermal” is derived from geological science. “Hydrothermal reactions” normally refers to the reactions running in the temperature range from 100 °C to 374 °C, which are the boiling point and critical point of water (Figure 1.1), respectively. The hydrothermal reactions beyond the critical point are called supercritical reactions. This method was firstly developed to mimic the geological processes for producing natural minerals.^{3,4} After that it was applied to produce technologically important materials, such as zeolites⁵ and quartz,^{6,7} which possess useful chemical and physical properties. This technique has further been applied to new scientific fields, including the origin of life under hydrothermal conditions^{8,9} and environmentally-friendly redox reactions under supercritical conditions.¹⁰

The composition of product and quality of crystal are extremely sensitive to the temperature, the degree of water fill, pH, stoichiometry of reactants and the rate of cooling. Therefore, it is possible to control the composition and quality of products by adjusting the above parameters. This is of great importance for the design and synthesis

of novel materials. Another advantage of hydrothermal synthesis over other traditional methods of crystal growth is the ability to generate crystalline phases those are not stable at their melting point. Also, materials having high vapor pressure can be produced by hydrothermal synthesis. The method is particularly suitable for the growth of good quality single crystals which can be used in X-ray diffraction crystallographic studies. Owing to the use of water containing dissolved oxygen as the solvent, the products are normally stable in moist air. A disadvantage of this method is that mineralizing agents,^{11,12,13} such as halides, hydroxide, and carbonates, are usually needed to help crystallization because of the low dielectric constant of water at high temperature and pressure.

Supercritical Reactions

As mentioned above, reactions taking place beyond the critical point of water are called supercritical reactions.¹⁴ In principle, synthesizing new compounds in supercritical water should just be a variation on lower temperature hydrothermal methods. However, the dramatically increased temperatures, and more importantly, pressures require specialized equipment and reaction containment procedures. Above the critical point of water (374 °C), PTFE, which begins to co-flow above 250 °C, is no longer suitable as a reaction container. The supercritical water (SCW) is quite corrosive towards most types of steel, so considerable thought must be taken into autoclave design. At present, quartz and noble metals are the most commonly used container materials for supercritical reactions. Quartz has the advantage of low cost and easy sealing using a hot gas flame. Although quartz is reactive towards even slightly basic water and fluoride, it is inert to

most other solutions, including strong acids, chloride, and sulfide solutions up to 600 °C. If quartz is insufficient, inert metals, such as silver, gold, or platinum can be used as the reaction container. Obviously, these materials are costly.

At temperatures and pressures above the critical point ($T = 374\text{ °C}$, $P = 22.1\text{ MPa}$), water is considered as a kind of highly compressed gas. It possesses the characteristics of both fluid and gaseous substances: the fluid behavior of dissolving soluble materials, and the gaseous behavior of excellent diffusibility. At high temperatures around the critical point, a large portion of the hydrogen bonds in liquid water break and the relative permittivity and viscosity of water decrease steeply. The density of supercritical water at the critical point is about 1/3 of that of ambient water. As a consequence, the diffusion of water will be very rapid and the mixing of reactants will be much faster than those taking place within ambient water. Due to the large compressibility of supercritical water, small changes in pressure and temperature can produce very substantial changes in density, which, in turn, affect diffusivity, viscosity, dielectric, and solvation properties, thus dramatically influencing the kinetics and mechanisms of chemical reactions in water.¹⁵ Therefore, it is possible to control the dissolving action and other physical properties of water by changing the pressures and temperatures. On the other hand, owing to the breaking of hydrogen bonds, the dielectric constant of water decreases dramatically and water behaves more like a nonpolar solvent. Similar to the hydrothermal reactions, mineralizing agents are needed in these reactions. Models of hydrothermal convection suggest that the near-critical conditions provide an optimal convective behavior due to unique combination of thermodynamic and transport properties in this region of the phase diagram of water.^{16,17}

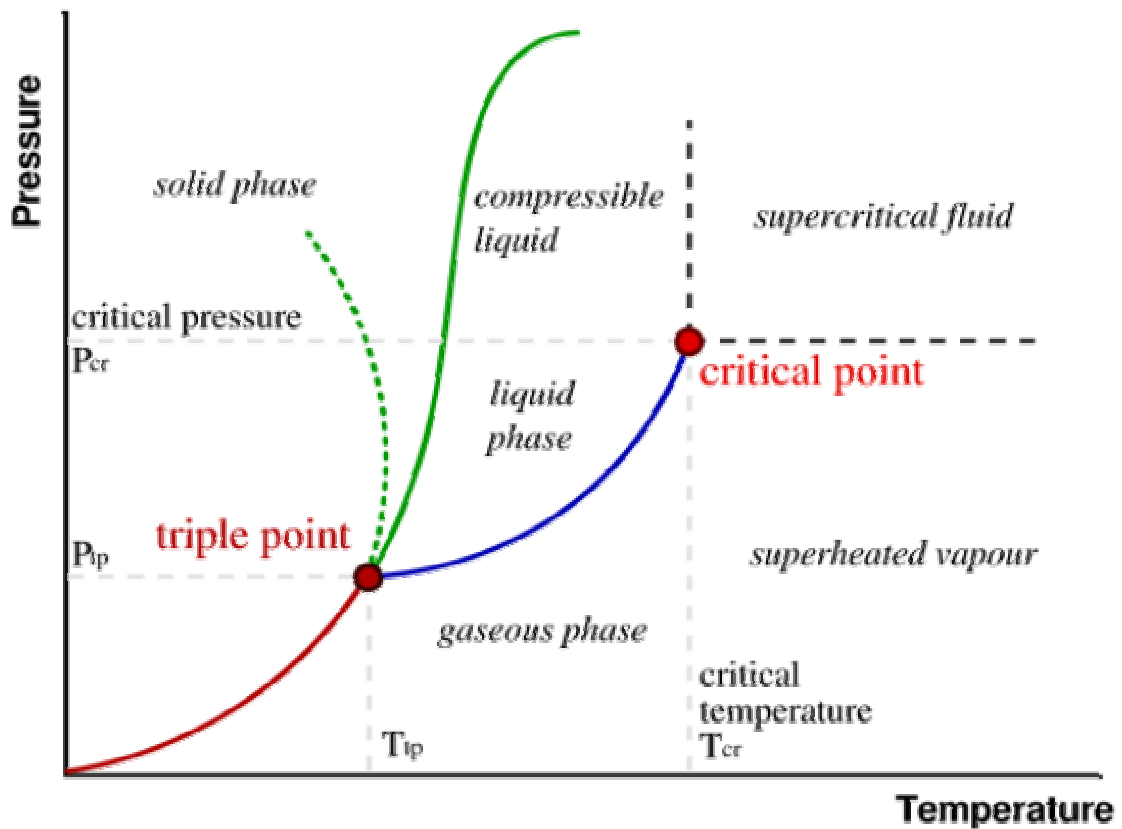


Figure 1.1. The pressure-temperature phase diagram of water. The dotted line gives the anomalous behaviour of water. The green lines mark the freezing point and the blue line the boiling point, showing how they vary with pressure.

Nonlinear Optical Materials

Since the demonstration of second-harmonic generation (SHG) of light in quartz by Franken et al. in 1961, nonlinear opticals (NLO) has attracting increasing attention around the world owing to their interesting optical properties. This group of materials can be used widely in telecommunications, optical computing, and dynamic image processing.

It is well known that the interaction of light with the electronic charge distribution around an ion can induces oscillations of the electron cloud. With light of relatively low intensity, the induced polarization P (the displacement of the electronic dipole moment per unit volume), is linearly proportional to the magnitude of the applied field E , namely

$$P = \chi^{(1)} \cdot E \quad (1.1)$$

where $\chi^{(1)}$ is the linear susceptibility, a function of the refractive index of the material. The linear dependence of the induced polarization on the electric field strength is, in fact, only an approximation and is valid only for small electric fields. For the light of high intensity, like laser radiations, the linear relationship between P and E is no longer sufficient, and a power series expansion in the field must be used, that is

$$P = \chi^{(1)} \cdot E + \chi^{(2)} \cdot E^2 + \chi^{(3)} \cdot E^3 + \dots \quad (1.2)$$

Where $\chi^{(2)}$, $\chi^{(3)}$ are the second and third order nonlinear susceptibilities of the material, respectively. The second term, including $\chi^{(2)}$, is responsible for the generation of second harmonic radiation with a frequency double that of the incident laser light.

To date, thousands of nonlinear crystals and their closely related isomorphs have been made. But only few of them can be potentially used as NLO materials due to some physical and chemical requirements, including chemical stability, transparency in the

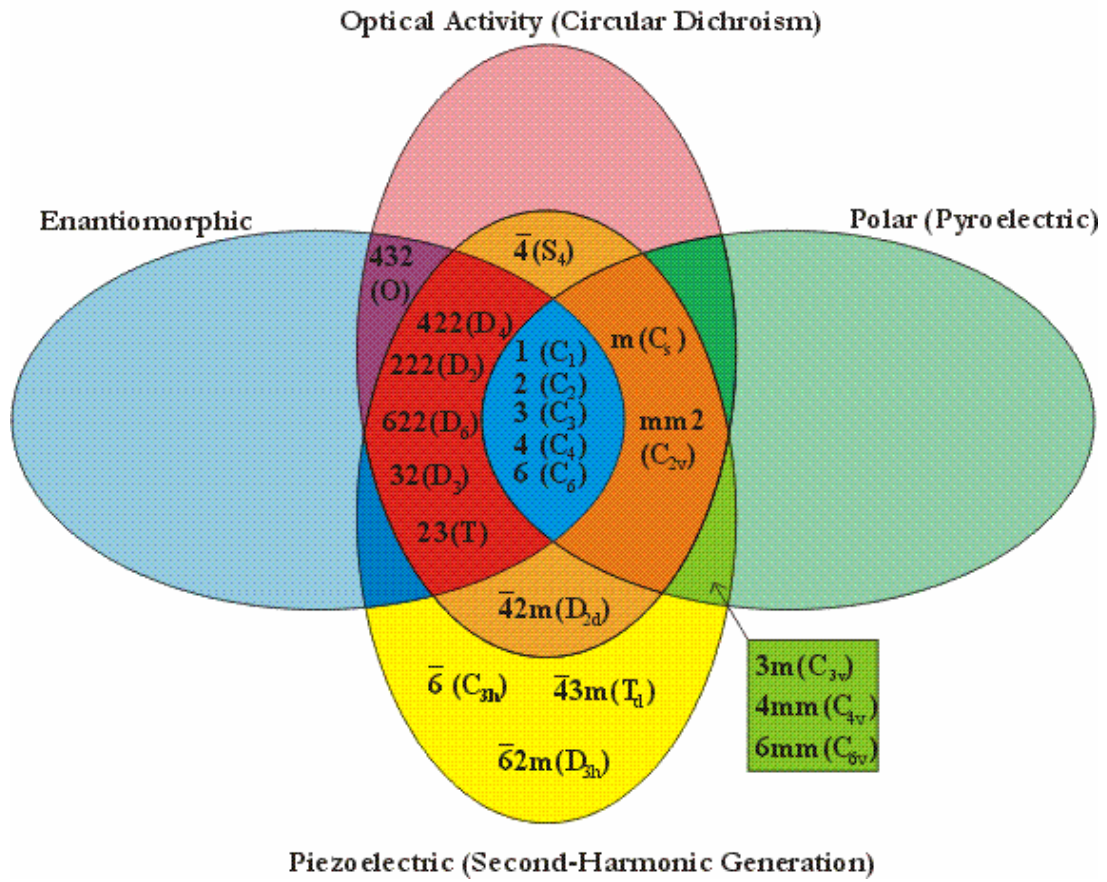


Figure 1.2. The non-centrosymmetric crystal schematic.

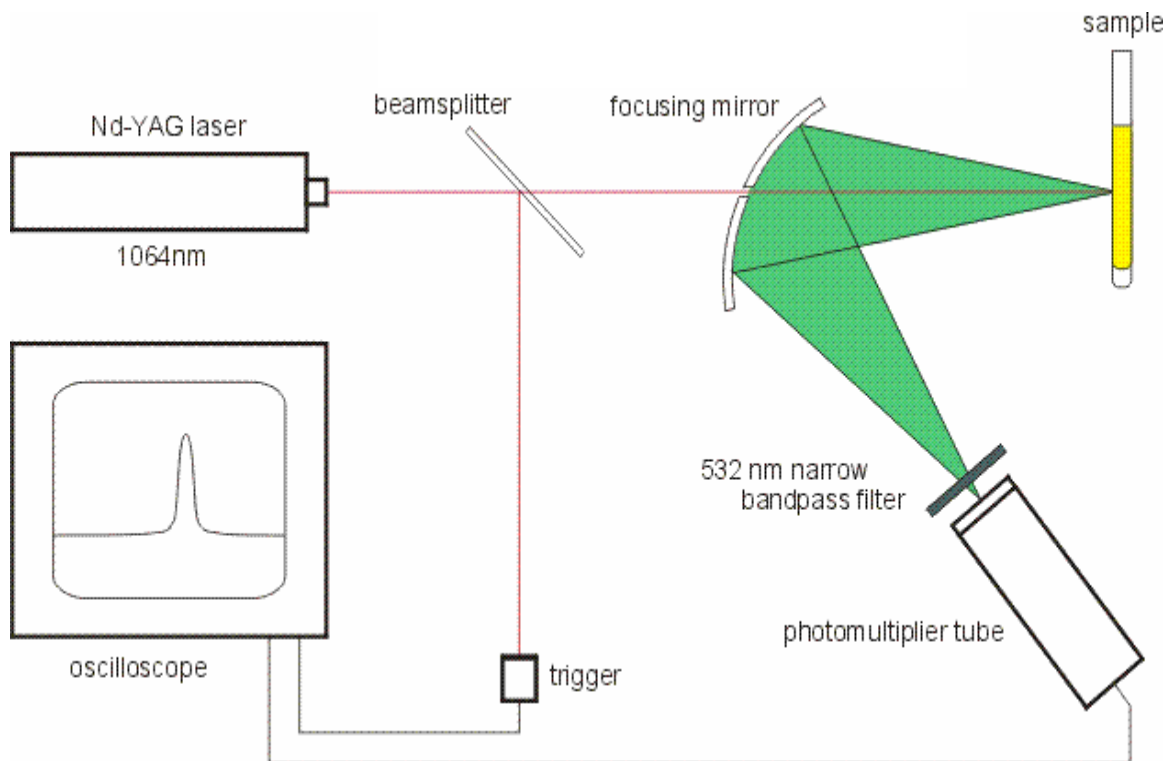


Figure 1.3. A modified Kurtz powder NLO instrument used to measure SHG activity.

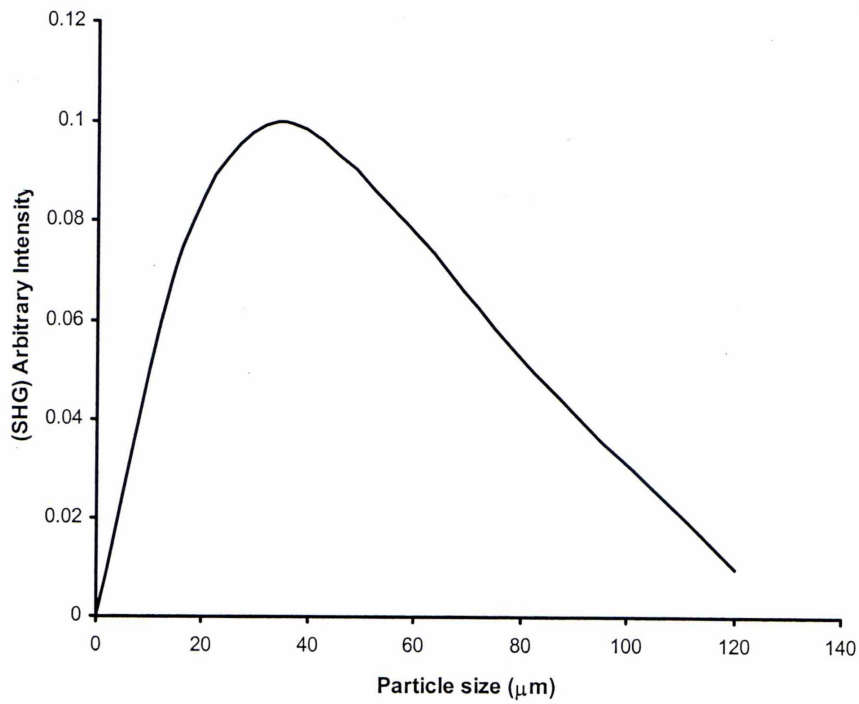
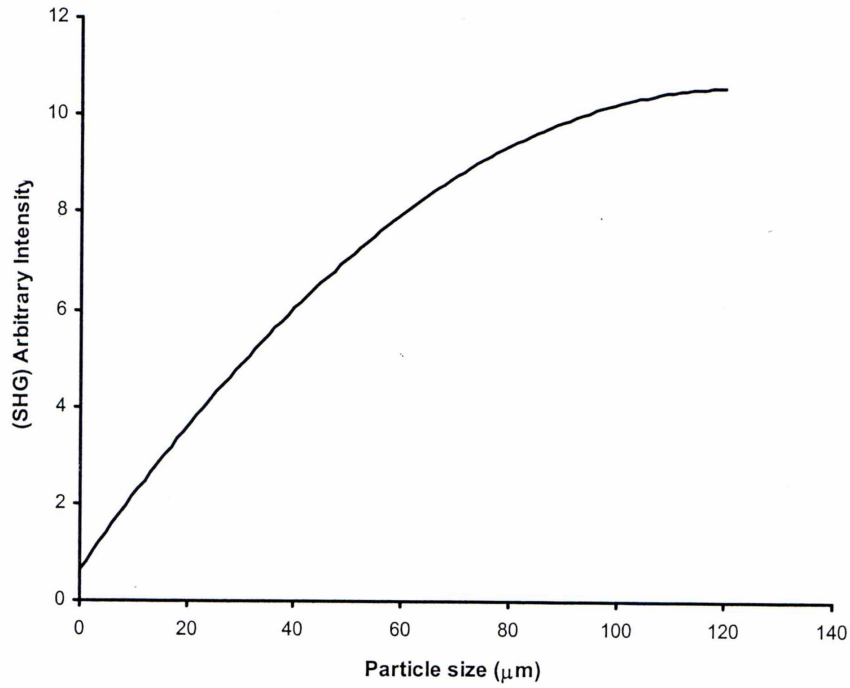


Figure 1.4. (top) A phase-matchable curve for a SHG material. (bottom) A non-phase-matchable curve for a SHG material.

relevant wavelengths, and the ability to withstand laser irradiation, and most importantly the materials must be crystallographically noncentrosymmetric (NCS). The interrelationships between NCS crystal classes was discussed in a review of Halasyamani and Poeppelmeier in 1998.¹⁸ It is necessary to point out that although all of SHG materials must have noncentrosymmetric structures, it is not correct to say all of these compounds possessing NCS exhibit SHG properties. As shown in Figure 1.2, 432(O), a NCS crystal class, is not SHG active. It is also shown that, besides SHG property, NCS can also have other interesting symmetry-dependent properties, including enantiomorphism (chirality), optical activity (circular dichroism), pyroelectricity (polar) and piezoelectricity.

Since first reported in 1968,¹⁹ Kurtz powder NLO measurements are becoming more popular for the evaluation of NLO materials. Before that, large single crystals (several mm) were required to investigate the SHG phenomenon. Figure 1.3 shows schematically a typical set-up for modified Kurtz powder NLO device. A commercially available Nd-YAG laser (1064 nm output), pulsed or continuous, is commonly selected as an incident light, since the radiation SHG light would appear at 532 nm (green) and could be observed by bare eyes.²⁰

The efficiency of a new NLO material is normally evaluated by comparing with some standard materials. As the first discovered NLO material, α -SiO₂ is used in many cases as a reference with NLO efficiency defined as 1.0 (dimensionless). Another traditional NLO standard material, LiNbO₃²¹ has an efficiency of 600 x α -SiO₂.

Actually, it is not accurate enough for evaluation of a new NLO material by just telling whether this material is NLO active and determining the efficiency. There are two types of NLO responses: phase matchable (type I) and non-phase-matchable (type II). For

type I materials, the phase velocity of the second-harmonic radiation is equal to that of the fundamental frequency.²¹ The efficiency of type I materials will increase with the particle size of powder and plateau at a maximum value. While for type II materials, their efficiency will reach a maximum and then decrease, as the particle size increases. Figure 1.4 (top) and Figure 1.4 (bottom) show schematically the phase matchable (LiNbO₃) and non-phase matchable (α -SiO₂) curves, respectively. Note that the curves are drawn to guide the eye, and are not fit to the real data. By running on a power NLO device, it is possible to determine if a new material is phase matchable or non-phase matchable and its bulk NLO susceptibility, $\langle d_{\text{eff}} \rangle$, can be calculated by applying these two equations below:

$$\langle d_{\text{eff}} \rangle_{\text{PM}} = [I^{2w} (A) / I^{2w} (\text{LiNbO}_3) \times 7.98 \times 10^2]^{1/2} \quad (1.3)$$

$$\langle d_{\text{eff}} \rangle_{\text{NPM}} = [I^{2w} (A) / I^{2w} (\alpha\text{-SiO}_2) \times 0.3048]^{1/2} \quad (1.4)$$

In equation 1.1 and equation 1.2, PM and NPM represent phase matchable and non-phase matchable, respectively, and $I^{2w} (A)$ is the intensity of unknown compound (A).

The most important NLO materials include β -BaB₂O₄, potassium titanyl phosphate (KTP), and MgO:LiNbO₃. These materials have been successfully applied in the amplification, modulation and conversion of the laser frequencies. Barium borate was first grown in needle-like crystalline form in 1968 and its sizeable single crystals were available in 1985. BaB₂O₄ exists in two distinct phases; a low-temperature β -phase and a high-temperature α -phase. The high-temperature α -phase of BaB₂O₄ is centrosymmetric and therefore does not possess any SHG properties. The low-temperature β -phase, on the other hand, has a non-centrosymmetric structure, and as such exhibits quadratic non-linearity. β -BaB₂O₄ has a wide transmission range, from approximately 200 nm to 3500

nm. and also has a broad phase-matchable range from 410 nm to 3500 nm. Its SHG coefficient is approximately 6 times greater than that of potassium dihydrogen phosphate (KDP). It has high damage threshold and resistance to thermal fracture. It is particularly useful for frequency conversion of high-intensity laser beam. However, since the crystal is relatively soft, polishing of the end faces can be difficult. It is also mildly hygroscopic and the polished surface can become fogged in humid air. KTP is commonly used for frequency doubling diode pumped solid-state lasers such as Nd:YAG and other neodymium-doped laser. It has relatively high optical damage threshold ($\sim 15 \text{ J/cm}^2$), a large optical nonlinearity (3 times greater than KDP) and excellent thermal stability. It has a Mohs hardness of about 5. However, it is prone to photochromic damage during high power 1064 nm wavelength SHG which tends to limit its use to low and medium power systems. MgO doped lithium niobate (MgO:LiNbO_3) has high refractive index and a high polarizability as a result of the lithium ion displacements in the ferroelectric phase and $\chi^{(2)}$ is 13 times greater than that of KDP. MgO is doped to increase the optical damage threshold. It is transparent for wavelength between 350 nm and 5200 nm and has a bandgap of around 4 eV. This material is used extensively in the telecoms market, eg. in the mobile telephones and optical modulators. However, the birefringence of MgO doped LiNbO_3 is highly temperature dependent, therefore, the crystal has to be accurately heated to achieve phase matching in this medium.

As mentioned above, although a large number of NLO materials have been developed and investigated, only limited amount of them are potentially useful owing to the simultaneous requirement for such characteristics as transparency, phase-matchability, high optical quality, nonlinearity, optical damage threshold and availability

in bulk form. Subsequently, intensive efforts are expended and continue today in search for new and better NLO materials. In the work, we applied hydrothermal method to grow new noncentrosymmetric compounds in crystal form. The products are normally stable in air and water. And if the mother solution of final product is acidic or basic, the crystals would be resistant to acid or base. The thermal stability of these compounds is generally investigated by Thermal Gravity Analysis (TGA) or Differential Scanning Calorimetry (DSC) in nitrogen or oxygen atmospheres. The transparency of these crystals in relevant wavelengths is studied by UV-Vis Diffuse Reflectance Spectroscopy.

Chemistry of Iodates and Selenites

It is well known that all SHG materials must have noncentrosymmetric (NCS) structures, therefore, the synthesis of new noncentrosymmetric compounds is of great importance for the development of SHG materials. At present, NCS compounds are produced mainly by incorporating noncentrosymmetric units into the architecture as building blocks. There are three major groups of noncentrosymmetric units: (1) Octahedrally coordinated d^0 transition metal cations (V^{5+} , Mo^{6+} , Nb^{5+} , W^{6+} , etc.) in which second-order Jahn-Teller distortion (SOJT) is prone to take place. (2) Some pyramidal ligands with nonbonding, but stereochemically active lone pair of electrons, such as IO_3^- or SeO_3^{2-} . (3) Large counter cations, like Cs^+ , Ba^{2+} , Ln^{3+} , which have irregular coordination environments.

In this work, the research of developing new SHG materials will focus on iodates and selenites of d-block and f-block elements. In the late 19th century, Blomstrand,²² Chrétien,²³ Rosenheim and Liebknecht,²⁴ et al., made a large number of transition metal

iodates and estimated the stoichiometry by elemental analysis. Then during the 1970's, Abrahams, Bernstein, Nassau, et. al. at Bell Lab rechecked most of previously reported transition metal iodates and synthesized several new lanthanide iodates.²⁵⁻³⁰ They studied the structures of these compounds by powder X-ray diffraction and single crystal X-ray diffraction, and also investigated some chemical and physical properties, including SHG, pyroelectric, piezoelectric, and magnetic properties with correlated instruments. In these compounds, such as $\text{Co}(\text{IO}_3)_2$,³¹ $\text{Cu}(\text{IO}_3)_2$,²⁷ and $\text{Ln}(\text{IO}_3)_3 \cdot n\text{H}_2\text{O}$ ($\text{Ln} = \text{Ce-Lu}$; $n = 0-6$),^{28,29} alignment of the pyramidal anion often occurs in these solids to create NCS structures, and the metals also impart additional electronic properties owing to the presence of unpaired electrons. Some selenite compounds of early transition metal, such as AVSeO_5 ($\text{A} = \text{Rb}^+, \text{Cs}^+$),³² $\text{A}(\text{VO})_3(\text{SeO}_3)_2$ ($\text{A} = \text{K}^+, \text{Cs}^+$),^{33,34,35} and $\text{A}_2(\text{MoO}_3)_3\text{SeO}_3$ ($\text{A} = \text{NH}_4^+, \text{K}^+, \text{Rb}^+, \text{or Cs}^+$)³⁶ were also found to be SHG active. In these compounds, both the selenite ligands and SOJT d^0 transition metal cations contribute to generate NCS structure. Besides the ability to produce NCS structures, both iodate and selenite are flexible ligands, they can have various binding modes to the metal center which results the plethora of structures (Figure 1.5). For instance, numerous selenite compounds of lanthanides were reported in a review written by Wickleder in 2003.³⁷

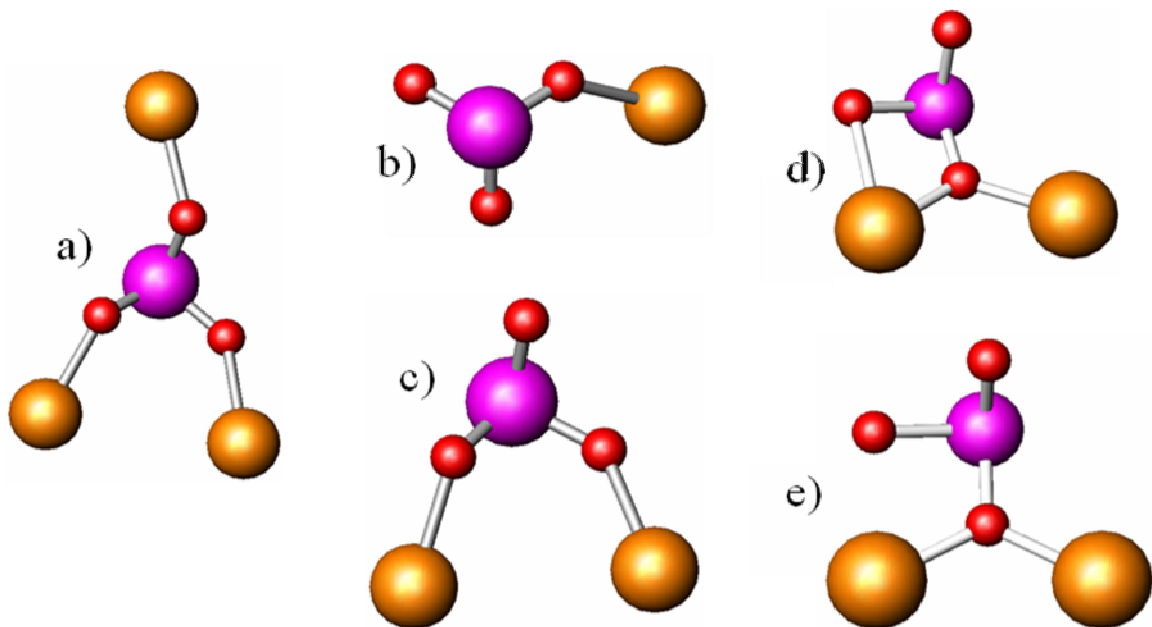


Figure 1.5. The various binding modes of the iodate, IO_3^- , anion to the metal center.

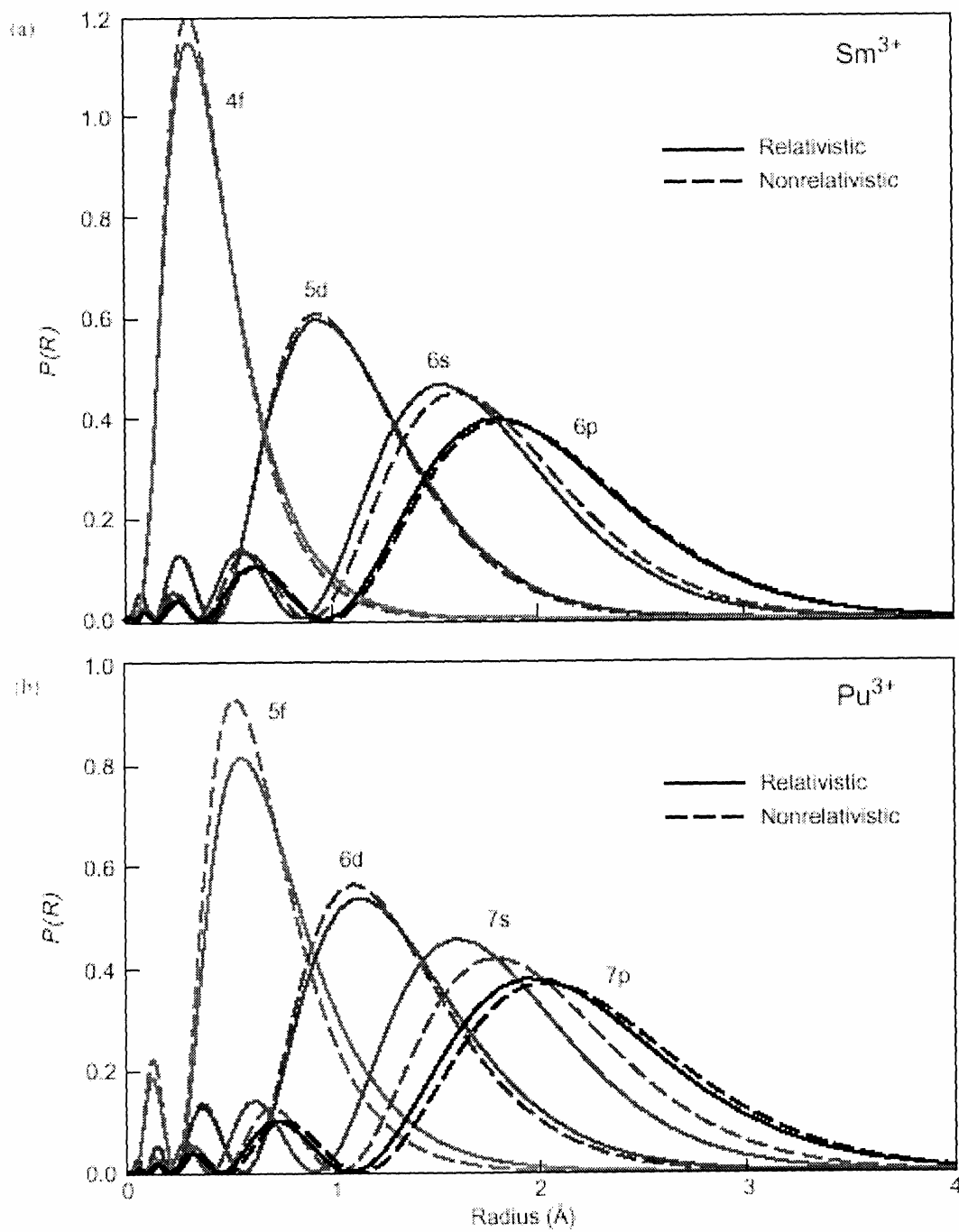


Figure 1.6. The radial probability of finding an electron from the nucleus of Sm^{3+} and Pu^{3+} . The broken lines demonstrate the nonrelativistic effect on the electrons.

Ac	Th	Pa	U	Np	Pu	Am	Cm
<u>+3</u>		+3	+3	+3	+3	<u>+3</u>	<u>+3</u>
	<u>+4</u>	<u>+4</u>	<u>+4</u>	<u>+4</u>	<u>+4</u>	<u>+4</u>	+4
		<u>+5</u>	+5	<u>+5</u>	+5	+5	
			<u>+6</u>	<u>+6</u>	+6	+6	
				+7	+7		

Figure 1.7. The oxidation states of the early actinide series. The environmentally important actinides are in bold.

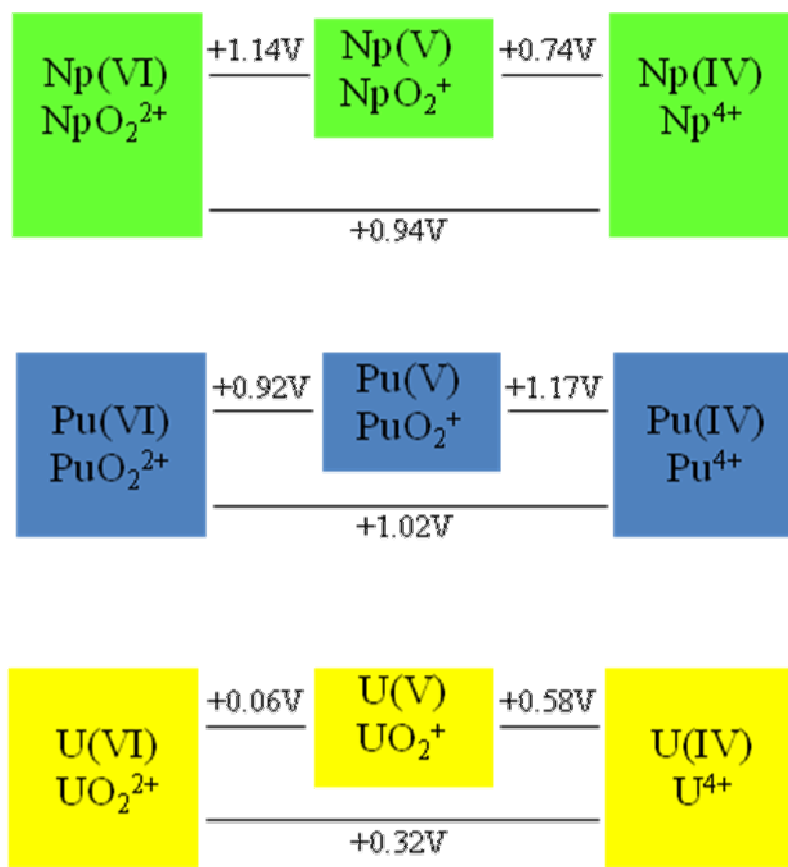


Figure 1.8. The redox potentials for Np, Pu and U in acidic media, demonstrating the close potential differences between oxidation states.

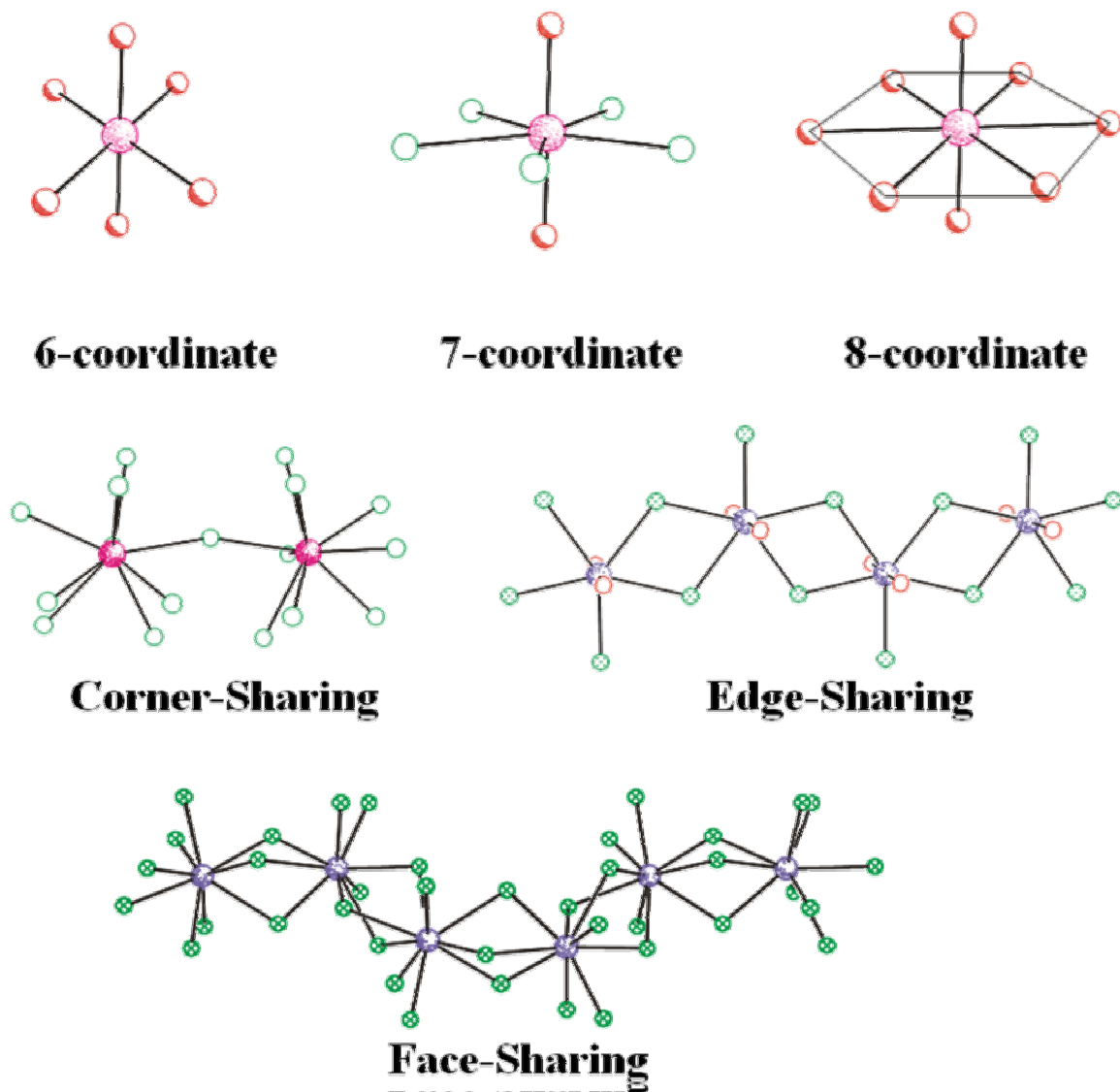
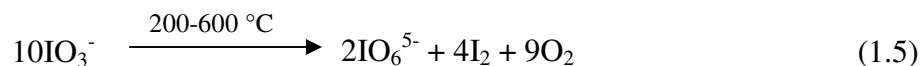


Figure 1.9. The UO_2^{2+} cation in tetragonal bipyramidal, pentagonal bipyramidal, and hexagonal bipyramidal environments as common building units for uranyl structure formation. They can be interconnected by corner-, edge-, or face-sharing with each other or other building units in order to construct different structure types.

As mentioned before, a large number of iodates and selenites of early transition metals and lanthanides have been made, and the structure-property relationships in these compounds have been well investigated. However, extremely limited information on noble metal iodates and selenites is available. Renewed interest in noble metal oxoanion compounds has led to the discovery of a plethora of remarkable solids including AuSO_4 ,³⁸ which contains a $\text{Au}^{\text{II}}\text{-Au}^{\text{II}}$ dimer, and polar $\text{Au}_2(\text{SeO}_3)_2(\text{SeO}_4)$,³⁹ which is constructed from square-planar Au^{III} and both selenite and selenate anions. Due to the inertness of noble metals to most acids, noble metal iodates and selenites can not be generated by reacting noble metal with acid directly under normal conditions, while for other noble metal sources, like their nitrates and chlorides, they are normally very stable and unreactive owing to the formation of strong bonds. Therefore, it is difficult to make iodate and selenite compounds through ligand exchange. Moreover, similar to other transition metal iodates, noble metal iodates are extremely insoluble, and they would precipitate quickly before crystallization can occur. In this work, new methods were developed to overcome these synthetic challenges, and several gold and palladium iodates and selenites have been successfully generated.

It is worth pointing out that iodates will disproportionate into metaperiodate and iodine at moderate to high temperatures as shown in equation 1.3. This thermal property indicates that traditional solid-state methods are not suitable for synthesis of iodate compounds. In contrast, the thermal disproportionation of iodate does not take place under mild hydrothermal conditions, which implies that this methodology is amenable for producing iodates.



Chemistry of Actinide Elements

Unlike the lanthanides which form a series of metals having very similar properties due to the lanthanide contraction, the actinides, as another series of *f*-block elements, are much more complex. Essentially, for the early actinides, they most resemble the early *d*-block metals with a tendency to possess various oxidation states and form stable complexes with ligands like sulfate, carbonate, chloride, and acetate. Unlike *4f* valence orbitals, which are deeply buried within atoms, *5f* valence orbitals extend more outward which allow more participation in covalent bonding. For instance, the difference of valence orbitals between *4f* in samarium (Sm^{3+}) and *5f* in plutonium (Pu^{3+}) is illustrated in Figure 1.6.⁴⁰ The relativistic effect of electrons within a heavier effective mass allow for more effective shielding of the electrons on inner orbitals, such as *s* and *p* orbitals, which results greater extension of *d* and *f* orbitals. As mentioned above, similar to early transition metals, the early actinides can possess a wide range of oxidation states, which results in more complicated chemistry of early actinides than that of lanthanides. As shown in Figure 1.7, except for thorium (Th) and curium (Cm), most of early actinides can possess three or more oxidation states in aqueous system. It is found that by adjusting the reaction conditions, like pH, it is possible to be able to control the oxidation state of these actinides. The most stable oxidation states of each actinides are underlined in Figure 1.7. In the case of uranium, if you take a look at its redox potentials (Figure 1.8), it is easy to understand that +6 is the most stable oxidation state in acidic media. It is

also shown in both Figure 1.7 and Figure 1.8 that Np^{+5} is the most stable oxidation state for neptunium in aqueous systems. For plutonium, it can have oxidation states of +4, +5 and +6 in solution. A very important characteristic for An^{+5} and An^{+6} ($\text{An} = \text{U}, \text{Np}$ and Pu) is that they normally exist as the *trans* dioxo cations, $\text{AnO}_2^+(\text{V})$ and AnO_2^{2+} , which are also called actinyl. Within these actinyl cations, the An-O bonds are relatively short (1.79(3) Å) and essentially linear ($\angle\text{O-An-O} \sim 180^\circ$). These two actinyl oxygen atoms are normally terminal and can not bind to any other cations. Owing to the existence of the actinyl unit, the further bonding of actinyl with other ligands (>2.1 Å) can occur only on the equatorial plane, which is perpendicular to the actinyl axis. These actinyl cations are typically coordinated by four, five or six ligands, arranged in the equatorial plane as square, pentagonal and hexagonal bipyramids, respectively (Figure 1.9). The bipyramids are capped by two O atoms of the actinyl cations. These actinyl polyhedral can be further linked together through different connecting modes, such as corner-sharing, edge-sharing and face-sharing, and results in the formation of various structures containing one-dimensional chains or two-dimensional sheets. As reported in a review paper by Burns in 2005,⁴¹ 85% of uranyl (UO_2^{2+}) cations have a five-coordinate environment, and 204 of 368 examined uranyl compounds contain infinite two dimensional sheets. Although some transition metals can have similar dioxo cations, such as VO_2^+ , MoO_2^{2+} , and WO_2^{2+} , these transition metal dioxo cations are *cis* with $\angle\text{O-M-O}$ about 110° . The actinides in lower oxidation states (+3 and +4) also exhibit a variety of coordination environments. For example, Pu^{4+} has been found to adopt an eight-coordinate dodecahedron or square anti-prism, a nine-coordinate tricapped trigonal prism, and a ten-coordinate bicapped square anti-prism. The lack of terminal dioxo atoms in lower oxidation state actinides increases

their coordination number and also elevates the likelihood of generating higher dimensional structures.⁴²⁻⁴⁵ In contrast, the late actinides starting from Americium (Am) tend to have lanthanide-like behavior, with a preference to the +3 oxidation state. This may be associated with the steady rise in ionization potentials across the series.

Iodate Chemistry of Spent Nuclear Fuel

Spent nuclear fuel (SNF), also called used nuclear fuel, is the product of nuclear fuel after the nuclear reaction. During the process of nuclear fission, uranium atoms within the nuclear fuel are split into smaller fission products, with large energy generated in the form of heat. These fission products will accumulate and interfere with efficiency until the fuel can no longer effectively produce energy. At this point, the used fuel is said to be "spent".

Although the fission by-products within the spent nuclear fuel can not produce more nuclear energy, they will continue to emit radiation until they achieve a stable form. This emission of energy is called radioactivity. Because of potential harm from radiation, the spent nuclear fuel must be disposed in deep geological formations, such as Yucca Mountain, where it has to be shielded and packed to prevent its migration into human environmental systems for a very long time until its radioactivity decreases naturally ("decays") to safe levels. According to United State Environmental Protection Agency (EPA) standards, the above natural decay process for spent nuclear fuel will take at least 10,000 years.

Thermal Neutron Fission of U-235

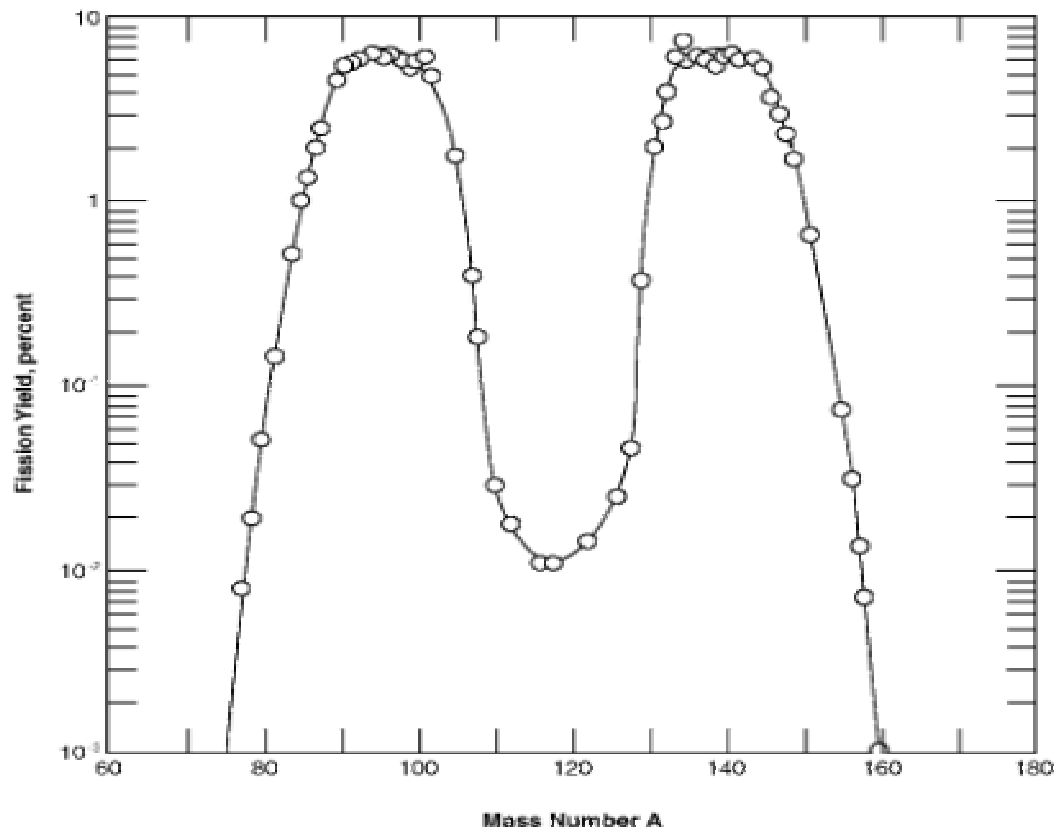


Figure 1.10. The wild variety of fission products of U²³⁵ in spent nuclear fuel.

Within the spent nuclear fuel, besides ^{238}U ($t_{1/2} = 4.46 \times 10^9$ years), 3% in mass of various fission products, including all elements from zinc to lanthanides, are generated by fission of uranium atoms. Among these fission products, some long-lived radionuclides, such as ^{90}Sr ($t_{1/2} = 28.9$ years), ^{137}Cs ($t_{1/2} = 30.2$ years), and ^{129}I ($t_{1/2} = 1.57 \times 10^7$ years), are of great importance in the issues of SNF waste disposal and environmental protection. Figure 1.10 shows the yields of fission products of ^{235}U versus their atomic weights. It is indicated that a nucleus of ^{235}U tends to produce two large but unequal nuclei, in the approximate mass ranges 90-100 and 130-145. It is necessary to point out that ^{129}I , as an important fission product, has a fission yield about 1%. Trace of transuranium actinides also present in the spent nuclear fuel. These include plutonium (^{239}Pu , $t_{1/2} = 2.41 \times 10^4$ years), neptunium (^{237}Np , $t_{1/2} = 2.14 \times 10^6$ years), americium (^{243}Am , $t_{1/2} = 7.38 \times 10^3$ years), and curium (^{247}Cm , $t_{1/2} = 1.56 \times 10^7$ years).

The goal of our SNF project is to investigate the possible chemical reactions which would take place in an environment containing spent nuclear fuel. In this work, the project will focus on the iodate chemistry of the actinide elements, especially for ^{238}U , ^{237}Np , and ^{239}Pu . It is well known that the initial forms of actinides in SNF are primarily the reduced forms, such as UO_2 , NpO_2 , and PuO_2 . While for ^{129}I , as a very bioavailable β -emitting radionuclide, it can exist in the forms of iodide (I^-), iodine (I_2), and iodate (IO_3^-) in the ground water taken from wells (e.g. J-13) near Yucca Mountain.⁴⁶ Owing to its high vapor pressure, iodine is expected to be concentrated on the surface and in grain boundaries in SNF and it can be oxidized into iodate by dissolved oxygen in water.⁴⁷ While I^- can not form strong complexes with actinide ions in aqueous media,⁴⁸ IO_3^- can form very stable, inner-sphere complexes with actinides.⁴⁹ Therefore, the products of the

reactions of actinides with iodate might play an important role in the potential release of the above mentioned long-lived radionuclides into the environment in the event of aged SNF contacting groundwater. It is necessary to point out that minute cracks and pores can be generated in the casings during the lifetime of stored SNF. This scenario will significantly limit the amount of water interacting with the nuclear waste. Herein, we show that the chemistry that occurs under hydrothermal conditions with limited amount of water can be dramatically different from what is predicted based on traditional homogeneous solution chemistry.⁵⁰

REFERENCES

1. Rabenau, A. *Angew. Chem. Int. Ed. Engl.* **1985**, 24, 1026.
2. Demianets, L. N.; Lobachev, A. N. *Curr. Top. In Mater. Sci.* **1981**, 7, 485.
3. Li, Y.; Burns, P. C. *J. Nuclear Mater.* **2001**, 299, 219.
4. Roy, R.; Tuttle, O. F. *Physics and Chemistry of the Earth*, Vol. 1, Ahrens, L. H.; Rankama, K.; Runcom, S. K. Eds., Pergamon, New York, **1956**, 138.
5. Barrer, R. M. *Hydrothermal Chemistry of Zeolite*, Academic Press, London, **1982**, 132.
6. Nacken, R. *Chem. Z.* **1950**, 74, 745.
7. Beuhler, E.; Walker, A. C.; *Ind. Eng. Chem.* **1950**, 42, 1369.
8. Lozcano, A. *Science*, **1993**, 260, 1154.
9. Balter, M. *Science*, **1998**, 280, 31.
10. Taro, O.; Akira, S. *Supercritical Water Reactor for Decomposition of Organic Materials in Water by Using Sub- or Supercritical Water*. Jpn. Kokai: Tokkyo Koho, JP10, **1998**, 314, 765.
11. Shevchenko, A. V.; Dudnik, E. V.; Ruban, A. K.; Danilenko, N. V.; Red'ko, V. P. *Powder Metallurgy and Metal Ceramics*, **2002**, 40, 544.
12. Guillot, M.; Richard-Plouet, M.; Vilminot, S. *J. Mater. Chem.* **2002**, 12, 851.
13. (a) Almond, P. M.; Deakin, L.; Mar, A.; Albrecht-Schmitt, T. E. *Inorg. Chem.* **2001**, 40, 886. (b) Almond, P. M.; Sykora, R. E.; Skanthakumar, S.; Soderholm, L.; Albrecht-Schmitt, T. E. *Inorg. Chem.* **2004**, 43, 958.

14. Kolis, J. W.; Korzenski, M. B. *Chemical Synthesis Using Supercritical Fluids*, **1999**, 213.
15. Kalinichev, A. G. *Reviews in Mineralogy & Geochemistry*, **2001**, 42,83
16. Norton, D. L. *Annu. Rev. Earth Planet Sci.* **1984**, 12, 155.
17. Jupp, R.; Schultz, A. *Nature*, **2000**, 880.
18. Halasyamani, P. S.; Poepelmeier, K. R. *Chem. Mater.* **1998**, 10, 2753.
19. Kurtz, S. K.; Perry, T. T. *J. Appl. Phys.* **1968**, 39,3798.
20. <http://www.chem.uh.edu/Faculty/Halasyamani/online/shg.html>.
21. Porter, Y.; Ok, K. M.; Bhuvanesh, N. S. P.; Halasyamani, P. S. *Chem. Mater.* **2001**, 13, 1910.
22. Blomstrand, C. W. *Z. Anorg. Chem.* **1892**, 1, 10.
23. Chretien, M. P. *Ann. Chim. Phys.* **1898**, 15, 358.
24. Rosenheim, A.; Liebknecht, O. *Liebigs Ann. Chem.* **1899**, 308, 40.
25. Abrahams, S. C.; Sherwood, R. C.; Bernstein, J. L.; Nassau, K. K. *Solid State Chem.* **1973**, 7, 205.
26. Nassau, K.; Cooper, A. S.; Shiever, J. W.; Prescott, B. E. *J. Solid State Chem.* **1973**, 8, 260.
27. Abrahams, S. C.; Sherwood, R. C.; Bernstein, J. L.; Nassau, K. *J. Solid State Chem.* **1973**, 8, 274,
28. Nassau, K.; Shiever, J. W.; Prescott, B. E.; Cooper, A. S. *J. Solid State Chem.* **1974**, 11, 314.
29. Nassau, K.; Shiever, J. W.; Prescott, B. E. *J. Solid State Chem.* **1975**, 14, 122.
30. Abrahams, S. C.; Bernstein, J. L.; Nassau, K. *J. Solid State Chem.* **1976**, 16, 173.

31. Nassau, K.; Shiever, J. W.; Prescott, B. E. *J. Solid State Chem.* **1973**, 7, 186.
32. Kwon, Y. U.; Lee, K. S.; Kim, Y. H. *Inorg. Chem.* **1996**, 35, 1161.
33. Vaughey, J. T.; Harrison, W. T. A.; Dussack, L. L.; Jacobson, A. J. *Inorg. Chem.* **1994**, 33, 4370.
34. Harrison, W. T. A.; Dussack, L. L.; Jacobson, A. K. *Acta Crystallorg. C* **1995**, 51, 2473.
35. Harrison, W. T. A. *Acta Crystallorg. C* **2000**, 56, 422.
36. (a) Harrison, W. T. A.; Dussack, L. L.; Jacobson, A. J. *Inorg. Chem.* **1994**, 33, 6043.
(b) Dussack, L. L.; Harrison, W. T. A.; Jacobson, A. J. *Mater. Res. Bull.* **1996**, 31, 249.
37. Wickleder, M. S. *Chem. Rev.* **2002**, 102, 2011
38. Wickleder, M. S. *Z. Anorg. Allg. Chem.* **2001**, 627, 2112.
39. Wickleder, M. S.; Buechner, O.; Wickleder, C.; El Sheik, S.; Brunklaus, G.; Eckert, H. *Inorg. Chem.* **2004**, 43, 5860.
40. Clark, D. L. *In Los Alamos Science: Challenges in Plutonium Science*, Number 26, 2000, 2, 382.
41. Burns, P. C. *Canada Mineralogist*, **2005**, 43, 1839.
42. Tanner, P. A.; Sze, T. H.; Mak, T. C.; Yip, W. H. *J. Crystallogr. & Spectro. Res.* **1992**, 22, 25
43. Sutorik, A. C.; Patschke, R.; Schindler, J.; Kannewurf, C. R.; Kanatzidis, M. G. *Chem.- A Eur. J.* **2000**, 6, 1601.
44. Piccoli, P. M. B.; Abney, K. D.; Schoonover, J. D.; Dorhout, P. K. *Inorg. Chem.* **2001**, 42, 2628.

45. Kim, J.; Norquist, A. J.; O'Hare, D. *J. Am. Chem. Soc.* **2003**, 125, 12688.
46. (a) Charlot, G. *Oxidation-Reduction Potentials*, Pergamon, London, 1958. (b) Bard, A. J.; Parsons, R.; Jordan, J. *Standard Potentials in Aqueous Solution*, Dekker, New York, 1985. (c) Bruchertseifer, H.; Cripps, R.; Guentary, S.; Jaeckel, B. *Anal. Bioanal. Chem.* **2003**, 375, 1107. (d) Huang, Z.; Ito, K.; Timerbaev, A. R.; Hirokawa, T. *Anal. Bioanal. Chem.* **2004**, 378, 1836.
47. Kaholek, M.; Triendl, L. *React. Kinet. Catal. Lett.* **1998**, 63, 297.
48. Crawford, M. J.; Ellern, A.; Karaghiosoff, K.; Mayer, P.; Noth, H.; Suter, M. *Inorg. Chem.* **2004**, 43, 7120.
49. (a) Choppin, G. R.; Khalili, F. I.; Rizkalla, E. N. *J. Coord. Chem.* **1992**, 26, 243. (b) Rao, P. R. V.; Patil, S. K. *Radiochem. Radioanal. Lett.* **1978**, 36, 169.
50. (a) Morss, L. R.; Edelstein, N. M.; Fuger, J. *The Chemistry of the Actinide and Transactinide Elements*, Springer, Heidelberg, 2006, Vol. 2, Ch. 6. (b) Katz, J. J.; Seaborg, G. T.; Morss, L. R. *The Chemistry of the Actinide Elements*, Chapman and Hall, New York, ed. 2, 1986, Vol. 1, Ch. 6.

CHAPTER 2

SYNTHESIS, STRUCTURES, AND PROPERTIES OF NOVEL GOLD AND PALLADIUM IODATES

ABSTRACT

Five new iodates of gold and palladium, $M^I\text{Au}(\text{IO}_3)_4$ ($M^I = \text{Na}, \text{K}, \text{Rb}$), $\text{K}_{2.5}\text{Pd}(\text{IO}_3)_4 \cdot \text{H}_{0.5}\text{IO}_3$, and $\text{Pd}(\text{IO}_3)_2$ have been prepared under mild hydrothermal conditions. $M^I\text{Au}(\text{IO}_3)_4$ and $\text{K}_{2.5}\text{Pd}(\text{IO}_3)_4 \cdot \text{H}_{0.5}\text{IO}_3$ have zero-dimensional structures. $M^I\text{Au}(\text{IO}_3)_4$ possess NCS structures that stem from the asymmetric $[\text{Au}(\text{IO}_3)_4]^-$ anions. Within these anions, four iodates are aligned on one side of the AuO_4 square plane. The structure of $\text{K}_{2.5}\text{Pd}(\text{IO}_3)_4 \cdot \text{H}_{0.5}\text{IO}_3$ has similar asymmetric $[\text{Pd}(\text{IO}_3)_4]^{2-}$ anions, but the individual anions are related through an inversion center, resulting in a centrosymmetric (CS) structure. In the structure of $\text{Pd}(\text{IO}_3)_2$, although Pd^{2+} also has a square planar geometry coordinated with four iodates through bridging oxygen atoms, four iodate anions sit on both sides of PdO_4 plane. The PdO_4 units are further joined together through two bidentated iodates to form a layer in the $[ab]$ plane. The layers are stacked along the c direction.

Crystallographic data: (193 K; Mo $K\alpha$, $\lambda = 0.71073 \text{ \AA}$): $\text{NaAu}(\text{IO}_3)_4$, triclinic, space group $P1$, $a = 5.4648(5) \text{ \AA}$, $b = 7.0082(7) \text{ \AA}$, $c = 8.1713(8) \text{ \AA}$, $\alpha = 105.897(2)^\circ$, $\beta = 95.280(2)^\circ$, $\gamma = 110.374(2)^\circ$, $V = 275.99(5) \text{ \AA}^3$, $Z = 1$; $\text{KAu}(\text{IO}_3)_4$, triclinic, space group

$P1$, $a = 5.6484(5) \text{ \AA}$, $b = 7.1935(7) \text{ \AA}$, $c = 8.1377(8) \text{ \AA}$, $\alpha = 105.264(2)^\circ$, $\beta = 93.585(2)^\circ$,
 $\gamma = 111.840(2)^\circ$, $V = 291.30(5) \text{ \AA}^3$, $Z = 1$; $\text{RbAu}(\text{IO}_3)_4$, monoclinic, space group $C2$, $a =$
 $13.5065(15) \text{ \AA}$, $b = 5.4540(6) \text{ \AA}$, $c = 8.3805(9) \text{ \AA}$, $\beta = 109.056(2)^\circ$, $V = 583.51(11) \text{ \AA}^3$, Z
 $= 2$; $\text{K}_{2.5}\text{Pd}(\text{IO}_3)_4 \cdot \text{H}_{0.5}\text{IO}_3$, monoclinic, space group $C2/m$, $a = 11.3270(13) \text{ \AA}$, $b =$
 $11.8246(14) \text{ \AA}$, $c = 12.9665(15) \text{ \AA}$, $\beta = 114.417(2)^\circ$, $V = 1581.4(3) \text{ \AA}^3$, $Z = 4$; $\text{Pd}(\text{IO}_3)_2$,
orthorhombic, space group $Pbca$, $a = 5.8308(8) \text{ \AA}$, $b = 6.0167(8) \text{ \AA}$, $c = 15.065(2) \text{ \AA}$, $V =$
 $528.5(1) \text{ \AA}^3$, $Z = 4$.

INTRODUCTION

Iodate compounds have been the subject of intense interest because of their propensity for adopting noncentrosymmetric structures that are often polar,¹⁻⁸ a feature that is aptly illustrated by $A[\text{MoO}_3(\text{IO}_3)]$ ($A = \text{Rb}, \text{Cs}$),⁹ $A[(\text{VO})_2(\text{IO}_3)_3\text{O}_2]$ ($A = \text{NH}_4, \text{Rb}, \text{Cs}$),¹⁰ and $\text{NaYI}_4\text{O}_{12}$.¹¹ This structural attribute can be exploited in the development of new nonlinear optical, pyroelectric, piezoelectric, and ferroelectric materials, with the first property being the most heavily investigated. Structure-property relationships in early d-block and f-block iodates are becoming well-developed.¹⁻¹¹ However, noble metal iodates are virtually unknown.¹²

Renewed interest in noble metal oxoanion compounds has led to the discovery of a plethora of remarkable solids including AuSO_4 , which contains a $\text{Au}^{\text{II}}\text{-Au}^{\text{II}}$ dimer,¹³ and polar $\text{Au}_2(\text{SeO}_3)_2(\text{SeO}_4)$, which is constructed from square-planar Au^{III} and both selenite and selenate anions.¹⁴ Despite repeated attempts over the past eight years, gold iodates have remained elusive for several reasons. First, common anions employed in gold reactions such as chloride and nitrate can interfere with the formation of these compounds. Second, iodate and periodate do not react appreciably with elemental gold, even under acidic conditions. Finally, as with many iodates, gold iodates are quite insoluble under normal conditions, precluding simple crystallization techniques. While for palladium compounds, no iodates have been reported yet.

In this work, concentrated selenic acid was chosen as a solvent to dissolve gold metal or palladium nitrate.^{15,16} The dissolved gold or palladium cations were then crystallized slowly with iodate during the cooling process. In the synthesis of gold iodates, periodate was applied as the source of iodate, it was slowly reduced to iodate by

water under hydrothermal condition^{9,17,18,19} which prevent the fast precipitation of gold iodate. The information about $\text{KAu}(\text{IO}_3)_4$ and $\text{K}_{2.5}\text{Pd}(\text{IO}_3)_4 \cdot \text{H}_{0.5}\text{IO}_3$ has been published as communication in *European Journal of Inorganic Chemistry*²⁰ and the remaining information is in preparation for publication.

EXPERIMENTAL

Syntheses. Gold metal, $\text{Pd}(\text{NO}_3)_2 \cdot 2\text{H}_2\text{O}$ (99.9%, Alfa-Aesar), HIO_3 (99.5%, Alfa-Aesar), NaIO_4 (99.8%, Alfa-Aesar), KIO_4 (99.9%, Alfa-Aesar), and RbIO_4 (99.9%, Alfa-Aesar) were used as received without further purification. Concentrated H_2SeO_4 solution was prepared by evaporating 40% H_2SeO_4 (Alfa-Aesar) at temperature around 200 °C. All of the four compounds were synthesized hydrothermally by heating at 200°C for 4 days and subsequently cooled to room temperature at a rate of 9 °C/h. Distilled and Millipore-filtered water with resistance of 18.2 $\text{M}\Omega \cdot \text{cm}$ was used in all reactions. SEM/EDX analyses were performed using a JEOL JSM-7000F. Sodium, potassium, rubidium, gold, palladium, and iodine standards were used to calibrate the results, and EDX ratios are within 3% of the ratios determined from single crystal X-ray diffraction experiments.

$\text{NaAu}(\text{IO}_3)_4$ was prepared by loading gold (74 mg, 0.375 mmol), NaIO_4 (285 mg, 1.332 mmol), 0.2 mL concentrated H_2SeO_4 solution, and 0.05 mL distilled and filtered water (Millipore) in a 23 mL PTFE-lined autoclave. The autoclave was sealed and heated at 200 °C in a box furnace. After 4 days, the furnace was cooled to room temperature at a rate of 9 °C/h. The product consisted of yellow crystals of $\text{NaAu}(\text{IO}_3)_4$ that had grown on the surface of unreacted gold metal, and a bright yellow solution, which was converted

into a yellow precipitate of $\text{Au}_2(\text{SeO}_3)_3$ when water was added. Yield for $\text{NaAu}(\text{IO}_3)_4$: 50 mg (15 % based on Au). EDX analysis provided a Na: Au: I ratio of 1:1:4 (17%:18%:65%).

$\text{KAu}(\text{IO}_3)_4$ was prepared by loading gold (70 mg, 0.355 mmol), KIO_4 (300 mg, 1.304 mmol), 0.2 mL concentrated H_2SeO_4 solution, and 0.05 mL distilled and filtered water (Millipore) in a 23 mL PTFE-lined autoclave. The autoclave was sealed and heated at 200 °C in a box furnace. After 4 days, the furnace was cooled to room temperature at a rate of 9 °C/h. The product consisted of yellow crystals of $\text{KAu}(\text{IO}_3)_4$ that had grown on the surface of unreacted gold metal, and a bright yellow solution, which was converted into a yellow precipitate of $\text{Au}_2(\text{SeO}_3)_3$ when water was added. Yield for $\text{KAu}(\text{IO}_3)_4$: 50 mg (15 % based on Au). EDX analysis provided a K: Au: I ratio of 1:1:4 (16%:17%:67%).

$\text{RbAu}(\text{IO}_3)_4$ was prepared by loading gold (71 mg, 0.360 mmol), RbIO_4 (363 mg, 1.312 mmol), 0.2 mL concentrated H_2SeO_4 solution, and 0.05 of distilled and filtered water (Millipore) in a 23 mL PTFE-lined autoclave. The autoclave was sealed and heated at 200 °C in a box furnace. After 4 days, the furnace was cooled to room temperature at a rate of 9 °C/h. The product consisted of yellow crystals of $\text{RbAu}(\text{IO}_3)_4$ that had grown on the surface of unreacted gold metal, and a bright yellow solution, which was converted into a yellow precipitate of $\text{Au}_2(\text{SeO}_3)_3$ when water was added. Yield for $\text{RbAu}(\text{IO}_3)_4$: 50 mg (15 % based on Au). EDX analysis provided a Rb: Au: I ratio of 1:1:4 (17%:18%:65%).

$\text{K}_{2.5}\text{Pd}(\text{IO}_3)_4 \cdot \text{H}_{0.5}\text{IO}_3$ was prepared by loading $\text{Pd}(\text{NO}_3)_2 \cdot 2\text{H}_2\text{O}$ (105.8 mg, 0.397 mmol), KIO_4 (284.2 mg, 1.236 mmol), and 0.5 mL distilled and filtered water (Millipore) in a 23 mL PTFE-lined autoclave. The autoclave was sealed and heated at 200 °C in a

box furnace. After 4 days, the furnace was cooled to room temperature at a rate of 9 °C/h. The product consisted of dark orange flakes of $\text{K}_{2.5}\text{Pd}(\text{IO}_3)_4 \cdot \text{H}_{0.5}\text{IO}_3$ and unreacted $\text{Pd}(\text{NO}_3)_2 \cdot 2\text{H}_2\text{O}$. Yield for $\text{K}_{2.5}\text{Pd}(\text{IO}_3)_4 \cdot \text{H}_{0.5}\text{IO}_3$: 54 mg (12 % based on Pd). EDX analysis provided a K:Pd:I ratio of 2.3:1:5.1 (27%:12%:61%).

$\text{Pd}(\text{IO}_3)_2$ was prepared by loading $\text{Pd}(\text{NO}_3)_2$ (185.4 mg, 1.091 mmol), HIO_3 (235.6 mg, 1.637 mmol), concentrated H_2SeO_4 (1 mL, 0.546 mmol), and 0.5 mL water in a 23-mL PTFE-lined autoclave. The autoclave was sealed and heated at 200 °C in a box furnace. After 4 days, the furnace was cooled to room temperature at a rate of 9 °C/h. The reaction product contained a single phase of dark orange crystals of $\text{Pd}(\text{IO}_3)_2$ immersed in a pale yellow mother liquor. The product was washed with water and methanol and allowed to dry. Yield: 271 mg (88.8% based on Pd). EDX analysis provided Pd:I ratio of 1:2 (32%:68%).

Crystallographic Studies. Tablets of $\text{NaAu}(\text{IO}_3)_4$, $\text{KAu}(\text{IO}_3)_4$, $\text{RbAu}(\text{IO}_3)_4$, $\text{K}_{2.5}\text{Pd}(\text{IO}_3)_4 \cdot \text{H}_{0.5}\text{IO}_3$, and $\text{Pd}(\text{IO}_3)_2$ with dimensions of 0.046 mm x 0.021 mm x 0.018 mm, 0.084 mm x 0.048 mm x 0.046 mm, 0.055 mm x 0.042 mm x 0.033 mm, 0.055 mm x 0.020 mm x 0.012 mm, and 0.092 mm x 0.089 mm x 0.023 mm, respectively, were mounted on thin glass fibers with epoxy, secured on a goniometer head, cooled to -80 °C with an Oxford Cryostat, and optically aligned on a Bruker SMART APEX CCD X-ray diffractometer using a digital camera. Intensity measurements were performed using graphite monochromated Mo-K α radiation from a sealed tube with a monocapillary collimator. SMART was used for preliminary determination of the cell parameters and data collection control. The intensities of reflections of a sphere were collected by a combination of 3 sets of exposures (frames). Each set had a different ϕ angle for the

crystal and each exposure covered a range of 0.3° in ω . A total of 1800 frames were collected with an exposure time per frame of 30 s for $\text{NaAu}(\text{IO}_3)_4$ and $\text{KAu}(\text{IO}_3)_4$, 10 s for $\text{RbAu}(\text{IO}_3)_4$ and $\text{Pd}(\text{IO}_3)_2$, and 60 s for $\text{K}_{2.5}\text{Pd}(\text{IO}_3)_4 \cdot \text{H}_{0.5}\text{IO}_3$, respectively.

Determination of integrated intensities and global cell refinement were performed with the Bruker SAINT (v 6.02) software package using a narrow-frame integration algorithm. An analytical absorption correction was applied followed by a semi-empirical absorption correction using SADABS.²¹ The program suite SHELXTL (v 6.12) was used for space group determination (XPREP), structure solution (XS), and refinement (XL).²² The final refinement included anisotropic displacement parameters for all non-hydrogen atoms and a secondary extinction parameter. Additional crystallographic details are listed in Table 2.1 and 2.2. Atomic coordinates and equivalent isotropic displacement parameters are given in Table 2.3 to Table 2.7.

Powder X-ray Diffraction. Powder X-ray diffraction patterns were collected with a Rigaku Miniflex powder X-ray diffractometer using $\text{Cu K}\alpha$ ($\lambda = 1.54056 \text{ \AA}$) radiation. The collected patterns were compared with that calculated from single crystal data using ATOMS.²³

Vibrational Spectroscopy. The IR spectra of $\text{KAu}(\text{IO}_3)_4$ and $\text{Pd}(\text{IO}_3)_2$ were taken from a sample in KBr with the spectrometer Shimadzu IR Prestige-21 in the wave number range of 4000 to 400 cm^{-1} . Raman spectroscopy experiments were performed at room temperature using backscattering geometry with 514.5 nm (2.41 eV) line of an argon-ion laser and an ISA U-1000 scanning double monochromator to disperse the Stokes Raman scattering spectra.

Thermal Analysis. For the investigation of the thermal behavior, 25 mg of $\text{KAu}(\text{IO}_3)_4$ and $\text{Pd}(\text{IO}_3)_2$ were placed in two platinum pans that were heated ($5\text{ }^\circ\text{C}/\text{min}$) up to $725\text{ }^\circ\text{C}$ under a nitrogen flow using a TGA Instruments Model Q50 V5.3 Build 171. The residue compositions were checked by powder X-ray diffraction.

UV-Vis Diffuse Reflectance Spectroscopy. Diffuse reflectance spectrum of $\text{KAu}(\text{IO}_3)_4$ was measured using a Shimadzu UV2501 spectrophotometer equipped with an integrating sphere attachment with BaSO_4 being used as the standard. The Kubelka-Monk function was used to convert diffuse reflectance data to absorption spectra.²⁴

Table 2.1. Crystallographic Data for NaAu(IO₃)₄, KAu(IO₃)₄, and RbAu(IO₃)₄.

Formula	NaAu(IO ₃) ₄	KAu(IO ₃) ₄	RbAu(IO ₃) ₄
Formula Mass	919.56	344.32	438.3
Color and habit	Yellow, block	Yellow, block	Yellow, block
Crystal system	Triclinic	Triclinic	Monoclinic
Space group	<i>P1</i> (No.1)	<i>P1</i> (No.1)	<i>C2</i> (No.2)
<i>a</i> (Å)	5.4648(5)	5.6484(5)	13.5065(15)
<i>b</i> (Å)	7.0082(7)	7.1935(7)	5.4540(6)
<i>c</i> (Å)	8.1713(8)	8.1377(8)	8.3805(9)
α (°)	105.897(2)	105.264(2)	90
β (°)	95.280(2)	93.585(2)	109.056(2)
γ (°)	110.374(2)	111.840(2)	90
<i>V</i> (Å ³)	275.99(5)	291.30(5)	583.5(1)
<i>Z</i>	1	1	2
<i>T</i> (K)	193	193	193
λ (Å)	0.71073	0.71073	0.71073
Maximum 2 θ (deg.)	56.56	56.58	56.56
ρ_{calcd} (g cm ⁻³)	5.533	5.567	5.589
$\mu(\text{Mo } K\alpha)$ (cm ⁻¹)	246.12	236.39	273.9
$R(F)$ for $F_o^2 > 2\sigma(F_o^2)$	0.0497	0.0289	0.0302
$R_w(F_o^2)^b$	0.1319	0.0762	0.0687

$$^a R(F) = \frac{\sum ||F_o| - |F_c||}{\sum |F_o|}. \quad ^b R_w(F_o^2) = \left[\frac{\sum [w(F_o^2 - F_c^2)^2]}{\sum wF_o^4} \right]^{1/2}.$$

Table 2.2. Crystallographic Data for $\text{K}_{2.5}\text{Pd}(\text{IO}_3)_4 \cdot \text{H}_{0.5}\text{IO}_3$ and $\text{Pd}(\text{IO}_3)_2$.

Compound	$\text{K}_{2.5}\text{Pd}(\text{IO}_3)_4 \cdot \text{H}_{0.5}\text{IO}_3$	$\text{Pd}(\text{IO}_3)_2$
Formula Mass	1116.24	456.2
Color and habit	Yellow, flake	Orange, block
Crystal System	Monoclinic	Orthorhombic
Space group	$C2/m$ (No. 12)	$Pbca$ (No.61)
a (Å)	11.3270(13)	5.8308(8)
b (Å)	11.8246(14)	6.0167(8)
c (Å)	12.9665(15)	15.065(2)
β (deg)	114.417(2)	
V (Å ³)	1581.4(3)	528.5(1)
Z	4	4
T (K)	193	193
λ (Å)	0.71073	0.71073
Maximum 2θ (deg.)	56.62	56.54
ρ_{calcd} (g cm ⁻³)	5.423	5.773
$\mu(\text{Mo } K\alpha)$ (cm ⁻¹)	116.67	151.5
$R(F)$ for $F_o^2 > \sigma(F_o^2)$ ^a	0.0277	0.0212
$R_w(F_o^2)$ ^b	0.0635	0.0515

$$^a R(F) = \frac{\sum ||F_o| - |F_c||}{\sum |F_o|}. \quad ^b R_w(F_o^2) = \left[\frac{\sum [w(F_o^2 - F_c^2)]^2}{\sum wF_o^4} \right]^{1/2}.$$

Table 2.3. Atomic Coordinates and Equivalent Isotropic Displacement Parameters for NaAu(IO₃)₄.

Atom	<i>x</i>	<i>y</i>	<i>z</i>	<i>U</i> _{eq} (Å ²) ^a
Na(1)	0.6272(29)	0.0571(22)	0.0613(20)	0.0232(25)
Au(1)	0.84903(17)	0.06296(15)	0.52142(13)	0.01125(27)
I(1)	0.2609(3)	-0.5955(3)	-0.0962(2)	0.0124(4)
I(2)	-0.0453(3)	-0.2403(3)	0.7490(2)	0.0125(4)
I(3)	0.3343 (3)	0.3651(3)	0.3887(2)	0.0126(4)
I(4)	0.9545(3)	-0.3033(3)	0.2182(2)	0.0118(4)
O(1)	0.9331(40)	-0.7141(40)	-0.2459(26)	0.0251(55)
O(2)	0.1076(44)	-0.6370(35)	0.0850(28)	0.0200(45)
O(3)	0.2739 (58)	-0.3043(35)	0.0663(38)	0.0754(68)
O(4)	-0.2877(35)	-0.1644(33)	0.6282(25)	0.0134(41)
O(5)	0.2360(41)	0.0298(32)	0.8219(29)	0.0180(41)
O(6)	-0.1932(41)	-0.2233(32)	0.9360(25)	0.0143(38)
O(7)	0.9725(38)	0.2903(35)	0.4071(28)	0.0151(42)
O(8)	0.3372(41)	0.1087(33)	0.2802(26)	0.0224(48)
O(9)	0.4744(38)	0.3882(27)	0.6104(27)	0.0152(45)
O(10)	0.7374(48)	-0.1561(32)	0.2869(25)	0.0170(43)
O(11)	0.0896(45)	-0.2990(37)	0.4286(26)	0.0178(45)
O(12)	0.6630(37)	-0.5507(30)	0.1458(27)	0.0125(39)

^a*U*_{eq} is defined as one-third of the trace of the orthogonalized **U**_{*ij*} tensor.

Table 2.4. Atomic Coordinates and Equivalent Isotropic Displacement Parameters for $\text{KAu}(\text{IO}_3)_4$.

Atom	x	y	z	$U_{\text{eq}} (\text{\AA}^2)^a$
K(1)	0.9432(10)	0.7912(7)	0.3537(6)	0.0139(9)
Au(1)	0.16068(13)	0.78797(11)	0.84000(10)	0.00879(19)
I(1)	0.6372(2)	0.09849(18)	0.70490(15)	0.0107(3)
I(2)	0.2529(2)	0.47603(17)	0.05007(14)	0.0093 (3)
I(3)	0.2629(2)	0.43593(17)	0.28440(4)	0.0093(3)
I(4)	0.5625(2)	0.13351(18)	0.22174(4)	0.0091(3)
O(1)	0.294(3)	0.024(2)	0.7395(19)	0.009(3)
O(2)	0.781(3)	0.119(3)	0.917(2)	0.019(3)
O(3)	0.622(4)	0.850(3)	0.589(2)	0.024(4)
O(4)	0.018(3)	0.555(2)	0.9381(19)	0.012(3)
O(5)	0.100(3)	0.471(3)	0.2362(18)	0.018(3)
O(6)	0.515(3)	0.739(2)	0.125(2)	0.014(3)
O(7)	0.071(3)	0.596(2)	0.6036(19)	0.010(3)
O(8)	-0.022(3)	0.194(2)	0.467(2)	0.018(3)
O(9)	0.405(4)	0.450(3)	0.744(2)	0.020(3)
O(10)	0.233(3)	-0.009(2)	0.0759(18)	0.013(3)
O(11)	0.436(3)	0.116(3)	0.4055(17)	0.019(4)
O(12)	0.571(3)	0.389(2)	0.222(2)	0.016(3)

^a U_{eq} is defined as one-third of the trace of the orthogonalized \mathbf{U}_{ij} tensor.

Table 2.5. Atomic Coordinates and Equivalent Isotropic Displacement Parameters for RbAu(IO₃)₄.

Atom	<i>x</i>	<i>y</i>	<i>z</i>	$U_{\text{eq}} (\text{\AA}^2)^a$
Rb(1)	0	0.8488(4)	0	0.0152(4)
Au(1)	0	0.01115(12)	1/2	0.01029(18)
I(1)	0.15396(6)	0.32245(14)	0.34532(9)	0.01128(19)
I(2)	0.17744(6)	0.27441(13)	0.83244(9)	0.01005(19)
O(1)	0.1187(6)	0.0091(19)	0.4112(10)	0.0136(16)
O(2)	0.0291(7)	0.3910(16)	0.1980(12)	0.0189(23)
O(3)	0.1487(6)	0.4893(20)	0.5265(10)	0.0165(18)
O(4)	0.1018(6)	0.9921(19)	0.7296(10)	0.0149(18)
O(5)	0.2972(6)	0.1872(17)	0.8010(11)	0.0154(20)
O(6)	0.1993(7)	0.1513(18)	0.0399(10)	0.0152(19)

^a U_{eq} is defined as one-third of the trace of the orthogonalized \mathbf{U}_{ij} tensor.

Table 2.6. Atomic Coordinates and Equivalent Isotropic Displacement Parameters for $\text{K}_{2.5}\text{Pd}(\text{IO}_3)_4 \cdot \text{H}_{0.5}\text{IO}_3$.

Atom	<i>x</i>	<i>y</i>	<i>z</i>	$U_{\text{eq}} (\text{\AA}^2)^a$
K(1)	0	0.25415(3)	0	0.0190(6)
K(1)	3/4	1/4	1/2	0.0265(6)
K(1)	0	0	1/2	0.0248(8)
Pd(1)	0.40283(5)	0	0.37419(5)	0.01139(13)
I(1)	0.64396(4)	0	0.28440(4)	0.01181(11)
I(2)	0.09694(4)	0	0.22174(4)	0.01357(12)
I(3)	0.37858(3)	0.24983(2)	0.25035(3)	0.01193(10)
I(4)	-0.26271(4)	0	-0.01821(4)	0.01504(12)
O(1)	0.5905(5)	0	0.3991(4)	0.0180(11)
O(2)	0.7582(3)	0.1145(3)	0.3369(3)	0.0197(8)
O(3)	0.2225(4)	0	0.3677(4)	0.0130(10)
O(4)	0.1547(3)	0.1141(3)	0.1612(3)	0.0328(9)
O(5)	0.5134(3)	0.3434(3)	0.3211(3)	0.0176(8)
O(6)	0.4468(3)	0.1523(3)	0.1802(3)	0.0175(8)
O(7)	0.4027(3)	0.1695(3)	0.3790(3)	0.0170(8)
O(8)	-0.1667(4)	0.1155(3)	0.0627(4)	0.0330(10)
O(9)	0.3782(6)	0	0.0507(6)	0.0361(16)

^a U_{eq} is defined as one-third of the trace of the orthogonalized \mathbf{U}_{ij} tensor.

Table 2.7. Atomic Coordinates and Equivalent Isotropic Displacement Parameters for Pd(IO₃)₂.

Atom	<i>x</i>	<i>y</i>	<i>z</i>	$U_{\text{eq}} (\text{\AA}^2)^a$
Pd(1)	1/2	1/2	0	0.00833(15)
I(1)	0.03615(4)	0.58818(4)	0.15158(2)	0.00821(13)
O(1)	-0.1125(5)	0.8268(5)	0.10448(19)	0.0110(6)
O(2)	0.1840(5)	0.5000(5)	0.05203(19)	0.0111(6)
O(3)	0.2558(5)	-0.0516(8)	0.21391(19)	0.0121(6)

^a U_{eq} is defined as one-third of the trace of the orthogonalized \mathbf{U}_{ij} tensor.

RESULTS AND DISCUSSION

Syntheses. The solution to the synthesis of a gold iodate proved to be the use of a strongly oxidizing mixed-anion system. In this case the reaction of elemental gold with concentrated selenic acid and KIO_4 under mild hydrothermal conditions results in the formation of $\text{K}[\text{Au}(\text{IO}_3)_4]$. As shown in Figure 2.1, single crystals of $\text{K}[\text{Au}(\text{IO}_3)_4]$ grow directly off the surface of the gold metal and ultimately passivate the surface. We speculate that selenic acid dissolves small quantities of the gold metal to yield a halo of Au^{III} that rapidly reacts with iodate to yield $\text{K}[\text{Au}(\text{IO}_3)_4]$ crystals. The in situ generation of iodate by the reduction of periodate by water is a critical feature of this reaction, because it allows the slow introduction of the key reactant that control the solubility.^{9,10,25}

In contrast to the difficulties in synthesizing $\text{K}[\text{Au}(\text{IO}_3)_4]$, the synthesis of its Pd^{II} analog, $\text{K}_{2.5}\text{Pd}(\text{IO}_3)_4 \cdot \text{H}_{0.5}\text{IO}_3$, proved to be quite straightforward as it can be prepared from the reaction of $\text{Pd}(\text{NO}_3)_2 \cdot 2\text{H}_2\text{O}$ with KIO_4 under mild hydrothermal conditions. Again the in situ reduction of IO_4^- to IO_3^- is utilized.

For the synthesis of $\text{Pd}(\text{IO}_3)_2$, concentrated selenic acid was added as a solvent to increase the solubility of $\text{Pd}(\text{NO}_3)_2 \cdot 2\text{H}_2\text{O}$. The attempts to make $\text{Pd}(\text{IO}_3)_2$ by reacting $\text{Pd}(\text{NO}_3)_2 \cdot 2\text{H}_2\text{O}$ directly with iodic acid failed.

Crystal Structures of $\text{M}^{\text{I}}\text{Au}(\text{IO}_3)_4$ ($\text{M}^{\text{I}} = \text{Na}, \text{K}, \text{Rb}$). The structure of $\text{KAu}(\text{IO}_3)_4$ is quite unusual in that it crystallizes in the lowest symmetry space group $P1$. The origin of the asymmetry becomes obvious by viewing the $[\text{Au}(\text{IO}_3)_4]^{1-}$ anion shown in Figure 2.2, and the packing of these anions in Figure 2.3. The $[\text{Au}(\text{IO}_3)_4]^{1-}$ anions contain square-planar Au^{III} bound by four monodentate iodate anions. As shown in Figure 2.2, all of the iodate anions in the $[\text{Au}(\text{IO}_3)_4]^{1-}$ anions are aligned on one side of

the AuO₄ square plane. Hence, these anions are highly polar, and pack in the lattice with identical orientation yielding a polar structure consistent with the space group. The Au-O bond lengths range from 1.981(9) Å to 1.987(9) Å, and are normal.²⁶ We have surveyed 28 high-resolution iodate crystal structures to arrive at a value of 1.792(5) Å for terminal I-O bonds. The terminal I-O bonds in the [Au(IO₃)₄]¹⁻ anions are normal in this respect. In contrast, I-O bond lengths for bridging or μ₂-O bonds from 32 different structures, show an average distance 1.831(5) Å. The bridging I-O bond lengths strain the normal limits and average 1.882(9) Å. The bridging I-O bond lengths are of a length expected for protonated moieties, suggesting polarization in the Au-O-I bonds. Some selected bond distances and bond angles in the structures of NaAu(IO₃)₄, NaAu(IO₃)₄ and NaAu(IO₃)₄ are listed in Table 2.8, Table 2.9, and Table 2.10, respectively. There are several other Au^{III} compounds with monodentate oxoanions that share features in common with the bonding found in K[Au(IO₃)₄]; these compounds include K[Au(NO₃)₄],²⁷ (H₅O₂)[Au(NO₃)₄]·H₂O,²⁸ and (ClO₂)[Au(ClO₄)₄].²⁹ In all three examples significant lengthening of the bridging E-O (E = N, Cl) bonds is observed.

Short contacts on the order of 2.5 to 2.8 Å between the oxygen atom from one iodate anion and the iodine atom of a neighboring iodate play a critical role in the structures of iodate compounds and minerals.³⁰ The importance of iodate...iodate interactions in the structure of KAu(IO₃)₄ can not be underestimated. We have previously shown that these interactions can lead to alignment of the lone pair of electrons on the iodate anions in Na₂[UO₂(IO₃)₄(H₂O)].³¹ This also occurs in the structure of KAu(IO₃)₄ where there are numerous intermolecular iodate...iodate interactions. These interactions stitch what appears to be a molecular structure into a complex polar network.



Figure 2.1. A photograph showing yellow crystals of $\text{K}[\text{Au}(\text{IO}_3)_4]$ that have grown directly on the surface of elemental gold under hydrothermal conditions. Crystals typically have maximum dimensions of several millimeters.

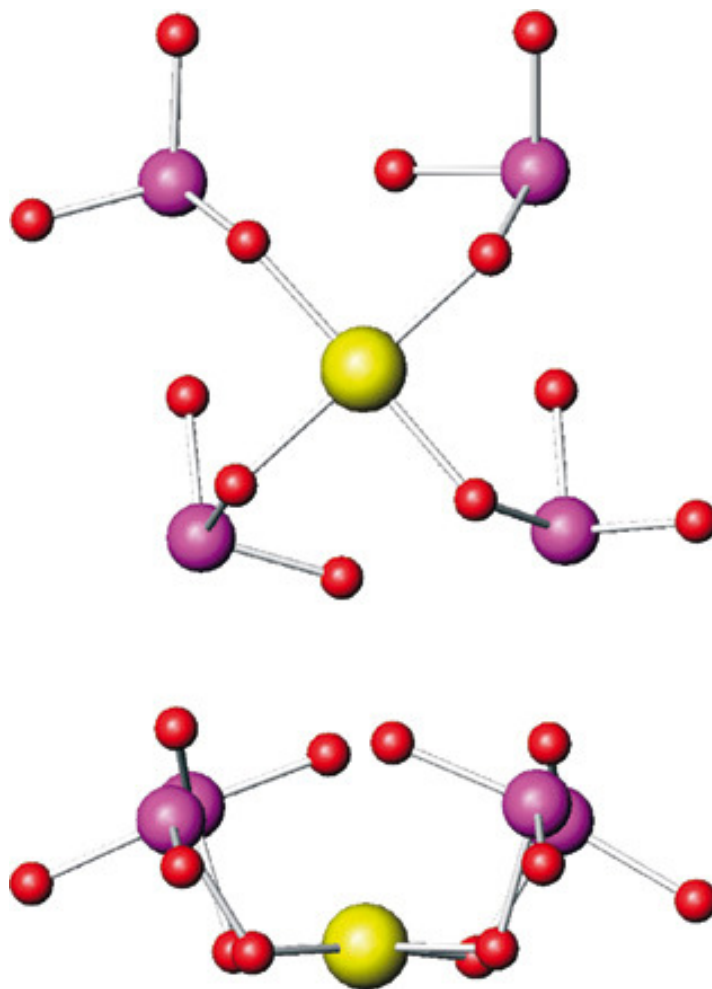


Figure 2.2. Two views of the $[\text{Au}(\text{IO}_3)_4]^{1-}$ anion in the structure of $\text{K}[\text{Au}(\text{IO}_3)_4]$. Gold is shown in yellow, iodine in magenta, and oxygen in red.

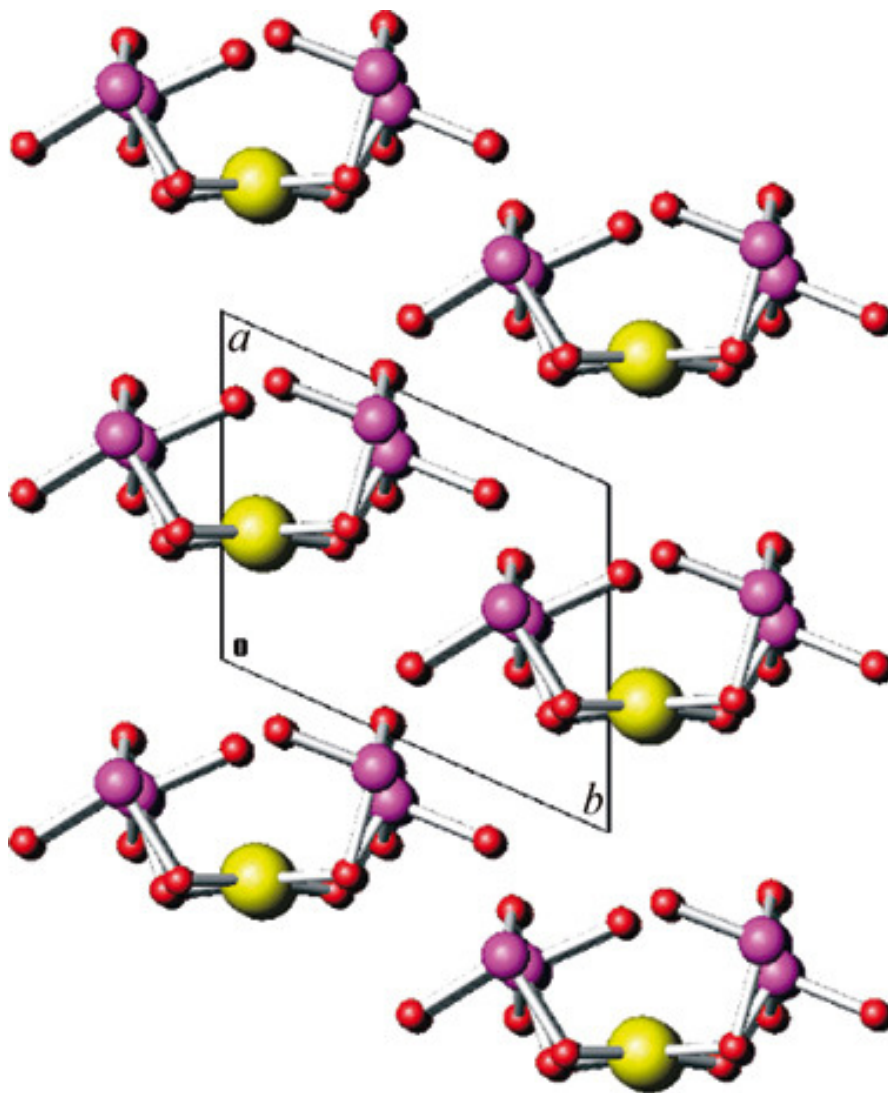


Figure 2.3. A view down the c axis of the structure of $\text{KAu}(\text{IO}_3)_4$ showing the polar stacking of the $[\text{Au}(\text{IO}_3)_4]^{1-}$ anions. K^+ cations have been omitted for clarity. Gold is shown in yellow, iodine in magenta, and oxygen in red.

Table 2.8. Selected Bond Distances (Å) and Angles (°) for NaAu(IO₃)₄.

Distances (Å)			
Au(1)-O(1)	1.995(20)	I(2)-O(5)	1.867(21)
Au(1)-O(4)	1.978(19)	I(2)-O(6)	1.788(18)
Au(1)-O(7)	2.012(20)	I(3)-O(7)	1.893(19)
Au(1)-O(10)	1.980(20)	I(3)-O(8)	1.779(21)
I(1)-O(1)	1.844(18)	I(3)-O(9)	1.841(19)
I(1)-O(2)	1.809(23)	I(4)-O(10)	1.856(20)
I(1)-O(3)	1.963(13)	I(4)-O(11)	1.795(18)
I(2)-O(4)	1.884(19)	I(4)-O(12)	1.799(19)

Angles (°)			
O(1)-Au(1)-O(4)	89.5(10)	O(4)-I(2)-O(5)	96.4(9)
O(1)-Au(1)-O(7)	91.5(11)	O(4)-I(2)-O(6)	94.2(9)
O(1)-Au(1)-O(10)	175.3(9)	O(5)-I(2)-O(6)	100.7(10)
O(4)-Au(1)-O(7)	177.6(8)	O(7)-I(3)-O(8)	101.5(10)
O(4)-Au(1)-O(10)	90.9(8)	O(7)-I(3)-O(9)	98.3(9)
O(7)-Au(1)-O(10)	88.0(8)	O(8)-I(3)-O(9)	97.3(8)
O(1)-I(1)-O(2)	91.8(10)	O(10)-I(4)-O(11)	98.2(10)
O(1)-I(1)-O(3)	90.7(12)	O(10)-I(4)-O(12)	88.7(9)
O(2)-I(1)-O(3)	97.9(10)	O(11)-I(4)-O(12)	102(1)

Table 2.9. Selected Bond Distances (Å) and Angles (°) for KAu(IO₃)₄.

Distances (Å)			
Au(1)-O(1)	1.981(9)	I(2)-O(5)	1.793(10)
Au(1)-O(4)	1.983(9)	I(2)-O(6)	1.818(9)
Au(1)-O(7)	1.988(9)	I(3)-O(7)	1.871(10)
Au(1)-O(10)	1.981(9)	I(3)-O(8)	1.774(10)
I(1)-O(1)	1.902(9)	I(3)-O(9)	1.810(9)
I(1)-O(2)	1.791(9)	I(4)-O(10)	1.873(9)
I(1)-O(3)	1.786(9)	I(4)-O(11)	1.783(10)
I(2)-O(4)	1.887(9)	I(4)-O(12)	1.823(9)

Angles (°)			
O(1)-Au(1)-O(4)	91.3(4)	O(4)-I(2)-O(5)	103.5(5)
O(1)-Au(1)-O(7)	177.6(4)	O(4)-I(2)-O(6)	98.5(4)
O(1)-Au(1)-O(10)	89.6(4)	O(5)-I(2)-O(6)	89.4(4)
O(4)-Au(1)-O(7)	88.7(4)	O(7)-I(3)-O(8)	100.1(5)
O(4)-Au(1)-O(10)	174.3(4)	O(7)-I(3)-O(9)	97.0(4)
O(7)-Au(1)-O(10)	90.2(4)	O(8)-I(3)-O(9)	100.1(4)
O(1)-I(1)-O(2)	96.8(4)	O(10)-I(4)-O(11)	91.8(4)
O(1)-I(1)-O(3)	94.6(4)	O(10)-I(4)-O(12)	97.6(5)
O(2)-I(1)-O(3)	100.8(5)	O(11)-I(4)-O(12)	93.2(4)

Table 2.10. Selected Bond Distances (Å) and Angles (°) for RbAu(IO₃)₄.

Distances (Å)			
Au(1)-O(1) x 2	1.976(7)	I(1)-O(3)	1.791(9)
Au(1)-O(4) x 2	1.969(8)	I(2)-O(4)	1.893(9)
I(1)-O(1)	1.904(10)	I(2)-O(5)	1.786(8)
I(1)-O(2)	1.775(9)	I(2)-O(6)	1.796(8)
Angles (°)			
O(1)-Au(1)-O(1')	179.4(6)	O(1)-I(1)-O(2)	96.9(4)
O(1)-Au(1)-O(4)	88.5(3)	O(1)-I(1)-O(3)	97.3(4)
O(1)-Au(1)-O(4')	91.4(3)	O(2)-I(1)-O(3)	101.0(4)
O(1')-Au(1)-O(4)	91.4(3)	O(4)-I(2)-O(5)	95.5(4)
O(1')-Au(1)-O(4')	88.5(3)	O(4)-I(2)-O(6)	91.7(4)
O(4)-Pd(1)-O(4')	179.4(6)	O(5)-I(2)-O(6)	99.9(4)

NaAu(IO₃)₄ also crystallizes in the lowest space group *P1* and its structure is very close to that of KAu(IO₃)₄. The selected bond distances and bond angles are listed in Table 2. Although RbAu(IO₃)₄ crystallizes in the higher symmetric monoclinic space group *C2*, its reduced unit cell also has *P1* symmetry. It has a very similar structure to that of KAu(IO₃)₄, and it also crystallizes in a polar structure.

Crystal Structure of K_{2.5}Pd(IO₃)₄·H_{0.5}IO₃. The complexation of Pd^{II} by four iodate anions yields [Pd(IO₃)₄]²⁻ anions. Unlike the [Au(IO₃)₄]¹⁻ anion, in which the bridging I-O bonds are slightly polarized with an average bond length of 1.882(9) Å, all I-O bond lengths in the [Pd(IO₃)₄]²⁻ anions are within the range of 1.790(4) to 1.865(5) Å, and no excessive lengthening of the bridging I-O bonds are observed. The [Pd(IO₃)₄]²⁻ anions are similar to [Au(IO₃)₄]¹⁻ in that all of the four iodate anions in the [Pd(IO₃)₄]²⁻ anions are aligned on one side of the PdO₄ square plane, as is shown in Figure 2.4. However, individual anions are related through inversion centers, and it crystallizes in the centrosymmetric space group *C2/m* (Figure 2.5). Selected bond distances and bond angles of K_{2.5}Pd(IO₃)₄·H_{0.5}IO₃ are listed in Table 2.11.

Crystal Structure of Pd(IO₃)₂. The structure of Pd(IO₃)₂ contains a crystallographically unique Pd(II) center in a classical four coordination environment with a square planar geometry. The Pd atom sits on an inversion center and is bound to four oxygen atoms belonging to four iodates. Unlike the other iodates described in this chapter, these four iodates sit on both sides of the PdO₄ plane (Figure 2.6). Within the [PdO₄] unit, the bond distances of Pd–O are 2.002(3) and 2.018(3) Å, and the angles of O–Pd–O are 88.8(1)° and 91.2(1)°, which are very close to an ideal planar square. Each [PdO₄] unit is connected to four neighboring [PdO₄] units through four bidentate iodate

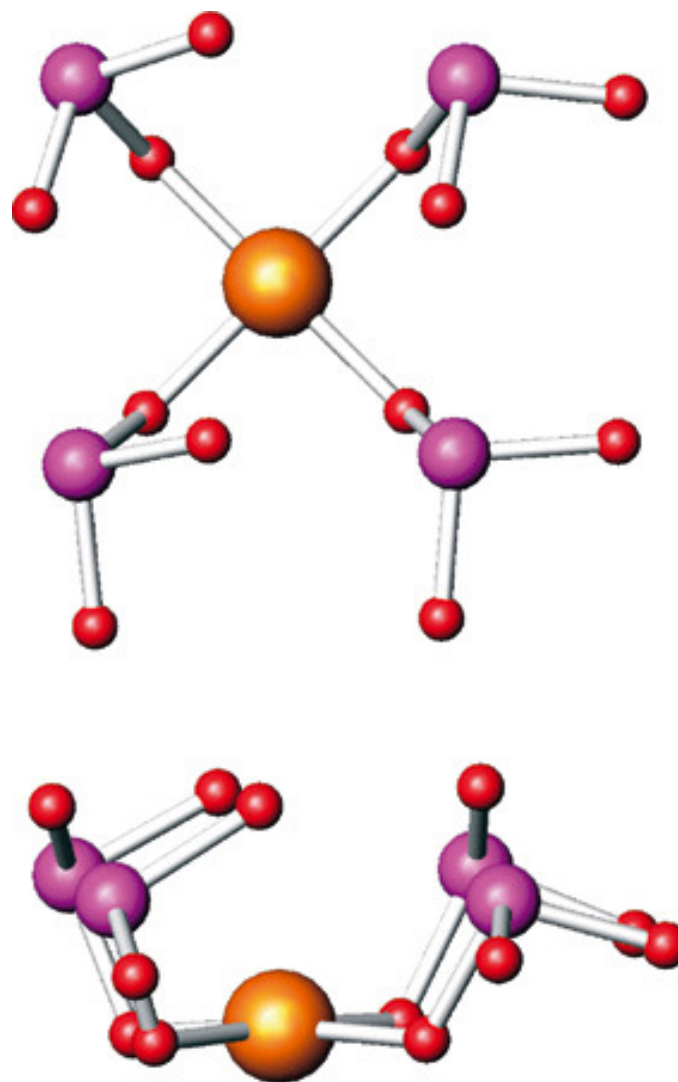


Figure 2.4. Two depictions of the $[\text{Pd}(\text{IO}_3)_4]^{2-}$ anion in the structure of $\text{K}_{2.5}\text{Pd}(\text{IO}_3)_4 \cdot \text{H}_{0.5}\text{IO}_3$. Palladium is shown in orange, iodine in magenta, and oxygen in red.

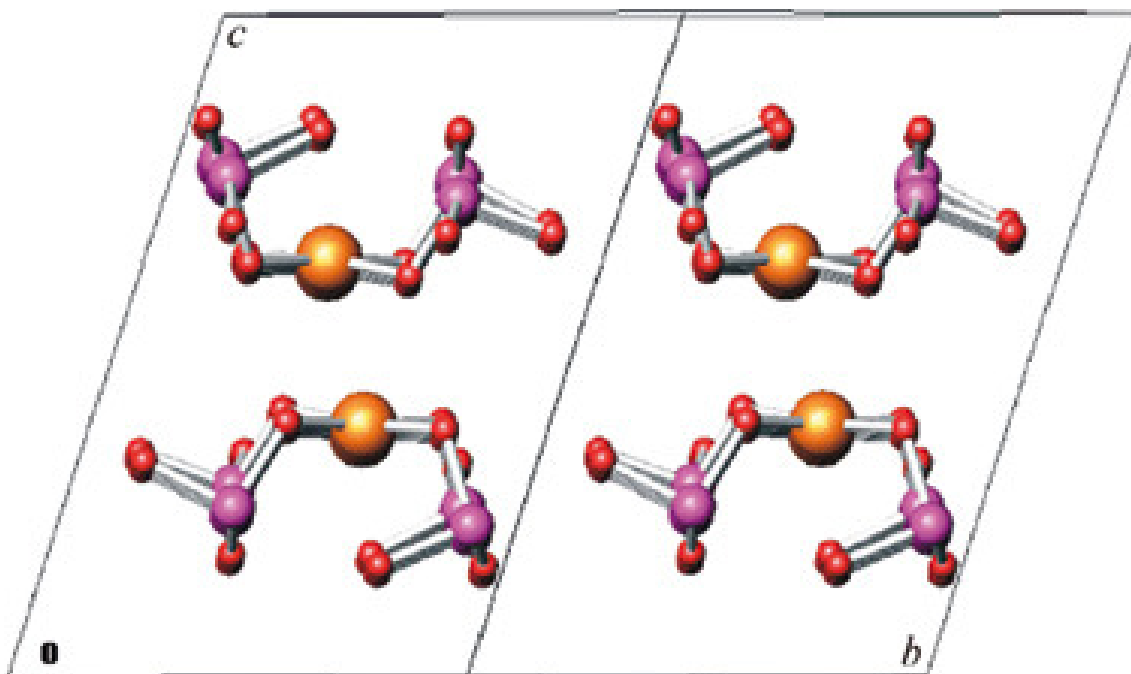


Figure 2.5. An illustration of the centrosymmetric packing of the $[\text{Pd}(\text{IO}_3)_4]^{2-}$ anions in $\text{K}_{2.5}\text{Pd}(\text{IO}_3)_4 \cdot \text{H}_{0.5}\text{IO}_3$. K^+ cations and iodate/iodic acid units have been omitted for clarity. Palladium is shown in orange, iodine in magenta, and oxygen in red.

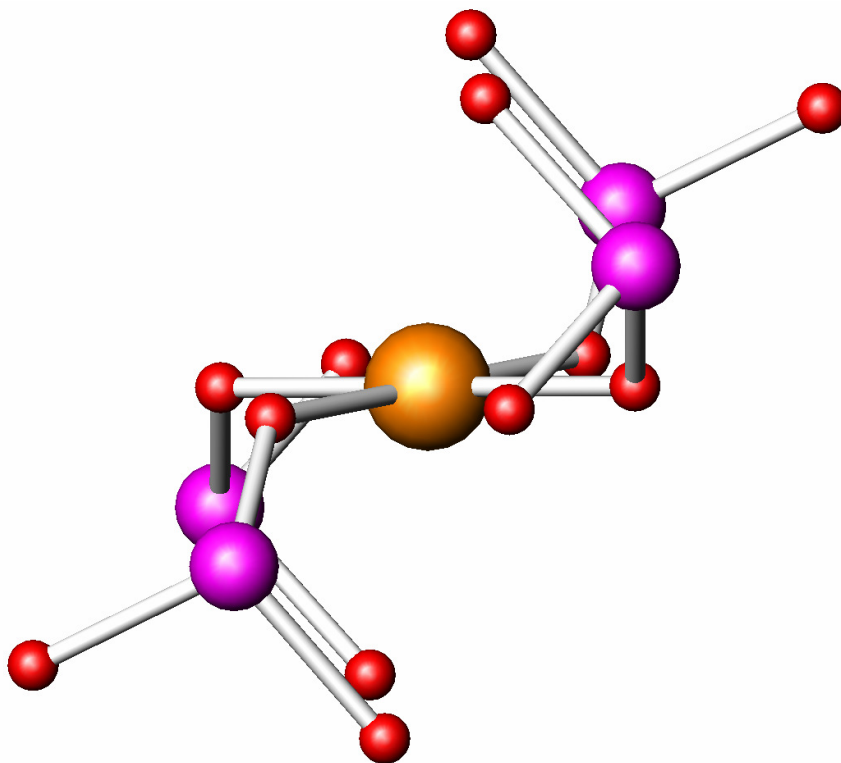


Figure 2.6. The depiction of the coordination environment of Pd²⁺ cations with iodate ligands in the structure of Pd(IO₃)₂. Palladium is shown in orange, iodine in magenta, and oxygen in red.

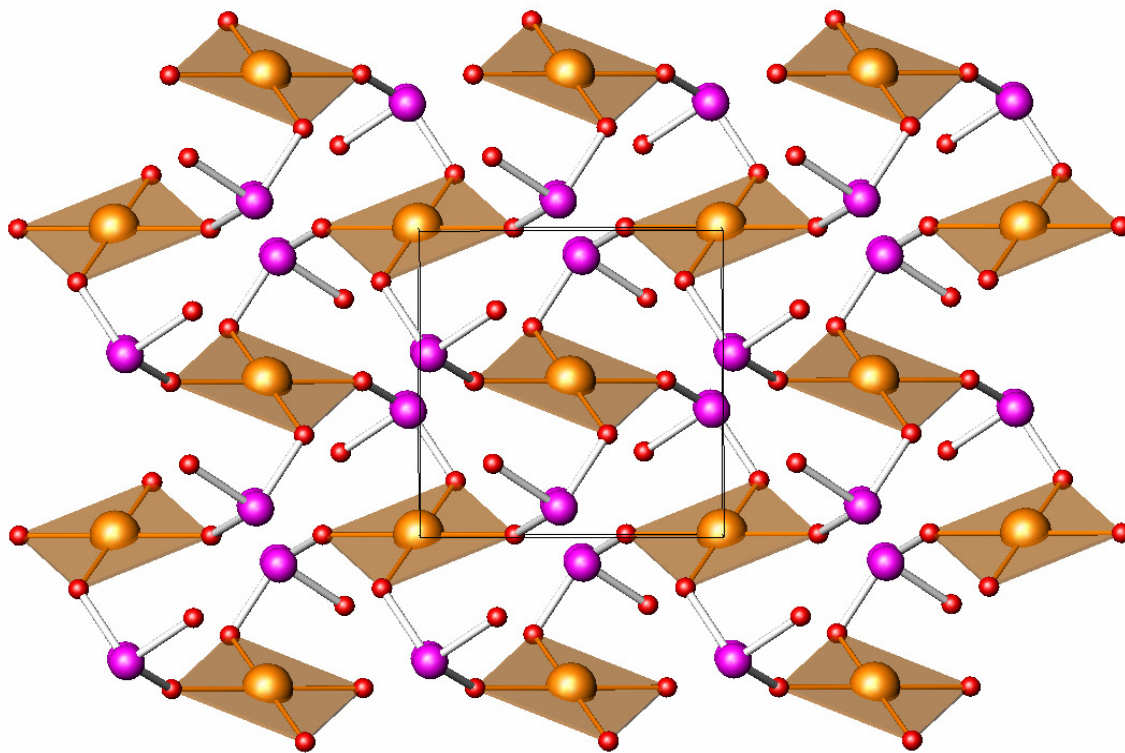


Figure 2.7. The depiction of the layered structure of $\text{Pd}(\text{IO}_3)_2$ in the $[ab]$ plane. Palladium square planes are shown in orange, iodine atoms in magenta, and oxygen atoms in red.

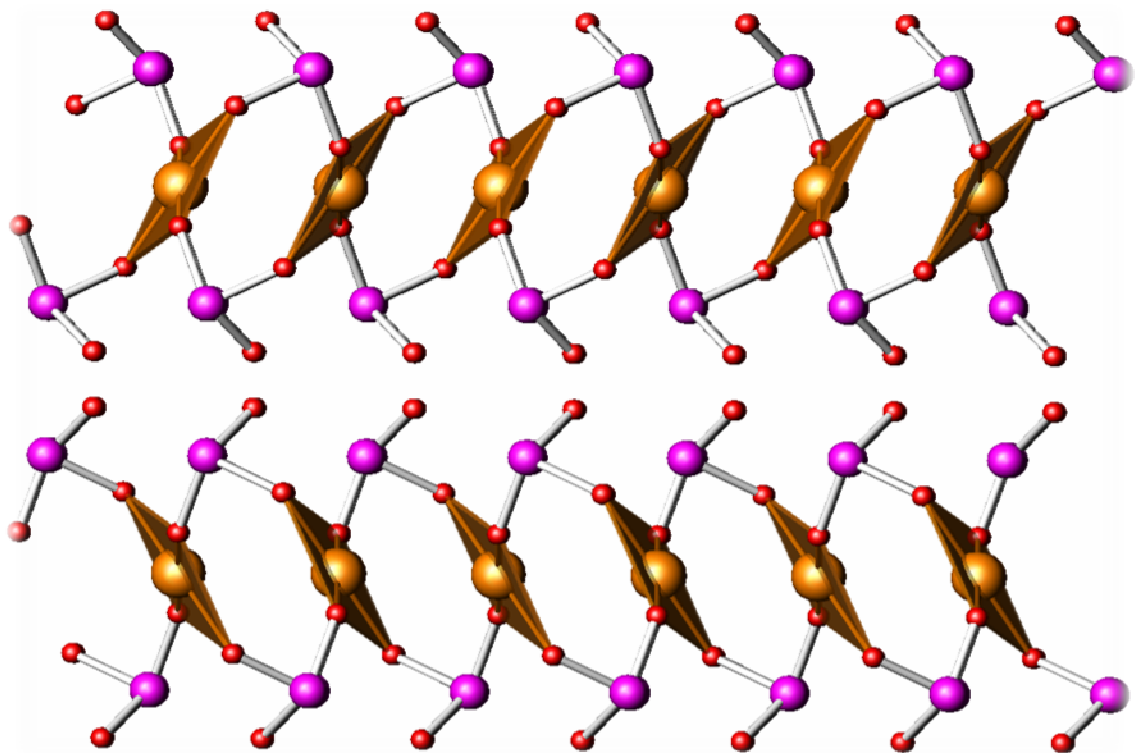


Figure 2.8. A depiction of the stacking mode in the layered structure of Pd(IO₃)₂ along the *c* axis. Palladium square planes are shown in orange, iodine atoms in magenta, and oxygen atoms in red.

Table 2.11. Selected Bond Distances (Å) and Angles (°) for $\text{K}_{2.5}\text{Pd}(\text{IO}_3)_4 \cdot \text{H}_{0.5}\text{IO}_3$.

Distances (Å)			
Pd(1)-O(1)	2.014(5)	I(2)-O(4) x 2	1.813(3)
Pd(1)-O(3)	2.009(4)	I(3)-O(5)	1.839(4)
Pd(1)-O(5) x 2	2.005(3)	I(3)-O(6)	1.827(3)
I(1)-O(1)	1.824(5)	I(3)-O(7)	1.800(3)
I(1)-O(2) x 2	1.801(3)	I(4)-O(8) x 2	1.790(4)
I(2)-O(3)	1.839(5)	I(1)-O(9)	1.865(5)

Angles (°)			
O(1)-Pd(1)-O(3)	173.8(2)	O(4)-I(2)-O(4)	96.2(3)
O(1)-Pd(1)-O(5)	90.5(1)	O(5)-I(3)-O(6)	94.5(2)
O(3)-Pd(1)-O(5)	89.3(1)	O(5)-I(3)-O(7)	101.4(2)
O(1)-I(1)-O(2)	96.9 (2)	O(6)-I(3)-O(7)	101.0(2)
O(2)-I(1)-O(2)	97.5(2)	O(8)-I(4)-O(9)	95.5(2)
O(3)-I(2)-O(4)	100.5(2)	O(8)-I(4)-O(8)	99.4(3)

Table 2.12. Selected Bond Distances (Å) and Angles (°) for Pd(IO₃)₂.

Distances (Å)			
Pd(1)-O(1) x 2	2.018(3)	I(1)-O(1)	1.849(3)
Pd(1)-O(2) x 2	2.002(3)	I(1)-O(2)	1.809(3)
		I(1)-O(3)	1.812(3)
Angles (°)			
O(1)-Pd(1)-O(1')	180.0(2)	O(1)-I(1)-O(2)	98.5(1)
O(1)-Pd(1)-O(2)	88.8(1)	O(1)-I(1)-O(3)	100.3(1)
O(1)-Pd(1)-O(2')	91.2(1)	O(2)-I(1)-O(3)	103.5(1)
O(1')-Pd(1)-O(2)	91.2(1)		
O(1')-Pd(1)-O(2')	88.1(1)		
O(2)-Pd(1)-O(2')	180.0(2)		

anions. The bridging bidentate IO_3^- has bond distances and angles range from 1.812(3) to 1.849(3) Å and 98.5(1)° to 103.5(1)°. The connection of $[\text{PdO}_4]$ units through bidentate IO_3^- anions is extended in the $[ab]$ plane to form a neutral molecular layer (Figure 2.7). The molecular layers further stack along the c axis (Figure 2.8). Selected bond distances and bond angles of $\text{K}_{2.5}\text{Pd}(\text{IO}_3)_4 \cdot \text{H}_{0.5}\text{IO}_3$ are listed in Table 2.12.

Vibrational Spectrum of $\text{KAu}(\text{IO}_3)_4$. The IR vibrational spectrum of $\text{K}[\text{Au}(\text{IO}_3)_4]$ (Figure 2.9) shows four weak bands at 519, 514, 503 and 499 cm^{-1} that are attributed to vibrations within the $[\text{AuO}_4]$ unit.^{32,33} Iodate stretching vibrations (ν_1 and ν_3) are found at 822, 803, 778, 765, 741, and 664 cm^{-1} .^{34,35,36} The Raman spectrum (Figure 2.10) shows two sharp peaks at 518 and 496 cm^{-1} that coincide well with the IR features. In addition, there is a broad envelope for the various iodate modes with discernible vibrational modes at 804, 769, 747, 738 and 683 cm^{-1} .

Vibrational Spectra of $\text{K}_{2.5}\text{Pd}(\text{IO}_3)_4 \cdot \text{H}_{0.5}\text{IO}_3$ and $\text{Pd}(\text{IO}_3)_2$. The critical feature of the vibrational spectrum of $\text{K}_{2.5}\text{Pd}(\text{IO}_3)_4 \cdot \text{H}_{0.5}\text{IO}_3$ is the presence of an I-OH stretch at 1180 cm^{-1} , confirming the protonation of the co-crystallized iodate moiety.³⁷ In addition, a low frequency band at 495 cm^{-1} is observed that might be attributable to a Pd-O stretching mode. A set of weak bands centered at 560 cm^{-1} can potentially be assigned to distortions of the $[\text{PdO}_4]$ square plane.^{38,39} Iodate stretching vibrations (ν_1 and ν_3) are found at 797, 782, 728, 696, 673 and 659 cm^{-1} .

In the IR vibrational spectrum of $\text{Pd}(\text{IO}_3)_2$ (Figure 2.11), a weak peak at 475 cm^{-1} can be attributed to vibrations within the $[\text{PdO}_4]$ unit. Several sharp peaks found at 803, 777, 752, 741, and 659 cm^{-1} are owing to the stretching vibrations (ν_1 and ν_3) of iodate. While in the Raman spectrum of $\text{Pd}(\text{IO}_3)_2$ (Figure 2.12), a weak peak around 453 cm^{-1} is

assigned to the vibrations within the $[\text{PdO}_4]$ unit. In addition, there are several peaks for the various iodate modes with discernible vibrational modes at 821, 807, 772, 741, 701 and 685 cm^{-1} .

Thermal Behavior of $\text{KAu}(\text{IO}_3)_4$ and $\text{Pd}(\text{IO}_3)_2$. The TGA curve shows $\text{KAu}(\text{IO}_3)_4$ is thermally stable up to $375 \text{ }^\circ\text{C}$ (Fig. 2.13). The first weight loss is in the temperature range of $376\text{--}472 \text{ }^\circ\text{C}$, and may correspond to the decomposition of $\text{KAu}(\text{IO}_3)_4$ into Au powder and KIO_3 . The observed weight loss of 21.7% is in good agreement with the calculated value (21.1%). The second weight loss starts from 500°C and can be attributed to disproportionation of iodate into iodine and periodate.

Similar to the thermal behavior of $\text{KAu}(\text{IO}_3)_4$,²⁵ the TGA data for $\text{Pd}(\text{IO}_3)_2$ also shows a two-step weight loss. As shown in Figure 2.14, $\text{Pd}(\text{IO}_3)_2$ is stable up to $325 \text{ }^\circ\text{C}$. The weight loss in the temperature range from 325 to $420 \text{ }^\circ\text{C}$ is due to decomposition of $\text{Pd}(\text{IO}_3)_2$. The observed weight loss of 28.2% is close to the theoretical value of 23.3%. The second weight loss starts from $550 \text{ }^\circ\text{C}$ is due to the disproportionation of iodate.

UV-Vis Diffuse Reflectance Spectroscopy of $\text{KAu}(\text{IO}_3)_4$. The transparency in the energy regions of interest is very important for potential NLO materials since minimal absorbance of the initial and the induced SHG lights can reduce laser damage to the materials and enhance their efficiency. In addition, the electronic spectra of these compounds can provide some fundamental information on the nature of conduction in these extended structures. UV-Vis diffuse reflectance spectrum of $\text{KAu}(\text{IO}_3)_4$, collected on the fine powders ground from its crystalline phase, is shown in Figure 2.15 within the energy range of 1 to 6 eV. As shown in Figure 2.15, $\text{KAu}(\text{IO}_3)_4$ is essentially transparent at wavelengths of 1064 nm and 532 nm, which represent the wavelengths of initial source

light and reduced SHG light, respectively. Extrapolation of absorbance⁴⁰ versus energy to absorbance equal to 0 provides an approximate band gap of 2.90 eV.^{41,42}

CONCLUSIONS

In conclusion, we have demonstrated that five new noble-metal iodates can be prepared under mild hydrothermal conditions. These compounds are the first members in a new family of noble-metal iodate compounds containing square-planar metal ions. The importance of these compounds lies in their ability to form polar structures that may allow for the development of new nonlinear optical, piezoelectric, pyroelectric, and ferroelectric materials. The structures of these new compounds were investigated by X-ray diffraction. In addition to the X-ray diffraction study, several other measurements, including IR, Raman, TGA and UV-Vis Diffuse Reflectance Spectrum were made with $\text{KAu}(\text{IO}_3)_4$ in order to make a more comprehensive investigation on its physical and chemical properties.

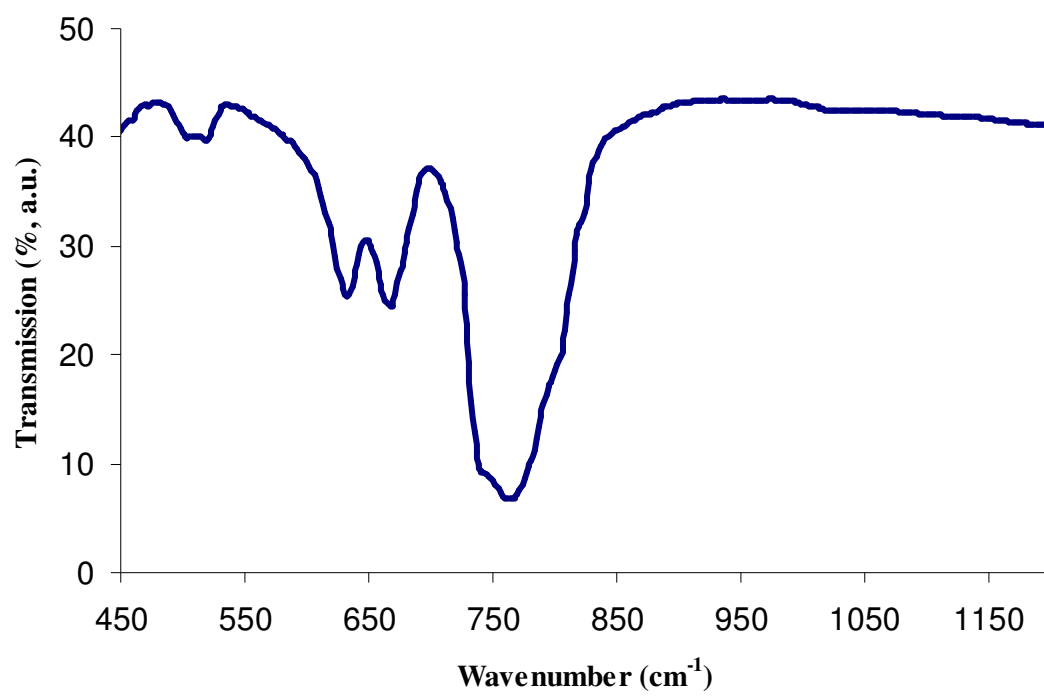


Figure 2.9. The IR spectrum of KAu(IO₃)₄.

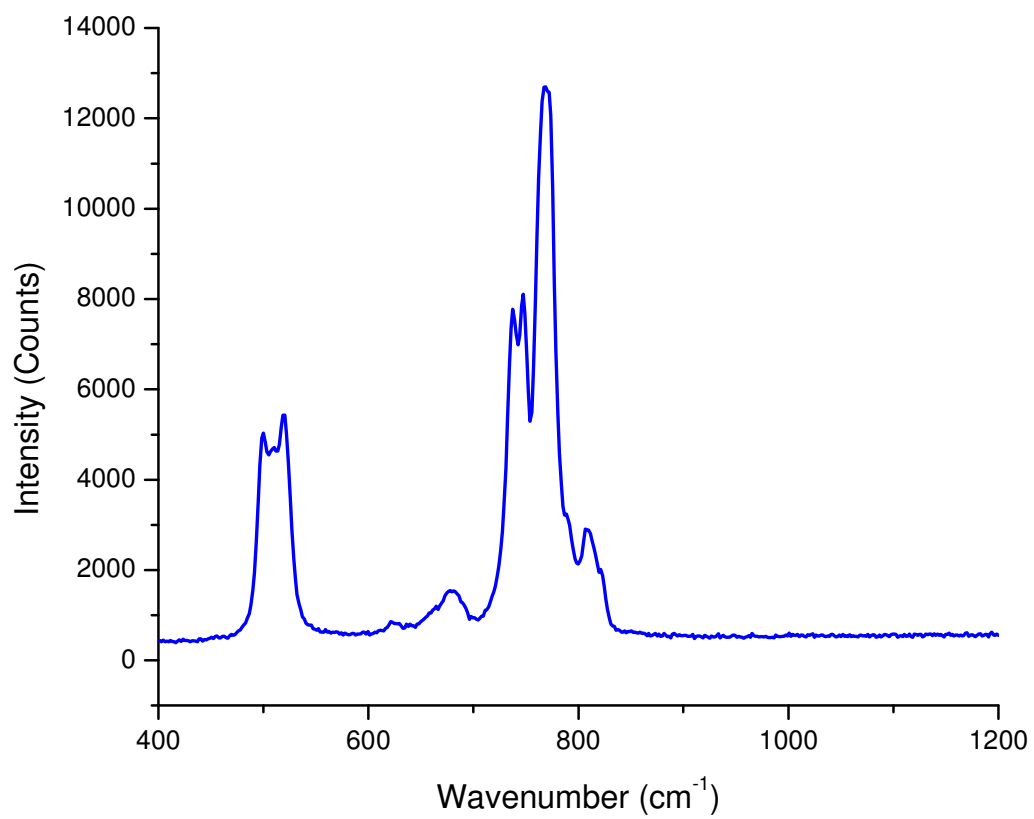


Figure 2.10. The Raman spectrum of KAu(IO₃)₄.

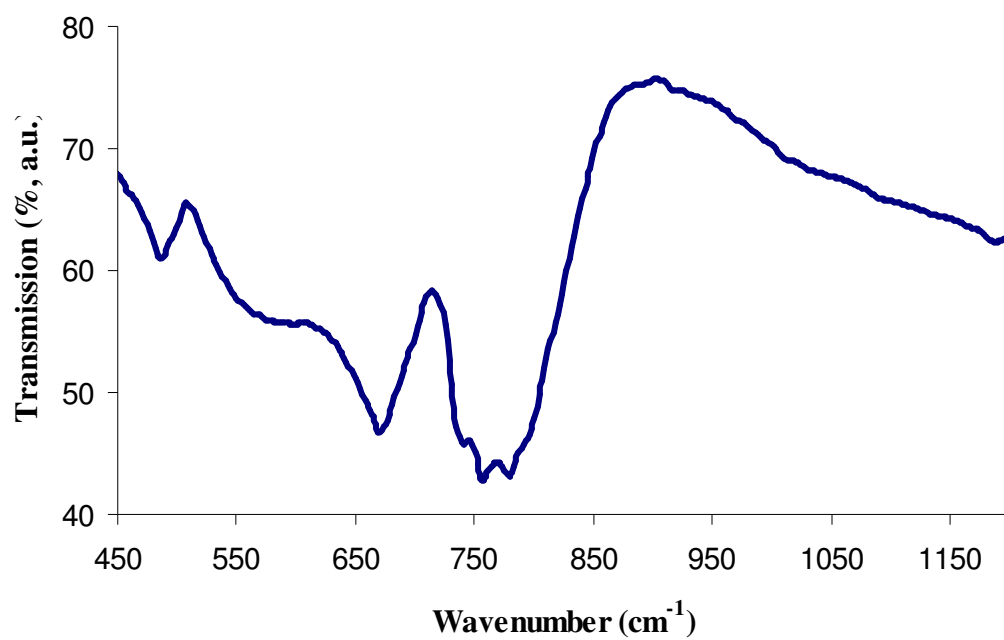


Figure 2.11. The IR spectrum of Pd(IO₃)₂.

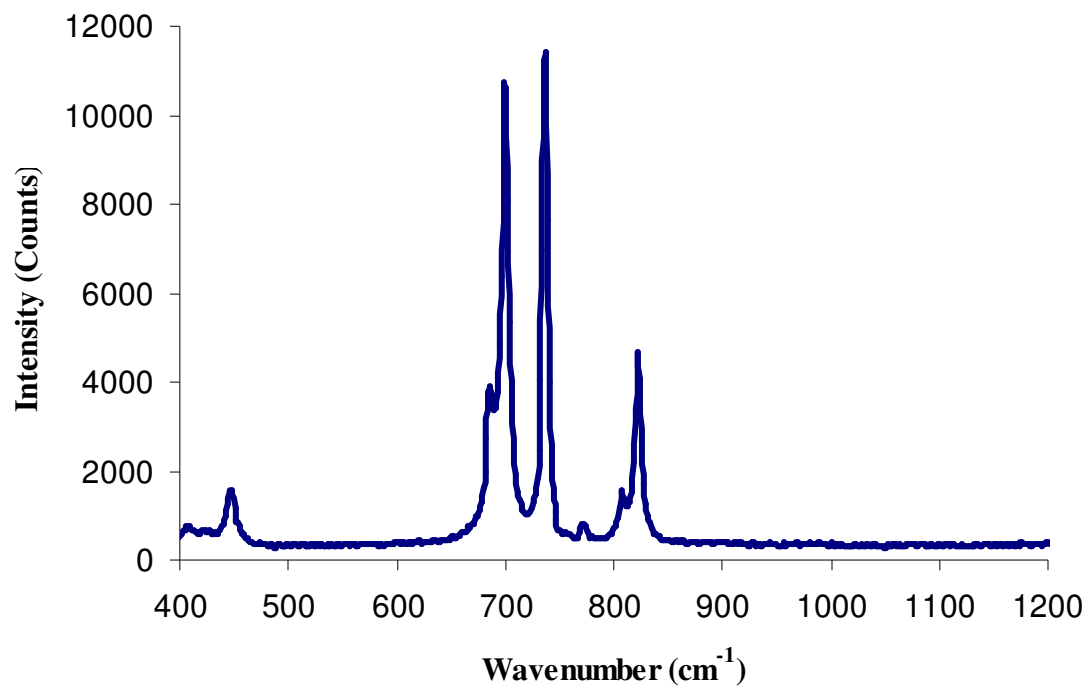


Figure 2.12. The Raman spectrum of Pd(IO₃)₂.

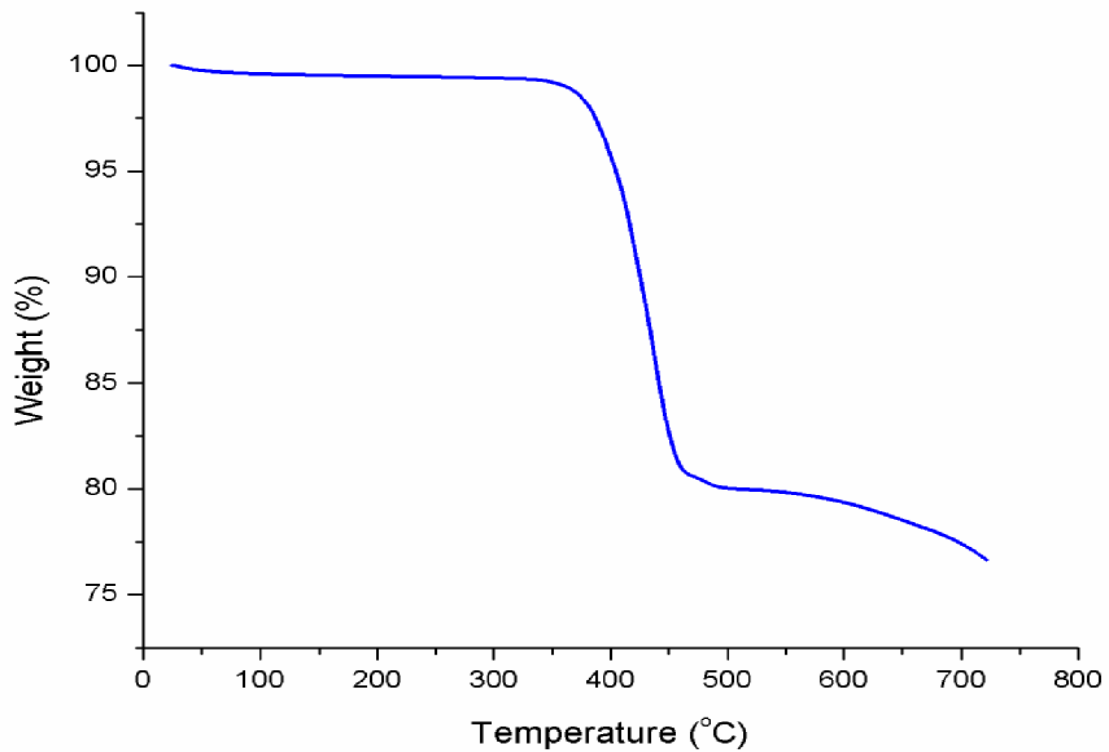


Figure 2.13. The TGA thermogram of $\text{KAu}(\text{IO}_3)_4$.

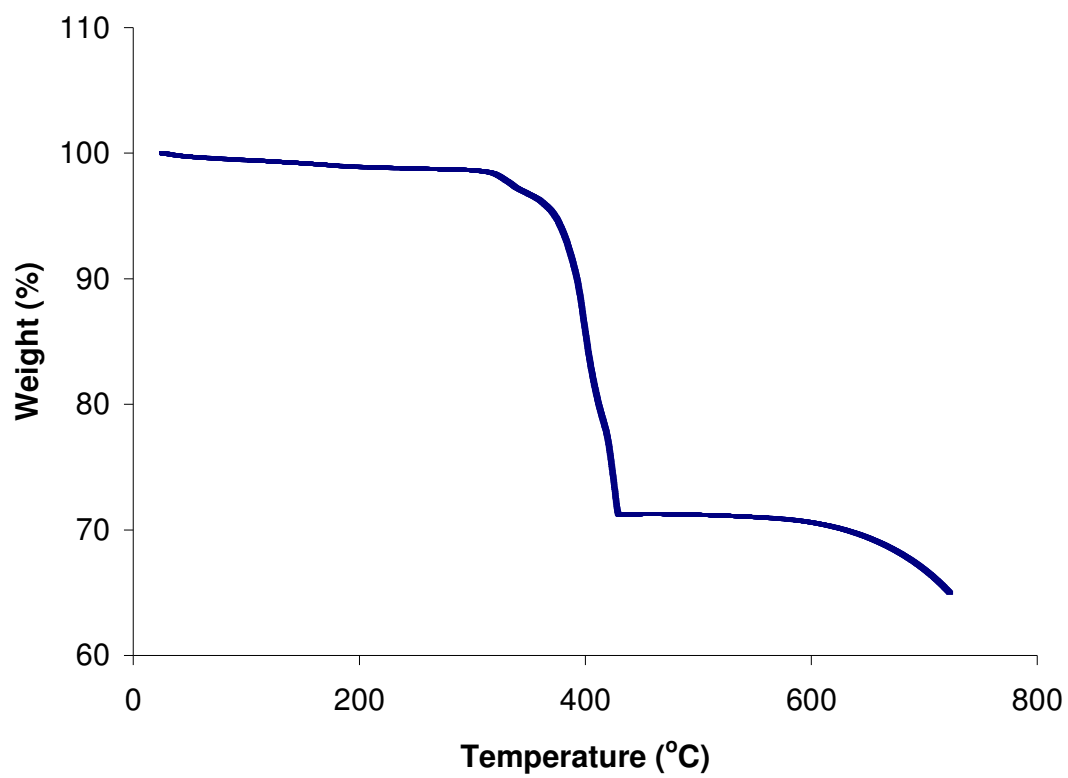


Figure 2.14. The TGA thermogram of Pd(IO₃)₂.

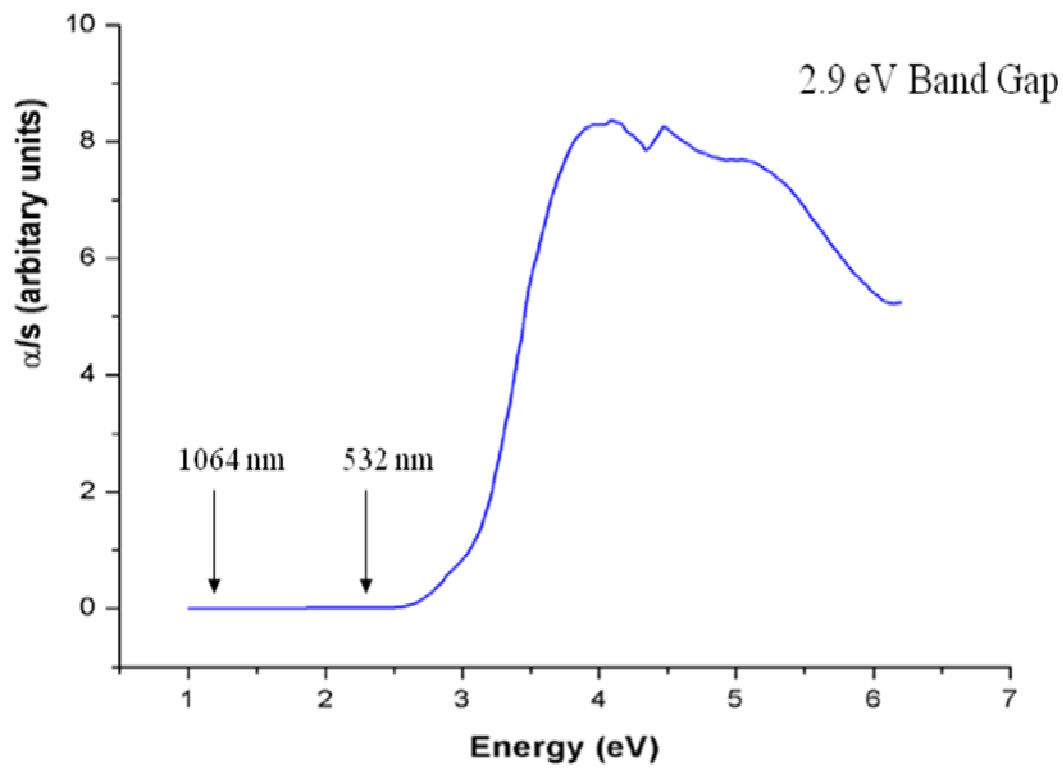


Figure 2.15. The UV-Vis Diffuse Reflectance spectrum of $\text{KAu}(\text{IO}_3)_4$.

REFERENCES

1. Svenson, C.; Abrahams, S. C.; Bernstein, J. L. *J. Solid State Chem.* **1981**, 36,195.
2. Nassau, K.; Shiever, J. W.; Prescott, B. E. *J. Solid State Chem.* **1973**, 7, 186.
3. Nassau, K.; Shiever, J. W.; Prescott, B. E.; Cooper, A. S. *J. Solid State Chem.* **1974**, 11, 314.
4. Liminga, R.; Abrahams, S. C.; Bernstein, J. L. *J. Chem. Phys.* **1975**, 62, 755.
5. Nassau, K.; Shiever, J. W.; Prescott, B. E. *J. Solid State Chem.* **1975**, 14, 122.
6. Abrahams, S. C.; Bernstein, J. L.; Nassau, K. *J. Solid State Chem.* **1976**, 16, 173.
7. Liminga, R.; Abrahams, S. C.; Bernstein, J. L. *J. Chem. Phys.* **1977**, 67, 1015.
8. Gupta, P. K. S.; Ammon, H. L.; Abrahams, S. C. *Acta Crystallogr., Sect. C* **1989**, 45, 175.
9. Sykora, R. E.; Ok, K. M.; Halasyamani, P. S.; Albrecht-Schmitt, T. E. *J. Am. Chem. Soc.* **2002**, 124, 1951.
10. Sykora, R. E.; Ok, K. M.; Halasyamani, P. S.; Wells, D. M.; Albrecht-Schmitt, T. E. *Chem. Mater.* **2002**, 14, 2741.
11. Ok, K. M.; Halasyamani, P. S. *Inorg. Chem.* **2005**, 44, 9353.
12. Schellhaas, F.; Frydrych, R. *Chem. Ber.* **1975**, 108, 364.
13. Wickleder, M. S. *Z. Anorg. Allg. Chem.* **2001**, 627, 2112.
14. Wickleder, M. S.; Buechner, O.; Wickleder, C.; El Sheik, S.; Brunklaus, G.; Eckert, H. *Inorg. Chem.* **2004**, 43, 5860.
15. Mitscherlich, E. *Pogg. Ann.* **1827**, 9, 623.
16. Lenher, V. *J. Am. Chem. Soc.* **1902**, 24, 354.
17. Bean, A. C.; Peper, S. M.; Albrecht-Schmitt, T. E. *Chem. Mater.* **2001**, 13, 1266.

18. Bean, A. C.; Ruf, M.; Albrecht-Schmitt, T. E. *Inorg. Chem.* **2001**, 40, 3959.
19. Assefa, Z.; Ling, J.; Haire, R. G.; Albrecht-Schmitt, T. E.; Sykora, R. E. *J. Solid State Chem.* **2006**, 179, 3653.
20. Ling, J.; Albrecht-Schmitt, T. E. *Euro. Inorg. Chem.* **2007**, 5, 652.
21. SADABS, Program for absorption correction using SMART CCD based on the method of Blessing; Blessing, R. H. *Acta Crystallogr. A* **1995**, 51, 33.
22. Sheldrick, G. M. *SHELXTL PC, Version 5.0, An Integrated System for Solving, Refining, and Displaying Crystal Structures from Diffraction Data*; Siemens Analytical X-ray Instrument, Inc.: Madison, WI, **1994**.
23. *ATOMS 6.1*; Shape Software: Kingsport, TN, **2004**.
24. Wendlandt, W. W.; Hecht, H. G.: *Reflectance Spectroscopy*. Interscience Publisher, New Yourk, 1966.
25. (a) Hector, A. L.; Henderson, S. J.; Levason, W.; Webster, M. Z. *Anorg. Allg. Chem.* **2002**, 628, 198. (b) Douglas, P.; Hector, A. L.; Levason, W.; Light, M. E.; Matthews, M. L.; Webster, M. Z. *Anorg. Allg. Chem.* **2004**, 630, 479.
26. Geb, J.; Jansen, M. *J. Solid State Chem.* **1996**, 122, 364.
27. (a) Addison, C. C.; Brownlee, G. S.; Logan, N. *J. Chem. Soc., Dalton Trans.* **1972**, 14, 1440. (b) Garner, C. D.; Wallwork, S. C. *J. Chem. Soc.* **1970**, 18, 3092.
28. Buechner, O.; Wickleder, M. S. *Z. Anorg. Allg. Chem.* **2004**, 630, 1079.
29. Cunin, F.; Deudon, C.; Favier, F.; Mula, B.; Pascal, J. L. *Inorg. Chem.* **2002**, 41, 4173.

30. (a) Burns, P. C.; Hawthorne, F. C. *Can. Mineral.* **1993**, 31, 313. (b) Cooper, M. A.; Hawthorne, F. C.; Roberts, A. C.; Grice, J. D.; Stirling, J. A. R.; Moffatt, E. A. *Am. Mineral.* **1998**, 83, 390.
31. Bray, T. H.; Beitz, J. V.; Bean, A. C.; Yu, Y.; Albrecht-Schmitt, T. E. *Inorg. Chem.* **2006**, 45, 8251.
32. Schwarzmann, E.; Fellwock, E. *Z. Naturforsch., Teil B* **1971**, 26, 1369.
33. Jansen, M.; Mudring, A. V. in *Gold, Process in Chemistry, Biochemistry and Technology* (Ed.: H. Schmidbaur), John Wiley & Sons, Chichester, **1999**, 753.
34. Pracht, G.; Lange, N.; Lutz, H. D. *Thermochim. Acta* **1997**, 293, 13.
35. Lutz, H. D.; Suchanek, E. *Spectrochim. Acta* **2000**, A56, 2707.
36. Schellenschlagger, V.; Pracht, G.; Lutz, H. D. *J. Raman Spectrosc.* **2001**, 32, 373.
37. Levason, W. *Coord. Chem. Rev.* **1997**, 161, 33.
38. Panagiotidis, K.; Glaum, R.; Schmedt auf der Guenne, J.; Hoffbauer, W.; Goerzel, H. *Z. Anorg. Allg. Chem.* **2005**, 631, 2371.
39. Nakamoto, K. *Infrared and Raman Spectra of Inorganic and Coordination Compounds-Part A: Theory and Applications in Inorganic Chemistry*, 5th ed., John Wiley & Sons, **1997**.
40. Glazer, A. M.; Stadnicka, K. *Acta Crystallogr.* **1989**, A45, 234.
41. Pankove, J. I.: *Optical Process in Semiconductors*. Prentice Hall, Inc., Engelwood Cliffs, NJ, **1971**.
42. Feger, C. R.; Kolis, J. W.; Gorny, K.; Pennington, C. J. *Solid State Chem.* **1999**, 143, 254.

CHAPTER 3

SYNTHESES, STRUCTURES, AND PROPERTIES OF THREE PALLADIUM SELENITES AND SELENATE, PdSeO₃, PdSe₂O₅ and Na₂Pd(SeO₄)₂

ABSTRACT

Three new palladium compounds, PdSeO₃, PdSe₂O₅, and Na₂Pd(SeO₄)₂, containing selenium oxoanions of both Se(IV) and Se(VI) have been prepared under mild hydrothermal conditions. PdSe₂O₅ and Na₂Pd(SeO₄)₂ both possess one-dimensional structures. Within the structure of PdSe₂O₅, [PdO₄] square planar building blocks are joined together through diselenite, Se₂O₅²⁻, anions, and form a zigzag chain along the *c* axis. In Na₂Pd(SeO₄)₂, [PdO₄] units are connected by two selenate, SeO₄²⁻, anions, and extend along the *a* axis to form a [Pd(SeO₄)₂]²⁻ chain. Na⁺ cations reside in the space between the [Pd(SeO₄)₂]²⁻ chains and act as counter cations. Unlike above two compounds, PdSeO₃ exhibits a layered structure. In the structure of PdSeO₃, [PdO₄] units are connected to each other by corner-sharing and form a zigzag chain along the *b* axis. The chains are further joined together by tridentate selenite, SeO₃²⁻, anions to form layers in the [*ab*] plane that stack along the *c* axis. Crystallographic data: (193 K; Mo K α , λ = 0.71073 Å): PdSeO₃, monoclinic, space group *P2₁/m*, *a* = 3.8884(5) Å, *b* = 6.4170(8) Å, *c* = 6.1051(7) Å, β = 96.413(2) $^\circ$, *V* = 151.38(3) Å³, *Z* = 2; PdSe₂O₅, monoclinic, space group *C2/c*, *a* = 12.198(2) Å, *b* = 5.5500(8) Å, *c* = 7.200(1) Å, β = 107.900(2) $^\circ$, *V* =

463.8(1) Å³, $Z = 4$; Na₂Pd(SeO₄)₂, triclinic, space group $P\bar{1}$, $a = 4.9349(11)$ Å, $b = 5.9981(13)$ Å, $c = 7.1512(15)$ Å, $\alpha = 73.894(4)^\circ$, $\beta = 86.124(4)^\circ$, $\gamma = 70.834(4)^\circ$, $V = 192.03(7)$ Å³, $Z = 1$.

INTRODUCTION

The aqueous and solid-state chemistry of selenium are extraordinarily rich, yielding a variety of Se(IV) and Se(VI) species that include H_2SeO_3 , HSeO_3^- , SeO_3^{2-} , $\text{Se}_2\text{O}_5^{2-}$, and SeO_4^{2-} .^{1,2} One of the primary interests in Se(IV) compounds is discerning the role that the lone-pair of electrons on the Se(IV) centers plays in the local and extended structures of these compounds. There are three major themes recognized for the effects of the lone-pair of electrons that are in addition to its local stereochemical activity. The first of these is dimensional reduction. For example, in the uranyl selenite system, the majority of uranyl-containing compounds are two-dimensional.³ However, $\text{Ca}[\text{UO}_2(\text{SeO}_3)_2]$ and $\text{Sr}[\text{UO}_2(\text{SeO}_3)_2]\cdot 2\text{H}_2\text{O}$ are both one-dimensional.⁴ The second effect is the formation of channels and cavities within extended networks to house the lone-pair of electrons. Cavity and channel formation is recognized in $\beta\text{-AgNpO}_2(\text{SeO}_3)$,⁵ $\text{M}_2(\text{SeO}_3)_3\cdot 3\text{H}_2\text{O}$ ($\text{M} = \text{Al}$,⁶ Ga ,⁷ Cr),⁸ $\text{In}(\text{OH})(\text{SeO}_3)$,⁹ $\text{Tb}_3\text{O}_2\text{Cl}(\text{SeO}_3)_2$,¹⁰ $\text{Tb}_5\text{O}_4\text{Cl}_3(\text{SeO}_3)_2$,¹⁰ and $\text{Tb}_2\text{Se}_2\text{O}_7$.¹¹ The third major effect is the formation of noncentrosymmetric structures as occurs in $\text{A}_2(\text{MoO}_3)_3\text{SeO}_3$ ($\text{A} = \text{Rb}$, Cs , Tl , NH_4),¹² $\text{Cs}(\text{VO}_2)_3(\text{SeO}_3)_2$,¹³ and $\text{Na}_2\text{MoSeO}_6$.¹⁴

Diselenite compounds containing the $\text{Se}_2\text{O}_5^{2-}$ anion are becoming increasingly common in Se(IV) oxoanion chemistry, and are known with f-block metals, e.g., in $\text{UO}_2\text{Se}_2\text{O}_5$,¹⁵ with alkaline-earth metals in AESe_2O_5 ($\text{AE} = \text{Mg}$,¹⁶ Ca ,¹⁷ Sr ,¹⁸ Ba),¹⁹ and with d-block metals, e.g., in MnSe_2O_5 ,²⁰ and $[\text{H}_2\text{pip}][\text{Cu}_2(\text{Se}_2\text{O}_5)_3]$.²¹ MSe_2O_5 ($\text{M} = \text{Pb}$, Cd , Mn) and $\text{Cr}_2(\text{Se}_2\text{O}_5)_3$ are also known and have been characterized by vibrational spectroscopy.²² The ammonium salt of diselenite, $(\text{NH}_4)_2\text{Se}_2\text{O}_5$, has been studied by neutron diffraction and shown to undergo a phase transition at 312 K.²³⁻²⁵ Despite the presence of two lone-pairs of electrons on the diselenite anion, most compounds are

centrosymmetric; notable exceptions include $\text{LiFe}(\text{Se}_2\text{O}_5)_2$,²⁶ $\text{Nb}_2\text{Se}_4\text{O}_{13}$,²⁷ $\text{Nd}_2(\text{Se}_2\text{O}_5)_3 \cdot \text{H}_2\text{SeO}_3 \cdot 2\text{H}_2\text{O}$,²⁸ and $\text{In}_2(\text{Se}_2\text{O}_5)_3$.²⁹ Small second-harmonic generation responses have been observed for the frequency-doubling of 1064 nm light by $\text{In}_2(\text{Se}_2\text{O}_5)_3$.²⁹ Magnetic ordering has been observed in diselenite compounds, e.g., in $\text{M}_2(\text{Se}_2\text{O}_5)_3$ ($\text{M} = \text{Cr}$,³⁰ Mn ,³¹ Fe ³⁰). Mixed selenite/diselenite compounds have also been reported and include $\text{Ca}_2(\text{HSeO}_3)_2(\text{Se}_2\text{O}_5)$,^{1,32} $\text{Ca}_2(\text{SeO}_3)(\text{Se}_2\text{O}_5)$,¹⁹ $\text{Au}_2(\text{SeO}_3)_2(\text{Se}_2\text{O}_5)$,³³ $\text{M}(\text{HSeO}_3)(\text{Se}_2\text{O}_5)$ ($\text{M} = \text{Fe}$,³⁴ Cr ³⁵), $\text{Sm}_2(\text{SeO}_3)(\text{Se}_2\text{O}_5)_2$,³⁶ $\text{La}(\text{Se}_2\text{O}_5)(\text{HSeO}_3)(\text{H}_2\text{O}) \cdot \text{H}_2\text{O}$,³⁷ and $\text{Ga}(\text{HSeO}_3)(\text{Se}_2\text{O}_5) \cdot 1.07\text{H}_2\text{O}$.³⁸

While it is generally and correctly predicted that selenate compounds containing SeO_4^{2-} would possess similar structures with that of sulfates, the fact is that selenates have proven to be far richer with examples of nanotubes being observed in the uranyl selenates, $(\text{C}_4\text{H}_{12}\text{N})_{14}[(\text{UO}_2)_{10}(\text{SeO}_4)_{17}(\text{H}_2\text{O})]^{39}$ and $\text{K}_5[(\text{UO}_2)_3(\text{SeO}_4)_5](\text{NO}_3)(\text{H}_2\text{O})_{3.5}$.⁴⁰ In this work we provide example of new Pd(II) compounds containing selenite, diselenite, and selenate anions with the synthesis, structures, and characterization of PdSeO_3 , PdSe_2O_5 , and $\text{Na}_2\text{Pd}(\text{SeO}_4)_2$. The information in this chapter has been published as a full paper in *Journal of Inorganic Chemistry*.⁴¹

EXPERIMENTAL

Syntheses. $\text{Pd}(\text{NO}_3)_2$ (99.9%, Alfa-Aesar), Na_2SeO_4 (99.8%, Alfa-Aesar), and KNO_3 (99.9%, Alfa-Aesar) were used as received without further purification. Concentrated H_2SeO_4 solution was prepared by evaporating 40% H_2SeO_4 (Alfa-Aesar) at $\sim 200^\circ\text{C}$. Distilled and Millipore-filtered water with resistance of 18.2 M Ω -cm was used in all reactions. SEM/EDX analyses were performed using a JEOL JSM-7000F. Sodium,

palladium, and selenium standards were used to calibrate the results, and the EDX ratios are within 3% of the ratios determined from single-crystal X-ray diffraction experiments.

PdSeO₃ was prepared by loading Pd(NO₃)₂ (101.0 mg, 0.438 mmol), KNO₃ (88.6 mg, 0.876 mmol), 0.2 mL of concentrated H₂SeO₄, and 0.5 mL of water in a 23-mL PTFE-lined autoclave. The autoclave was sealed and heated at 200 °C in a box furnace. After 4 days, the furnace was cooled to room temperature at a rate of 9 °C/h. The reaction product contained a single phase of dark orange crystals immersed in a pale yellow mother liquor. The product was washed with water and methanol and allowed to dry. Yield: 84 mg (82% based on Pd). EDX analysis provided a Pd:Se ratio of 1:1 (47:53).

PdSe₂O₅ was prepared by loading Pd(NO₃)₂ (183.0 mg, 0.794 mmol), KNO₃ (160.6 mg, 1.588 mmol), 0.4 mL of concentrated H₂SeO₄, and 0.5 mL of water in a 23-mL PTFE-lined autoclave. The autoclave was sealed and heated at 200 °C in a box furnace. After 4 days, the furnace was cooled to room temperature at a rate of 9 °C/h. The reaction product contained a single phase of orange crystals immersed in a colorless mother liquor. The product was washed with water and methanol and allowed to dry. Yield: 183 mg (66.9% based on Pd). EDX analysis provided a Pd:Se ratio of 1:2 (34:66).

Na₂Pd(SeO₄)₂ was prepared by loading Pd(NO₃)₂ (116.5 mg, 0.506 mmol), Na₂SeO₄ (191.2 mg, 1.012 mmol), 0.3 mL of concentrated H₂SeO₄, and 0.5 mL of water in a 23-mL PTFE-lined autoclave. The autoclave was sealed and heated at 200 °C in a box furnace. After 4 days, the furnace was cooled to room temperature at a rate of 9 °C/h. The reaction product consisted of yellow crystals of Na₂Pd(SeO₄)₂ as major product and orange crystals of PdSe₂O₅ as minor product. The product was washed with water

and methanol and allowed to dry. Yield: 120 mg (54.3% based on Pd). EDX analysis provided a Na:Pd:Se ratio of 2:1:2 (42:19:39).

Crystallographic Studies. Single crystals of PdSeO₃, PdSe₂O₅, and Na₂Pd(SeO₄)₂ with dimensions of 0.035 mm × 0.033 mm × 0.010 mm, 0.092 mm × 0.089 mm × 0.023 mm, and 0.110 mm × 0.039 mm × 0.020 mm were selected and mounted on glass fibers with epoxy and aligned on a Bruker SMART APEX CCD X-ray diffractometer with a digital camera. Intensity measurements were performed using graphite-monochromated Mo K α radiation from a sealed tube with a monocapillary collimator. The intensities and positions of reflections of a sphere were collected by a combination of three sets of exposure frames. Each set had a different ϕ angle for the crystal, and each exposure covered a range of 0.3 $^\circ$ in ω . A total of 1800 frames was collected with an exposure time per frame of 30 s for PdSeO₃, 10 s for PdSe₂O₅, and 20 s for Na₂Pd(SeO₄)₂.

Determination of integrated intensities and global cell refinement were performed with the Bruker SAINT (v 6.02) software package using a narrow-frame integration algorithm. A numerical absorption correction was applied on the basis of the indexed crystal faces followed by a semi-empirical absorption correction using SADABS.⁴² The program suite SHELXTL (v 5.1) was used for space group determination (XPREP), direct methods structure solution (XS), and least-squares refinement (XL).⁴³ The final refinements included anisotropic displacement parameters for all atoms and a secondary extinction parameter. Crystallographic details are listed in Table 3.1. Atomic coordinates and equivalent isotropic displacement parameters for all atoms within PdSeO₃, PdSe₂O₅ and Na₂Pd(SeO₄)₂ are listed in Table 3.2, Table 3.3 and Table 3.4, respectively.

Table 3.1. Crystallographic Data for PdSeO₃, PdSe₂O₅, and Na₂Pd(SeO₄)₂.

Formula	PdSeO ₃	PdSe ₂ O ₅	Na ₂ Pd(SeO ₄) ₂
Formula Mass	233.36	344.32	438.3
Color and habit	Orange, plate	Orange, prism	Yellow, block
Crystal system	Monoclinic	Monoclinic	Triclinic
Space group	<i>P2₁/m</i> (No. 11)	<i>C2/c</i> (No. 15)	<i>P</i> $\bar{1}$ (No. 2)
<i>a</i> (Å)	3.8884(5)	12.198(2)	4.9349(11)
<i>b</i> (Å)	6.4170(8)	5.5500(8)	5.9981(13)
<i>c</i> (Å)	6.1051(7)	7.200(1)	7.1512(15)
α (°)	90	90	73.894(4)
β (°)	96.413(2)	107.900(2)	86.124(4)
γ (°)	90	90	70.834(4)
<i>V</i> (Å ³)	151.38(3)	463.8(1)	192.03(7)
<i>Z</i>	2	4	1
<i>T</i> (K)	193	193	193
λ (Å)	0.71073	0.71073	0.71073
Maximum 2 θ (deg.)	56.54	56.58	56.60
ρ_{calcd} (g cm ⁻³)	5.120	4.931	3.790
$\mu(\text{Mo } K\alpha)$ (cm ⁻¹)	179.25	196.1	120.15
$R(F)$ for $F_o^2 > 2\sigma(F_o^2)$	0.0190	0.0234	0.0241
$R_w(F_o^2)^b$	0.0476	0.0596	0.0656

$$^a R(F) = \frac{\sum ||F_o| - |F_c||}{\sum |F_o|}. \quad ^b R_w(F_o^2) = \left[\frac{\sum [w(F_o^2 - F_c^2)^2]}{\sum wF_o^4} \right]^{1/2}.$$

Powder X-ray Diffraction. Powder X-ray diffraction patterns were collected with a Rigaku Miniflex powder X-ray diffractometer using Cu K α ($\lambda = 1.54056 \text{ \AA}$) radiation. The collected patterns were compared with those calculated from single-crystal data using ATOMS.⁴⁴

Vibrational Spectroscopy. IR spectra of the title compounds were taken from a sample in KBr with the spectrometer Shimadzu IR Prestige-21 in the wavenumber range of 4000-400 cm^{-1} .

Thermal Analysis. For the investigation of the thermal behavior, 12 mg of the title compounds were heated (3 $^{\circ}\text{C}/\text{min}$) up to 600 $^{\circ}\text{C}$ under a nitrogen flow using a TA differential scanning calorimeter (DSC) Instruments Model 2920. The residue compositions were checked by powder X-ray diffraction.

RESULTS AND DISCUSSION

Synthesis of PdSeO₃, PdSe₂O₅, and Na₂Pd(SeO₄)₂. Both PdSeO₃ and PdSe₂O₅ were synthesized by reacting Pd(NO₃)₂, KNO₃, and concentrated H₂SeO₄ under mild hydrothermal condition. In these two reactions, some of the SeO₄²⁻ was reduced to SeO₃²⁻ as occurs in the preparations of Th(SeO₃)(SeO₄)⁴⁵ and Ag₄(Mo₂O₅)(SeO₄)₂(SeO₃).⁴⁶ The relatively strong oxidizing power of selenate ($E^{\circ} = 1.151 \text{ V}$) might be sufficient to oxidize water under hydrothermal conditions. In the preparation of PdSe₂O₅, the concentration of H₂SeO₄ was double that in the synthesis of PdSeO₃. At higher concentrations of H₂SeO₄, the formation of PdSe₂O₅, instead of PdSeO₃, was more favorable, which is consistent with previously reported results.³⁸ The

Table 3.2. Atomic Coordinates and Equivalent Isotropic Displacement Parameters for PdSeO₃.

Atom	<i>x</i>	<i>y</i>	<i>z</i>	$U_{\text{eq}} (\text{\AA}^2)^a$
Pd(1)	0	0	0	0.00914(15)
Se(1)	0.56076(10)	1/4	0.32661(7)	0.00960(16)
O(1)	0.7088(8)	1/4	0.0602(5)	0.0114(6)
O(2)	0.2979(6)	0.0407(4)	0.2873(4)	0.0124(4)

^a U_{eq} is defined as one-third of the trace of the orthogonalized \mathbf{U}_{ij} tensor.

Table 3.3. Atomic Coordinates and Equivalent Isotropic Displacement Parameters for PdSe₂O₅.

Atom	<i>x</i>	<i>y</i>	<i>z</i>	$U_{\text{eq}} (\text{\AA}^2)^a$
Pd(1)	1/2	1/2	1/2	0.00734(17)
Se(1)	0.36144(3)	0.08919(7)	0.67930(5)	0.00781(17)
O(1)	0.3714(2)	0.2700(5)	0.4971(4)	0.0110(6)
O(2)	0.3710(2)	0.3087(4)	0.3426(3)	0.0111(6)
O(3)	1/2	-0.0516(8)	3/4	0.0106(8)

^a U_{eq} is defined as one-third of the trace of the orthogonalized \mathbf{U}_{ij} tensor.

Table 3.4. Atomic coordinates and equivalent isotopic displacement parameters for $\text{Na}_2\text{Pd}(\text{SeO}_4)_2$.

Atom	x	y	z	$U_{\text{eq}} (\text{\AA}^2)^a$
Na(1)	-0.1998(3)	0.2674(2)	0.8126(2)	0.0175(3)
Pd(1)	1/2	0	1/2	0.00984(14)
Se(1)	0.11685(5)	-0.31450(5)	0.71516(4)	0.01022(14)
O(1)	0.2606(4)	-0.2155(4)	0.5022(3)	0.0115(4)
O(2)	0.2087(4)	0.3087(4)	0.3426(3)	0.0162(4)
O(3)	0.2852(4)	-0.6003(4)	0.8164(3)	0.0177(5)
O(4)	0.1031(8)	-0.3164(4)	0.8513(3)	0.0169(4)

^a U_{eq} is defined as one-third of the trace of the orthogonalized \mathbf{U}_{ij} tensor.

role of KNO_3 in these reactions is not clear, but the attempts to make these two compounds in the absence of KNO_3 failed. In the synthesis of $\text{Na}_2\text{Pd}(\text{SeO}_4)_2$, the addition of Na_2SeO_4 to the reaction mixture allowed for the isolation of a selenate compound. Small amounts of PdSe_2O_5 were also found as a byproduct.

Crystal Structure of PdSeO_3 . The structure of PdSeO_3 contains a crystallographically unique Pd(II) center in a classical four coordinate environment with a square planar geometry. The Pd atom resides on the origin (inversion center), and is bound to four oxygen atoms from four selenite anions. The Pd-O bond distances within the $[\text{PdO}_4]$ unit are 2.021(2) and 2.008(2) Å, and the O-Pd-O angles are 88.95(11)° and 91.05(11)°, which are close to the idealized geometry. Two $[\text{PdO}_4]$ units are joined together through corner-sharing to form a chain that extends down the *b* axis. The palladium chains are further connected by tridentate SeO_3^{2-} anions and form a layered structure, as shown in Figure 3.1. There are two crystallographically unique oxygen atoms within the selenite anions. O(1) is connected to two Pd atoms with Se-O bond distance of 1.785(1) Å, while O(2) is connected to one Pd atom with a Se-O bond distance of 1.689(2) Å. The bridging tridentate SeO_3^{2-} anion has bond angles ranging from 97.0(1)° to 105.4(2)°. The palladium selenite layers further stack along the *c* axis, as is shown in Figure 3.1A. The calculated bond valence sums (BVS) for Pd(1) and Se(1) are 2.193 and 3.855, respectively.^{47,48} Selected bond distances and bond angles are given in Table 3.5.

Crystal Structure of PdSe_2O_5 . In the structure of PdSe_2O_5 , Pd(II) ions also have a square planar four-coordinate environment. The Pd atoms sit on an inversion center and are bound to four oxygen atoms from two $\text{Se}_2\text{O}_5^{2-}$ anions. The Pd-O bond distances

within the [PdO₄] unit are 2.017(3) and 2.018(3) Å, which are nearly equal. The O-Pd-O angles show significant deviations from 90° with the lowest and highest values being 84.3(1)° and 95.7(1)°. Each [PdO₄] unit is connected to two other [PdO₄] units through two Se₂O₅²⁻ anions and forms a chain, as is shown in Figure 3.2. The chains extend along the *c* axis. In the bridging Se₂O₅²⁻ anions, each selenium atom has two oxygen atoms bound to two [PdO₄] squares. The bond distances of Se(1)-O(1) and Se(1)-O(2) are 1.685(3) and 1.672(3) Å, respectively. The remaining oxygen atom O(3) is bound to two selenium atoms as a bridge with a Se-O bond distance of 1.788(2) Å. The BVS values for Pd(1) and Se(1) are 2.174 and 3.926, respectively.^{47,48} Selected bond distances are given in Table 3.6.

Crystal Structure of Na₂Pd(SeO₄)₂. Similar to PdSe₂O₅, the title compound exhibits a one-dimensional chain structure. The Pd atoms in the structure reside on a center of inversion and are coordinated by four oxygen atoms in a square planar geometry. The bond distances within the [PdO₄] unit are 2.014(2) and 2.019(2) Å. The O-Pd-O angles are 85.48(8)° and 94.52(8)°. [PdO₄] units connect with two neighboring [PdO₄] units through two bidentate SeO₄²⁻ anions to form one-dimensional chains, as is shown in Figure 3.3. The chains extend along the *a* axis. In the SeO₄²⁻ anions, the bond distances of the selenium atom to bridging oxygen atoms are 1.675(2) and 1.673(2) Å, while those for the terminated oxygen atoms are 1.617(2) and 1.616(2) Å. There is only one crystallographically unique Na⁺ cation in this structure. Na(1) has a six-coordinate environment with Na-O bond distances ranging from 2.342(2) to 2.762(3) Å. The BVS

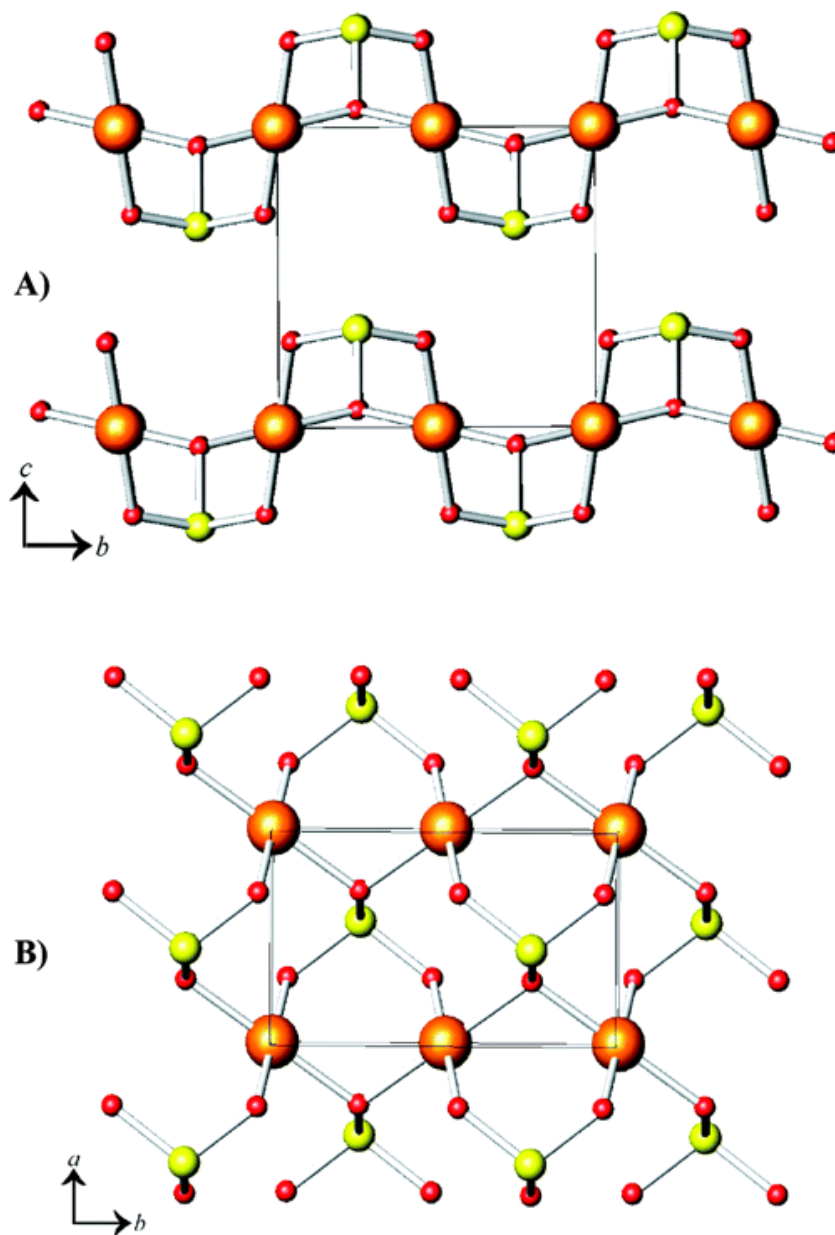


Figure 3.1. (A) View of the structure of PdSeO₃ showing [PdO₄] units joined together through corner-sharing to form a chain that extends down the *b* axis. The palladium chains are further connected by tridentate SeO₃²⁻ anions. (B) A depiction of the neutral layers in PdSeO₃. Orange (large), yellow (medium) and red (small) balls represent Pd, Se and O atoms, respectively.

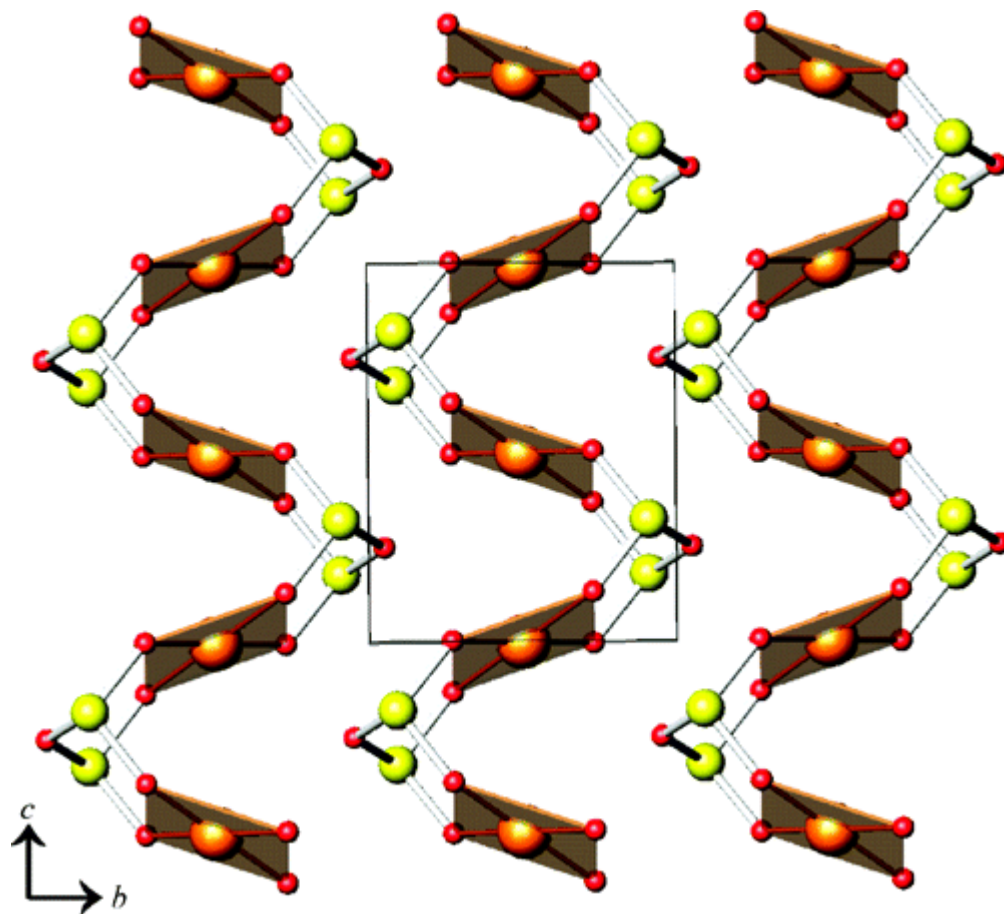


Figure 3.2. Illustration of the one-dimensional chains formed from $[\text{PdO}_4]$ units and $\text{Se}_2\text{O}_5^{2-}$ anions in the structure of PdSe_2O_5 . Orange (large), yellow (medium) and red (small) balls represent Pd, Se and O atoms, respectively.

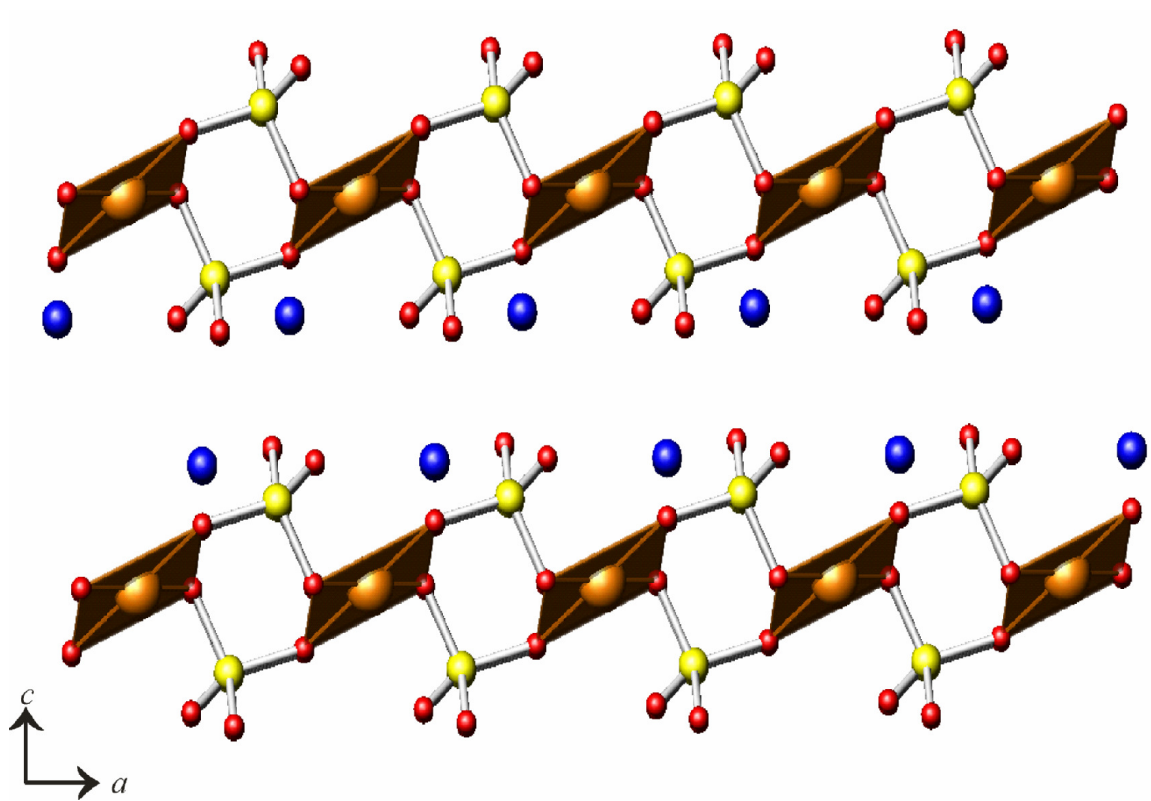


Figure 3.3. View of the one-dimensional $[\text{Pd}(\text{SeO}_4)_2]^{2-}$ chains in $\text{Na}_2\text{Pd}(\text{SeO}_4)_2$. Orange (large), yellow (medium), blue (medium), and red (small) balls represent Pd, Se, Na and O atoms, respectively.

Table 3.5. Selected Bond Distances (Å) and Angles (°) for PdSeO₃.

Distances (Å)			
Pd(1)-O(1) × 2	2.021(2)	Se(1)-O(1)	1.785(3)
Pd(1)-O(2) × 2	2.008(2)	Se(1)-O(2)	1.689(2)
Angles (°)			
O(1)-Pd(1)-O(1')	180	O(1)-Se(1)-O(2)	97.01(10)
O(1)-Pd(1)-O(2)	91.05(11)	O(1)-Se(1)-O(2')	97.01(10)
O(1)-Pd(1)-O(2')	88.95(11)	O(2)-Se(1)-O(2')	105.37(16)
O(1')-Pd(1)-O(2)	88.95(11)		
O(1')-Pd(1)-O(2')	91.05(11)		
O(2)-Pd(1)-O(2')	180		

Table 3.6 Selected Bond Distances (Å) and Angles (°) for PdSe₂O₅.

Distances (Å)			
Pd(1)-O(1) × 2	2.018(3)	Se(1)-O(1)	1.685(3)
Pd(1)-O(2) × 2	2.017(3)	Se(1)-O(2)	1.672(3)
		Se(1)-O(3)	1.788(2)
Angles (°)			
O(1)-Pd(1)-O(1')	180	O(1)-Se(1)-O(2)	105.8(2)
O(1)-Pd(1)-O(2)	84.3(1)	O(1)-Se(1)-O(3)	101.2(1)
O(1)-Pd(1)-O(2')	95.7(1)	O(2)-Se(1)-O(3)	102.1(1)
O(1')-Pd(1)-O(2)	95.7(1)		
O(1')-Pd(1)-O(2')	84.3(1)		
O(2)-Pd(1)-O(2')	180		

Table 3.7. Selected Bond Distances (Å) and Angles (°) for Na₂Pd(SeO₄)₂.

Distances (Å)			
Pd(1)-O(1) × 2	2.014(2)	Se(1)-O(1)	1.675(2)
Pd(1)-O(2) × 2	2.019(2)	Se(1)-O(2)	1.673(2)
		Se(1)-O(3)	1.616(2)
		Se(1)-O(4)	1.617(2)
Angles (°)			
O(1)-Pd(1)-O(1')	180	O(1)-Se(1)-O(2)	105.2(1)
O(1)-Pd(1)-O(2)	94.52(8)	O(1)-Se(1)-O(3)	111.2(1)
O(1)-Pd(1)-O(2')	85.48(8)	O(1)-Se(1)-O(4)	109.4(1)
O(1')-Pd(1)-O(2)	85.48(8)	O(2)-Se(1)-O(3)	104.5(1)
O(1')-Pd(1)-O(2')	94.52(8)	O(2)-Se(1)-O(4)	112.6(1)
O(2)-Pd(1)-O(2')	180	O(3)-Se(1)-O(4)	113.7(1)

values for Na(1), Pd(1), and Se(1) are 1.094, 2.181, and 5.902, respectively.^{47,48} Selected bond distances are given in Table 3.7.

Vibrational Spectroscopy. The infrared spectra of these three palladium compounds consist of two primary regions. Several weak bands centered at 560 cm^{-1} can be assigned to the distortions of the $[\text{PdO}_4]$ square plane.^{49,50} In the IR spectrum of PdSeO_3 , five sharp bands at 807, 730, 672, 621, and 591 cm^{-1} are attributable to the vibrational modes of SeO_3^{2-} .⁵¹ Four sharp bands occur at 828, 786, 722, and 675 cm^{-1} in the IR spectrum of PdSe_2O_5 are due to the stretching vibrations of Se-O bonds within the $\text{Se}_2\text{O}_5^{2-}$ anions.^{22,29} The vibrational bands of SeO_4^{2-} in $\text{Na}_2\text{Pd}(\text{SeO}_4)_2$ are found at 882, 869, 861, 846, and 832 cm^{-1} , and match well with the previously reported vibrational data for selenate.⁵²

Thermal Analysis. The thermal behavior of selenites and selenates is of interest because there are multiple mechanisms of decomposition including loss of oxygen by selenate and decomposition of the selenate and selenite anions to yield SeO_2 .^{51,53} PdSeO_3 and PdSe_2O_5 exhibit similar thermal properties. Both of them show a broad endothermic peak in the temperature ranges of $350\text{-}560\text{ }^\circ\text{C}$ in their DSC thermograms. The composition of the final residue for the above two compounds is pure PdO, which is identified by powder X-ray diffraction. By contrast, the DSC thermogram of $\text{Na}_2\text{Pd}(\text{SeO}_4)_2$ shows two endothermic peaks centered at 310 and $450\text{ }^\circ\text{C}$, respectively. The small and sharp endothermic peak at $310\text{ }^\circ\text{C}$ is due to the loss of O_2 during the decomposition of SeO_4^{2-} to SeO_3^{2-} . The second strong and broad endothermic peak in the temperature range of $360\text{-}550\text{ }^\circ\text{C}$ is attributed to the loss SeO_2 from SeO_3^{2-} , which is

similar to the thermal behavior of PdSeO₃ and PdSe₂O₅. The composition of the final residue is identified as pure PdO by powder X-ray diffraction.

CONCLUSIONS

In this work, we have detailed the syntheses, structures, vibrational spectroscopy, and thermal behavior of three new Pd(II) compounds containing oxoanions of selenium. What makes these compounds unusual is the presence of a square planar metal center, which has been previously known primarily from Au(III) compounds with different compositions and structures, e.g., Au₂(SeO₃)₂(Se₂O₅)³³ and Au₂(SeO₃)₂(SeO₄).⁵⁴ Both of these aforementioned compounds are layered, whereas both PdSe₂O₅ and Na₂Pd(SeO₄)₂ are one-dimensional. The presence of the lone-pair of electrons on the Se(IV) centers may lead to the low-dimensional structures observed for PdSeO₃ and PdSe₂O₅. Both of these compounds are centrosymmetric despite the presence of the lone-pair of electrons.

REFERENCES

1. Dumm, J. Q.; Brown, P. W. *J. Am. Ceram. Soc.* **1997**, *80*, 2488.
2. Chen, F.; Burns, P. C.; Ewing, R. C. *J. Nucl. Mater.* **1999**, *275*, 81.
3. (a) Burns, P. C.; Miller, M. L.; Ewing, R. C. *Can. Mineral.* **1996**, *34*, 845. (b) Burns, P. C. In *Uranium: Mineralogy, Geochemistry and the Environment*; Burns, P. C., Finch, R., Eds.; Mineralogical Society of America: Washington, DC, 1999; Chapter 1. (c) Burns, P. C. *Mater. Res. Soc. Symp. Proc.* **2004**, *802*, 89. (d) Burns, P. C. *Can. Mineral.* **2005**, *43*, 1839.
4. Almond, P. M.; Peper, S. M.; Bakker, E.; Albrecht-Schmitt, T. E. *J. Solid State Chem.* **2002**, *168*, 358.
5. Albrecht-Schmitt, T. E.; Almond, P. M.; Sykora, R. E. *Inorg. Chem.* **2003**, *42*, 3788.
6. Harrison, W. T. A.; Stucky, G. D.; Morris, R. E.; Cheetham, A. K. *Acta Crystallogr. C* **1992**, *48*, 1365.
7. Rastsvetaeva, R. K.; Andrianov, V. I.; Volodina, A. N. *Dokl. Akad. Nauk. SSSR* **1986**, *291*, 352.
8. Harrison, W. T. A.; Stucky, G. D.; Cheetham, A. K. *Eur. J. Solid State Inorg. Chem.* **1993**, *30*, 347.
9. Paterson, B.; Harrison, W. T. A. *Z. Anorg. Allg. Chem.* **2007**, *633*, 158.
10. Wontcheu, J.; Schleid, T. *Z. Anorg. Allg. Chem.* **2005**, *631*, 309.
11. Wontcheu, J.; Schleid, T. *Z. Anorg. Allg. Chem.* **2002**, *628*, 1941.
12. (a) Dussack, L. L.; Harrison, W. T. A.; Jacobson, A. J. *Mater. Res. Bull.* **1996**, *31*, 249. (b) Harrison, W. T. A.; Dussack, L. L.; Jacobson, A. J. *Inorg. Chem.* **1994**, *33*, 6043.

13. Harrison, W. T. A. *Acta Crystallogr.* **2000**, C56, E422.
14. Porter, Y.; Halasyamani, P. S. *J. Solid State Chem.* **2003**, 174, 441.
15. Trombe, J. C.; Galy, J. *J. Solid State Chem.* **1986**, 61, 308.
16. Mueller, H.; Unterderweide, K.; Engelen, B. *Z. Kristallogr.* **1996**, 211, 700.
17. Delage, C.; Carpy, A.; Goursolle, M. *Acta Crystallogr. B* **1982**, 38, 1278.
18. Effenberger, H. *Acta Crystallogr. C* **1987**, 43, 182.
19. Giester, G.; Lengauer, C. L. *Monatsh. Chem.* **1998**, 129, 445.
20. Bonvoisin, J.; Galy, J.; Trombe, J. C. *J. Solid State Chem.* **1993**, 107, 171.
21. Feng, M. L.; Prosvirin, A. V.; Mao, J. G.; Dunbar, K. R. *Chem.-Eur. J.* **2006**, 12, 8312.
22. Gopinath, A. B.; Devanarayanan, S. *Int. J. Modern Phys. B* **1999**, 13, 2645.
23. Makarova, I. P.; Muradyan, L. A.; Rider, E. E.; Sarin, V. A.; Vinogradova, I. S.; Simonov, V. I. *Kristallogr.* **1990**, 35, 889.
24. Makarova, I. P.; Muradyan, L. A.; Vinogradova, I. S.; Simonov, V. I. *Ferroelect.* **1990**, 107, 275.
25. Chomnilpan, S. *Acta Crystallogr. B* **1980**, 36, 675.
26. Giester, G. *Monatsh. Chem.* **1993**, 124, 1107.
27. Halasyamani, P. S.; O'Hare, D. *Chem. Mater.* **1998**, 10, 646.
28. Stancheva, M.; Petrova, R.; Macicek, J. *Acta Crystallogr. C* **1998**, 54, 699.
29. Ok, K. M.; Halasyamani, P. S. *Chem. Mater.* **2002**, 14, 2360.
30. Lafront, A. M.; Bonvoisin, J.; Trombe, J. C. *J. Solid State Chem.* **1996**, 122, 130.
31. Malela, S. P.; Khandelwal, B. L. *Zh. Neorg. Khim.* **1980**, 25, 3019.
32. Valkonen, J. *J. Solid State Chem.* **1986**, 65, 363.

33. Jones, P. G.; Schwarzmann, E.; Sheldrick, G. M.; Timpe, H. *Z. Naturforsch. B* **1981**, *36*, 1050.
34. Muilu, H.; Valkonen, J. *Acta Chem. Scand. A* **1987**, *A41*, 183.
35. Wildner, M.; Andrut, M. *J. Solid State Chem.* **1998**, *135*, 70.
36. Wickleder, M. S. *Z. Anorg. Allg. Chem.* **2006**, *632*, 2377.
37. Feng, M. L.; Mao, J. G. *J. Alloy Compd.* **2005**, *391*, 33.
38. Morris, R. E.; Cheetham, A. K. *Chem. Mater.* **1994**, *6*, 67.
39. Krivovichev, S. V.; Kahlenberg, V.; Tananaev, I. G.; Kaindl, R.; Mersdorf, E.; Myasoedov, B. F. *J. Am. Chem. Soc.* **2005**, *127*, 1072.
40. Krivovichev, S. V.; Kahlenberg, V.; Kaindl, R.; Mersdorf, E.; Tananaev, I. G.; Myasoedov, B. F. *Angew. Chem., Int. Ed.* **2005**, *44*, 1134.
41. Ling, J.; Albrecht-Schmitt, T. E. *Inorg. Chem.* **2007**, *46*, 5686.
42. SADABS, Program for absorption correction using SMART CCD based on the method of Blessing; Blessing, R. H. *Acta Crystallogr. A* **1995**, *51*, 33.
43. Sheldrick, G. M. *SHELXTL PC, Version 5.0, An Integrated System for Solving, Refining, and Displaying Crystal Structures from Diffraction Data*; Siemens Analytical X-ray Instrument, Inc.: Madison, WI, **1994**.
44. *ATOMS 6.1*; Shape Software: Kingsport, TN, **2004**.
45. Sullens, T. A.; Almond, P. M.; Byrd, J. A.; Beitz, J. V.; Bray, T. H.; Albrecht-Schmitt, T. E. *J. Solid State Chem.* **2006**, *179*, 1192.
46. Ling, J.; Albrecht-Schmitt, T. E. *J. Solid State Chem.* **2007**, *180*, 1601.
47. Brown, I. D.; Altermatt, D. *Acta Crystallogr. B* **1985**, *41*, 244.
48. Brese, N. E.; O'Keeffe, M. *Acta Crystallogr. B* **1991**, *47*, 192.

49. Panagiotidis, K.; Glaum, R.; Schmedt auf der Guenne, J.; Hoffbauer, W.; Goerzel, H. *Z. Anorg. Allg. Chem.* **2005**, *631*, 2371.
50. Nakamoto, K. *Infrared and Raman Spectra of Inorganic and Coordination Compounds- Part A: Theory and Applications in Inorganic Chemistry*, 5th ed.; John Wiley and Sons: New York 1997.
51. Verma, V. P. *Thermochim. Acta* **1999**, *327*, 63.
52. Sathjanandan, L.; McCory, L. D.; Margrave, J. L. *Spectrochim. Acta* **1964**, *20*, 957.
53. Havlicek, D.; Micka, Z.; Boublikova, R. *Coll. Czech. Chem. Commun.* **1995**, *60*, 969.
54. Wickleder, M. S.; Buechner, O.; Wickleder, C.; El Sheik, S.; Brunklaus, G.; Eckert, H. *Inorg. Chem.* **2004**, *43*, 5860.

CHAPTER 4
SYNTHESIS, STRUCTURES, AND PROPERTIES OF NEW TRANSITION
METAL SELENITES, $\text{Ag}_4(\text{Mo}_2\text{O}_5)(\text{SeO}_3)(\text{SeO}_4)$, $\text{Ag}_2(\text{MoO}_3)\text{SeO}_3$, and
 $\text{AgNbO}(\text{SeO}_3)_2$

ABSTRACT

$\text{Ag}_4(\text{Mo}_2\text{O}_5)(\text{SeO}_4)_2(\text{SeO}_3)$ has been synthesized by reacting AgNO_3 , MoO_3 , and selenic acid under mild hydrothermal conditions. The structure of this compound consists of *cis*- MoO_2^{2+} molybdenyl units that are bridged to neighboring molybdenyl moieties by selenate anions and by a bridging oxo anion. These dimeric units are joined by selenite anions to yield zigzag one-dimensional chains that extended down the *c*-axis. Individual chains are polar with the C_2 distortion of the Mo(VI) octahedra aligning on one side of each chain. However, the overall structure is centrosymmetric because neighboring chains have opposite alignment of the C_2 distortion. Upon heating

$\text{Ag}_4(\text{Mo}_2\text{O}_5)(\text{SeO}_4)_2(\text{SeO}_3)$ loses SeO_2 in two distinct steps to yield Ag_2MoO_4 .

Crystallographic data: (193 K; $\text{MoK}\alpha$, $\lambda = 0.71073 \text{ \AA}$): orthorhombic, space group *Pbcm*,

$a = 5.6557(3)$, $b = 15.8904(7)$, $c = 15.7938(7) \text{ \AA}$, $V = 1419.41(12) \text{ \AA}^3$, $Z = 4$, $R(F) =$

2.72% for 121 parameters with 1829 reflections with $I > 2\sigma(I)$. $\text{Ag}_2(\text{MoO}_3)_3\text{SeO}_3$ was

synthesized by reacting AgNO_3 with MoO_3 , SeO_2 , and HF under hydrothermal conditions.

The structure of $\text{Ag}_2(\text{MoO}_3)_3\text{SeO}_3$ consists of three crystallographically unique Mo(VI) centers that are in 2+2+2 coordination environments with two long, two intermediate, and two short bonds. These MoO_6 units are connected to form a molybdenyl ribbon that extends along the c -axis. These ribbons are further connected together through tridentate selenite anions to form two-dimensional layers in the $[bc]$ plane. Crystallographic data: (193 K; $\text{MoK}\alpha$, $\lambda = 0.71073 \text{ \AA}$): monoclinic, space group $P2_1/n$, $a = 7.7034(5)$, $b = 11.1485(8)$, $c = 12.7500(9) \text{ \AA}$, $\beta = 105.018(1)$ $V = 1002.7(2) \text{ \AA}^3$, $Z = 4$, $R(F) = 3.45\%$ for 164 parameters with 2454 reflections with $I > 2\sigma(I)$. $\text{Ag}_2(\text{MoO}_3)_3\text{SeO}_3$ decomposes to $\text{Ag}_2\text{Mo}_3\text{O}_{10}$ on heating above $550 \text{ }^\circ\text{C}$. $\text{AgNbO}(\text{SeO}_3)_2$ was synthesized by reacting AgNO_3 , Nb and H_2SeO_4 under hydrothermal conditions. The structure of $\text{AgNbO}(\text{SeO}_3)_2$ consists of two crystallographically unique Nb(VI) centers which possessing a distorted octahedral geometry. These NbO_6 octahera are distorted along c axis and connect with each other by corner-sharing to form polar chains along c direction. For the chains composed by different Nb centers, they are heading to opposite direction and cancel some part of polarity in the whole structure. Crystallographic data: (193 K; $\text{MoK}\alpha$, $\lambda = 0.71073 \text{ \AA}$): orthorhombic, space group $Cmc2_1$, $a = 32.271(3)$, $b = 7.7573(6)$, $c = 7.3434(6) \text{ \AA}$, $V = 1838.3(3) \text{ \AA}^3$, $Z = 12$, $R(F) = 3.26\%$ for 155 parameters with 2177 reflections with $I > 2\sigma(I)$.

INTRODUCTION

Mixed-valent selenate selenite compounds that contain Se(VI) in form of SeO_4^{2-} and Se(IV) in SeO_3^{2-} represent a growing family of transition metal and f-block oxoanion solids that display new structural motifs and important optical properties. This family includes a single mineral, schmiederit, $\text{Pb}_2\text{Cu}_2(\text{OH})_4(\text{SeO}_3)(\text{SeO}_4)$,¹ five lanthanide compounds, $\text{Er}_2(\text{SeO}_3)_2(\text{SeO}_4)\cdot 2\text{H}_2\text{O}$,² $\text{La}(\text{HSeO}_3)(\text{SeO}_4)\cdot 2\text{H}_2\text{O}$,³ $\text{Nd}_2(\text{SeO}_4)(\text{SeO}_3)_2(\text{H}_2\text{O})_2$,⁴ $\text{Pr}_4(\text{SeO}_3)_2(\text{SeO}_4)\text{F}_6$,⁵ $\text{NaSm}(\text{SeO}_3)(\text{SeO}_4)$,⁵ the hydrated double salt, $\text{Na}_2\text{SeO}_4\cdot\text{H}_2\text{SeO}_3\cdot\text{H}_2\text{O}$,⁶ the five transition metal compounds $\text{Li}_2\text{Cu}_3(\text{SeO}_3)_2(\text{SeO}_4)_2$,⁷ $\text{Hg}_3(\text{SeO}_3)_2(\text{SeO}_4)$,⁸ $\text{Fe}(\text{HSeO}_3)(\text{SeO}_4)\cdot\text{H}_2\text{O}$,⁹ $\text{RbFe}(\text{SeO}_3)(\text{SeO}_4)$,⁹ and $\text{Au}_2(\text{SeO}_3)_2(\text{SeO}_4)$,¹⁰ and three early actinide-containing solids, $\text{Th}(\text{SeO}_3)(\text{SeO}_4)$,¹¹ $[\text{C}_5\text{H}_{14}\text{N}][\text{UO}_2(\text{SeO}_4)(\text{SeO}_2\text{OH})]$,¹² and $[\text{C}_5\text{H}_{14}\text{N}]_4[(\text{UO}_2)_3(\text{SeO}_4)_4(\text{HSeO}_3)(\text{H}_2\text{O})](\text{H}_2\text{SeO}_3)(\text{HSeO}_4)$ ¹³

One of the reasons for investigating this group of compounds is to investigate the effect that the lone-pair of electrons on the selenite anions has on the local and extended structures. In this regard there are several known effects. First, small channels and cavities often form to house the lone-pair of electrons as occurs in $\beta\text{-AgNpO}_2(\text{SeO}_3)$.¹⁴ Second, lone-pair alignment of selenite can take place to yield polar structures (e.g. in $\text{Au}_2(\text{SeO}_3)_2(\text{SeO}_4)$ ¹⁰ and $\text{A}_2(\text{MoO}_3)_3\text{SeO}_3$ ($\text{A}=\text{Rb}, \text{Cs}, \text{Tl}, \text{NH}_4$).¹⁵ When the latter effect occurs the materials are capable of displaying a wide variety of important properties including nonlinear optical behavior, as well as pyro-, piezo-, and ferroelectricity.^{16,17} In this report we disclose the synthesis, structure, vibrational spectroscopy, and thermal behavior of the new Mo(VI) selenate selenite, $\text{Ag}_4(\text{Mo}_2\text{O}_5)(\text{SeO}_4)_2(\text{SeO}_3)$. This compound contains polar chains, however, the overall structure is centrosymmetric. In

addition, we also provide information on a new member of the $A_2(\text{MoO}_3)_3\text{SeO}_3$ ($A=\text{Rb}$, Cs , Tl , NH_4) family,¹⁵ $\text{Ag}_2(\text{MoO}_3)_3\text{SeO}_3$, whose structure differs significantly from previous members.

As an octahedrally coordinated d^0 transition metal, intraoctahedral distortions are often observed for $\text{Nb}(\text{V})$ and result in the formation of asymmetric NbO_6 building blocks. These distortions are widely believed to be attributable to the second-order Jahn-Teller effect, in which the empty $d\pi$ orbitals of the d^0 transition metal would mix with the filled $p\pi$ orbitals of O^{2-} and as a consequence, both the energy and symmetry of NbO_6 would decrease.^{18,19} Although a certain number of niobium phosphates and sulfates have been made,^{20,21,22} very few of selenite compounds of niobium are reported.²³ In this work, by following the thought of making new SHG materials by combining two types of asymmetric building blocks, NbO_6 and SeO_3^{2-} , we produced a new niobium selenite compound, $\text{AgNbO}(\text{SeO}_3)_2$, which crystallized in a noncentrosymmetric structure. The information in this chapter has been published as a full paper in *Journal of Solid State Chemistry*.²⁴

EXPERIMENTAL

Syntheses. AgNO_3 (99.9%, Alfa-Aesar), MoO_3 (99.95%, Alfa-Aesar), H_2SeO_4 (40%, Alfa-Aesar), Nb (99.98%, Alfa-Aesar), SeO_2 (99.4%, Alfa-Aesar) and HF (48%, Alfa-Aesar) were used as received without further purification. Distilled and Millipore filtered water with resistance of 18.2 $\text{M}\Omega\text{-cm}$ was used in all reactions. SEM/EDX analyses were performed using a JEOL JSM-7000F. Silver, molybdenum, and selenium standards were used to calibrate the results.

Ag₄(Mo₂O₅)(SeO₄)₂(SeO₃) was synthesized by loading AgNO₃ (185.4 mg, 1.091 mmol), MoO₃ (235.6 mg, 1.637 mmol), H₂SeO₄ (1.00 mL, 3.89 mmol), and 0.5 mL water in a 23-mL PTFE-lined autoclave. The autoclave was sealed and heated at 200 °C in a box furnace. After 3 days, the furnace was cooled to room temperature at a rate of 9 °C/h. The reaction product contained a single phase of pale yellow crystals immersed in a colorless mother liquor. The product was washed with water and methanol and allowed to dry. Yield: 271 mg (88.8% based on Ag). EDX analysis provided Ag:Mo:Se ratio of 4:2:3 (44%:23%:33%).

Ag₂(MoO₃)₃SeO₃ was synthesized by loading AgNO₃ (192.5 mg, 1.133 mmol), MoO₃ (244.6 mg, 1.699 mmol), SeO₂ (62.9 mg, 0.567 mmol), HF (0.1 mL, 2.76 mmol), and 0.5 mL water in a 23-mL PTFE-lined autoclave. The autoclave was sealed and heated at 180 °C in a box furnace. After 4 days, the furnace was cooled to room temperature at a rate of 9 °C/h. The product was washed with water and methanol. Orange crystals and an unidentified yellow powder were left to dry in the air. Yield: 272 mg (62.1% based on Ag). EDX analysis of the orange crystals provided a Ag:Mo:Se ratio of 2:3:1 (34%:50%:16%).

AgNbO(SeO₃)₂ was synthesized by loading AgNO₃ (235.6 mg, 1.386 mmol), Nb (64.4 mg, 0.693 mmol), H₂SeO₄ (1.00 mL, 3.89 mmol), and 0.5 mL water in a 23-mL PTFE-lined autoclave. The autoclave was sealed and heated at 200 °C in a box furnace. After 10 days, the furnace was cooled to room temperature at a rate of 9 °C/h. The product was washed with water and methanol and allowed to dry. The reaction product contained lots of colorless needles of AgNbO(SeO₃)₂ as the major product, a few pale yellow blocks of Ag₂SeO₄ and some unreacted niobium metal powder as the impurity.

Yield: 174.8 mg (53.6% based on Nb). EDX analysis provided Ag:Nb:Se ratio of 1:1:2 (27%:24%:49%).

Crystallographic Studies. Single crystals of $\text{Ag}_4(\text{Mo}_2\text{O}_5)(\text{SeO}_4)_2(\text{SeO}_3)$, $\text{Ag}_2(\text{MoO}_3)_3\text{SeO}_3$, and $\text{AgNbO}(\text{SeO}_3)_2$ with dimensions of 0.106 mm \times 0.072 mm \times 0.035 mm, 0.102 mm \times 0.052 mm \times 0.028 mm, and 0.120 mm \times 0.019 mm \times 0.019 mm, respectively, were selected and mounted on quartz fibers with epoxy and aligned on a Bruker SMART APEX CCD X-ray diffractometer with a digital camera. Intensity measurements were performed using graphite monochromated Mo $K\alpha$ radiation from a sealed tube with a monocapillary collimator. The intensities and positions of reflections of a sphere were collected by a combination of 3 sets of exposure frames. Each set had a different φ angle for the crystal and each exposure covered a range of 0.3° in ω . A total of 1800 frames were collected with an exposure time per frame of 20 s for $\text{Ag}_4(\text{Mo}_2\text{O}_5)(\text{SeO}_4)_2(\text{SeO}_3)$, 10 s for $\text{Ag}_2(\text{MoO}_3)_3\text{SeO}_3$, and 40 s for $\text{AgNbO}(\text{SeO}_3)_2$.

Determination of integrated intensities and global cell refinement were performed with the Bruker SAINT (v 6.02) software package using a narrow-frame integration algorithm. A semi-empirical absorption correction was applied using SADABS.²⁵ The program suite SHELXTL (v 5.1) was used for space group determination (XPREP), direct methods structure solution (XS), and least-squares refinement (XL).²⁶ The final refinements included anisotropic displacement parameters for all atoms and a secondary extinction parameter. Some crystallographic details are listed in Table 4.1 and Table 4.2, and the final positional parameters can be found in Table 4.3, Table 4.4, and Table 4.5.

Powder X-ray Diffraction. Powder X-ray diffraction patterns were collected with a Rigaku Miniflex powder X-ray diffractometer using Cu $K\alpha$ ($\lambda=1.54056 \text{ \AA}$)

radiation. The collected patterns were compared with these calculated from single crystal data using ATOMS.²⁷

Vibrational Spectroscopy. The IR spectra of $\text{Ag}_4(\text{Mo}_2\text{O}_5)(\text{SeO}_4)_2(\text{SeO}_3)$ and $\text{Ag}_2(\text{MoO}_3)_3\text{SeO}_3$ were taken from samples in KBr pellets with using a Shimadzu IR Prestige-21 in the wave number range of $4000\text{--}400\text{ cm}^{-1}$. Raman spectroscopy experiments were performed at room temperature using backscattering geometry with 514.5 nm (2.41 eV) line of an argon-ion laser and an ISA U-1000 scanning double monochromator to disperse the Stokes Raman scattering spectra.

Thermal Analysis. For the investigation of the thermal behavior, 25 mg of the title compounds were placed in two platinum pans that were heated ($5\text{ }^\circ\text{C}/\text{min}$) up to $725\text{ }^\circ\text{C}$ under a nitrogen flow using a TGA Instruments Model Q50 V5.3 Build 171. The residue compositions were checked by powder X-ray diffraction.

Table 4.1. Crystallographic Data for $\text{Ag}_4(\text{Mo}_2\text{O}_5)(\text{SeO}_4)_2(\text{SeO}_3)$ and $\text{Ag}_2(\text{MoO}_3)_3\text{SeO}_3$.

Compound	$\text{Ag}_4(\text{Mo}_2\text{O}_5)(\text{SeO}_4)_2(\text{SeO}_3)$	$\text{Ag}_2(\text{MoO}_3)_3\text{SeO}_3$
Formula Mass	1116.24	774.52
Color and habit	Yellow, block	Orange, block
Crystal System	Orthorhombic	Monoclinic
Space group	<i>Pbcm</i> (No. 57)	<i>P2₁/n</i> (No.14)
<i>a</i> (Å)	5.6557(3)	7.3034(5)
<i>b</i> (Å)	15.8904(7)	11.1485(8)
<i>c</i> (Å)	15.7938(7)	12.7500(9)
α (deg)	90	90
β (deg)	90	105.018(1)
γ (deg)	90	90
<i>V</i> (Å ³)	1419.4(1)	1002.7(2)
<i>Z</i>	4	4
<i>T</i> (K)	193	193
λ (Å)	0.71073	0.71073
Maximum 2 θ (deg.)	56.62	56.58
ρ_{calcd} (g cm ⁻³)	5.223	5.131
$\mu(\text{Mo } K\alpha)$ (cm ⁻¹)	149.05	111.78
$R(F)$ for $F_o^2 > \sigma(F_o^2)$ ^a	0.0272	0.0345
$R_w(F_o^2)$ ^b	0.0661	0.0833

$$^a R(F) = \frac{\sum ||F_o| - |F_c||}{\sum |F_o|}. \quad ^b R_w(F_o^2) = \left[\frac{\sum [w(F_o^2 - F_c^2)^2]}{\sum wF_o^4} \right]^{1/2}.$$

Table 4.2. Crystallographic Data for AgNbO(SeO₃)₂.

Compound	AgNbO(SeO ₃) ₂
Formula Mass	470.70
Color and habit	Colorless, needle
Crystal System	Orthorhombic
Space group	<i>Cmc</i> 2 ₁ (No. 36)
<i>a</i> (Å)	32.271(3)
<i>b</i> (Å)	7.7573(6)
<i>c</i> (Å)	7.3434(6)
<i>V</i> (Å ³)	1838.3(3)
<i>Z</i>	12
<i>T</i> (K)	193
λ (Å)	0.71073
Maximum 2 θ (deg.)	56.58
ρ_{calcd} (g cm ⁻³)	5.102
$\mu(\text{Mo } K\alpha)$ (cm ⁻¹)	169.31
$R(F)$ for $F_o^2 > \sigma(F_o^2)$ ^a	0.0326
$R_w(F_o^2)$ ^b	0.0987

^a $R(F) = \sum \left| |F_o| - |F_c| \right| / \sum |F_o|$. ^b $R_w(F_o^2) = \left[\sum \left[w(F_o^2 - F_c^2)^2 \right] / \sum wF_o^4 \right]^{1/2}$.

Table 4.3. Atomic Coordinates and Equivalent Isotropic Displacement Parameters for $\text{Ag}_4(\text{Mo}_2\text{O}_5)(\text{SeO}_4)_2(\text{SeO}_3)$.

Atom	<i>x</i>	<i>y</i>	<i>z</i>	$U_{\text{eq}} (\text{\AA}^2)^a$
Ag(1)	0.17767(10)	0.34503(4)	1/4	0.01739(13)
Ag(2)	0.69721(10)	0.50077(3)	1/4	0.01628(13)
Ag(3)	0.17562(7)	0.50367(2)	0.42003(3)	0.01659(11)
Mo(1)	0.64349(7)	0.67226(3)	0.41167(2)	0.00993(11)
Se(1)	0.24643(12)	0.63408(4)	1/4	0.01036(14)
Se(2)	0.67276(8)	0.35891(3)	0.39988(3)	0.01122(12)
O(1)	0.4373(6)	0.6037(2)	0.3320(2)	0.0154(7)
O(2)	0.0814(10)	0.5493(3)	1/4	0.0240(12)
O(3)	0.3496(6)	0.7579(2)	0.3787(2)	0.0166(7)
O(4)	0.6559(6)	0.3745(2)	0.5031(2)	0.0160(7)
O(5)	0.9259(7)	0.3933(2)	0.3647(2)	0.0207(8)
O(6)	0.4597(7)	0.4102(2)	0.3515(2)	0.0201(8)
O(7)	0.1765(7)	0.2146(2)	0.1627(2)	0.0189(8)
O(8)	0.7973(6)	0.5849(2)	0.4450(2)	0.0168(7)
O(9)	0.6977(8)	3/4	1/2	0.0132(9)

^a U_{eq} is defined as one-third of the trace of the orthogonalized \mathbf{U}_{ij} tensor.

Table 4.4. Atomic Coordinates and Equivalent Isotropic Displacement Parameters for $\text{Ag}_2(\text{MoO}_3)_3\text{SeO}_3$.

Atom	<i>x</i>	<i>y</i>	<i>z</i>	$U_{\text{eq}} (\text{\AA}^2)^a$
Ag(1)	0.13073(6)	0.41724(3)	0.93163(2)	0.01347(12)
Ag(2)	-0.14522(6)	0.24812(3)	0.05667(3)	0.01355(12)
Mo(1)	-0.41376(5)	0.40227(3)	0.80118(3)	0.00636(12)
Mo(2)	-0.44934(5)	0.07632(3)	0.81194(3)	0.00635(12)
Mo(3)	0.15004(6)	0.08270(3)	0.94463(3)	0.00637(12)
Se(1)	-0.15215(6)	0.19103(4)	0.69478(3)	0.00888(13)
O(1)	0.2569(5)	0.0813(3)	0.8413(3)	0.0149(8)
O(2)	0.3410(5)	0.0749(3)	0.0545(3)	0.0143(8)
O(3)	-0.1195(5)	0.0967(3)	0.8039(3)	0.0113(7)
O(4)	0.0588(5)	-0.0811(3)	0.9479(3)	0.0092(7)
O(5)	0.0857(5)	0.2486(2)	0.9649(3)	0.0087(7)
O(6)	-0.0541(5)	0.4132(3)	0.8162(3)	0.0125(7)
O(7)	0.3099(5)	0.4144(3)	0.0948(3)	0.0120(7)
O(8)	0.3220(5)	0.4167(3)	0.8805(3)	0.0160(8)
O(9)	0.0986(5)	0.5828(3)	0.9663(3)	0.0092(7)
O(10)	-0.3352(5)	0.2368(3)	0.9448(3)	0.0149(8)
O(11)	-0.2494(5)	0.2440(3)	0.1603(3)	0.0156(8)
O(12)	0.1204(5)	0.2661(3)	0.1905(3)	0.0102(7)

^a U_{eq} is defined as one-third of the trace of the orthogonalized \mathbf{U}_{ij} tensor.

Table 4.5. Atomic Coordinates and Equivalent Isotropic Displacement Parameters for AgNbO(SeO₃)₂.

Atom	<i>x</i>	<i>y</i>	<i>z</i>	$U_{\text{eq}} (\text{\AA}^2)^a$
Ag(1)	0.83335(8)	-0.0112(2)	0.98471(14)	0.0217(5)
Ag(2)	0	0.4898(2)	0.50451(16)	0.0176(8)
Nb(1)	0.83333(8)	-0.51231(19)	0.01660(15)	0.0066(3)
Nb(2)	0	0.9897(2)	0.4769(2)	0.0082(5)
Se(1)	0.90292(7)	0.2388(2)	0.74294(15)	0.0077(4)
Se(2)	0.76375(7)	-0.2387(3)	0.24379(15)	0.0073(4)
Se(3)	0.93039(7)	0.7388(3)	0.74658(15)	0.0084(5)
O(1)	0.8774(4)	0.3355(12)	0.5614(16)	0.010(2)
O(2)	0.8768(3)	0.3292(12)	0.9230(18)	0.011(2)
O(3)	0.8827(6)	0.0436(16)	0.7352(11)	0.015(3)
O(4)	0.7893(4)	-0.3311(13)	0.4271(18)	0.013(2)
O(5)	0.7908(4)	-0.3329(14)	0.0601(17)	0.014(3)
O(6)	0.7846(5)	-0.0451(17)	0.2390(11)	0.017(3)
O(7)	0.9520(6)	0.5436(17)	0.7484(10)	0.019(4)
O(8)	0.9565(4)	0.8333(13)	0.9281(17)	0.012(2)
O(9)	0.9570(4)	0.8265(13)	0.5592(17)	0.015(3)
O(10)	0.8331(6)	-0.5878(13)	0.2452(10)	0.007(2)
O(11)	0	0.911(2)	0.2373(16)	0.015(4)

^a U_{eq} is defined as one-third of the trace of the orthogonalized \mathbf{U}_{ij} tensor.

Table 4.6. Selected Bond Distances (Å) and Angles (°) for $\text{Ag}_4(\text{Mo}_2\text{O}_5)(\text{SeO}_4)_2(\text{SeO}_3)$.

Distances (Å)			
Mo(1)–O(1)	2.032(4)	Se(1)–O(1) x 2	1.754(3)
Mo(1)–O(3)	2.210(4)	Se(1)–O(2)	1.638(5)
Mo(1)–O(4)	2.288(4)	Se(2)–O(3)	1.645(4)
Mo(1)–O(7)	1.694(4)	Se(2)–O(4)	1.651(4)
Mo(1)–O(8)	1.721(4)	Se(2)–O(5)	1.630(4)
Mo(1)–O(9)	1.889(1)	Se(2)–O(6)	1.643(4)
Angles (°)			
O(1)–Mo(1)–O(3)	75.7(1)	O(7)–Mo(1)–O(9)	98.9(2)
O(1)–Mo(1)–O(4)	76.4(1)	O(8)–Mo(1)–O(9)	102.7(2)
O(1)–Mo(1)–O(7)	97.4(2)	Mo(1)–O(9)–Mo(1)	161.3(3)
O(1)–Mo(1)–O(8)	92.7(2)		
O(1)–Mo(1)–O(9)	154.3(2)	O(1)–Se(1)–O(1)	95.2(2)
O(3)–Mo(1)–O(4)	77.4(1)	O(1)–Se(1)–O(2)	97.2(2)
O(3)–Mo(1)–O(7)	92.6(2)	O(1)–Se(1)–O(2)	97.2(2)
O(3)–Mo(1)–O(8)	161.6(2)	O(3)–Se(2)–O(4)	110.0(2)
O(3)–Mo(1)–O(9)	83.9(1)	O(3)–Se(2)–O(5)	109.0(2)
O(4)–Mo(1)–O(7)	169.2(2)	O(3)–Se(2)–O(6)	109.5(2)
O(4)–Mo(1)–O(8)	86.1(2)	O(4)–Se(2)–O(5)	109.7(2)
O(4)–Mo(1)–O(9)	84.2(1)	O(4)–Se(2)–O(6)	110.0(2)
O(7)–Mo(1)–O(8)	154.3(2)	O(5)–Se(2)–O(6)	108.6(2)

Table 4.7. Selected Bond Distances (Å) and Angles (°) for Ag₂(MoO₃)₃SeO₃.

Distances (Å)			
Mo(1)–O(1)	1.697(4)	Mo(2)–O(9')	2.373(4)
Mo(1)–O(2)	1.704(3)	Mo(3)–O(4')	1.972(3)
Mo(1)–O(3)	2.300(3)	Mo(3)–O(5)	2.288(4)
Mo(1)–O(4)	1.948(3)	Mo(3)–O(9')	1.951(3)
Mo(1)–O(4')	2.300(4)	Mo(3)–O(10)	1.717(4)
Mo(1)–O(5)	1.942(1)	Mo(3)–O(11)	1.687(4)
Mo(2)–O(5)	1.974(3)	Mo(3)–O(12)	2.236(3)
Mo(2)–O(6)	1.721(4)		
Mo(2)–O(7)	2.152(3)	Se(1)–O(3)	1.711(3)
Mo(2)–O(8)	1.687(4)	Se(1)–O(7)	1.703(3)
Mo(2)–O(9)	1.926(3)	Se(1)–O(12)	1.716(4)

Angles (°)			
O(1)–Mo(1)–O(2)	101.2(2)	O(7)–Mo(2)–O(9)	82.7(1)
O(1)–Mo(1)–O(3)	82.4(2)	O(7)–Mo(2)–O(9')	79.0(1)
O(1)–Mo(1)–O(4)	103.7(2)	O(8)–Mo(2)–O(9)	104.7(2)
O(1)–Mo(1)–O(4')	166.5(2)	O(8)–Mo(2)–O(9')	169.9(2)
O(1)–Mo(1)–O(5)	106.8(2)	O(9)–Mo(2)–O(9')	74.3(1)
O(2)–Mo(1)–O(3)	176.3(2)	O(4')–Mo(3)–O(5)	72.7(1)
O(2)–Mo(1)–O(4)	98.4(2)	O(4')–Mo(3)–O(9')	107.0(2)
O(2)–Mo(1)–O(4')	92.2(2)	O(4')–Mo(3)–O(10)	95.8(2)

O(2)–Mo(1)–O(5)	96.6(2)	O(4')–Mo(3)–O(11)	102.1(2)
O(3)–Mo(1)–O(4)	81.5(1)	O(4')–Mo(3)–O(12)	83.5(1)
O(3)–Mo(1)–O(4')	84.2(1)	O(5)–Mo(3)–O(9')	75.0(1)
O(3)–Mo(1)–O(5)	176.3(2)	O(5)–Mo(3)–O(10)	96.9(2)
O(4)–Mo(1)–O(4')	72.4(1)	O(5)–Mo(3)–O(11)	160.4(2)
O(4')–Mo(1)–O(5)	73.0(1)	O(5)–Mo(3)–O(12)	77.4(1)
O(5)–Mo(2)–O(6)	91.2(2)	O(9')–Mo(3)–O(10)	94.7(2)
O(5)–Mo(2)–O(7)	82.6(1)	O(9')–Mo(3)–O(11)	106.0(2)
O(5)–Mo(2)–O(8)	106.3(2)	O(9')–Mo(3)–O(12)	83.0(1)
O(5)–Mo(2)–O(9)	145.7(2)	O(10)–Mo(3)–O(11)	102.5(2)
O(5)–Mo(2)–O(9')	72.6(1)	O(10)–Mo(3)–O(12)	174.1(2)
O(6)–Mo(2)–O(7)	166.5(2)	O(11)–Mo(3)–O(12)	83.3(2)
O(6)–Mo(2)–O(8)	102.4(2)		
O(6)–Mo(2)–O(9)	96.1(2)	O(3)–Se(1)–O(7)	98.4(2)
O(6)–Mo(2)–O(9')	87.7(2)	O(3)–Se(1)–O(12)	97.3(2)
O(7)–Mo(2)–O(8)	90.9(2)	O(7)–Se(1)–O(12)	101.5(2)

Table 4.8. Selected Bond Distances (Å) and Angles (°) for AgNbO(SeO₃)₂.

Distances (Å)			
Nb(1)–O(1)	2.004(11)	Se(1)–O(1)	1.737(11)
Nb(1)–O(2)	1.988 (10)	Se(1)–O(2)	1.718(12)
Nb(1)–O(4)	1.981(11)	Se(1)–O(3)	1.650(13)
Nb(1)–O(5)	1.980(12)	Se(2)–O(4)	1.734(12)
Nb(1)–O(10)	1.778(8)	Se(2)–O(5)	1.765(12)
Nb(1)–O(10)	2.139(8)	Se(2)–O(6)	1.646(14)
Nb(2)–O(8) X 2	1.996(11)	Se(3)–O(7)	1.668(14)
Nb(2)–O(9) X 2	1.974(12)	Se(3)–O(8)	1.739 (12)
Nb(2)–O(11)	1.862(13)	Se(3)–O(9)	1.758(12)
Nb(2)–O(11)	2.062(13)		

Angles (°)			
O(1)–Nb(1)–O(2)	88.8(6)	O(8)–Nb(2)–O(11)	93.2(5)
O(1)–Nb(1)–O(4)	169.5(6)	O(9)–Nb(2)–O(9)	89.4(7)
O(1)–Nb(1)–O(5)	89.1(4)	O(9)–Nb(2)–O(11)	94.6(5)
O(1)–Nb(1)–O(10)	84.7(6)	O(9)–Nb(2)–O(11)	87.4(5)
O(2)–Nb(1)–O(4)	90.7(4)	O(11)–Nb(2)–O(11)	177.2(3)
O(2)–Nb(1)–O(5)	168.3(6)	O(1)–Se(1)–O(2)	100.5(7)
O(2)–Nb(1)–O(10)	84.6(6)	O(1)–Se(1)–O(3)	100.5(6)
O(4)–Nb(1)–O(5)	89.3(6)	O(2)–Se(1)–O(3)	101.9(5)
O(4)–Nb(1)–O(10)	84.9(6)	O(4)–Se(2)–O(5)	100.8(8)

O(5)–Nb(1)–O(10)	83.8(6)	O(4)–Se(2)–O(6)	101.5(5)
O(10)–Nb(1)–O(10)	177.9(4)	O(5)–Se(2)–O(6)	99.2(6)
O(8)–Nb(2)–O(8)	89.3(7)	O(7)–Se(3)–O(8)	100.0(6)
O(8)–Nb(2)–O(9)	90.1(6)	O(7)–Se(2)–O(9)	98.8(6)
O(8)–Nb(2)–O(9)	172.2(3)	O(8)–Se(2)–O(9)	101.6(7)

RESULTS AND DISCUSSION

Synthesis of $\text{Ag}_4(\text{Mo}_2\text{O}_5)(\text{SeO}_4)_2(\text{SeO}_3)$, $\text{Ag}_2(\text{MoO}_3)_3\text{SeO}_3$, and $\text{AgNbO}(\text{SeO}_3)_2$.

There are a number of methods that have been applied to the synthesis of mixed-valent selenate selenite compounds. Under hydrothermal conditions, SeO_4^{2-} can be reduced to SeO_3^{2-} as occurs in the preparation of $\text{Au}_2(\text{SeO}_3)_2(\text{SeO}_4)$.¹⁰ In the synthesis of $\text{Nd}_2(\text{SeO}_4)(\text{SeO}_3)_2(\text{H}_2\text{O})_2$, a portion of the SeO_4^{2-} was reduced to SeO_3^{2-} with 1,10-phenanthroline.⁴ $\text{Na}_2\text{SeO}_4 \cdot \text{H}_2\text{SeO}_3 \cdot \text{H}_2\text{O}$ was prepared by slow evaporation of an aqueous solution containing Na_2SeO_4 and H_2SeO_3 at room temperature.⁶ Mixed-valent Se(IV)/Se(VI) compounds can also be obtained by oxidizing SeO_2 with HNO_3 , e.g. in the preparation of $\text{Er}_2(\text{SeO}_3)_2(\text{SeO}_4) \cdot 2\text{H}_2\text{O}$.²

In this work, $\text{Ag}_4(\text{Mo}_2\text{O}_5)(\text{SeO}_4)_2(\text{SeO}_3)$ was prepared as a pure phase by reacting AgNO_3 , MoO_3 , and H_2SeO_4 under mild hydrothermal conditions. Here some of the SeO_4^{2-} was reduced to SeO_3^{2-} as occurs in the preparation of $\text{Th}(\text{SeO}_3)(\text{SeO}_4)$.¹¹ There are two options for explaining the reduction of selenate to selenite. The first of these is that the relatively strong oxidizing power of selenate ($E^\circ = 1.151 \text{ V}$) might be sufficient under these conditions to oxidize water. Second, the selenate might thermally decompose to yield selenite. The moderate heating conditions used here allow for the isolation of partially reduced compounds. The synthesis of $\text{Ag}_4(\text{Mo}_2\text{O}_5)(\text{SeO}_4)_2(\text{SeO}_3)$ is quite reproducible, and occurs in high yield, suggesting that an impurity is not responsible for the reduction of the selenate anion.

Orange crystals of $\text{Ag}_2(\text{MoO}_3)_3\text{SeO}_3$ were synthesized hydrothermally by reacting AgNO_3 , MoO_3 , SeO_2 , and HF . Although fluoride is not incorporated in the compound, HF apparently plays an important role in the synthesis because attempts to prepare

$\text{Ag}_2(\text{MoO}_3)_3\text{SeO}_3$ in the absence of HF were unsuccessful. The substitution of nitric acid for hydrofluoric acid was not successful. Fluoride is probably serving as a mineralizing agent.

In the synthesis of $\text{AgNbO}(\text{SeO}_3)_2$, niobium metal was oxidized to Nb^{+5} by selenic acid, and, as a result, selenic acid was reduced to selenite. As opposed to the synthesis of $\text{Ag}_4(\text{Mo}_2\text{O}_5)(\text{SeO}_4)_2(\text{SeO}_3)$ and $\text{Ag}_2(\text{MoO}_3)_3\text{SeO}_3$, which are produced by heating at 200 °C for 3 days, a longer period (10 days) is needed for generating $\text{AgNbO}(\text{SeO}_3)_2$. Attempts to produce $\text{AgNbO}(\text{SeO}_3)_2$ under shorter periods failed.

Crystal Structure of $\text{Ag}_4(\text{Mo}_2\text{O}_5)(\text{SeO}_4)_2(\text{SeO}_3)$. The structure of the title compound contains one crystallographically unique Mo(VI) center in classical 2+2+2 coordination environments with two long, two intermediate, and two short bonds. The Mo–O bond distances are 1.694(4), 1.721(4), 1.889(4), 2.032(4), 2.210(4), and 2.288(4) Å. The two shortest bonds define MoO_2^{2+} molybdenyl units where the oxo atoms are terminal. The Mo centers are shifted along a C_2 -axis of each octahedron by 0.356(1) Å from the center of the six oxygen atoms. The MoO_6 units share a single corner to create dimers. The bridging Mo(1)–O(9) bond has a bond distance of 1.889(1) Å, and a Mo(1)–O(9)–Mo(1) angle of 161.3(3)° that are typical when compared with previously reported crystallographic data of Mo_2O_{11} units.^{28,29,30} Within each dimer two selenate anions bridge the Mo(VI) centers. The dimers are in turn linked into zigzag one-dimensional chains by selenite anions, as is shown in Fig. 4.1. The chains extend down the c -axis. Individual chains are polar with the C_2 distortion of the Mo(VI) octahedra aligning on one side of each chain. However, the overall structure is centrosymmetric because neighboring chains have opposite alignment of the C_2 distortion, as is depicted in

Fig. 4.2. The bridging selenite anions contain a stereochemically active lone-pair of electrons that oppositely align in the *b* direction, resulting in a cancellation of polarity produced by this group. There are no long contacts between the Se atom in the selenite anion and neighboring oxygen atoms within the structure. Selected bond distances and bond angles are given in Table 4.6. The calculated bond-valence sum (BVS) of Mo(1) is 5.994.^{31,32} Se(1) is coordinated by three oxygen atoms in a trigonal pyramidal geometry with Se(1)–O bond distances of 1.638(5) Å (terminal) and 1.754(3) Å (bridging). Se(2) is present in a tetrahedral environment, and has Se(2)–O bonds averaging 1.642(4) Å. The calculated bond valence sums of Se(1) and Se(2) are 3.932 and 5.897, respectively.^{31,32} There are three crystallographically unique Ag⁺ centers in the structure of Ag₄(Mo₂O₅)(SeO₄)₂(SeO₃). Ag(1) resides in a trigonal prismatic environment with Ag–O bond distances ranging from 2.429(4) to 2.490(4) Å. Ag(2) and Ag(3) are five- and six-coordinate, respectively, and both have highly irregular geometries. Ag(2) has Ag–O bond distances in the range of 2.306(6)–2.553(4) Å, while those of Ag(3) range from 2.415(4) to 2.579(4) Å. The calculated bond valence sums of Ag(1), Ag(2), and Ag(3) are 1.001, 0.798, and 0.929, respectively.^{31,32}

Crystal Structure of Ag₂(MoO₃)₃SeO₃. Although Ag₂(MoO₃)₃SeO₃ has a similar formula with A₂(MoO₃)₃SeO₃ (A=Rb, Cs, Tl, NH₄), it crystallizes in the monoclinic space group *P2₁/n* instead of the hexagonal space group *P6₃*.¹⁵ The A₂(MoO₃)₃SeO₃ (A=Rb, Cs, Tl, NH₄) family of compounds consists of two-dimensional anionic slabs related to WO₃ that are capped on one side by selenite. The structure of Ag₂(MoO₃)₃SeO₃ consists of three crystallographically unique Mo(VI) centers that are also in classical 2+2+2 coordination environments with two long, two intermediate, and

two short bonds. In each MoO₆ unit, three oxygen atoms are shared with four neighboring [MoO₆] units through edge- and corner-sharing, and with one oxygen atom from the selenite anion. The remaining two oxygen atoms are terminal with O–Mo–O angles of 101.2(2)°, 102.4(2)°, and 102.5(2)° for Mo(1), Mo(2), and Mo(3), respectively. These MoO₆ units are connected to form a molybdenyl ribbon that extends along the *c*-axis as is shown in Fig. 4.3. Selected bond distances and bond angles are given in Table 4.7. The BVS values of Mo(1), Mo(2), and Mo(3) are 5.99, 6.05, and 5.98, respectively.^{31,32} These ribbons are further connected together through tridentate selenite anions to form a two-dimensional layer in [*bc*] plane, and stacks along the *a*-axis as is shown in Fig. 4.4. The bridging tridentate selenite anions have Se–O bond distances of 1.703(3), 1.711(3), and 1.716(4) Å, with a BVS value of 3.94 for the selenium atom.^{31,32} Unlike the A₂(MoO₃)₃SeO₃ (A=Rb, Cs, Tl, NH₄) family of compounds, which have the lone-pair of electrons on the Se atoms located on one side of the molybdenum oxide sheets as indicated by the polar space group, as shown in Figure 4.3, the selenite groups in Ag₂(MoO₃)₃SeO₃ have opposing orientations in each layer. There are two crystallographically unique Ag⁺ centers in the structure of Ag₂(MoO₃)₃SeO₃. Ag(1) has Ag–O bond distances in the range of 2.400(3)–2.592(3) Å, while those of Ag(2) range from 2.272(4) to 2.481(3) Å. Ag(1)O₆ units edge-share with adjacent Ag(2)O₆ polyhedra. The calculated bond valence sums of Ag(1) and Ag(2) are 0.944 and 1.176, respectively.^{31,32}

Crystal Structure of AgNbO(SeO₃)₂. The structure of AgNbO(SeO₃)₂ contains two crystallographically unique Nb(VI) centers possessing a distorted octahedral geometry. These octahedra are distorted along the *c* axis with short bond distances of

1.778(8) Å (Nb(1)) or 1.862(13) Å (Nb(2)), and long distance of 2.139(8) Å (Nb(1)) or 2.062(13) Å (Nb(2)). The remaining four Nb–O bonds are sitting in the $[ab]$ plane and have bond distances in the range of 1.974(12) Å to 2.004(11) Å. As shown in Figure 4.5, these distorted NbO₆ units connect with each other by corner-sharing and form one-dimensional chains along c axis. What is surprising is that all of Nb centers within a chain are shifted in the same direction away from the octahedral center and generate polarity along the c axis. It is necessary to point out that different chains composed by different Nb centers are heading to opposite directions which will cancel the polarity of each other. As can be seen from the bond distances of Nb–O reported above, Nb(1)O₆ octahedra are more polarized than Nb(2)O₆ octahedra and some polarity still remains as a whole structure. Within these polar chains, adjacent Nb octahedra are further linked by two bidentate selenites and result in a more rigid structure. These bridging selenites have average Se–O bond distances of 1.655(14) Å (terminal) and 1.742(12) Å (bridging). Selected bond distances and bond angles are given in Table 4.8. The calculated bond-valence sum (BVS) of Nb(1) and Nb(2) are 4.997 and 5.012 respectively.^{31,32} The calculated bond valence sums of Se(1), Se(2) and Se(3) are 3.937, 4.011, and 3.982, respectively.^{31,32} There are two crystallographically unique Ag⁺ centers in the structure of AgNbO(SeO₃)₂. As shown in Figure 4.6, both Ag(1) and Ag(2) reside in a rectangular planar environment with Ag–O bond distances ranging from 2.404(13) to 2.465(13) Å. The calculated bond valence sums of Ag(1) and Ag(2) are 1.001, and 0.929, respectively.^{31,32}

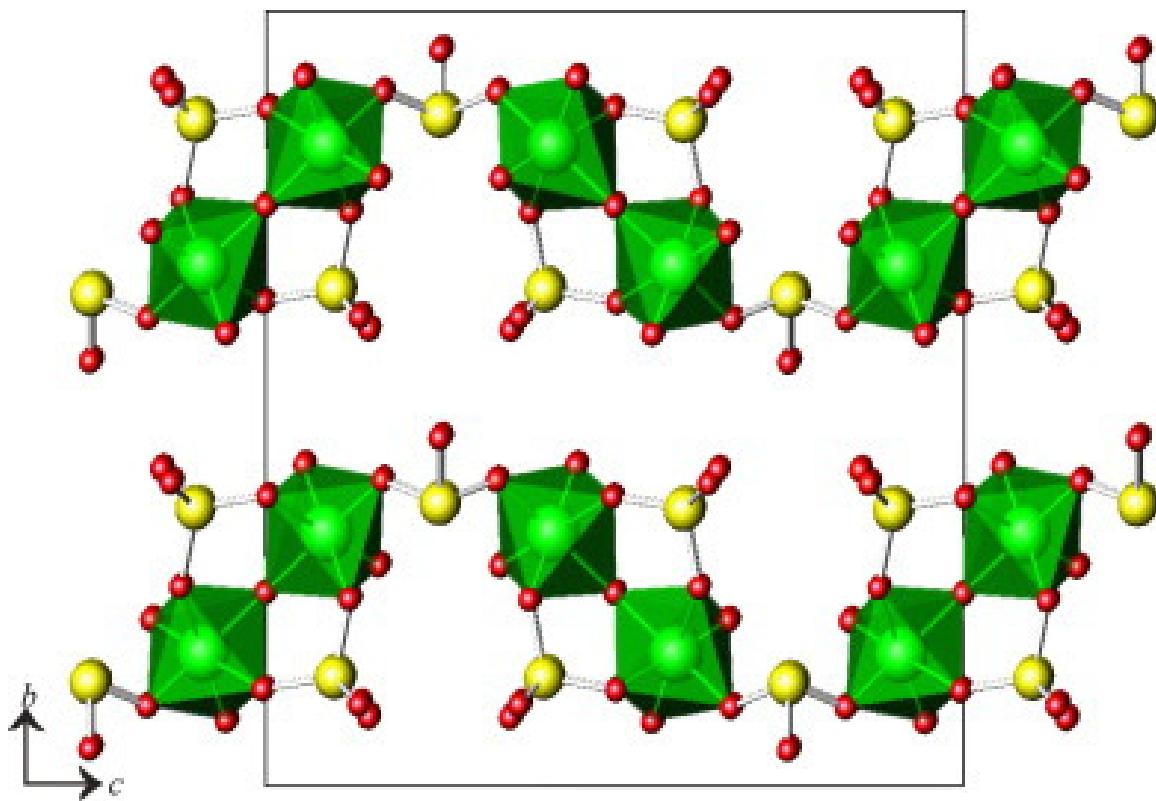


Figure 4.1. A view of the one-dimensional $[(\text{Mo}_2\text{O}_5)(\text{SeO}_4)_2(\text{SeO}_3)]^{4-}$ chains that extend down the c -axis in the structure of $\text{Ag}_4(\text{Mo}_2\text{O}_5)(\text{SeO}_4)_2(\text{SeO}_3)$. Green polyhedra represent the MoO_6 building blocks, yellow (medium) and red (small) balls stand for selenium and oxygen atoms, respectively. Silver atoms are deleted for the purpose of clarity.

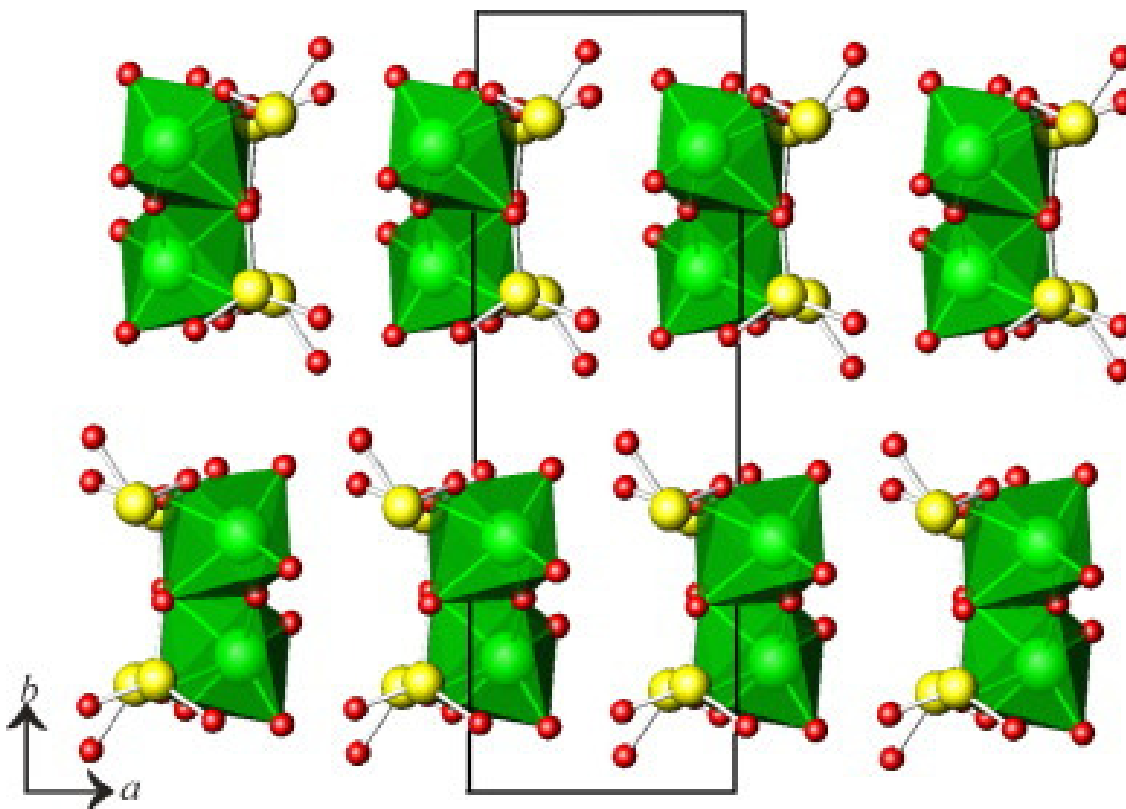


Figure 4.2. A depiction of individual polar $[(\text{Mo}_2\text{O}_5)(\text{SeO}_4)_2(\text{SeO}_3)]^{4-}$ chains with the C_2 distortion of the Mo(VI) octahedra aligning on one side of each chain in $\text{Ag}_4(\text{Mo}_2\text{O}_5)(\text{SeO}_4)_2(\text{SeO}_3)$. Green polyhedra represent the MoO_6 building blocks, yellow (medium) and red (small) balls stand for selenium and oxygen atoms, respectively. Silver atoms are deleted for the purpose of clarity.

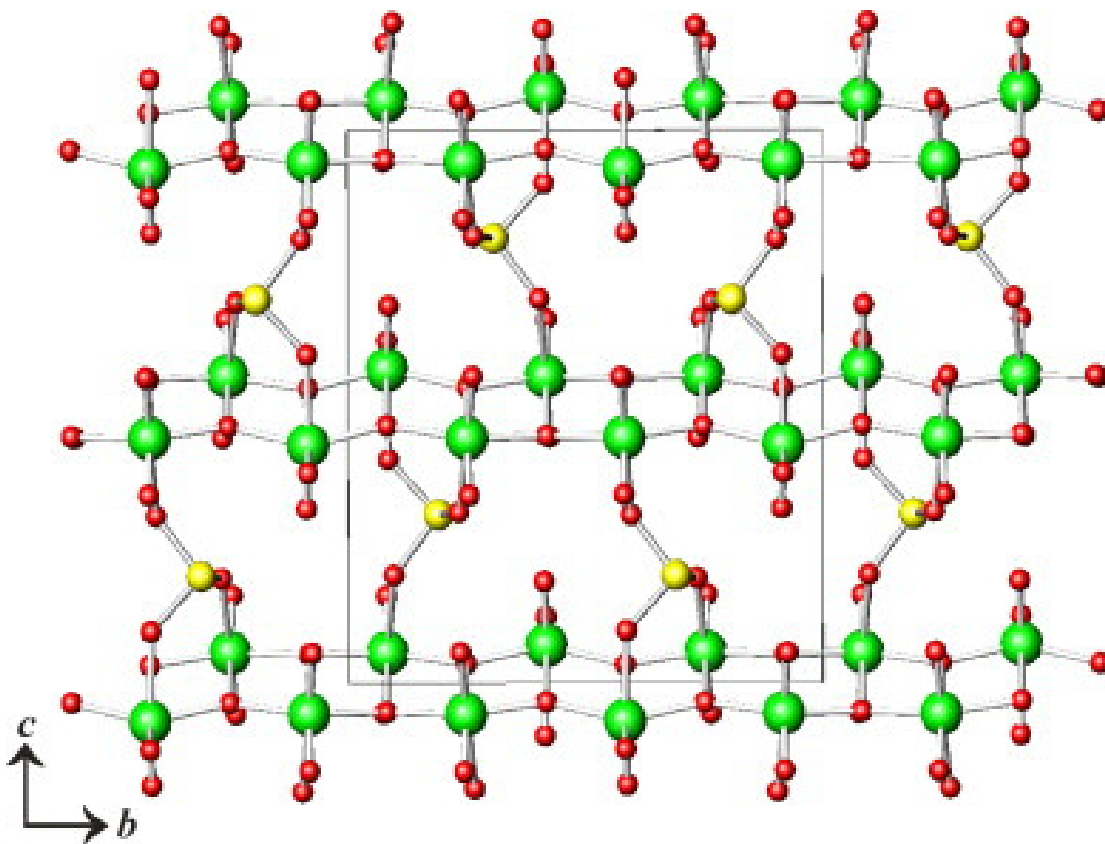


Figure 4.3. A view of the two-dimensional $[(\text{MoO}_3)_3\text{SeO}_3]^{2-}$ layer in $\text{Ag}_2(\text{MoO}_3)_3\text{SeO}_3$ that extends in the $[bc]$ plane. Green (large), yellow (medium) and red (small) balls stand for selenium and oxygen atoms, respectively. Silver atoms are deleted for the purpose of clarity.

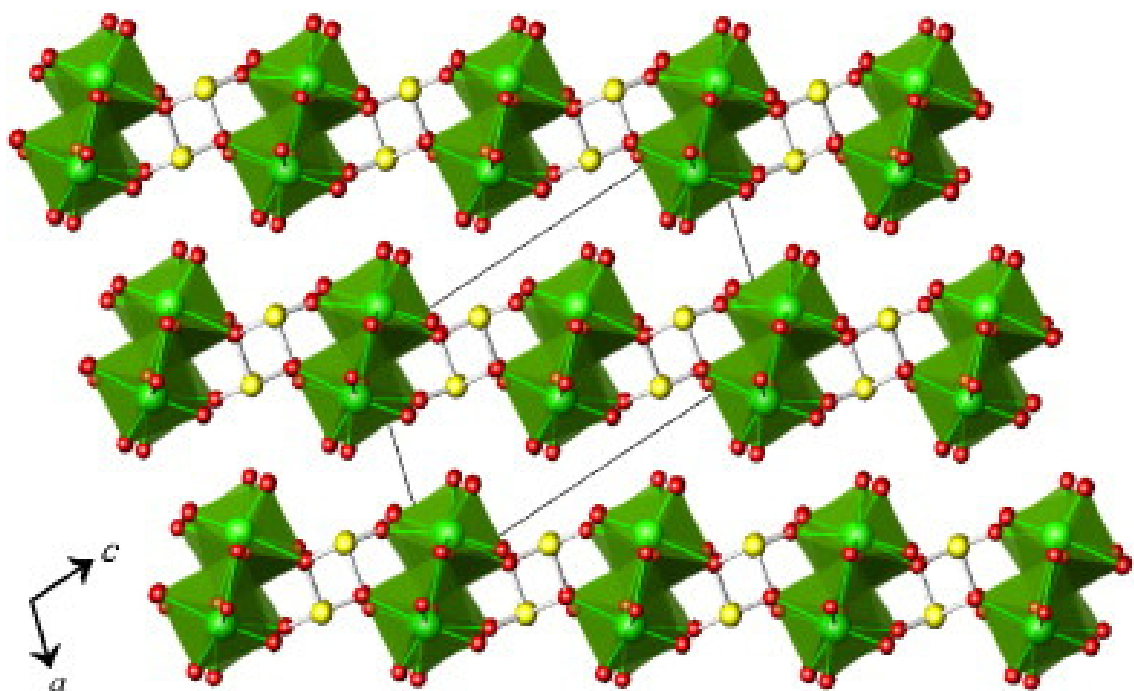


Figure 4.4. An illustration of the stacking of the $[(\text{MoO}_3)_3\text{SeO}_3]^{2-}$ layers in $\text{Ag}_2(\text{MoO}_3)_3\text{SeO}_3$. Green (large), yellow (medium) and red (small) balls stand for selenium and oxygen atoms, respectively. Silver atoms are deleted for the purpose of clarity.

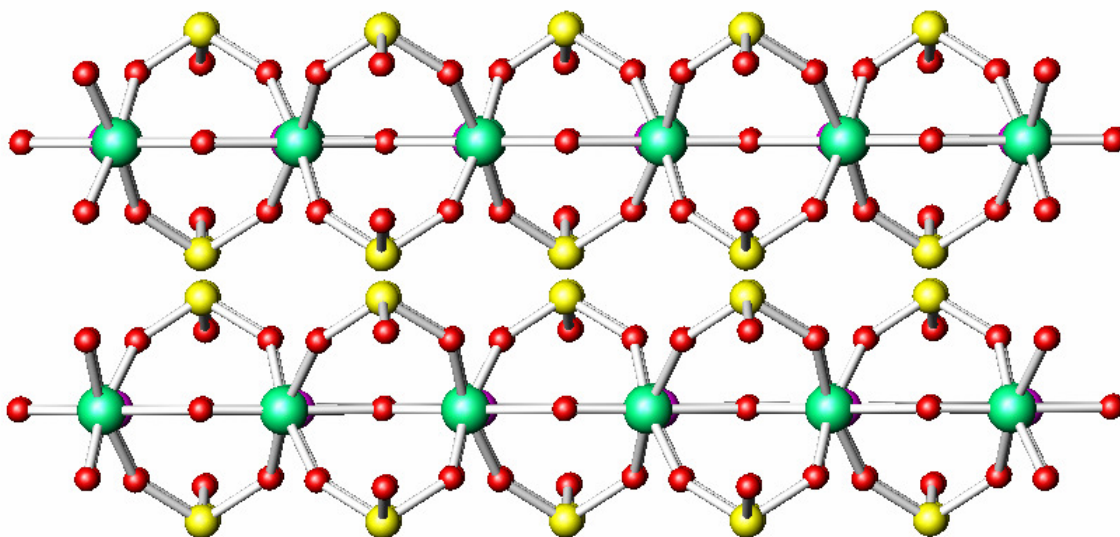


Figure 4.5. An illustration of two one-dimensional chains formed by corner-sharing connection of Nb(1) (top) and Nb(2) (below) octahedra along c axis in the structure of $\text{AgNbO}(\text{SeO}_3)_2$. Green (large), yellow (medium) and red (small) balls stand for selenium and oxygen atoms, respectively. Silver atoms are deleted for the purpose of clarity.

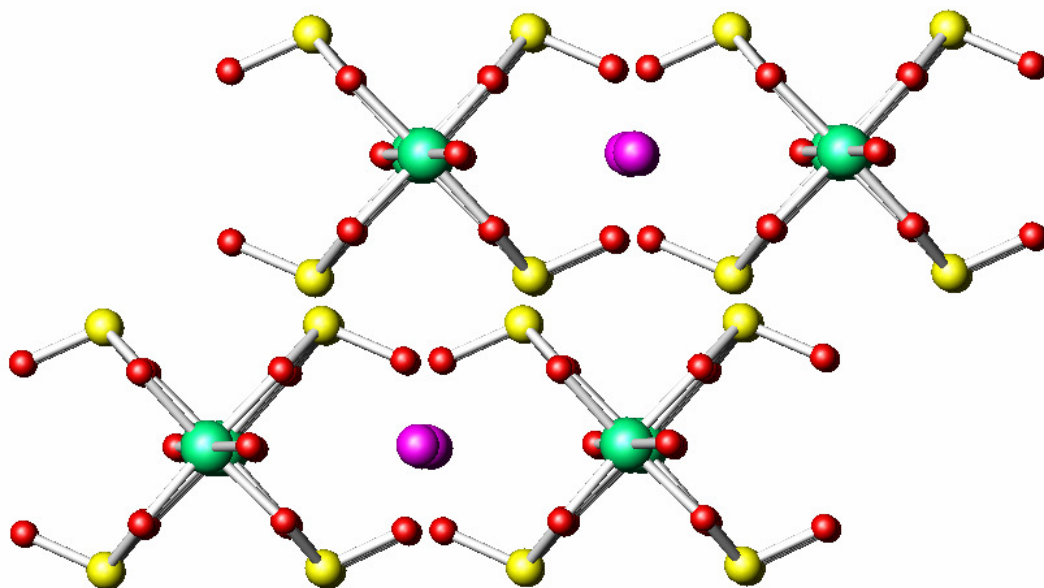


Figure 4.6. A view of the structure of $\text{AgNbO}(\text{SeO}_3)_2$ along the c axis. Green (large), purple (large), yellow (medium) and red (small) balls stand for niobium, silver, selenium and oxygen atoms, respectively.

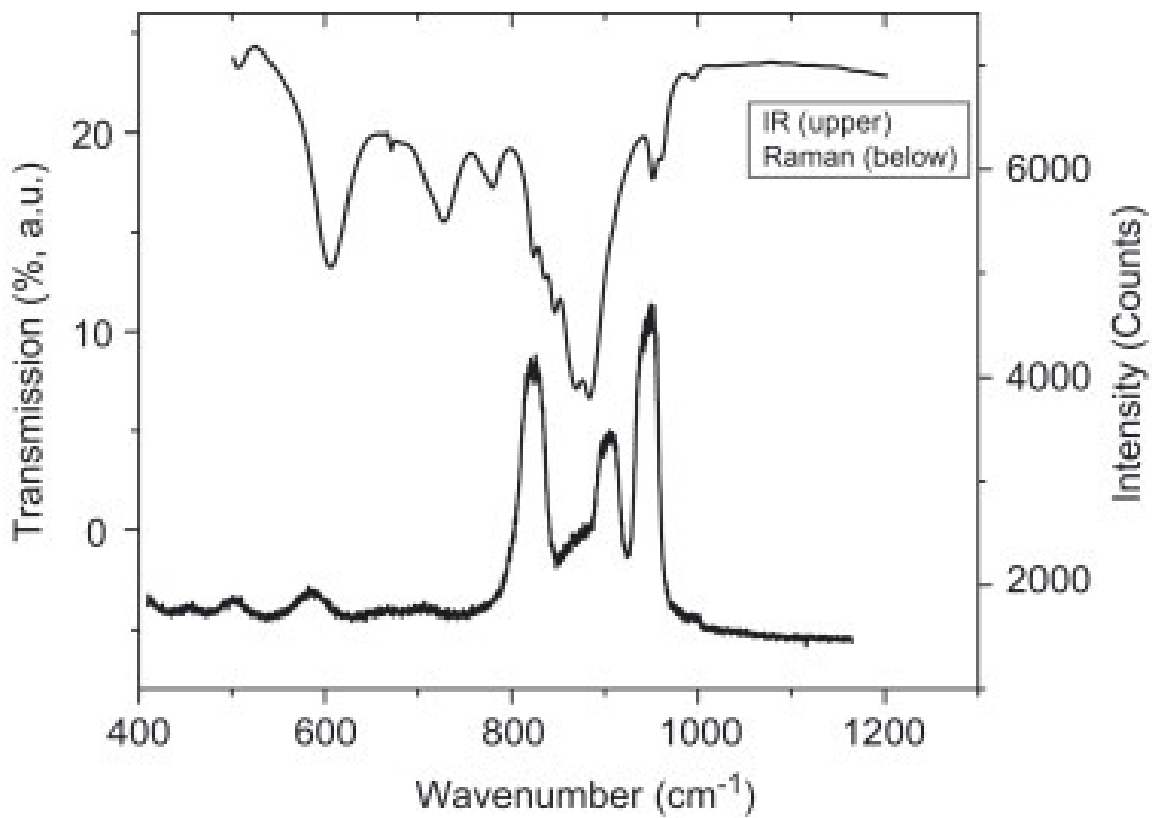


Figure 4.7. IR and Raman spectra of $\text{Ag}_4(\text{Mo}_2\text{O}_5)(\text{SeO}_4)_2(\text{SeO}_3)$.

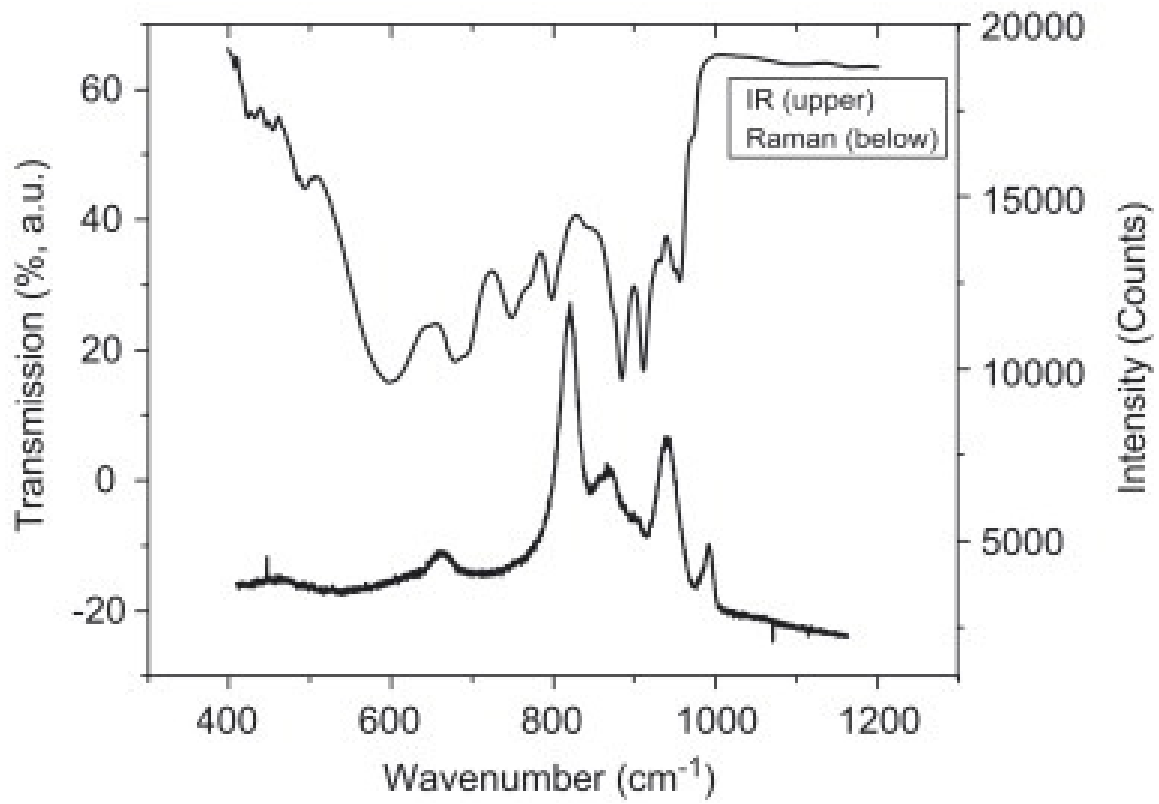


Figure 4.8. IR and Raman spectra of $\text{Ag}_2(\text{MoO}_3)_3\text{SeO}_3$.

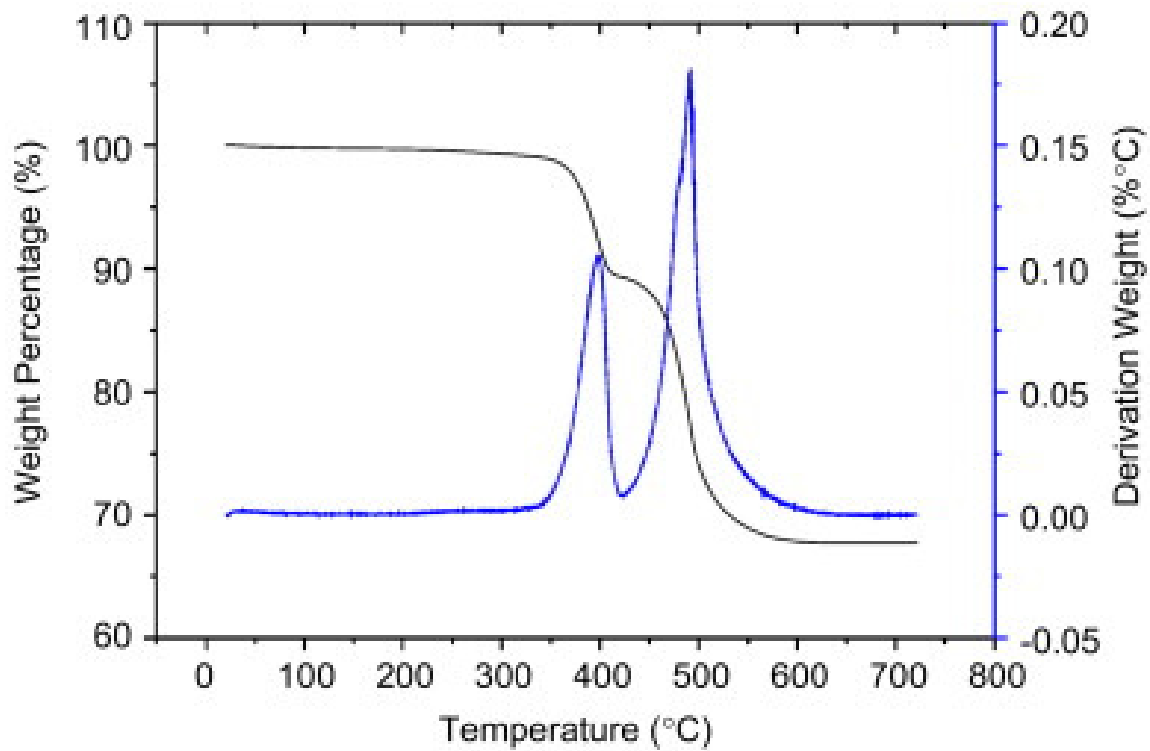


Figure 4.9. A TGA thermogram for $\text{Ag}_4(\text{Mo}_2\text{O}_5)(\text{SeO}_4)_2(\text{SeO}_3)$.

Vibrational Spectra of $\text{Ag}_4(\text{Mo}_2\text{O}_5)(\text{SeO}_4)_2(\text{SeO}_3)$, $\text{Ag}_2(\text{MoO}_3)_3\text{SeO}_3$ and $\text{AgNbO}(\text{SeO}_3)_2$. The vibrational spectrum of $\text{Ag}_4(\text{Mo}_2\text{O}_5)(\text{SeO}_4)_2(\text{SeO}_3)$ is complex; It consists of three primary regions. The highest wavenumber region with three bands observed at 991, 954, and 945 cm^{-1} in IR spectrum and one band at 960 cm^{-1} in Raman spectrum is attributable to vibrational modes from the MoO_2^{2+} units.³³ The second zone has IR bands at 884, 868, 846, 836, and 825 cm^{-1} that can be assigned to stretches of the Se–O bond in the SeO_4^{2-} anions.³⁴ Finally, two bands in the IR are found at 781 and 726 cm^{-1} that are attributed to the stretches of Se–O bonds in SeO_3^{2-} anions.³⁵ The Raman spectrum of $\text{Ag}_4(\text{Mo}_2\text{O}_5)(\text{SeO}_4)_2(\text{SeO}_3)$ shows two bands at 815 and 907 cm^{-1} that are due to stretching modes of the SeO_3^{2-} and SeO_4^{2-} , respectively. The IR and Raman spectra of $\text{Ag}_4(\text{Mo}_2\text{O}_5)(\text{SeO}_4)_2(\text{SeO}_3)$ are shown in Fig. 4.7.

In the IR spectrum of $\text{Ag}_2(\text{MoO}_3)_3\text{SeO}_3$ there are bands at 974, 957, 950, 932, and 911 cm^{-1} that are associated with stretches of the molybdenyl units. Six bands at 798, 769, 748, 692, 677, and 599 cm^{-1} are assigned as characteristic vibrational modes for SeO_3^{2-} anions. The Raman spectrum of $\text{Ag}_2(\text{MoO}_3)_3\text{SeO}_3$ shows two sharp bands at 865 and 820 cm^{-1} and one broad band at 664 cm^{-1} that are due to vibrational modes of the SeO_3^{2-} anions. One weak band at 899 cm^{-1} and one sharp band at 942 cm^{-1} are assigned to the stretching modes of the MoO_2^{2+} units. The IR and Raman spectra of $\text{Ag}_2(\text{MoO}_3)_3\text{SeO}_3$ are shown in Fig. 4.8.

In the IR spectrum of $\text{AgNbO}(\text{SeO}_3)_2$, two bands at 876 and 630 cm^{-1} are related to stretching vibrations of Nb–O.³⁶ Five bands at 792, 705, 687, 602, and 587 cm^{-1} are assigned as characteristic vibrational modes for SeO_3^{2-} anions.

Thermal Analysis of $\text{Ag}_4(\text{Mo}_2\text{O}_5)(\text{SeO}_4)_2(\text{SeO}_3)$ and $\text{Ag}_2(\text{MoO}_3)_3\text{SeO}_3$. The thermal behavior of selenates and selenites is of interest because there are multiple mechanisms of decomposition including loss of oxygen by selenate and decomposition of the selenate and selenite anions to yield SeO_2 .^{35,37} The thermal decomposition of $\text{Ag}_4(\text{Mo}_2\text{O}_5)(\text{SeO}_4)_2(\text{SeO}_3)$ follows a two-step mechanism shown in Fig. 4.9. The TGA curve shows the compound is thermally stable up to 375 °C. The first weight loss is in the temperature range of 376–406 °C, and may correspond to the release of SeO_2 from a SeO_3^{2-} anion. The observed weight loss of 9.95% is in good agreement with the calculated value (9.94%). The second weight loss from 469 to 510 °C can be attributed to the loss of two SeO_2 units and one O_2 molecule released from two SeO_4^{2-} anions. The second experimental weight loss of 22.2% is also consistent with the calculated value (22.7%). The powder X-ray diffraction data of the final residue corresponds with pure Ag_2MoO_4 .³⁸ Therefore, the two-step decomposition mechanism can potentially be described by the following equations:



Similar to the thermal behavior of $\text{A}_2(\text{MoO}_3)_3\text{SeO}_3$ ($\text{A}=\text{Rb}, \text{Cs}, \text{Tl}$),¹⁵ the TGA data for $\text{Ag}_2(\text{MoO}_3)_3\text{SeO}_3$ shows a one-step weight loss over a broad range from 350 to 550 °C. The final residue is identified as pure $\text{Ag}_2\text{Mo}_3\text{O}_{10}$ by powder X-ray diffraction.³⁹ The observed weight loss of 14.1% is close to the theoretical value of 14.3% calculated for the elimination of one SeO_2 from $\text{Ag}_2(\text{MoO}_3)_3\text{SeO}_3$.

CONCLUSION

In this report we have provided the details on the syntheses, structures, vibrational spectroscopy, and thermal behavior of $\text{Ag}_4(\text{Mo}_2\text{O}_5)(\text{SeO}_4)_2(\text{SeO}_3)$, $\text{Ag}_2(\text{MoO}_3)_3\text{SeO}_3$ and $\text{AgNbO}(\text{SeO}_3)_2$. For $\text{Ag}_4(\text{Mo}_2\text{O}_5)(\text{SeO}_4)_2(\text{SeO}_3)$ and $\text{Ag}_2(\text{MoO}_3)_3\text{SeO}_3$, despite the fact that both of these compounds possess oxoanions with a stereochemically active lone-pair of electrons, both compounds crystallize in centrosymmetric space groups. For $\text{AgNbO}(\text{SeO}_3)_2$, polar chains are formed by corner connection of distorted NbO_6 octahedra along the c axis. But adjacent chains composed by different Nb centers are aligned in an antiparallel manner and cancel some part of polarization in the whole structure. All of above compounds are low-dimensional, a feature that might be attributable to the presence of the selenite anions. $\text{Ag}_4(\text{Mo}_2\text{O}_5)(\text{SeO}_4)_2(\text{SeO}_3)$ and $\text{Ag}_2(\text{MoO}_3)_3\text{SeO}_3$ thermally decompose at elevated temperatures through the loss of SeO_2 .

REFERENCES

1. Effenberger, H. *Mineral. Petrol.* **1987**, 36, 3.
2. Morris, R. E.; Wilkinson, A. P.; Cheetham, A. K. *Inorg. Chem.* **1992**, 31, 4774.
3. Harrison, W. T. A.; Zhang, Z. *Eur. J. Solid State Inorg. Chem.* **1997**, 34, 599..
4. Berdonosov, P. S.; Schmidt, P.; Dityatyev, O. A.; Dolgikh, V. A.; Lightfoot, P.; Ruck, M. *Z. Anorg. Allg. Chem.* **2004**, 630, 1395.
5. Krugermann, I.; Wickleder, M. S. *Z. Anorg. Allg. Chem.* **2002**, 628, 147.
6. Baran, J.; Lis, T.; Marchewka, M.; Ratajczak, H. *J. Mol. Struct.* **1991**, 250, 13.
7. Giester, G. *Monatsh. Chem.* **1989**, 120, 661.
8. Weil, M.; Kolitsch, U. *Acta Crystallogr.* **2002**, C 58, 47.
9. Giester, G. *Monatsh. Chem.* **1992**, 123, 957.
10. Wickleder, M. S.; Buchner, O.; Wickleder, C.; el Sheik, S.; Brunklaus, G.; Eckert, H. *Inorg. Chem.* **2004**, 43, 5860.
11. Sullens, T. A.; Almond, P. M.; Byrd, J. A.; Beitz, J. V.; Bray T. H.; Albrecht-Schmitt, T. E. *J. Solid State Chem.* **2006**, 179, 1192.
12. Krivovichev, S. V.; Tananaev, I. G.; Kahlenberg, V.; Myasoedov, B. F. *Dokl. Phys. Chem.* **2005**, 403, 124.
13. Krivovichev, S. V.; Tananaev, I. G.; Kahlenberg, V.; Myasoedov, B. F. *Radiochemistry* **2006**, 48, 217.
14. Albrecht-Schmitt, T. E.; Almond, P. M.; Sykora, R. E. *Inorg. Chem.* **2003**, 42, 3788.

15. (a) Harrison, W. T. A.; Dussack, L. L.; Jacobson, A. J. *Inorg. Chem.* **1994**, 33, 6043.
(b) Dussack, L. L.; Harrison, W. T. A.; Jacobson, A. J. *Mater. Res. Bull.* **1996**, 31, 249.
16. Halasyamani, P. S.; Poeppelmeier, K. R. *Chem. Mater.* **1998**, 10, 2753.
17. Ok, K. M.; Chi, E. O.; Halasyamani, P. S. *Chem. Soc. Rev.* **2006**, 35, 710.
18. Goodenough, J. B.; Longo, J. M. *Crystallographic and magnetic properties of perovskite and perovskite-related compounds.*; Eds.; Springer-Verlag: Berlin, **1970**, Vol. 4.
19. Wheeler, R. A.; Whangbo, M. H.; Hughbanks, T.; Hoffmann, R.; Burdett, J. K.; Albright, T. A. *J. Am. Chem. Soc.* **1986**, 108, 2222.
20. Liu, G. Z.; Zheng, S. T.; Yang, G. Y. *Chem. Commun.* **2007**, 751.
21. Kinomura, N.; Kumada, N. *Inorg. Chem.* **1990**, 29, 5217.
22. Bostroem, M.; Gemmi, M.; Schnelle, W.; Eriksson, L. *J. Solid State Chem.* **2004**, 177, 1738.
23. Halasyamani, P.S.; O'Hare, D. *Chem. Mater.* **1998**, 10, 646.
24. Ling, J.; Albrecht-Schmitt, T. E. *J. Solid State Chem.* **2007**, 180, 1601.
25. Sheldrick, G. M. *Acta Crystallogr.* **1995**, A 51, 33.
26. Sheldrick, G. M. SHELXTL PC, Version 5.0, An Integrated System for Solving, Refining, and Displaying Crystal Structures from Diffraction Data, Siemens Analytical X-ray Instrument, Inc., Madison, WI **1994**.
27. ATOMS 6.1, Shape Software, **2004**.
28. Kitanovski, N.; Golobic, A.; Ceh, B. *Inorg. Chem. Commun.* **2006**, 9, 296.
29. Rao, K. P.; Balraj, V.; Minimol, M. P.; Vidyasagar, K. *Inorg. Chem.* **2004**, 43, 4610.

30. Xiao, D.; Hou, Y.; Wang, E.; Wang, S.; Li, Y.; De, G.; Xu, L.; Hu, C. *J. Mol. Struct.* **2003**, 659, 13.
31. Brown, I. D.; Altermatt, D. *Acta Crystallogr.* **1985**, B 41, 244.
32. Brese, N. E.; O'Keeffe, M. *Acta Crystallogr.* **1991**, B 47, 192.
33. Stiefel, E. I.; In: Wilkinson, G.; Gillard, R. D.; McCleverty, J. A. Editors, *Comprehensive Coordination Chemistry* vol. 3, Pergamon Press, London **1978**, 1380.
34. Sathjanandan, K.; McCory, L. D.; Margrave, J. L. *Spectrochim. Acta* **1964**, 20, 957.
35. Verma, V. P. *Thermochim. Acta* **1999**, 327, 63.
36. Da Silva, J. C. G.; Vieira, M. D.; De Oliveira Andrade, W.; Dos Santos, A. C. B. *J. Mater. Sci.* **2005**, 40, 4455
37. Havlicek, D.; Micka, Z.; Boublikova, R. *Coll. Czech. Chem. Commun.* **1995**, 60, 969.
38. Lindqvist, I. *Nova Acta Reg. Soc. Sci. Upsa.* **1950**, 15, 22.
39. Gatehouse, B. M.; Leverett, P. *J. Chem. Soc.* **1968**, A 6, 1398.

CHAPTER 5
HYDROTHERMAL SYNTHESIS AND STRUCTURAL CHARACTERIZATION
OF LATE LANTHANIDE IODATES

ABSTRACT

The reaction of Lu^{3+} or Yb^{3+} and H_5IO_6 in aqueous media at 180 °C leads to the formation of $\text{Yb}(\text{IO}_3)_3(\text{H}_2\text{O})$ or $\text{Lu}(\text{IO}_3)_3(\text{H}_2\text{O})$, respectively, while the reaction of Yb metal with H_5IO_6 under similar reaction conditions gives rise to the anhydrous iodate, $\text{Yb}(\text{IO}_3)_3$. Under supercritical conditions Lu^{3+} reacts with HIO_3 and KIO_4 to yield the isostructural $\text{Lu}(\text{IO}_3)_3$. The structures have been determined by single-crystal X-ray diffraction. Crystallographic data are (MoK α , $\lambda=0.71073$ Å): $\text{Yb}(\text{IO}_3)_3$, monoclinic, space group $P2_1/n$, $a = 8.6664(9)$ Å, $b = 5.9904(6)$ Å, $c = 14.8826(15)$ Å, $\beta = 96.931(2)^\circ$, $V = 766.99(13)$ Å³, $Z = 4$, $R(F) = 4.23\%$ for 114 parameters with 1880 reflections with $I > 2\sigma(I)$; $\text{Lu}(\text{IO}_3)_3$, monoclinic, space group $P2_1/n$, $a = 8.6410(9)$, $b = 5.9961(6)$, $c = 14.8782(16)$ Å, $\beta = 97.028(2)^\circ$, $V = 765.08(14)$ Å³, $Z = 4$, $R(F) = 2.65\%$ for 119 parameters with 1756 reflections with $I > 2\sigma(I)$; $\text{Yb}(\text{IO}_3)_3(\text{H}_2\text{O})$, monoclinic, space group $C2/c$, $a = 27.2476(15)$, $b = 5.6296(3)$, $c = 12.0157(7)$ Å, $\beta = 98.636(1)^\circ$, $V = 1822.2(2)$ Å³, $Z = 8$, $R(F) = 1.51\%$ for 128 parameters with 2250 reflections with $I > 2\sigma(I)$; $\text{Lu}(\text{IO}_3)_3(\text{H}_2\text{O})$, monoclinic, space group $C2/c$, $a = 27.258(4)$, $b = 5.6251(7)$, $c = 12.0006(16)$ Å, $\beta = 98.704(2)^\circ$, $V = 1818.8(4)$ Å³, $Z = 8$, $R(F) = 1.98\%$ for 128

parameters with 2242 reflections with $I > 2\sigma(I)$. The f elements in all of the compounds are found in seven-coordinate environments and bridged with monodentate, bidentate, or tridentate iodate anions. Both $\text{Lu}(\text{IO}_3)_3(\text{H}_2\text{O})$ and $\text{Yb}(\text{IO}_3)_3(\text{H}_2\text{O})$ display distinctively different vibrational profiles from their respective anhydrous analogs. Hence, the Raman profile can be used as a complementary diagnostic tool to discern the different structural motifs of the compounds.

INTRODUCTION

Lanthanide iodates have been studied for their nonlinear optical properties including second harmonic generation,¹ and have been shown to exhibit piezoelectric² and pyroelectric effects.^{3,4} In attempts to prepare acentric structures of lanthanide iodates, no less than six anhydrous structure types have been reported,¹ in addition to numerous hydrated structures ranging from hemihydrates to pentahydrates.^{1,5} The known structure type that incorporates the broadest range of trivalent rare earth elements is the type I $Ln(IO_3)_3$ structure, which has been reported for Ce–Lu (except Pm),^{1,6} Y¹, Am,⁷ and Cm.⁸ Structural data for many of the iodates have been limited by the inability to grow single crystals. Single-crystal X-ray diffraction has been used to determine the structures of several anhydrous^{6,7,8,9,10} and hydrated^{4,5,11,12,13} trivalent *f*-element iodates.

We have recently begun studying the iodates of the trivalent 5*f* elements.^{7,8,10} While the chemistry of the lanthanide iodates is fueled by the search for novel optoelectronic materials, the actinide iodates are of interest regarding their radiation stability^{7,8,14} and their low solubilities, where the latter can be utilized in chemical separations.^{15,16,17} We have shown that one can prepare the Type I $Ln(IO_3)_3$ structure type with Am⁷ and Cm,⁸ but the $Bi(IO_3)_3$ structure type¹⁸ is formed with the smaller Cf ion.¹⁰ With the earlier actinide elements, uranium through plutonium, structural data only exist for the iodates with the high-valent states of the actinides, e.g. $UO_2(IO_3)_2$,¹⁹ $NpO_2(IO_3)_2$,²⁰ and $PuO_2(IO_3)_2 \cdot H_2O$.²¹

To aid our systematic studies of the actinide iodates, it is desirable to draw comparisons with their lanthanide analogs and lanthanide elements are often used as models for the rarer and radioactive actinide elements. While working out schemes for

preparing single crystals of the smaller trivalent actinide iodates, we prepared a new structure type for the iodates that has not been previously reported. Herein we report the syntheses, structures, and Raman spectroscopy for a new lanthanide iodate structural family containing the lanthanide elements with the smallest radii, $Ln(\text{IO}_3)_3(\text{H}_2\text{O})$ ($Ln = \text{Yb}, \text{Lu}$). In addition, we have isolated single crystals of $\text{Yb}(\text{IO}_3)_3$ and $\text{Lu}(\text{IO}_3)_3$ that adopt the $\text{Bi}(\text{IO}_3)_3$ structure type,¹⁸ and have also characterized them using single-crystal X-ray diffraction and Raman spectroscopy. The information in this chapter has been published as a full paper in *Journal of Solid State Chemistry*.²²

EXPERIMENTAL

Syntheses. $\text{Lu}(\text{NO}_3)_3 \cdot x\text{H}_2\text{O}$ (99.9%, Alfa Aesar), $\text{Yb}(\text{NO}_3)_3 \cdot x\text{H}_2\text{O}$ (99.9%, Research Chemicals), Yb metal (99+%, Cerac), KIO_4 (99.8%, Alfa Aesar), HIO_3 (99.5%, Alfa Aesar), and H_5IO_6 (98%, Alfa Aesar) were used as received without further purification. Distilled and Millipore filtered water was used in all reactions. The reactions reported here produced the highest yield of the respective compounds.

$\text{Yb}(\text{IO}_3)_3$. The synthesis of $\text{Yb}(\text{IO}_3)_3$ involved loading Yb metal filings (3.92 mg, 22.7 μmol) and H_5IO_6 (19.5 mg, 85.6 μmol) into a quartz ampoule followed by the addition of water (0.10 mL). The ampoule was flame sealed and placed in a box furnace that had been preheated to 180 °C. After 70 h, the furnace was turned off and allowed to self-quench to 20 °C. The sole crystalline product, $\text{Yb}(\text{IO}_3)_3$, was isolated in the form of colorless irregularly shaped crystals located beneath a colorless mother liquor.

$\text{Lu}(\text{IO}_3)_3$. $\text{Lu}(\text{NO}_3)_3 \cdot x\text{H}_2\text{O}$ (77.0 mg, 0.213 mmol), KIO_4 (98.1 mg, 0.426 mmol), and HIO_3 (75.0 mg, 0.426 mmol) were loaded into a quartz ampoule (1.15 mL volume)

along with 150 μL of water. The ampoule was frozen and sealed under vacuum. After thawing, the ampoule was placed in a Leco Tem-Press 27-mL autoclave filled with water and counter pressured with 2500 psi of argon. The autoclave was heated to 425 $^{\circ}\text{C}$, where it was held for three days and then slow cooled to 25 $^{\circ}\text{C}$ at the rate of 1 $^{\circ}\text{C}/\text{h}$. The product consisted of colorless columnar needles of $\text{Lu}(\text{IO}_3)_3$.

$\text{Yb}(\text{IO}_3)_3(\text{H}_2\text{O})$ and $\text{Lu}(\text{IO}_3)_3(\text{H}_2\text{O})$. The synthesis of $\text{Yb}(\text{IO}_3)_3(\text{H}_2\text{O})$ involved mixing $\text{Yb}(\text{NO}_3)_3$ (126 μL , 0.1 M) and H_5IO_6 (8.63 mg, 37.9 μmol) in a 1 mL quartz reaction vessel. The reaction vessel was sealed, placed in a box furnace, and then heated to 180 $^{\circ}\text{C}$ where the reaction occurred under autogenously generated pressure. After 88 h, the furnace was cooled at 10 $^{\circ}\text{C}/\text{h}$ to 100 $^{\circ}\text{C}$, then turned off and allowed to self-quench to 20 $^{\circ}\text{C}$. The sole solid product was colorless single crystals of $\text{Yb}(\text{IO}_3)_3(\text{H}_2\text{O})$ submersed in a colorless mother liquor. The synthesis of $\text{Lu}(\text{IO}_3)_3(\text{H}_2\text{O})$ involved mixing $\text{Lu}(\text{NO}_3)_3$ (20 μL , 0.1 M) and H_5IO_6 (60 μL , 0.1 M) in a quartz reaction vessel. The reaction vessel was sealed and placed in a box furnace and then heated to 180 $^{\circ}\text{C}$ where the reaction occurred under autogenously generated pressure. After 67 h, the furnace was cooled at 20 $^{\circ}\text{C}/\text{h}$ to 100 $^{\circ}\text{C}$, then turned off and self-quenched to 20 $^{\circ}\text{C}$. The obtained product was colorless single crystals of $\text{Lu}(\text{IO}_3)_3(\text{H}_2\text{O})$ beneath a colorless mother liquor.

Crystallographic Studies. Crystals of $\text{Yb}(\text{IO}_3)_3$, $\text{Lu}(\text{IO}_3)_3$, $\text{Yb}(\text{IO}_3)_3(\text{H}_2\text{O})$, and $\text{Lu}(\text{IO}_3)_3(\text{H}_2\text{O})$ with dimensions of 0.136 mm \times 0.064 mm \times 0.042 mm, 0.064 mm \times 0.028 mm \times 0.027 mm, 0.456 mm \times 0.072 mm \times 0.012 mm, and 0.570 mm \times 0.080 mm \times 0.010 mm, respectively, were selected, mounted on quartz fibers with epoxy, and aligned on a Bruker SMART APEX CCD X-ray diffractometer with a digital camera. Intensity measurements were performed using graphite-monochromated

MoK α radiation from a sealed tube with a monocapillary collimator. The intensities and positions of reflections of a sphere were collected by a combination of three sets of exposure frames. Each set had a different ϕ angle for the crystal and each exposure covered a range of 0.3° in ω . A total of 1800 frames were collected with an exposure time per frame of 20 s for Yb(IO₃)₃(H₂O), Lu(IO₃)₃(H₂O), and Yb(IO₃)₃ and 30 s for Lu(IO₃)₃.

Determination of integrated intensities and global cell refinement were performed with the Bruker SAINT (v 6.02) software package using a narrow-frame integration algorithm. An analytical absorption correction was applied based on the indexed crystal faces followed by a semi-empirical absorption correction using SADABS.²³ The program suite SHELXTL (v 5.1) was used for space group determination (XPREP), direct methods structure solution (XS), and least-squares refinement (XL).²⁴ The final refinements included anisotropic displacement parameters for all atoms and a secondary extinction parameter. Some crystallographic details are listed in Table 5.1 and Table 5.2. The final positional parameters can be found in Table 5.3 to Table 5.6.

Raman Spectroscopy. Raman spectroscopic experiments were performed using an argon-ion laser (Coherent, model 306) and a double-meter spectrometer (Jobin-Yvon Ramanor model HG.2S). As a double-meter spectrometer, the Ramanor has a total of four slits (one entrance, one exit and two internal slits) that are manually controlled. Based on the manufacturer's calibration, the maximum resolution for the monochromator at 514.5 nm is 0.5 cm^{-1} . However, the resolution for the spectra reported here varies from sample to sample. In fact the signal intensity is a function of four factors: the applied laser power, the sample properties (how absorptive/reflective the sample is and the

intrinsic strength of the Raman modes), and the widths of the spectrometer's entrance and exit slits. Some tradeoff was attained between the resolving power and intensity of the Raman signal. In some cases, the excitation wavelength was also changed to optimize the signal. The 528.7 nm green laser line was the principal excitation source that provided optimal signal for most of the samples. Hence, the resolution of each spectrum reported in this manuscript is different from the maximum attainable value. The actual resolution of the Raman signal for the samples varied between 1 and 2 cm^{-1} . Most of the spectra were collected at dwell time of 0.5 s/pt, and the signal detection was acquired using a water-cooled photo-multiplier tube (Hamamatsu R636). The analog signal from the PMT was digitized using an ADC interfaced with the instrument and the data stored in a personal computer. The LabSpec (version 3.04) software controlled scanning and other instrumental functions. The samples were all crystalline, and the Raman data were performed on capillary tubes compacted with these crystalline materials. Hence, the sample orientation is random and a polarizer was not used on either the incident radiation or the collection of the Raman signal scattered from the sample. We are, thus, unable to address any polarization effect. The Raman collection lens and the monochromator entrance slit were positioned at 90° to the incident radiation. The reported spectra are uncorrected for any instrumental responses. However, the monochromator positions and wavenumber accuracies were calibrated daily using the sharp Hg line at 18312.7 cm^{-1} (546.1 nm) using a fluorescent lamp. Additional calibration was conducted using the tri-azaphospha-adamantane ligand; several sharp and strong Raman bands in the region of interest were used as standards.

Table 5.1. Crystallographic Data for Yb(IO₃)₃ and Lu(IO₃)₃.

Compound	Yb(IO ₃) ₃	Lu(IO ₃) ₃
Formula Mass	697.74	699.67
Color and habit	Colorless, prism	Colorless, needle
Crystal system	Monoclinic	Monoclinic
Space group	<i>P2₁/n</i> (No. 14)	<i>P2₁/n</i> (No. 14)
<i>a</i> (Å)	8.6664(9)	8.6410(9)
<i>b</i> (Å)	5.9904(6)	5.9961(6)
<i>c</i> (Å)	14.8826(15)	14.8782(16)
β (°)	96.931(2)	97.028(2)
<i>V</i> (Å ³)	766.99(13)	765.08(14)
<i>Z</i>	4	4
<i>T</i> (K)	173	193
λ (Å)	0.71073	0.71073
Maximum 2θ (deg.)	56.64	56.54
ρ_{calcd} (g cm ⁻³)	6.042	6.074
$\mu(\text{Mo } K\alpha)$ (cm ⁻¹)	242.94	250.34
$R(F)$ for $F_o^2 > 2\sigma(F_o^2)$ ^a	0.0423	0.0239
$R_w(F_o^2)$ ^b	0.1341	0.0541

$$^a R(F) = \frac{\sum ||F_o| - |F_c||}{\sum |F_o|}. \quad ^b R_w(F_o^2) = \left[\frac{\sum [w(F_o^2 - F_c^2)]^2}{\sum wF_o^4} \right]^{1/2}.$$

Table 5.2. Crystallographic Data for Yb(IO₃)₃(H₂O) and Lu(IO₃)₃(H₂O).

Compound	Yb(IO ₃) ₃ (H ₂ O)	Lu(IO ₃) ₃ (H ₂ O)
Formula Mass	715.76	717.69
Color and habit	Colorless, plate	Colorless, plate
Crystal System	Monoclinic	Monoclinic
Space group	<i>C2/c</i> (no. 15)	<i>C2/c</i> (no. 15)
<i>a</i> (Å)	27.2476(15)	27.258(4)
<i>b</i> (Å)	5.6296(3)	5.6251(7)
<i>c</i> (Å)	12.0157(7)	12.0006(16)
β (°)	98.636(1)	98.704(2)
<i>V</i> (Å ³)	1822.2(2)	1818.8(4)
<i>Z</i>	8	8
<i>T</i> (K)	173	173
λ (Å)	0.71073	0.71073
Maximum 2θ (deg.)	56.58	56.64
ρ _{calcd} (g cm ⁻³)	5.218	5.242
μ(Mo <i>Kα</i>) (cm ⁻¹)	204.66	210.76
<i>R</i> (<i>F</i>) for <i>F</i> _o ² > 2σ(<i>F</i> _o ²) ^a	0.0151	0.0198
<i>R</i> _w (<i>F</i> _o ²) ^b	0.0345	0.0523

$$^a R(F) = \sum \| |F_o| - |F_c| \| / \sum |F_o|. \quad ^b R_w(F_o^2) = \left[\sum \left[w(F_o^2 - F_c^2)^2 \right] / \sum wF_o^4 \right]^{1/2}.$$

Table 5.3. Atomic Coordinates and Equivalent Isotropic Displacement Parameters for Yb(IO₃)₃.

Atom	Site	<i>x</i>	<i>y</i>	<i>z</i>	$U_{\text{eq}} (\text{\AA}^2)^a$
Yb(1)	4 <i>e</i>	0.5419(1)	0.7197(1)	0.8948(1)	0.007(1)
I(1)	4 <i>e</i>	0.8320(1)	0.3500(2)	0.9795(1)	0.006(1)
I(2)	4 <i>e</i>	0.6175(1)	0.4060(2)	0.6985(1)	0.006(1)
I(3)	4 <i>e</i>	0.2809(1)	0.1926(2)	0.8558(1)	0.006(1)
O(1)	4 <i>e</i>	0.7698(15)	0.5290(20)	0.8831(9)	0.010(3)
O(2)	4 <i>e</i>	0.3627(16)	0.6350(20)	0.9861(9)	0.012(3)
O(3)	4 <i>e</i>	0.9108(15)	0.5630(20)	0.0615(9)	0.010(3)
O(4)	4 <i>e</i>	0.5852(15)	0.6840(20)	0.7434(8)	0.008(2)
O(5)	4 <i>e</i>	0.4588(17)	0.4160(30)	0.6090(10)	0.015(3)
O(6)	4 <i>e</i>	0.7770(16)	0.4930(20)	0.6363(8)	0.011(3)
O(7)	4 <i>e</i>	0.3693(16)	0.9470(20)	0.8110(9)	0.012(3)
O(8)	4 <i>e</i>	0.3558(15)	0.1350(20)	0.9714(9)	0.012(3)
O(9)	4 <i>e</i>	0.4223(15)	0.4000(20)	0.8289(10)	0.012(3)

^a U_{eq} is defined as one-third of the trace of the orthogonalized \mathbf{U}_{ij} tensor.

Table 5.4. Atomic Coordinates and Equivalent Isotropic Displacement Parameters for Lu(IO₃)₃.

Atom	Site	<i>x</i>	<i>y</i>	<i>z</i>	$U_{\text{eq}} (\text{\AA}^2)^a$
Lu(1)	4 <i>e</i>	0.5418(1)	0.7186(1)	0.8940(1)	0.008(1)
I(1)	4 <i>e</i>	0.8316(1)	0.3495(1)	0.9797(1)	0.007(1)
I(2)	4 <i>e</i>	0.6176(1)	0.4061(1)	0.6983(1)	0.008(1)
I(3)	4 <i>e</i>	0.2814(1)	0.1930(1)	0.8566(1)	0.008(1)
O(1)	4 <i>e</i>	0.7694(5)	0.5287(7)	0.8830(3)	0.012(1)
O(2)	4 <i>e</i>	0.3630(5)	0.6384(8)	0.9856(3)	0.016(1)
O(3)	4 <i>e</i>	0.9098(5)	0.5600(7)	0.0613(3)	0.011(1)
O(4)	4 <i>e</i>	0.5853(5)	0.6821(7)	0.7430(3)	0.010(1)
O(5)	4 <i>e</i>	0.4557(5)	0.4157(8)	0.6091(3)	0.016(1)
O(6)	4 <i>e</i>	0.7774(5)	0.4912(7)	0.6359(3)	0.011(1)
O(7)	4 <i>e</i>	0.3727(5)	0.9492(7)	0.8126(3)	0.013(1)
O(8)	4 <i>e</i>	0.3516(5)	0.1339(8)	0.9729(3)	0.014(1)
O(9)	4 <i>e</i>	0.4215(5)	0.4021(7)	0.8297(3)	0.013(1)

^a U_{eq} is defined as one-third of the trace of the orthogonalized \mathbf{U}_{ij} tensor.

Table 5.5. Atomic Coordinates and Equivalent Isotropic Displacement Parameters for Yb(IO₃)₃(H₂O).

Atom	Site	<i>x</i>	<i>y</i>	<i>z</i>	$U_{\text{eq}} (\text{\AA}^2)^a$
Yb(1)	8 <i>f</i>	0.0835(1)	0.2058(1)	0.4311(1)	0.008(1)
I(1)	8 <i>f</i>	0.2145(1)	0.1905(1)	0.3479(1)	0.008(1)
I(2)	8 <i>f</i>	0.1669(1)	0.7413(1)	0.5587(1)	0.007(1)
I(3)	8 <i>f</i>	0.0933(1)	0.7010(1)	0.2367(1)	0.008(1)
O(1)	8 <i>f</i>	0.1561(1)	0.0646(4)	0.3798(2)	0.013(1)
O(2)	8 <i>f</i>	0.2183(1)	0.0181(5)	0.2227(2)	0.014(1)
O(3)	8 <i>f</i>	0.2560(1)	0.0195(5)	0.4490(2)	0.017(1)
O(4)	8 <i>f</i>	0.1362(1)	0.5342(5)	0.4539(2)	0.014(1)
O(5)	8 <i>f</i>	0.1147(1)	0.9414(5)	0.5654(2)	0.013(1)
O(6)	8 <i>f</i>	0.1609(1)	0.5715(4)	0.6835(2)	0.012(1)
O(7)	8 <i>f</i>	0.0600(1)	0.6761(5)	0.0950(2)	0.013(1)
O(8)	8 <i>f</i>	0.0571(1)	0.9265(4)	0.2951(2)	0.015(1)
O(9)	8 <i>f</i>	0.0637(1)	0.4414(2)	0.2835(2)	0.014(1)
O(10)	8 <i>f</i>	-0.0028(1)	0.1986(5)	0.4043(2)	0.015(1)

^a U_{eq} is defined as one-third of the trace of the orthogonalized \mathbf{U}_{ij} tensor.

Table 5.6. Atomic Coordinates and Equivalent Isotropic Displacement Parameters for Lu(IO₃)₃(H₂O).

Atom	Site	<i>x</i>	<i>y</i>	<i>z</i>	$U_{\text{eq}} (\text{\AA}^2)^a$
Lu(1)	8 <i>f</i>	0.0835(1)	0.2056(1)	0.4302(1)	0.007(1)
I(1)	8 <i>f</i>	0.2143(1)	0.1905(1)	0.3475(1)	0.008(1)
I(2)	8 <i>f</i>	0.1667(1)	0.7399(1)	0.5580(1)	0.007(1)
I(3)	8 <i>f</i>	0.0933(1)	0.7011(1)	0.2362(1)	0.008(1)
O(1)	8 <i>f</i>	0.1558(1)	0.0635(5)	0.3788(2)	0.012(1)
O(2)	8 <i>f</i>	0.2183(1)	0.0188(6)	0.2216(2)	0.013(1)
O(3)	8 <i>f</i>	0.2557(1)	0.0179(6)	0.4484(2)	0.017(1)
O(4)	8 <i>f</i>	0.1361(1)	0.5302(6)	0.4536(2)	0.013(1)
O(5)	8 <i>f</i>	0.1143(1)	0.9387(6)	0.5637(2)	0.013(1)
O(6)	8 <i>f</i>	0.1609(1)	0.5705(5)	0.6829(2)	0.012(1)
O(7)	8 <i>f</i>	0.0601(1)	0.6775(5)	0.0939(2)	0.013(1)
O(8)	8 <i>f</i>	0.0572(1)	0.9273(6)	0.2953(2)	0.014(1)
O(9)	8 <i>f</i>	0.0634(1)	0.4411(5)	0.2828(2)	0.013(1)
O(10)	8 <i>f</i>	-0.0024(1)	0.1976(6)	0.4044(3)	0.016(1)

^a U_{eq} is defined as one-third of the trace of the orthogonalized \mathbf{U}_{ij} tensor.

RESULTS AND DISCUSSION

Syntheses. The reactions of 0.1 M ytterbium or lutetium nitrate solutions with periodic acid at 180 °C leads to the formation of $\text{Yb}(\text{IO}_3)_3(\text{H}_2\text{O})$ and $\text{Lu}(\text{IO}_3)_3(\text{H}_2\text{O})$ single crystals, respectively, in the form of colorless tablets. This reaction involves the reduction of the periodate to form iodate and the simultaneous oxidation of H_2O to oxygen and H^+ . This reduction of periodate to iodate has been previously noted under similar synthetic conditions.^{7,19}

Type I $\text{Ln}(\text{IO}_3)_3$ iodates have been reported for Ce–Lu,¹ Y,¹ Am,⁷ and Cm.⁸ The reaction of the larger trivalent *f*-element ions with H_5IO_6 under mild hydrothermal conditions produces the Type I iodate phase.^{7,8} For the smallest trivalent lanthanide ions, Yb^{3+} and Lu^{3+} , the hydrothermal reaction reported here produces $\text{Ln}(\text{IO}_3)_3(\text{H}_2\text{O})$ ($\text{Ln} = \text{Yb, Lu}$). The formation of $\text{Yb}(\text{IO}_3)_3 \cdot 2\text{H}_2\text{O}$ and $\text{Lu}(\text{IO}_3)_3 \cdot 2\text{H}_2\text{O}$ have been previously reported^{11,12} by reacting the appropriate amorphous lanthanide periodate with excess periodic acid in aqueous solution at 160 °C. We have been successful in preparing $\text{Yb}(\text{IO}_3)_3$, containing the $\text{Bi}(\text{IO}_3)_3$ structure type,¹⁸ by reacting Yb metal with H_5IO_6 under hydrothermal conditions. Under these conditions, H_5IO_6 presumably oxidizes both Yb and H_2O . Only by using supercritical conditions (425 °C) have we been able to grow crystals of the anhydrous lutetium iodate, $\text{Lu}(\text{IO}_3)_3$.

Crystal Structures of $\text{Yb}(\text{IO}_3)_3$ and $\text{Lu}(\text{IO}_3)_3$. The anhydrous iodates $\text{Yb}(\text{IO}_3)_3$ and $\text{Lu}(\text{IO}_3)_3$ adopt the $\text{Bi}(\text{IO}_3)_3$ structure type.¹⁸ Surprisingly, the larger Nd^{3+} cation can also be induced to form crystals in this class.⁹ We have also recently shown that $\text{Cf}(\text{IO}_3)_3$ conforms to this crystal system as well.¹⁰ Since $\text{Yb}(\text{IO}_3)_3$ and $\text{Lu}(\text{IO}_3)_3$ are isostructural, below we only discuss the structure of $\text{Lu}(\text{IO}_3)_3$; the structural features found in $\text{Yb}(\text{IO}_3)_3$

are the same as that for $\text{Lu}(\text{IO}_3)_3$, with only slight variations in bond distances and angles.

The most distinctive feature of this structure is the environment of the M^{3+} cations. These cations are situated in monocapped trigonal prismatic environments with Lu–O bond distances ranging from 2.234(4) to 2.341(4) Å. In addition to these seven contacts, there are two much longer Lu···O interactions of 2.847(5) and 3.279(5) Å that cap two additional faces of the trigonal prism. The local environment of the Lu^{3+} cation is shown in Fig. 5.1, and the overall structure of $\text{Lu}(\text{IO}_3)_3$ is two dimensional as shown in Fig. 5.2. However, there is an unusual one-dimensional substructure that consists of chains of LuO_7 polyhedra and iodate anions. The LuO_7 units edge share to yield a Lu...Lu distance of 4.230(5) Å. There are three crystallographically unique iodine atoms in $\text{Lu}(\text{IO}_3)_3$, where the I–O bond distances are normal and range from 1.797(4) to 1.828(4) Å. The O–I–O bond angles show significant variations, and range from 90.4(2) to 101.1(2)°. A detailed list of bond lengths and angles for $\text{Yb}(\text{IO}_3)_3$ and $\text{Lu}(\text{IO}_3)_3$ can be found in Table 5.7 and Table 5.8.

Crystal Structures of $\text{Yb}(\text{IO}_3)_3(\text{H}_2\text{O})$ and $\text{Lu}(\text{IO}_3)_3(\text{H}_2\text{O})$. $\text{Yb}(\text{IO}_3)_3(\text{H}_2\text{O})$ and $\text{Lu}(\text{IO}_3)_3(\text{H}_2\text{O})$ are isostructural, and for brevity both structures will be discussed simultaneously. The Ln(1) positions in the structures of both $\text{Yb}(\text{IO}_3)_3(\text{H}_2\text{O})$ and $\text{Lu}(\text{IO}_3)_3(\text{H}_2\text{O})$ are coordinated by six iodate anions and one water molecule giving rise to a LnO_7 coordination polyhedron as shown in Fig. 5.3. Crystallographically, there are three unique iodine atoms, I(1), I(2), and I(3), in the structure. Each of these iodine atoms is coordinated by three oxygen atoms, in a trigonal pyramidal arrangement, and each possesses a lone pair of electrons. In the structures of $\text{Yb}(\text{IO}_3)_3(\text{H}_2\text{O})$ and $\text{Lu}(\text{IO}_3)_3(\text{H}_2\text{O})$, iodate anions are found to be monodentate, bidentate, and tridentate. Although it is not

uncommon for at least two types of iodate coordination to be present in an *f*-element iodate structure,^{25,26} the presence of three distinct coordination modes is not as prevalent.¹² The iodate anions in Yb(IO₃)₃(H₂O) and Lu(IO₃)₃(H₂O) each contain three different I–O bond distances, and therefore have site symmetries of C₁. This lowering of the expected C_{3v} site symmetry for an isolated iodate anion is very commonly observed in the structures of solid-state iodates.

The iodate ion formed by I(1) is a monodentate ligand that coordinates Ln(1) through O(1) and contains two terminal oxygen atoms, O(2) and O(3). I(2) is found in a bidentate iodate anion that coordinates with O(4) and O(5) and contains one terminal oxygen atom, O(6). The tridentate iodate anion, formed with I(3), coordinates Ln(1) with all three of its oxygen atoms, O(7), O(8), and O(9). Therefore, each Ln(1) position is coordinated with one I(1)O₃[−], two I(2)O₃[−], and three I(3)O₃[−]. The seventh and last oxygen atom bonded to Ln(1) is O(10), the oxygen from the coordinated water molecule. Three LnO₇ polyhedra are linked together by each triply bridging I(3)O₃[−] anion, resulting in two-dimensional layers as shown in Fig. 5.4. The bidentate I(2)O₃[−] anions additionally bridge two interlayer LnO₇ polyhedra leading to more rigid layers, while the monodentate I(1)O₃[−] anions are all coordinated on one side of each layer. The Ln-coordinated water molecules terminate the opposite side of each layer. These layers stack upon one another and are connected only by noncovalent interactions. The layers alternate in direction so that iodate-terminated and water-terminated sides of the layers interact with one another. This stacking pattern is illustrated in Fig. 5.5.

The Ln–O bond lengths for the LnO₇ polyhedra range from 2.216(2) to 2.332(2) Å and 2.212(3) to 2.315(3) Å for Yb(IO₃)₃(H₂O) and Lu(IO₃)₃(H₂O),

respectively. These distances are within the range found for other iodate structures of these elements.^{11,12} The iodate anions have I–O bond lengths ranging from 1.799(2) to 1.838(3) Å, well within the range found for other lanthanide and actinide iodates. In addition, each iodine atom forms two or three longer bonds to oxygen atoms with distances from 2.550(3) to 2.958(3) Å. A detailed list of bond lengths and angles for Yb(IO₃)₃(H₂O) and Lu(IO₃)₃(H₂O) can be found in Table 5.9 and Table 5.10.

The bond valence sums for all of the atomic positions have been calculated.²⁷ The values for Yb(3.12) and Lu(3.08) are consistent with Ln(III), while the iodine atoms have average values of 4.96 and 4.94 for Yb(IO₃)₃(H₂O) and Lu(IO₃)₃(H₂O), respectively, and support the assignment of these positions as I(V). The bond valence sums for the oxygen positions of the iodate groups range from 1.68 to 2.26 for Yb(IO₃)₃(H₂O) and 1.67–2.22 for Lu(IO₃)₃(H₂O). The O(10) position, assigned as the coordinated water molecule in both structures, has a bond valence of 0.40 for Yb(IO₃)₃(H₂O) and 0.39 for Lu(IO₃)₃(H₂O) and is consistent with their assignments.

Raman Spectra of Yb(IO₃)₃ and Lu(IO₃)₃. In Fig. 5.6, the Raman spectra of Lu(IO₃)₃ and Yb(IO₃)₃ are shown in the I–O stretching frequency region. Consistent with the size of the metal ions and structural similarities of the two compounds, the Raman profiles are quite similar in both energy position and relative intensity of the peaks. In the I–O stretching frequency region, the Raman spectrum of Lu(IO₃)₃ exhibits three regions with a strong doublet at 699 and 723 cm⁻¹, a broad doublet at 767 and 782 cm⁻¹, and a strong band at 842 cm⁻¹ present. The Raman bands of Yb(IO₃)₃ exhibit a similar profile and there is only a slight shift in energies. Hence, the corresponding bands are observed

at 703 and 725 cm^{-1} with a shoulder at 747 cm^{-1} , a doublet at 768 and 786 cm^{-1} , and at higher energies, there occur a sharp band at 840 cm^{-1} and a weak broad band at 812 cm^{-1} .

Previous interpretations²⁸⁻³⁴ of Raman spectra corresponding to the I–O vibrations in iodate salts of trivalent lanthanide and actinide systems are based on the assumption that little inter-ionic coupling exists between the crystallographically unique IO_3^- anions.³²⁻³⁶ Hence, each of the spectral regions described above can be associated with the unique iodate anions. Within each unique iodate ion, the presence of intra-ionic vibrational coupling is dependent on several factors. In previous studies of iodate salts of mono- and divalent cations, systems where one of the I–O bond distances is significantly shorter than the other two distances were found to display uncoupled symmetric stretching.³²⁻³⁶ In such instances, the asymmetric component appears at a lower energy when compared to the symmetric stretching frequency. In addition, an intensity comparison can help to differentiate between these two modes as the symmetric component usually displays a more intense band than the asymmetric component.

Each of the three spectral regions shows the presence of weak shoulders and/or components both on the high- and low-energy sides of the most intense bands. Based on this observation lack of intra-ionic coupling can not be excluded.

The I–O bond distances at the three unique sites are essentially indistinguishable having average values of 1.822, 1.818, and 1.812 Å at I(1), I(2), and I(3) sites, respectively. However, the average O–I–O angle at the I(1) site is smaller as compared with the other two sites (94.4, 97.2, and 97.9 at the I(1), I(2), and I(3) sites, respectively). Following the previous suggestions,³¹⁻³⁵ it can be argued that the smaller O–I–O angle at the I(1) site induces a higher frequency shift to the I–O symmetric stretching mode at this

site. Hence, the band at 842 cm^{-1} (along with the shoulder at 813 cm^{-1}) is assigned to this site.

The cation interaction with the oxygen atoms at the different iodate sites is used to glean the influence of the lanthanide ion on the frequency of the I–O vibrational profile. The Lu–O distance at the I(1) site is, on average, shorter by 0.01 to 0.03 Å, as compared to the I(2) and I(3) sites, respectively. Similar differences have been noted previously in the structures of Cm, Am, and Cf iodates.^{7,8,10} Thus, it is reasonable to assume that greater electron density is withdrawn from the iodate unit at this site. A consequence is the strengthening of the I–O stretching frequency, which is consistent with the assignment of the highest I–O vibrational band (at 842 cm^{-1}) to the I(1) site.

In Fig. 5.7, the Raman profiles of the two compounds are shown in the low-energy region covering the bending and lattice vibrational modes. In the I–O stretching region, the two compounds show similar profiles, especially at room temperature, where all the bands match each other. As shown in Fig. 5.7c for the $\text{Yb}(\text{IO}_3)_3$ compound, a highly resolved spectrum is obtained upon cooling the material to liquid N_2 temperature. As a result, in the $80\text{--}500\text{ cm}^{-1}$ region, a total of 23 well resolved bands are now observed. The bending mode region (covering $300\text{--}500\text{ cm}^{-1}$) provides a total of 11 well-resolved bands at liquid N_2 temperature compared with the 18 bending modes expected from group theory. The bands below 300 cm^{-1} are assigned to lattice modes. The major bands in $\text{Lu}(\text{IO}_3)_3$ are observed in similar energy positions, albeit unresolved at room temperature, confirming the structural similarity of the two compounds.

Raman Spectra of $\text{Yb}(\text{IO}_3)_3(\text{H}_2\text{O})$ and $\text{Lu}(\text{IO}_3)_3(\text{H}_2\text{O})$. As described earlier, the structural features of these two compounds are dominated by the presence of three

crystallographically unique iodate ions. At the I(1) site, two of the oxygen atoms are terminal with only one oxygen coordinated to the metal center. Close inspection of the different interactions at this site indicates that the terminal oxygens are shorter (by $\sim 0.03 \text{ \AA}$) than the I–O distances involving the coordinated oxygen atoms. Similarly, at the I(2) site where one of the oxygen atoms (O(6)) is terminal, the I–O distance is shorter by 0.025 \AA when compared with that of the two coordinated oxygen atoms. It is only at the I(3) site, where all three oxygens are coordinated, that a more uniform I–O distance is observed. The variations in the I–O interactions are expected to limit intra-ionic coupling of the $\nu_{\text{I-O}}$ vibrations at least for the I(1) and I(2) sites.

It was stated earlier that the hydrated analogs of Lu- and Yb-iodates have significantly different structural features as compared with the anhydrous compounds. The consequences of these structural differences on the Raman profile are demonstrated in Fig. 5.8. Both $\text{Lu}(\text{IO}_3)_3(\text{H}_2\text{O})$ and $\text{Yb}(\text{IO}_3)_3(\text{H}_2\text{O})$ display distinctively different vibrational profiles from their respective anhydrous analogs. Hence, the Raman profile can be used as a complementary diagnostic tool, along with X-ray diffraction, to discern the different structural motifs of the compounds.

In the I–O stretching region of $\text{Lu}(\text{IO}_3)_3(\text{H}_2\text{O})$ (Fig. 5.8a) the most intense band is observed at 742 cm^{-1} . There is a shift to higher frequency by $\sim 20 \text{ cm}^{-1}$ when compared with the anhydrous analog (723 cm^{-1}). In contrast, the highest Raman band in the spectrum appears at a lower energy (834 cm^{-1}), as compared to the value for the anhydrous $\text{Lu}(\text{IO}_3)_3$ shown in Fig. 5.6a. As is the case with the anhydrous system, the monohydrate analogs of both Yb and Lu display similar Raman profiles presumably due

to the similarities in size of the metal ions and identical structural features of the two compounds.

The regions covering the bending and lattice modes of these compounds are shown in Fig. 5.9. The spectral profiles for these regions are quite different from those of the anhydrous compounds, although no significant changes, either in energy positions or relative intensities are evident between the spectra of the two hydrated lanthanide iodates. The bending mode region ($300\text{--}500\text{ cm}^{-1}$) consists of significantly fewer Raman bands (about seven bands) as compared with the profiles for the anhydrous compounds, whereas only 8 bands have been observed in the lattice mode region ($80\text{--}300\text{ cm}^{-1}$).

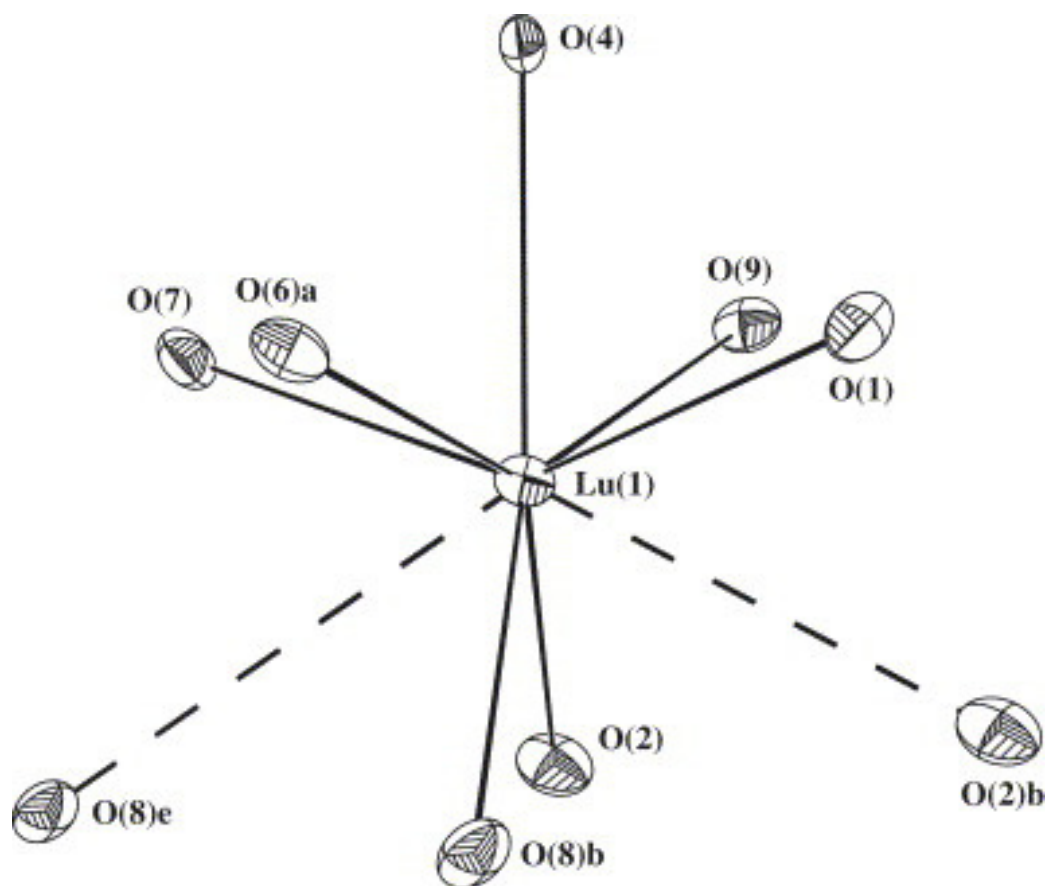


Figure 5.1. The coordination environment of the Lu site in $\text{Lu}(\text{IO}_3)_3$ (50% probability ellipsoids are shown). Operations used to generate symmetry equivalent atoms: (a) $1.5-x$, $0.5+y$, $1.5-z$; (b) $1-x$, $1-y$, $2-z$; (e) x , $1+y$, z .

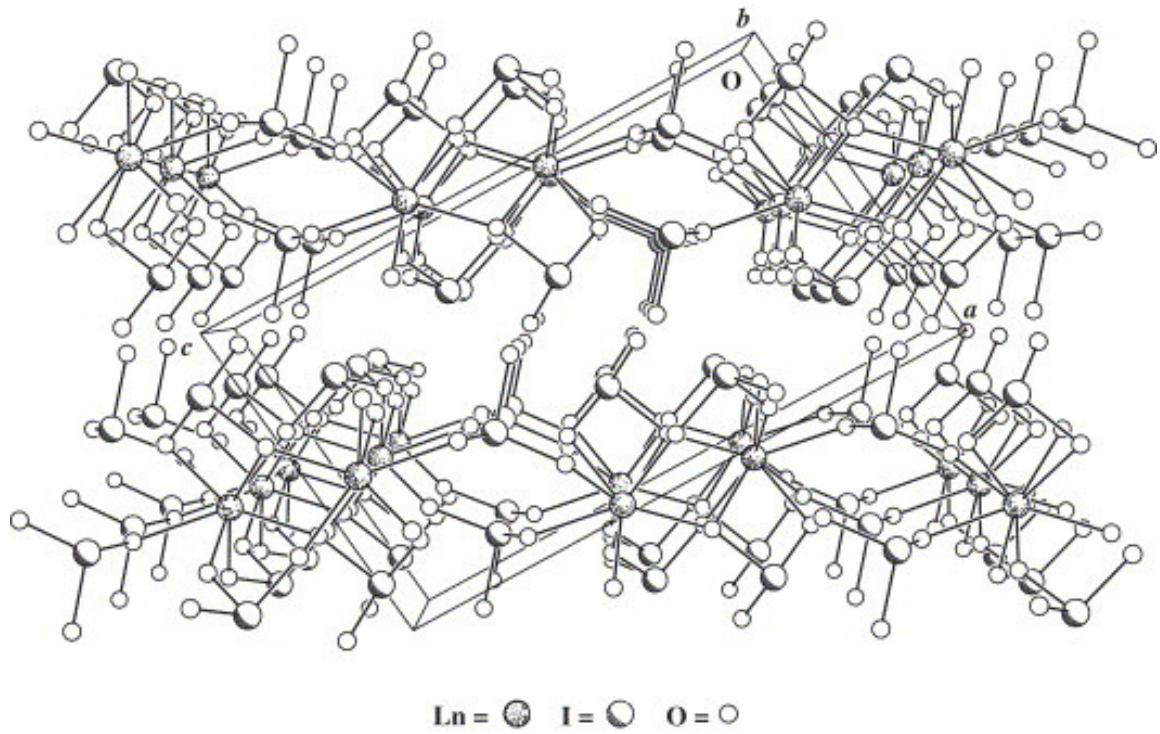


Figure 5.2 A packing diagram viewed along the b -axis showing the stacking of the two-dimensional layers in $Ln(IO_3)_3$ ($Ln = Yb, Lu$).

Table 5.7. Selected Bond Distances (Å) and Angles (°) for Yb(IO₃)₃.

Distances (Å)			
Yb(1)–O(1)	2.306(13)	I(1)–O(2)b	1.823(13)
Yb(1)–O(2)	2.241(13)	I(1)–O(3)c	1.841(13)
Yb(1)–O(4)	2.338(12)	I(2)–O(4)	1.830(13)
Yb(1)–O(6)a	2.351(14)	I(2)–O(5)	1.797(14)
Yb(1)–O(7)	2.279(14)	I(2)–O(6)	1.830(13)
Yb(1)–O(8)b	2.254(13)	I(3)–O(7)d	1.823(14)
Yb(1)–O(9)	2.341(4)	I(3)–O(8)	1.798(13)
I(1)–O(1)	1.819(14)	I(3)–O(9)	1.822(13)
Angles (°)			
O(1)–I(1)–O(2)b	89.8(6)	O(4)–I(2)–O(6)	94.8(6)
O(1)–I(1)–O(3)c	99.5(6)	O(7)d–I(3)–O(8)	94.4(6)
O(2)b–I(1)–O(3)c	93.6(6)	O(7)d–I(3)–O(9)	98.5(6)
O(4)–I(2)–O(5)	96.0(6)	O(8)–I(3)–O(9)	99.6(6)
O(5)–I(2)–O(6)	99.9(6)		

Table 5.8. Selected Bond Distances (Å) and Angles (°) for Lu(IO₃)₃.

Distances (Å)			
Lu(1)–O(1)	2.295(4)	I(1)–O(2)b	1.820(4)
Lu(1)–O(2)	2.234(4)	I(1)–O(3)c	1.823(4)
Lu(1)–O(4)	2.333(4)	I(2)–O(4)	1.818(4)
Lu(1)–O(6)a	2.341(4)	I(2)–O(5)	1.808(4)
Lu(1)–O(7)	2.255(4)	I(2)–O(6)	1.828(4)
Lu(1)–O(8)b	2.260(5)	I(3)–O(7)d	1.820(4)
Lu(1)–O(9)	2.314(4)	I(3)–O(8)	1.797(4)
I(1)–O(1)	1.822(4)	I(3)–O(9)	1.821(4)
Angles (°)			
O(1)–I(1)–O(2)b	90.4(2)	O(4)–I(2)–O(6)	95.2(2)
O(1)–I(1)–O(3)c	99.6(2)	O(7)d–I(3)–O(8)	94.5(2)
O(2)b–I(1)–O(3)c	93.6(2)	O(7)d–I(3)–O(9)	98.3(2)
O(4)–I(2)–O(5)	95.8(2)	O(8)–I(3)–O(9)	101.1(2)
O(5)–I(2)–O(6)	100.6(2)		

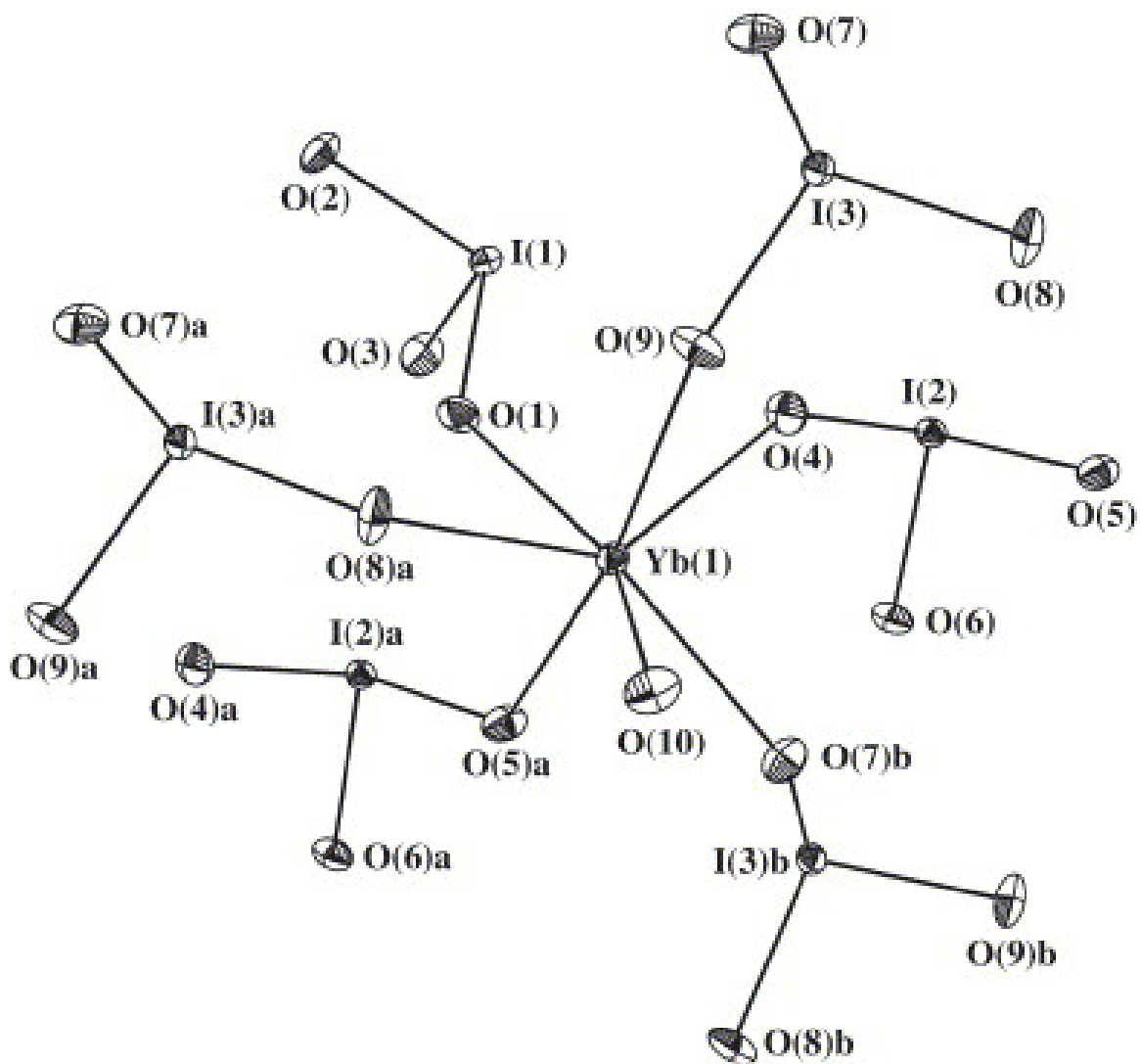


Figure 5.3. The coordination environment of the Yb site in $\text{Yb}(\text{IO}_3)_3(\text{H}_2\text{O})$ (50% probability ellipsoids are shown). Operations used to generate symmetry equivalent atoms: (a) $x, y-1, z$; (b) $x, 1-y, 1/2+z$

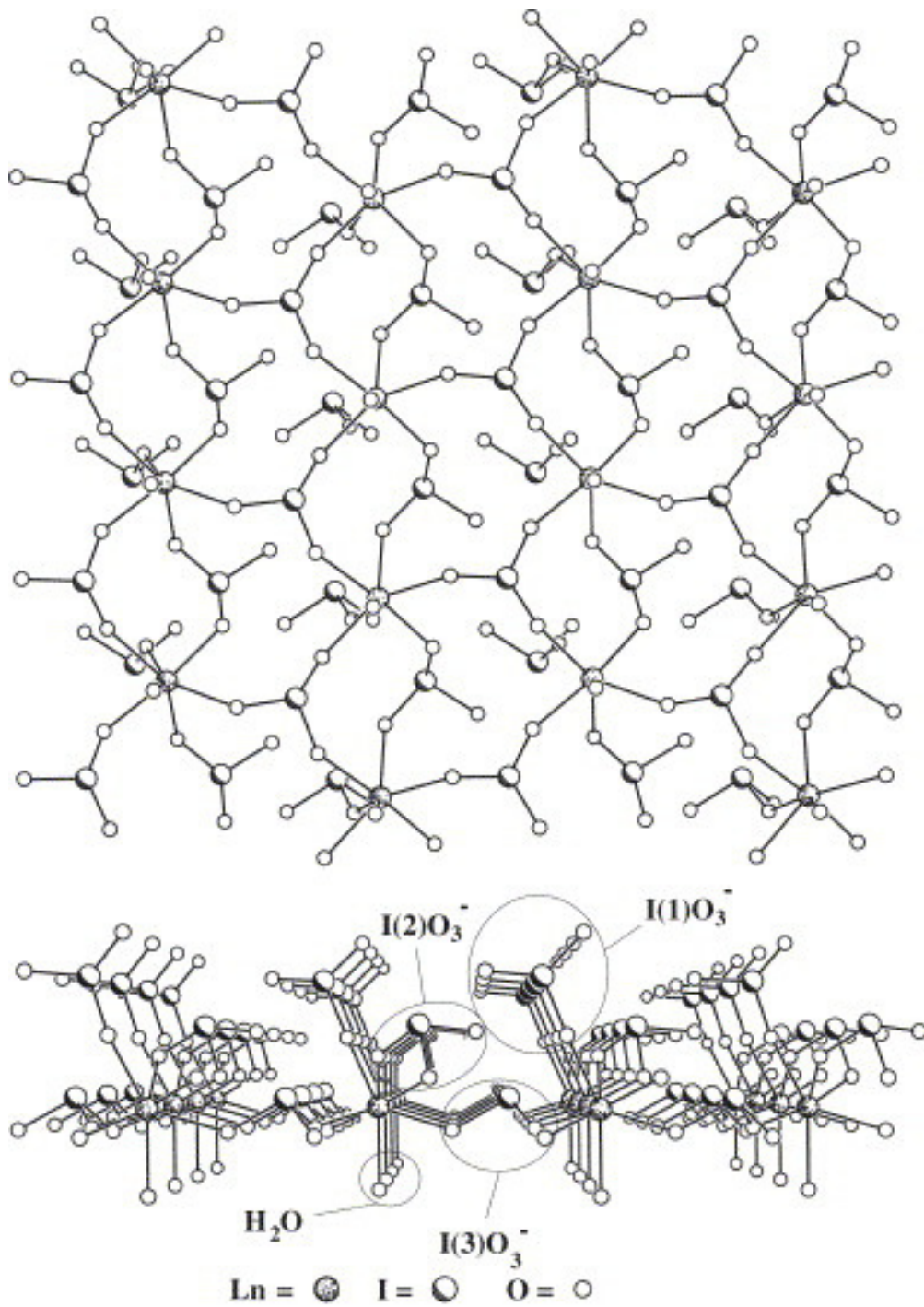


Figure 5.4. A ball and stick plot of a two-dimensional layer in $Ln(IO_3)_3(H_2O)$ ($Ln = Yb, Lu$) viewed (a) perpendicular to the layer or (b) parallel to the layer.

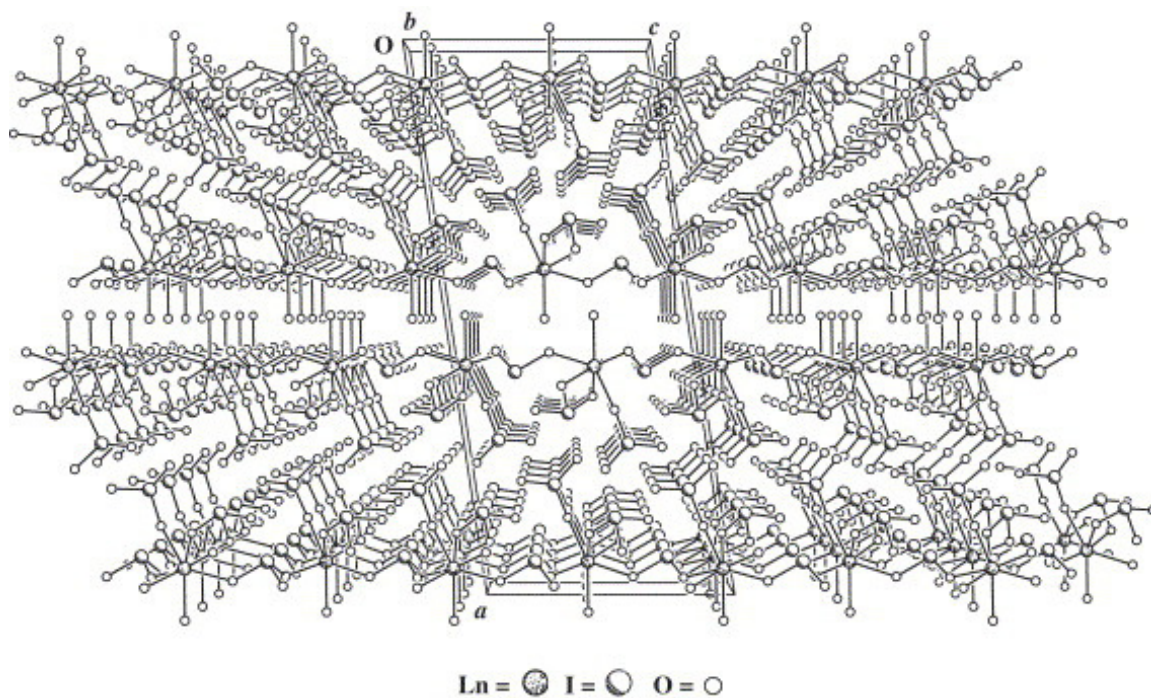


Figure 5.5. A packing diagram showing the stacking of the two-dimensional layers in $\text{Ln}(\text{IO}_3)_3(\text{H}_2\text{O})$ ($\text{Ln} = \text{Yb}, \text{Lu}$).

Table 5.9. Selected Bond Distances (Å) and Angles (°) for Yb(IO₃)₃(H₂O).

Distances (Å)			
Yb(1)–O(1)	2.301(2)	I(1)–O(2)	1.807(2)
Yb(1)–O(4)	2.332(2)	I(1)–O(3)	1.808(3)
Yb(1)–O(5)a	2.265(2)	I(2)–O(4)	1.824(2)
Yb(1)–O(7)b	2.259(2)	I(2)–O(5)	1.824(2)
Yb(1)–O(8)a	2.303(2)	I(2)–O(6)	1.806(2)
Yb(1)–O(9)	2.216(2)	I(3)–O(7)	1.811(2)
Yb(1)–O(10)	2.325(3)	I(3)–O(8)	1.812(2)
I(1)–O(1)	1.833(2)	I(3)–O(9)	1.799(2)
Angles (°)			
O(1)–I(1)–O(2)	97.32(12)	O(5)–I(2)–O(6)	97.04(11)
O(1)–I(1)–O(3)	97.37(12)	O(7)–I(3)–O(8)	101.17(12)
O(2)–I(1)–O(3)	99.51(12)	O(7)–I(3)–O(9)	92.63(11)
O(4)–I(2)–O(5)	98.38(12)	O(8)–I(3)–O(9)	98.78(12)
O(4)–I(2)–O(6)	98.37(11)		

Table 5.10. Selected Bond Distances (Å) and Angles (°) for Lu(IO₃)₃(H₂O).

Distances (Å)			
Lu(1)–O(1)	2.295(3)	I(1)–O(2)	1.810(3)
Lu(1)–O(4)	2.312(3)	I(1)–O(3)	1.807(3)
Lu(1)–O(5)a	2.262(3)	I(2)–O(4)	1.828(3)
Lu(1)–O(7)b	2.254(3)	I(2)–O(5)	1.823(3)
Lu(1)–O(8)a	2.288(3)	I(2)–O(6)	1.803(3)
Lu(1)–O(9)	2.212(3)	I(3)–O(7)	1.812(3)
Lu(1)–O(10)	2.315(3)	I(3)–O(8)	1.817(3)
I(1)–O(1)	1.838(3)	I(3)–O(9)	1.803(3)

Angles (°)			
O(1)–I(1)–O(2)	97.26(13)	O(5)–I(2)–O(6)	97.21(13)
O(1)–I(1)–O(3)	97.31(14)	O(7)–I(3)–O(8)	101.37(14)
O(2)–I(1)–O(3)	99.39(14)	O(7)–I(3)–O(9)	92.77(13)
O(4)–I(2)–O(5)	98.22(14)	O(8)–I(3)–O(9)	98.65(14)
O(4)–I(2)–O(6)	98.08(13)		

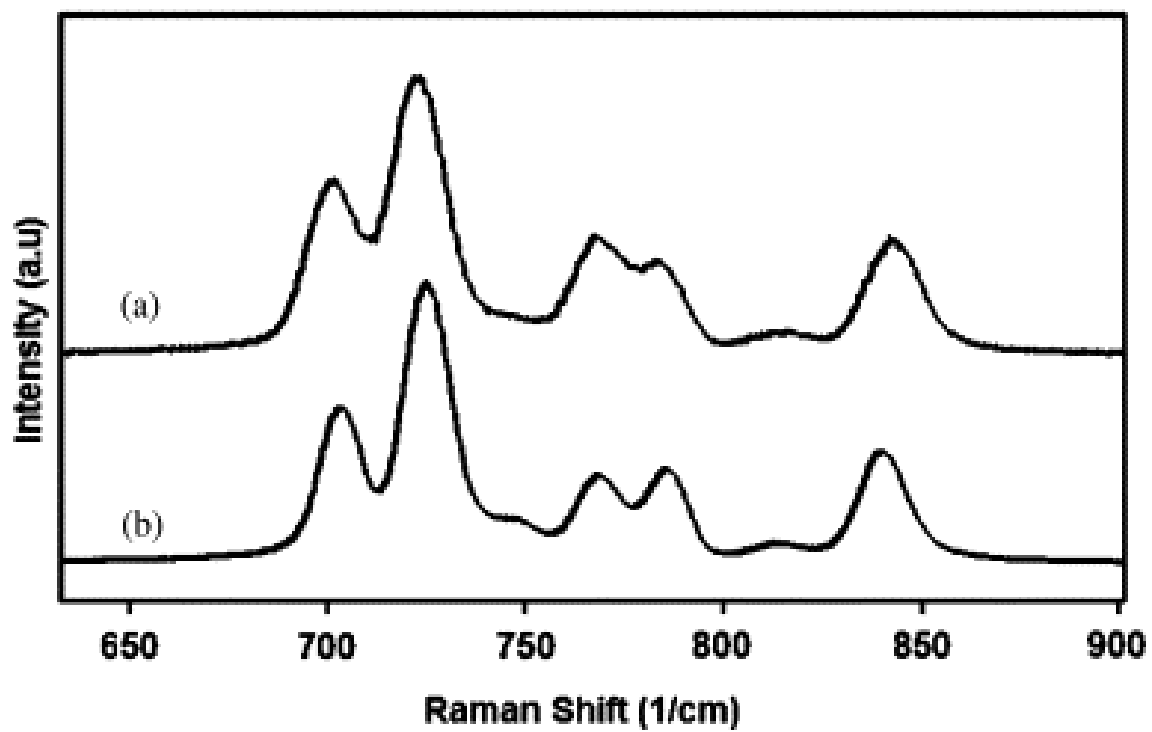


Figure 5.6. Raman spectrum of (a) $\text{Lu}(\text{IO}_3)_3$, and (b) $\text{Yb}(\text{IO}_3)_3$ at room temperature in the I–O stretching frequency region.

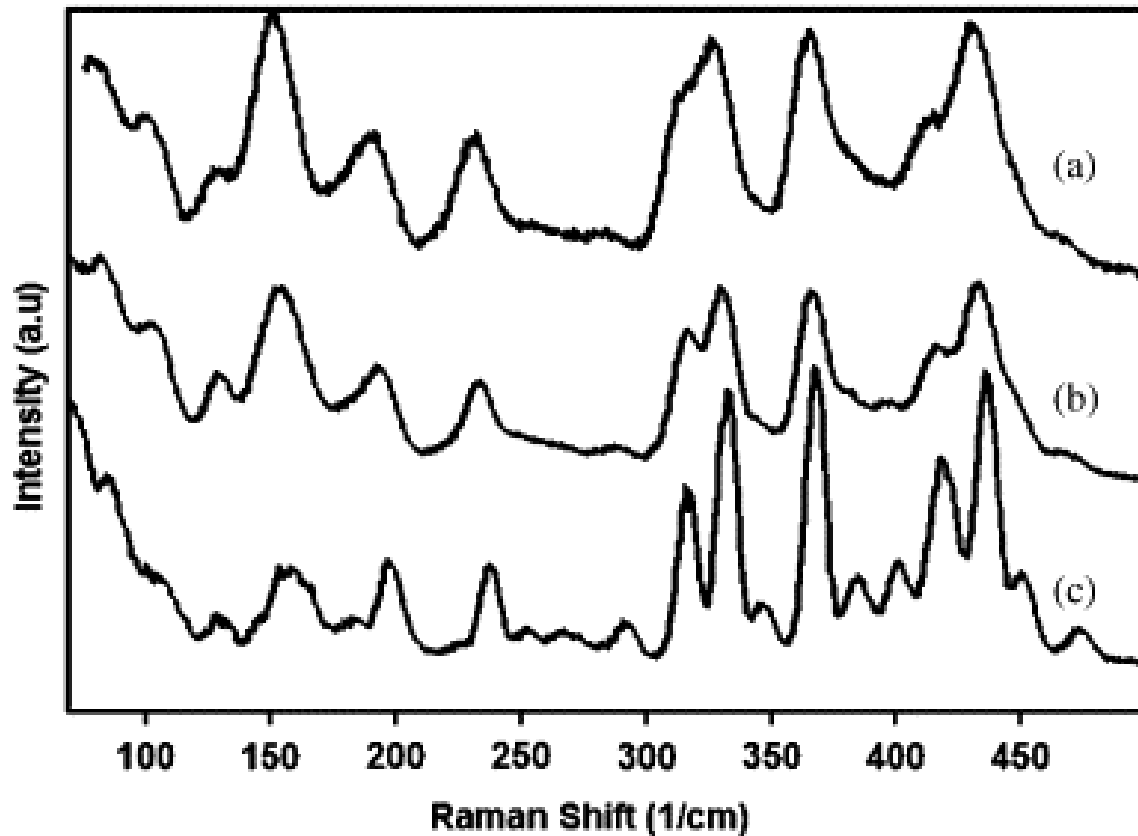


Figure 5.7. Raman spectrum of (a) $\text{Lu}(\text{IO}_3)_3$, and (b) $\text{Yb}(\text{IO}_3)_3$ at room temperature covering the iodate bending and lattice vibrational regions; (c) Raman spectrum of $\text{Yb}(\text{IO}_3)_3$ collected at liquid N_2 temperature. A highly resolved spectrum was obtained at low temperature.

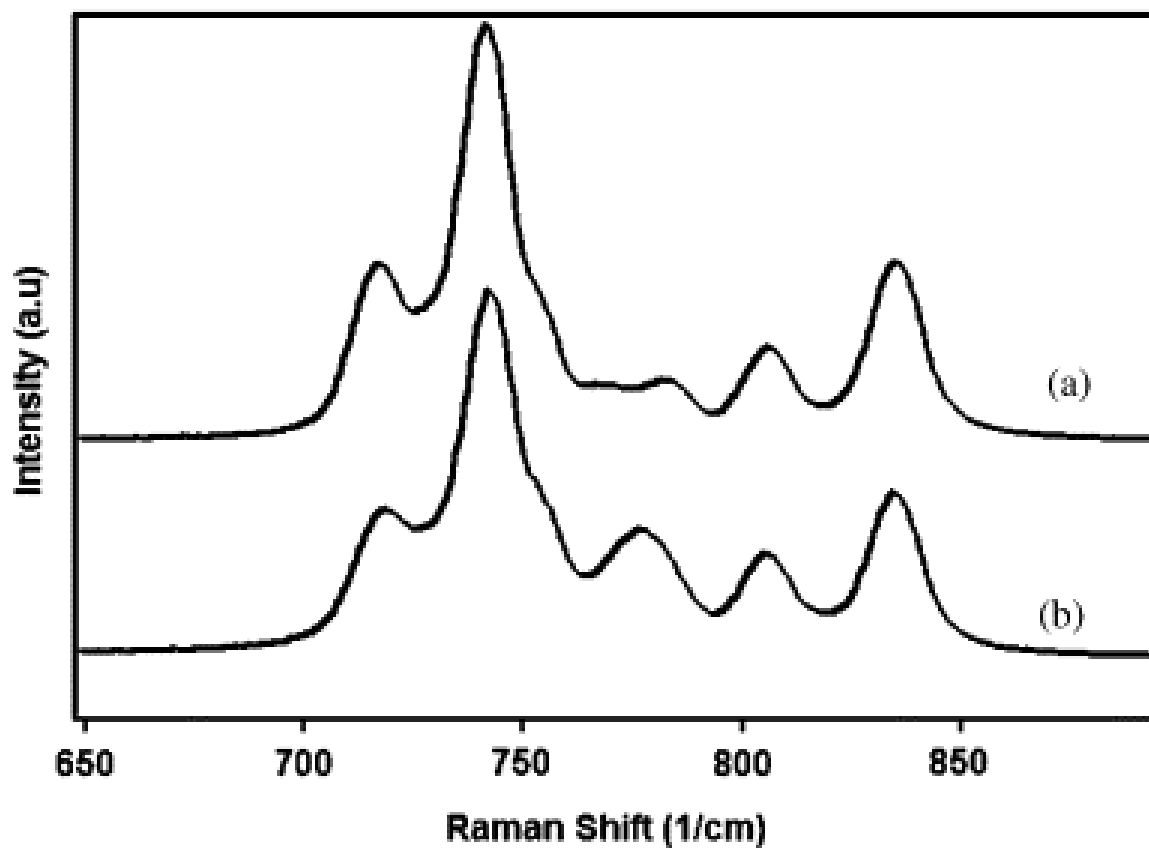


Figure 5.8. Raman spectrum of (a) $\text{Lu}(\text{IO}_3)_3(\text{H}_2\text{O})$, and (b) $\text{Yb}(\text{IO}_3)_3(\text{H}_2\text{O})$ at room temperature in the I–O stretching region.

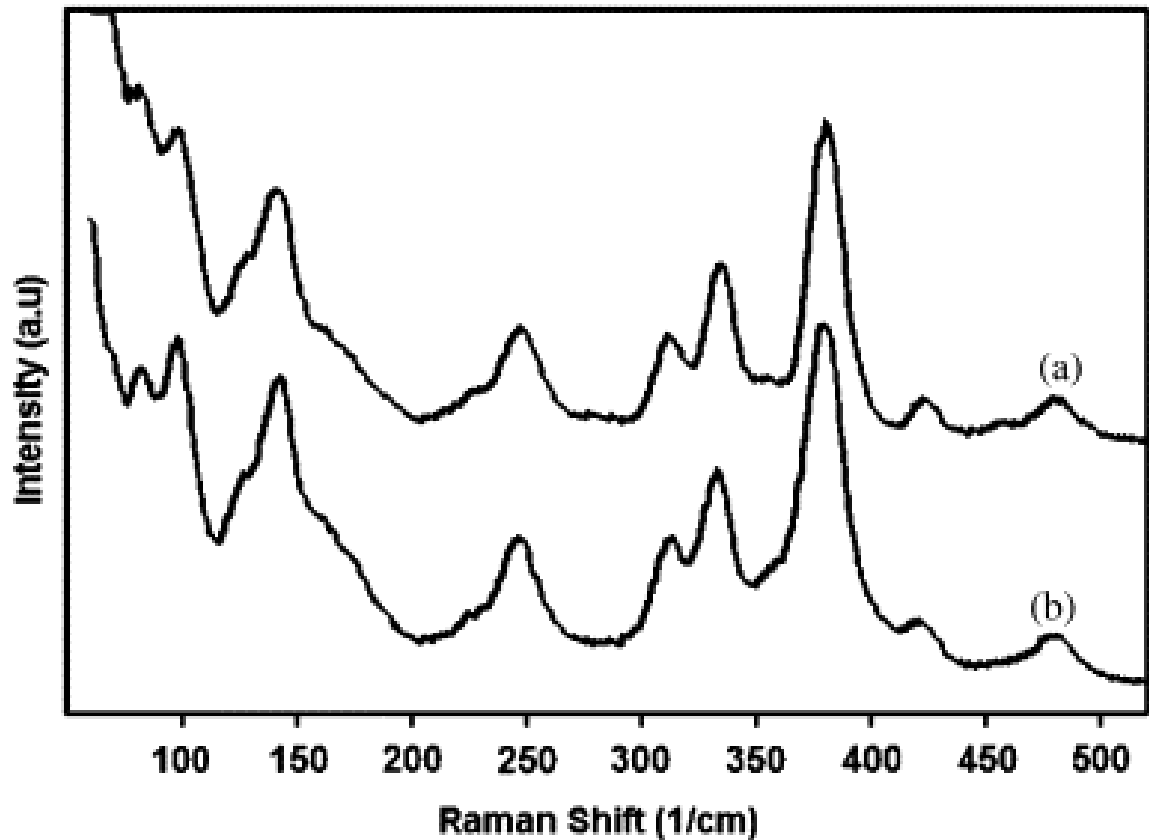


Figure 5.9. Raman spectrum of (a) Lu(IO₃)₃(H₂O), and (b) Yb(IO₃)₃(H₂O) at room temperature in the iodate bending and lattice vibrational regions.

CONCLUSIONS

Four new metal iodates, $\text{Yb}(\text{IO}_3)_3$, $\text{Lu}(\text{IO}_3)_3$, $\text{Yb}(\text{IO}_3)_3(\text{H}_2\text{O})$, and $\text{Lu}(\text{IO}_3)_3(\text{H}_2\text{O})$, have been isolated as single crystals through the use of hydrothermal reactions. Structural determinations using single-crystal X-ray diffraction have shown that the materials are all alike in that they contain two-dimensional structures; the two anhydrous iodates are isostructural as are the hydrated compounds. These mono-hydrated iodates represent a novel structure type, while the anhydrous compounds crystallize in the $\text{Bi}(\text{IO}_3)_3$ structure type, as found previously for several other *f*-element iodates. Raman spectra have been collected for all four lanthanide iodates. Although $\text{Yb}(\text{IO}_3)_3$ and $\text{Lu}(\text{IO}_3)_3$ show similar profiles due to their isostructural nature, as do $\text{Yb}(\text{IO}_3)_3(\text{H}_2\text{O})$ and $\text{Lu}(\text{IO}_3)_3(\text{H}_2\text{O})$, the differences in the Raman vibrational profiles between the two classes of compounds is significant. Therefore, Raman spectroscopy can be used to discern the different structural motifs of these two classes of materials.

REFERENCES

1. Abrahams, S. C.; Bernstein, J. L., Nassau, K. *J. Solid State Chem.* **1976**, 16, 173.
2. Abrahams, S. C.; Bernstein, J. L. *Solid State Comm.* **1978**, 27, 973.
3. Abrahams, S. C.; Bernstein, J. L. *J. Chem. Phys.* **1978**, 69, 2505.
4. Liminga, R.; Abrahams, S. C.; Bernstein, J. L. *J. Chem. Phys.* **1975**, 62, 755.
5. Hector, A. L.; Levason W.; Webster, M. *Inorg. Chim. Acta* **2000**, 298, 43.
6. Liminga, R.; Abrahams S. C.; Bernstein, J. L. *J. Chem. Phys.* **1977**, 67, 1015.
7. Sykora, R. E.; Assefa, Z.; Haire R. G.; Albrecht-Schmitt, T. E. *Inorg. Chem.* **2005**, 44, 5667.
8. Sykora, R. E.; Assefa, Z.; Haire R. G.; Albrecht-Schmitt, T. E. *J. Solid State Chem.* **2004**, 177,4413.
9. Chen, X.; Xue, H.; Chang, X.; Zang, H.; Xiao, W. *J. Alloys Compd.* **2005**, 398, 173.
10. Sykora, R. E.; Assefa, Z.; Haire R. G.; Albrecht-Schmitt, T. E. *Inorg. Chem.* **2006**, 45, 475.
11. Douglas, P.; Hector, A. L.; Levason, W.; Light, M. E.; Matthews, M. L.; Webster, M. *Z. Anorg. Allg. Chem.* **2004**, 630, 479.
12. Hector, A. L.; Henderson, S. J.; Levason, W.; Webster, M. *Z. Anorg. Allg. Chem.* **2002**, 628, 198.
13. Sen Gupta, P. K.; Ammon, H. L.; Abrahams, S. C. *Acta Crystallogr.* **1989**, C 45, 175.
14. Runde, W.; Bean A. C.; Scott, B. L. *Chem. Comm.* **2003**, 1848.
15. Stoughton, R. W.; Duffield, R. B. US Patent No. 2,856,261, **1958**.

16. Fries, B. A. US Patent No. 2,926,067, **1960**.
17. Weaver, B. *Anal. Chem.* **1968**, 40, 1894..
18. Bentría, B.; Benbental, D.; Bagieu-Beucher, M.; Masse, R.; Mosset, A. *J. Chem. Crystallogr.* **2003**, 33, 867.
19. Bean, A. C.; Peper, S. M.; Albrecht-Schmitt, T. E. *Chem. Mater.* **2001**, 13, 1266.
20. Albrecht-Schmitt, T. E.; Almond P. M.; Sykora, R. E. *Inorg. Chem.* **2003**, 42, 3788.
21. Runde, W.; Bean, A. C.; Albrecht-Schmitt T. E.; Scott, B. L. *Chem. Comm.* **2003**, 478.
22. Assefa, Z.; Ling, J.; Haire, R. G.; Albrecht-Schmitt, T. E.; Sykora, R. E. *J. Solid State Chem.* **2006**, 179, 3653
23. SADABS, *Acta Crystallogr.* **1995**,A 51, 33.
24. Sheldrick, G. M. SHELXTL PC, version 5.0, An integrated system for solving, refining, and displaying crystal structures from diffraction data, Siemens Analytical X-ray Instruments, Inc., Madison, WI **1994**.
25. Sykora, R. E.; Bean, A. C.; Scott, B. L.; Runde, W.; Albrecht-Schmitt, T. E. *J. Solid State Chem.* **2004**. 177, 725.
26. Sykora, R. E.; McDaniel, S. M.; Wells, D. M.; Albrecht-Schmitt, T. E. *Inorg. Chem.* **2002**, 41, 5126.
27. Brese, N. E.; O'Keeffe, M. *Acta. Crystallogr.* **1991**, B 47, 192.
28. Bean, A. C.; Scott, B. L.; Albrecht-Schmitt, T. E.; Runde, W. *Inorg. Chem.* **2003**, 42, 5632.
29. Pracht, G.; Lange, N.; Lutz, H. D. *Thermochim. Acta* **1997**, 13, 293.
30. Lutz, H. D.; Alici, E.; Kellersohn, T. *J. Raman Spectrosc.* **1990**, 21,387.

31. During, J. R.; Bonner, O. D.; Breazeale, W. H. *J. Phys. Chem.* **1965**, 69, 3886.
32. Schellenschlager, V.; Pracht, G.; Lutz, H. D. *J. Raman Spectrosc.* **2001**, 32, 373.
33. Lutz, H. D.; Suchanek, E. *Spectrochim. Acta* **2000**, A 56, 2707.
34. Pracht, G.; Nagel, R.; Suchanek, E.; Lange, N.; Lutz, H. D. *Z. Anorg. Allg. Chem.* **1998**, 624, 1355.
35. Lutz, H. D.; Christian, H.; Eckers, W. *Spectrochim. Acta* **1985**, A 41, 637.
36. Lutz, H. D.; Kellersohn, T.; Müller, B.; Henning, J. *Spectrochim. Acta* **1988**, A 44, 497.

CHAPTER 6

INTERCALATION OF IODIC ACID INTO THE LAYERED URANYL IODATE, $\text{UO}_2(\text{IO}_3)_2(\text{H}_2\text{O})$

ABSTRACT

$\text{UO}_2(\text{IO}_3)_2(\text{H}_2\text{O}) \cdot 2\text{HIO}_3$, with iodic acid intercalated into the layered uranyl iodate, $\text{UO}_2(\text{IO}_3)_2(\text{H}_2\text{O})$, has been synthesized by reacting $\text{UO}_2(\text{NO}_3)_2 \cdot 6\text{H}_2\text{O}$ with excess iodic acid under mild hydrothermal conditions. This is the first example of this type of reaction with iodic acid.

The structure of $\text{UO}_2(\text{IO}_3)_2(\text{H}_2\text{O}) \cdot 2\text{HIO}_3$ has nearly identical $\text{UO}_2(\text{IO}_3)_2(\text{H}_2\text{O})$ layers as the previously reported structure of $\text{UO}_2(\text{IO}_3)_2(\text{H}_2\text{O})$ in the $[ab]$ plane. Iodic acid molecules are intercalated into the gap between the $\text{UO}_2(\text{IO}_3)_2(\text{H}_2\text{O})$ layers and results in the increase of unit cell value along c axis. The intercalated iodic acid molecules are stabilized by weak interactions between the iodic acid molecules and iodates anions. Crystallographic data: (193 K; Mo $K\alpha$, $\lambda = 0.71073 \text{ \AA}$): orthorhombic, space group $Pbcn$, $a = 8.3347(7)$, $b = 7.6594(6)$, $c = 20.899(2) \text{ \AA}$, $V = 1334.15(19) \text{ \AA}^3$, $Z = 4$, $R(F) = 2.45\%$ for 92 parameters with 1579 reflections with $I > 2\sigma(I)$.

INTRODUCTION

Uranyl iodates are known primarily for their ability to form novel one-dimensional topologies.¹ However, the importance of these compounds is equally well addressed by their potential formation during the oxidative dissolution of spent nuclear fuel, where it is expected that some of the long-lived β -emitter, ^{129}I ($t_{1/2} = 1.7 \times 10^7$ year), will be converted to iodate, which can then bind solubilized uranium in the form of UO_2^{2+} to form uranyl iodates. While the structural chemistry of uranyl iodates is relatively mature, little is known about the physicochemical properties of these compounds, with the exceptions of $\text{UO}_2(\text{IO}_3)_2$,² $\text{UO}_2(\text{IO}_3)_2(\text{H}_2\text{O})$,² and $\text{K}[\text{UO}_2(\text{IO}_3)_3]$.³ $\text{UO}_2(\text{IO}_3)_2$ and $\text{UO}_2(\text{IO}_3)_2(\text{H}_2\text{O})$ have been shown to interconvert in supercritical water, and their thermal properties are well understood.² $\text{K}[\text{UO}_2(\text{IO}_3)_3]$ exhibits selective ion exchange of its K^+ cations for Cs^+ cations.³

Among iodate compounds in general, there are a small number of acidic solids that are thought to possess iodate in its protonated form, i.e., as HIO_3 . Examples of these compounds include $\text{K}_3\text{Am}_3(\text{IO}_3)_{12} \cdot \text{HIO}_3$ ⁴ and $3\text{La}(\text{IO}_3)_3 \cdot \text{HIO}_3 \cdot 7\text{H}_2\text{O}$.⁵ Given that these solids typically contain heavy atoms, resolution of the H atom positions is challenging. Iodic acid is a neutral molecule, and it is therefore possible that some of these compounds are the result of the intercalation of iodic acid into a preexisting structure. However, it is likely that the iodic acid cocrystallizes along with the other components of the system because these iodic acid molecules are typically part of hydrogen bonding and iodate...iodate networks that are integral parts of the overall structures. Herein we demonstrate the direct intercalation of iodic acid into the layered structure of

UO₂(IO₃)₂(H₂O). The information in this chapter has been published as a communication in *Journal of Inorganic Chemistry*.⁶

EXPERIMENTAL

Synthesis. UO₂(NO₃)₂·6H₂O (98%, Alfa-Aesar), and HIO₃ (99.5%, Alfa-Aesar) were used as received without further purification. Distilled and Millipore filtered water with resistance of 18.2 MΩ cm was used in all reactions. The PTFE liners were used for all reactions. SEM/EDX analyses were performed using a JEOL JSM-7000F. *While the UO₃ contains depleted U, standard precautions for handling radioactive materials should be followed. Old sources of depleted U should not be used, as the daughter elements of natural decay are highly radioactive and present serious health risks.*

UO₂(IO₃)₂(H₂O)·2HIO₃ was prepared by loading UO₂(NO₃)₂·6H₂O (0.056 g, 0.112 mmol), HIO₃ (0.585 g, 3.321mmol), and 0.5 mL of distilled and Millipore-filtered water in a 23-mL poly(tetrafluoroethylene)-lined autoclave. The autoclave was heated at 200 °C for 3 days and then cooled at a rate of 9 °C/h to room temperature. Clusters of yellow block crystals of UO₂(IO₃)₂(H₂O)·2HIO₃ were isolated, washed with methanol, and allowed to dry. Yield: 59 mg (53% yield based on U). EDX analysis provided U:I ratio of 1:4 (21%:79%).

Crystallographic Studies. A single crystal of UO₂(IO₃)₂(H₂O)·2HIO₃ with dimension of 0.086 mm × 0.071 mm × 0.054 mm was selected and mounted on a quartz fiber with epoxy and aligned on a Bruker SMART APEX CCD X-ray diffractometer with a digital camera. Intensity measurements were performed using graphite-monochromated Mo Kα radiation from a sealed tube with a monocapillary collimator. The intensities and

positions of reflections of a sphere were collected by a combination of 3 sets of exposure frames. Each set had a different φ angle for the crystal and each exposure covered a range of 0.3° in ω . A total of 1800 frames were collected with an exposure time per frame of 30 s for $\text{UO}_2(\text{IO}_3)_2(\text{H}_2\text{O})\cdot 2\text{HIO}_3$.

Determination of integrated intensities and global cell refinement were performed with the Bruker SAINT (v 6.02) software package using a narrow-frame integration algorithm. A semi-empirical absorption correction was applied using SADABS.¹⁸ The program suite SHELXTL (v 5.1) was used for space group determination (XPREP), direct methods structure solution (XS), and least-squares refinement (XL).¹⁹ The final refinements included anisotropic displacement parameters for all atoms and a secondary extinction parameter. Some crystallographic details of $\text{UO}_2(\text{IO}_3)_2(\text{H}_2\text{O})\cdot 2\text{HIO}_3$ and $\text{UO}_2(\text{IO}_3)_2(\text{H}_2\text{O})$ are listed in Table 6.1, and the final positional parameters can be found in Table 6.2.

Powder X-ray Diffraction. Powder X-ray diffraction pattern was collected with a Rigaku Miniflex powder X-ray diffractometer using Cu $K\alpha$ ($\lambda=1.54056 \text{ \AA}$) radiation. The collected patterns were compared with that calculated from single-crystal data using ATOMS.²⁰

Vibrational Spectroscopy. The IR spectrum of $\text{UO}_2(\text{IO}_3)_2(\text{H}_2\text{O})\cdot 2\text{HIO}_3$ was taken from samples in KBr pellets with using a Shimadzu IR Prestige-21 in the wave number range of $4000\text{--}400 \text{ cm}^{-1}$.

Thermal Analysis. The data were collected using differential scanning calorimeter TA Instrument, model 2920. The samples of known mass encapsulated in the

Table 6.1. Crystallographic Data for $\text{UO}_2(\text{IO}_3)_2(\text{H}_2\text{O}) \cdot 2\text{HIO}_3$ and $\text{UO}_2(\text{IO}_3)(\text{H}_2\text{O})^2$.

Compound	$\text{UO}_2(\text{IO}_3)_2(\text{H}_2\text{O}) \cdot 2\text{HIO}_3$	$\text{UO}_2(\text{IO}_3)(\text{H}_2\text{O})^2$
Formula Mass	813.75	637.85
Color and habit	Yellow, prism	Yellow, prism
Crystal System	Orthorhombic	Orthorhombic
Space group	<i>Pbcn</i> (No. 60)	<i>Pbcn</i> (No. 60)
<i>a</i> (Å)	8.3347(7)	8.452(2)
<i>b</i> (Å)	7.6594(6)	7.707(2)
<i>c</i> (Å)	20.8988 (17)	12.271(3)
<i>V</i> (Å ³)	1334.15 (19)	799.3(3)
<i>Z</i>	4	4
<i>T</i> (K)	193	193
λ (Å)	0.71073	0.71073
Maximum 2 θ (deg.)	56.60	56.58
ρ_{calcd} (g cm ⁻³)	4.051	5.300
$\mu(\text{Mo } K\alpha)$ (cm ⁻¹)	191.53	280.05
$R(F)$ for $F_o^2 > \sigma(F_o^2)$ ^a	0.0245	0.0306
$R_w(F_o^2)$ ^b	0.0630	0.0536

$$^a R(F) = \frac{\sum ||F_o| - |F_c||}{\sum |F_o|}. \quad ^b R_w(F_o^2) = \left[\frac{\sum [w(F_o^2 - F_c^2)^2]}{\sum wF_o^4} \right]^{1/2}.$$

Table 6.2. Atomic Coordinates and Equivalent Isotropic Displacement Parameters for $\text{UO}_2(\text{IO}_3)_2(\text{H}_2\text{O})\cdot 2\text{HIO}_3$.

Atom	<i>x</i>	<i>y</i>	<i>z</i>	$U_{\text{eq}} (\text{\AA}^2)^a$
U(1)	0	0.01387(4)	1/4	0.01029(10)
I(1)	0.30562(4)	-0.16647(5)	0.374744(17)	0.00991(10)
I(2)	0.66775(4)	-0.45151(5)	0.442059(17)	0.01251(10)
O(1)	0.1137(5)	-0.0876(6)	0.3451(2)	0.0138(8)
O(2)	0.3877(6)	-0.2395(5)	0.2996(2)	0.0171(9)
O(3)	0.4023(5)	0.0461(5)	0.3742(2)	0.0164(9)
O(4)	0.8754(6)	-0.3609(6)	0.4455(2)	0.0225(10)
O(5)	0.5821(6)	-0.2418(6)	0.4266(2)	0.0190(9)
O(6)	0.6486(6)	-0.4700(6)	0.5274(2)	0.0192(10)
O(7)	-0.1755(5)	0.0134(6)	0.2983(2)	0.0173(9)
O(8)	0	-0.3079(8)	1/4	0.0188(13)

^a U_{eq} is defined as one-third of the trace of the orthogonalized \mathbf{U}_{ij} tensor.

Table 6.3. Selected Bond Distances (Å) and Angles (°) for $\text{UO}_2(\text{IO}_3)_2(\text{H}_2\text{O})\cdot 2\text{HIO}_3$.

Distances (Å)			
U(1)–O(1) X 2	2.335(4)	I(1)–O(1)	1.819(4)
U(1)–O(2) X 2	2.349(4)	I(1)–O(2)	1.803(4)
U(1)–O(7) X 2	1.778(5)	I(1)–O(3)	1.817(4)
U(1)–O(8)	2.464(4)	I(2)–O(4)	1.866(5)
		I(2)–O(5)	1.787(4)
		I(2)–O(6)	1.796(5)

Angles (°)			
O(1)–U(1)–O(1)	141.1(2)	O(2)–U(1)–O(8)	143.5(1)
O(1)–U(1)–O(2)	74.4(2)	O(7)–U(1)–O(7)	179.8(3)
O(1)–U(1)–O(2)	143.6(2)	O(7)–U(1)–O(8)	89.9(2)
O(1)–U(1)–O(7)	98.6(2)	O(1)–I(1)–O(2)	98.1(2)
O(1)–U(1)–O(7)	81.3(2)	O(1)–I(1)–O(3)	95.2(2)
O(1)–U(1)–O(8)	70.6(1)	O(2)–I(1)–O(3)	96.0(2)
O(2)–U(1)–O(2)	72.9(2)	O(4)–I(2)–O(5)	92.5(2)
O(2)–U(1)–O(7)	85.7(2)	O(4)–I(2)–O(6)	94.2(2)
O(2)–U(1)–O(7)	94.5(2)	O(5)–I(2)–O(6)	102.4(2)

aluminum container, was heated under nitrogen atmosphere from 30 °C to 600 °C with heating rate of 10°C /minute.

RESULTS AND DISCUSSION

Synthesis of $\text{UO}_2(\text{IO}_3)_2(\text{H}_2\text{O})\cdot 2\text{HIO}_3$. When $\text{UO}_2(\text{NO}_3)_2\cdot 6\text{H}_2\text{O}$ is reacted with a 2-5-fold excess of iodic acid under mild hydrothermal conditions, the only compound that results is $\text{UO}_2(\text{IO}_3)_2(\text{H}_2\text{O})$. When the amount of iodic acid is increased 10-fold, a mixture of $\text{UO}_2(\text{IO}_3)_2(\text{H}_2\text{O})$ and $\text{UO}_2(\text{IO}_3)_2(\text{H}_2\text{O})\cdot 2\text{HIO}_3$ is found. When the amount of iodic acid is increased 30-fold, pure samples of $\text{UO}_2(\text{IO}_3)_2(\text{H}_2\text{O})\cdot 2\text{HIO}_3$ can be prepared. More importantly, if $\text{UO}_2(\text{IO}_3)_2(\text{H}_2\text{O})$ is reacted with large excesses of iodic acid, $\text{UO}_2(\text{IO}_3)_2(\text{H}_2\text{O})\cdot 2\text{HIO}_3$ is also found to form. There has historically been controversy over the formula and density of uranyl iodates. We have noted that crystals of $\text{UO}_2(\text{IO}_3)_2(\text{H}_2\text{O})\cdot 2\text{HIO}_3$ are morphologically similar to those of $\text{UO}_2(\text{IO}_3)_2(\text{H}_2\text{O})$, which may have created confusion.

Crystal Structure of $\text{UO}_2(\text{IO}_3)_2(\text{H}_2\text{O})\cdot 2\text{HIO}_3$. The structure of $\text{UO}_2(\text{IO}_3)_2(\text{H}_2\text{O})\cdot 2\text{HIO}_3$ consists of neutral $\text{UO}_2(\text{IO}_3)_2(\text{H}_2\text{O})$ layers that are interconnected by iodic acid molecules, as is shown in Figure 6.1. The individual $\text{UO}_2(\text{IO}_3)_2(\text{H}_2\text{O})$ layers found in $\text{UO}_2(\text{IO}_3)_2(\text{H}_2\text{O})\cdot 2\text{HIO}_3$ are nearly identical with those found for the parent compound, $\text{UO}_2(\text{IO}_3)_2(\text{H}_2\text{O})$ and consist of a UO_2^{2+} cation bound by four bridging iodate anions and a water molecule to form a UO_7 pentagonal bipyramid. The terminal U=O bond distances of 1.778(5) Å (×2) and bridging U-O bond distances of 2.335(4) (×2) and 2.349(4) Å (×2) deviate only slightly from that of $\text{UO}_2(\text{IO}_3)_2(\text{H}_2\text{O})$, as does the longest bond distance to the terminal water molecule of 2.464(6) Å. The similarities between the

layers found in $\text{UO}_2(\text{IO}_3)_2(\text{H}_2\text{O})$ and $\text{UO}_2(\text{IO}_3)_2(\text{H}_2\text{O})\cdot 2\text{HIO}_3$ can also be expressed in terms of the dimensions of the unit cells in the $[ab]$ plane. For the parent compound, these dimensions are $8.452(2) \times 7.707(2)$ Å, whereas those for the intercalated product are $8.3347(7) \times 7.6594(6)$ Å. Both compounds crystallize in the orthorhombic space group $Pbcn$, and the differences in the units cells are primarily found in the c direction, where $\text{UO}_2(\text{IO}_3)_2(\text{H}_2\text{O})$ is $12.271(3)$ Å and $\text{UO}_2(\text{IO}_3)_2(\text{H}_2\text{O})\cdot 2\text{HIO}_3$ is $20.899(2)$ Å. Taken together, these metrics indicate that $\text{UO}_2(\text{IO}_3)_2(\text{H}_2\text{O})\cdot 2\text{HIO}_3$ differs from $\text{UO}_2(\text{IO}_3)_2(\text{H}_2\text{O})$ only in the intercalation of two molecules of iodic acid per formula unit.

The iodic acid molecules located between the layers show I-O bond distances of $1.787(4)$, $1.796(5)$, and $1.866(5)$ Å. We have surveyed 28 high-resolution iodate crystal structures to arrive at a value of $1.792(5)$ Å for terminal I-O bonds. In contrast, I-O bond distances for bridging or μ_2 -O bonds from 32 different structures show an average distance of $1.831(5)$ Å. Fortunately, during the course of other studies, we were able to prepare $\text{K}_2\text{SeO}_4\cdot 2\text{HIO}_3$,⁷ which contains a single protonated I-OH moiety. Here the bond distance is $1.912(2)$ Å. On the basis of these data, it can be concluded that the proton is localized on O(4) with the longest I-O bond. There are several short interactions of appropriate length for a hydrogen bond between O(4) and O atoms within the layers. In addition to hydrogen bonds, iodate...iodate interactions play a critical role in stabilizing many iodate compounds.⁸ In $\text{UO}_2(\text{IO}_3)_2(\text{H}_2\text{O})$, these interactions interconnect the layers and are probably the origin of the crystallinity and low solubility of this phase. These interactions also exist in $\text{UO}_2(\text{IO}_3)_2(\text{H}_2\text{O})\cdot 2\text{HIO}_3$. The intermolecular I...O interactions range from $2.611(5)$ to $2.802(5)$ Å.

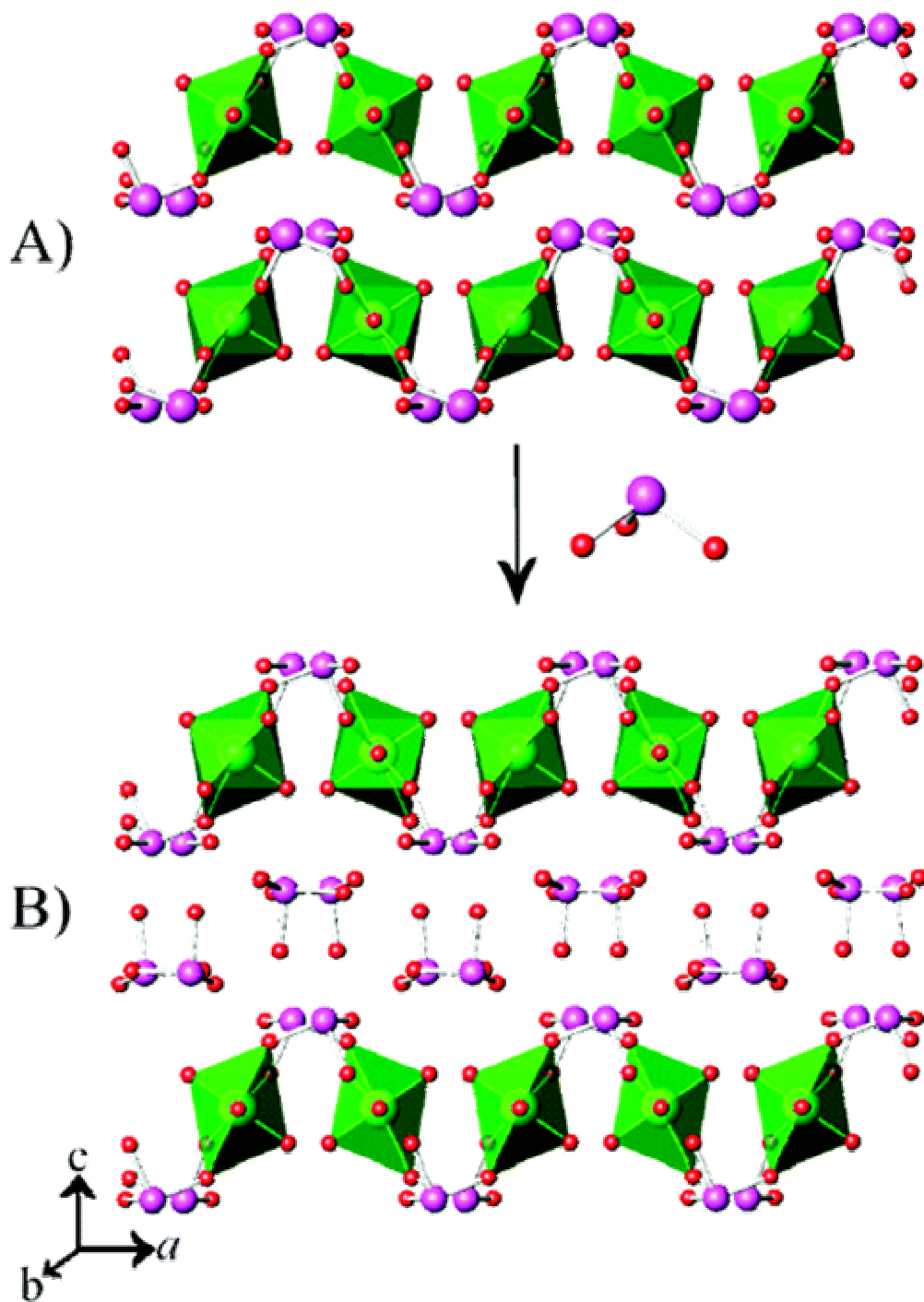


Figure 6.1. Depiction of the intercalation of iodic acid into $\text{UO}_2(\text{IO}_3)_2(\text{H}_2\text{O})$ (A) to yield $\text{UO}_2(\text{IO}_3)_2(\text{H}_2\text{O}) \cdot 2\text{HIO}_3$ (B) UO_7 pentagonal bipyramids are shown in green, I atoms in purple, and O atoms in red.

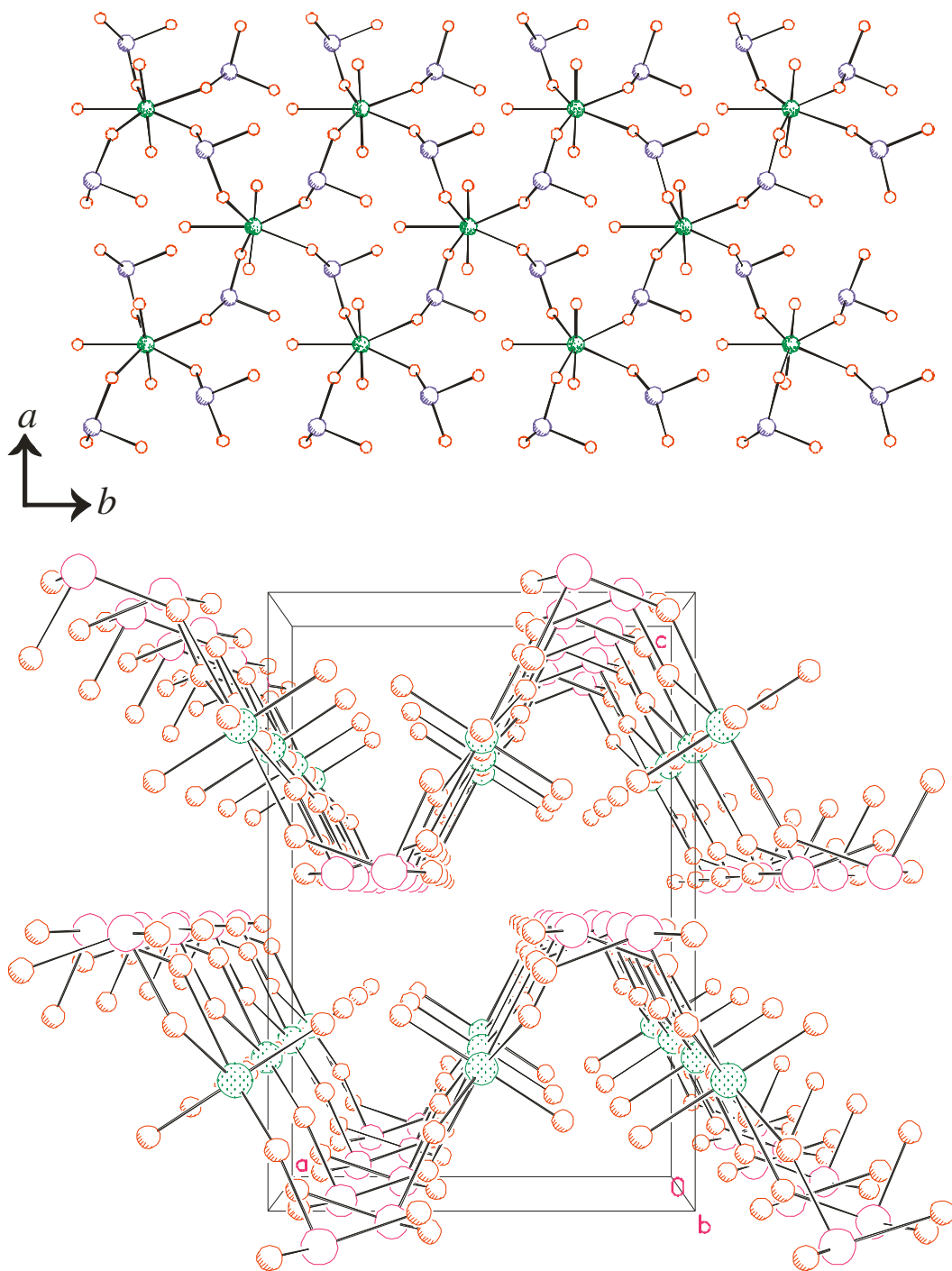


Figure 6.2. (top) View down the *c* axis of the [UO₂(IO₃)₂(H₂O)] layers in UO₂(IO₃)₂(H₂O).² (bottom) Packing of the highly corrugated [UO₂(IO₃)₂(H₂O)] layers in UO₂(IO₃)₂(H₂O) viewed down the *b* axis.²

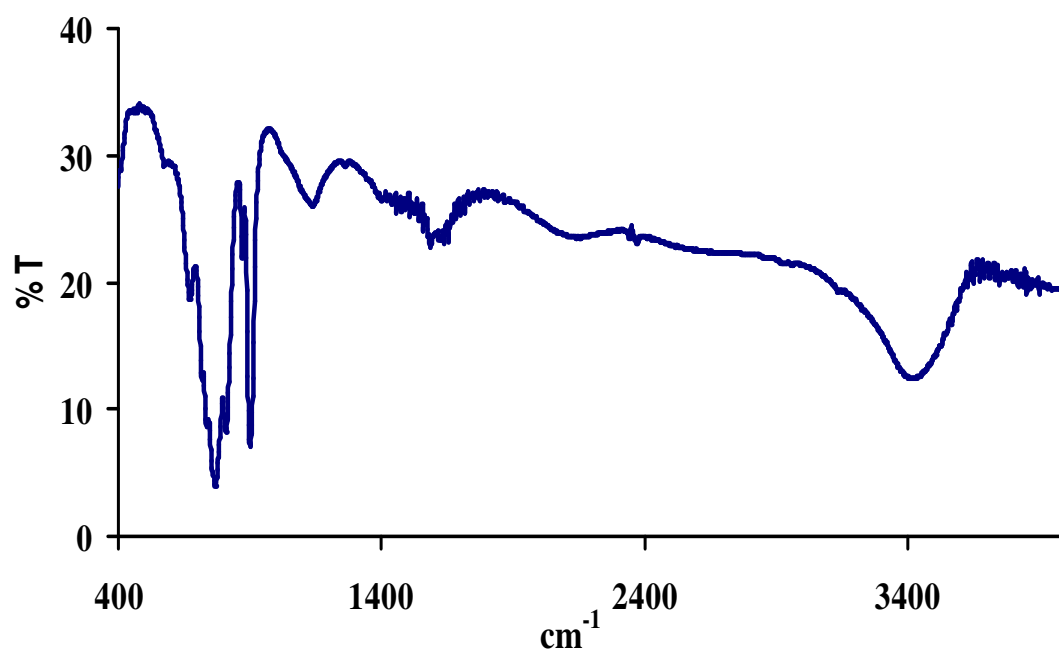


Figure 6.3. IR spectrum of $\text{UO}_2(\text{IO}_3)_2(\text{H}_2\text{O}) \cdot 2\text{HIO}_3$.

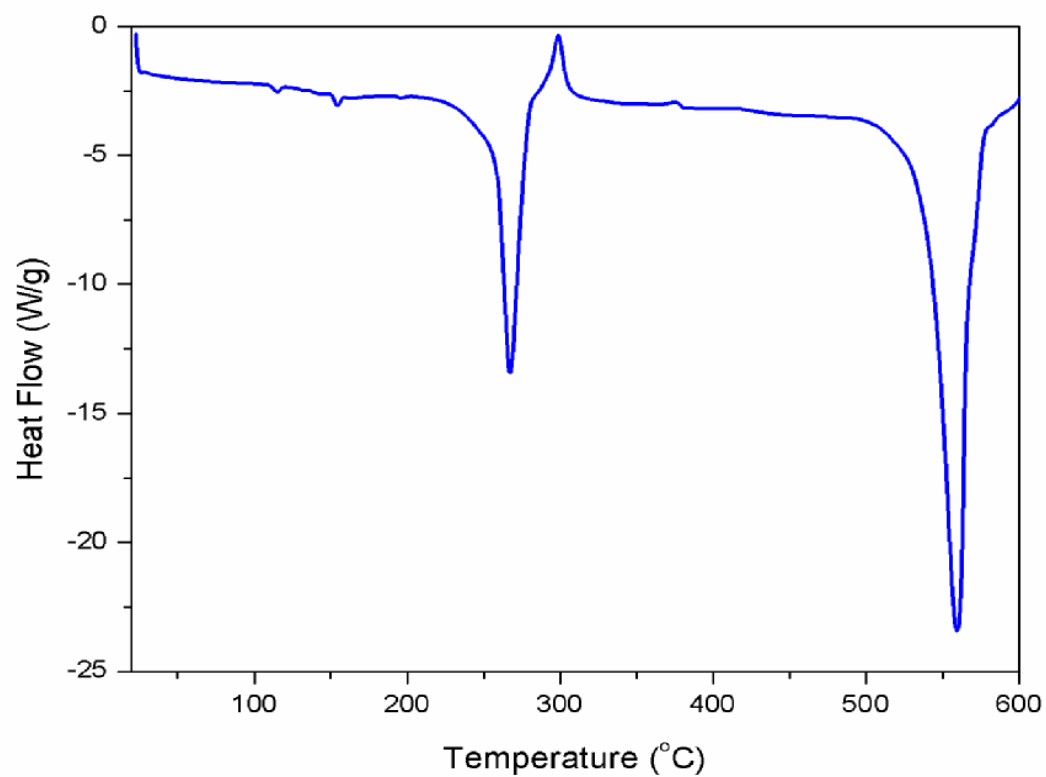


Figure 6.4. DSC thermogram of $\text{UO}_2(\text{IO}_3)_2(\text{H}_2\text{O}) \cdot 2\text{HIO}_3$.

Vibrational Spectroscopy. The IR spectrum of $\text{UO}_2(\text{IO}_3)_2(\text{H}_2\text{O})\cdot 2\text{HIO}_3$ is particularly rich in that it shows a characteristic I-OH stretch at 1138 cm^{-1} .⁹ In addition, both asymmetric and symmetric uranyl modes are observed at 902 and 872 cm^{-1} , respectively. Iodate stretches (ν_1 and ν_3) are found at 810 , 770 , 759 , 735 , 718 , and 671 cm^{-1} ,¹⁰ and an iodate bending mode (δ) is found at 573 cm^{-1} . The ν and δ modes for the bound water are found at 3410 and 1587 cm^{-1} , respectively.

Thermal Analysis. A calorimetric study of $\text{UO}_2(\text{IO}_3)_2(\text{H}_2\text{O})\cdot 2\text{HIO}_3$ reveals two endotherms at 267 and $559\text{ }^\circ\text{C}$. These features are similar to those found for the parent compound and are ascribed to the loss of water and thermal disproportionation of iodate, respectively. Water loss occurs at a lower temperature for $\text{UO}_2(\text{IO}_3)_2(\text{H}_2\text{O})\cdot 2\text{HIO}_3$ than for $\text{UO}_2(\text{IO}_3)_2(\text{H}_2\text{O})$. The new feature in the thermogram of $\text{UO}_2(\text{IO}_3)_2(\text{H}_2\text{O})\cdot 2\text{HIO}_3$ is an exotherm that immediately follows the loss of water at $299\text{ }^\circ\text{C}$. We suggest that this exothermic feature represents the filling of the open-coordination site previously occupied by water by an O atom from an iodic acid molecule in the interlayer space, yielding $\text{UO}_2(\text{IO}_3)_2(\text{HIO}_3)\cdot \text{HIO}_3$.

In addition to the intercalation of iodic acid, there are other protonated oxoanions, which are of interest from the perspective of the oxidation of spent nuclear fuel, that might intercalate into $\text{UO}_2(\text{IO}_3)_2(\text{H}_2\text{O})$. Selenous acid is a high priority in this regard.¹¹ Future publications will detail ongoing efforts to explore the intercalation of neutral molecules into $\text{UO}_2(\text{IO}_3)_2(\text{H}_2\text{O})$.

CONCLUSIONS

A first example of direct intercalation of iodic acid molecules into layered uranyl phase was discovered in this work. It could be potentially applied in the mitigation of the release of ^{129}I from spent nuclear fuel. The iodic acid intercalated hydrated uranyl iodate has been made by reacting $\text{UO}_2(\text{NO}_3)_2 \cdot 6\text{H}_2\text{O}$ with a 30 fold excess of iodic acid under hydrothermal conditions. It was also successfully synthesized by reacting hydrated uranyl iodate ($\text{UO}_2(\text{IO}_3)_2(\text{H}_2\text{O})$) with excess iodic acid. Similar to the structure of $\text{UO}_2(\text{IO}_3)_2(\text{H}_2\text{O})$, the iodic acid intercalated hydrated uranyl iodate has an identical two-dimensional layer structure in the $[ab]$ plane. The intercalation of iodic acid molecules into $\text{UO}_2(\text{IO}_3)_2(\text{H}_2\text{O})$ structure enlarges the gap between two adjacent layers and results in a much larger unit cell constant on the c axis. A characteristic I-OH stretch at 1138 cm^{-1} in the IR spectrum of $\text{UO}_2(\text{IO}_3)_2(\text{H}_2\text{O}) \cdot 2\text{HIO}_3$ confirms the existence of iodic acid in the structure. The DSC spectrum indicates that the iodic acid intercalated hydrated uranyl iodate is stable up to $267\text{ }^\circ\text{C}$.

REFERENCES

1. (a) Sykora, R. E.; McDaniel, S. M.; Wells, D. M.; Albrecht-Schmitt, T. E. *Inorg. Chem.* **2002**, *41*, 5126. (b) Sykora, R. E.; Wells, D. M.; Albrecht-Schmitt, T. E. *Inorg. Chem.* **2002**, *41*, 2304. (c) Bean, A. C.; Ruf, M.; Albrecht-Schmitt, T. E. *Inorg. Chem.* **2001**, *40*, 3959.
2. Bean, A. C.; Peper, S. M.; Albrecht-Schmitt, T. E. *Chem. Mater.* **2001**, *13*, 1266.
3. Shvareva, T. Y.; Almond, P. M.; Albrecht-Schmitt, T. E. *J. Solid State Chem.* **2005**, *178*, 499.
4. Runde, W.; Bean, A. C.; Scott, B. L. *Chem. Commun.* **2003**, *15*, 1848.
5. Abrahams, S. C.; Bernstein, J. L.; Nassau, K. *J. Appl. Crystallogr.* **1976**, *9*, 357.
6. Ling, J.; Albrecht-Schmitt, T. E. *Inorg. Chem.* **2007**, *46*, 346.
7. Synthesis of $K_2SeO_4 \cdot 2HIO_3$: 0.2152 g KIO_4 (99.8%, Alfa-Aesar), 0.7 mL H_2SeO_4 (40%, Alfa-Aesar) and 0.2 mL of distilled water were loaded into a 23 mL autoclave and heated at 200°C for 4 days. After cooled down to temperature at rate of 9°C/h, the product was washed with water and methanol and then dried. Colorless crystals of the title compounds were collected with yield of 36% based on iodate; Crystallographic study: A single crystal of $K_2SeO_4 \cdot 2HIO_3$ with dimension of 0.055 mm x 0.020 mm x 0.012 mm was selected and mounted on a quartz fiber with epoxy and aligned on a Bruker SMART APEX CCD X-ray diffractometer with a digital camera. A total of 1800 frames were collected with an exposure time per frame of 60 s for the title compound; Crystallographic data: (193 K; Mo $K\alpha$, $\lambda = 0.71073 \text{ \AA}$) monoclinic, space group $C2/c$, $a = 20.2713(13)$, $b = 4.8809(3)$, $c = 14.0473(9) \text{ \AA}$, $\beta =$

- 132.807(1)°, $V = 1019.67(11) \text{ \AA}^3$, $Z = 4$, $R(F) = 2.17\%$ for 74 parameters with 1262 reflections with $I > 2\sigma(I)$.
8. (a) Burns, P. C.; Hawthorne, F. C. *Can. Mineral.* **1993**, *31*, 313. (b) Cooper, M. A.; Hawthorne, F. C.; Roberts, A. C.; Grice, J. D.; Stirling, J. A. R.; Moffatt, E. A. *Am. Mineral.* **1998**, *83*, 390.
9. Levason, W. *Coord. Chem. Rev.* **1997**, *161*, 33.
10. (a) Pracht, G.; Lange, N.; Lutz, H. D. *Thermochim. Acta* **1997**, *293*, 13. (b) Lutz, H. D.; Alici, E.; Kellersohn, T. H. *J. Raman Spectrosc.* **1990**, *21*, 387. (c) Schellenschlager, V.; Pracht, G.; Lutz, H. D. *J. Raman Spectrosc.* **2001**, *32*, 373. (d) Lutz, H. D.; Suchanek, E. *Spectrochim. Acta* **2000**, *A56*, 2707. (e) Pracht, G.; Nagel, R.; Suchanek, E.; Lange, N.; Lutz, H. D. *Z. Anorg. Allg. Chem.* **1998**, *624*, 1355. (f) Kellersohn, T. H.; Alici, E.; Eber, D.; Lutz, H. D. *Z. Kristallogr.* **1993**, *203*, 225.
11. Krivovichev, S. V.; Tananaev, I. G.; Kahlenberg, V.; Myasoedov, B. F. *Radiochemistry* **2006**, *48*, 217.

CHAPTER 7

**CRITICAL ROLE OF WATER CONTENT IN THE FORMATION AND
REACTIVITY OF URANIUM AND NEPTUNIUM IODATES UNDER
HYDROTHERMAL CONDITIONS: IMPLICATIONS FOR THE OXIDATIVE
DISSOLUTION OF SPENT NUCLEAR FUEL**

ABSTRACT

The reactions of $^{237}\text{NpO}_2$ with excess iodate under acidic hydrothermal conditions result in the isolation of the neptunium(IV), neptunium(V), and neptunium(VI) iodates, $\text{Np}(\text{IO}_3)_4$, $\text{Np}(\text{IO}_3)_4 \cdot n\text{H}_2\text{O} \cdot n\text{HIO}_3$, $\text{NpO}_2(\text{IO}_3)$, $\text{NpO}_2(\text{IO}_3)_2(\text{H}_2\text{O})$, and $\text{NpO}_2(\text{IO}_3)_2 \cdot \text{H}_2\text{O}$, depending on both the pH and the amount of water present in the reactions. Reactions with less water and lower pH favor reduced products. UO_2 reacts with iodate under these conditions to yield uranium(VI) iodates solely. The structures of anhydrous $\text{Np}(\text{IO}_3)_4$ is reported and consists of one-dimensional chains of dodecahedral Np(IV) cations bridged by iodate anions. The structure of $\text{Np}(\text{IO}_3)_4 \cdot n\text{H}_2\text{O} \cdot n\text{HIO}_3$ is constructed from NpO_9 tricapped-trigonal prisms that are bridged by iodate into a polar three-dimensional framework structure. Second-harmonic-generation measurements on a polycrystalline sample of the Th analogue of $\text{Np}(\text{IO}_3)_4 \cdot n\text{H}_2\text{O} \cdot n\text{HIO}_3$ reveal a response of approximately

12× that of α -SiO₂. Single-crystal magnetic susceptibility measurements of Np(IO₃)₄ show magnetically isolated Np(IV) ions.

INTRODUCTION

Under the oxidizing conditions present in the groundwater taken from wells near Yucca Mountain, introduced iodine should occur in the form of both iodide, I^- , and iodate, IO_3^- .¹ Although I^- is not expected to form strong complexes with actinide ions in aqueous media,² IO_3^- forms stable, inner-sphere complexes with actinides.³ The remarkable insolubility of actinide iodates has been used for decades to precipitate actinides selectively from fission products and other elements.⁴ The initial forms of actinides in spent nuclear fuel (SNF) are primarily reduced, e.g., UO_2 , NpO_2 , and PuO_2 . Owing to its high vapor pressure, iodine is expected to be concentrated near the surface and in grain boundaries in SNF where it could react with dissolved oxygen in water to form iodate.⁵ Therefore, the products of the reactions of tetravalent actinides with iodate might play an important role in the potential release of several key long-lived radionuclides (e.g., ^{129}I , $t_{1/2} = 1 \times 10^7$ y (y = years); ^{238}U , $t_{1/2} = 4.46 \times 10^9$ y; ^{237}Np , $t_{1/2} = 2.14 \times 10^6$ y) into the environment in the event of aged SNF contacting groundwater. During the lifetime of stored SNF, it is possible that minute cracks and pores will form in the casings. This scenario will significantly limit the amount of groundwater interacting with the nuclear waste. Herein, we show that the chemistry that occurs under hydrothermal conditions where a limited amount of water is present can be different from what is predicted based on homogeneous solution redox potentials.⁶ The information in this chapter has been published as a full paper in *Journal of Inorganic Chemistry*.⁷

EXPERIMENTAL

Syntheses. $\text{Th}(\text{NO}_3)_4 \cdot x\text{H}_2\text{O}$ (99%, Alfa Aesar), UO_2 (99.8%, Alfa Aesar, depleted), $^{237}\text{NpO}_2$ (99.9%, Oak Ridge, $t_{1/2} = 2.14 \times 10^6$ y), and HfO_3 (99.5%, Alfa Aesar) were used as received. Distilled and Millipore-filtered water with a resistance of 18.2 $\text{M}\Omega \cdot \text{cm}$ was used in all reactions. Reactions were run in Parr 4749 autoclaves with custom-made 10 mL poly(tetrafluoroethylene) liners. All reactions were conducted with 10 mg of AnO_2 (An = U, Np) and a 10-fold molar amount of iodic acid unless otherwise noted. For the Th reactions, $\text{Th}(\text{NO}_3)_4 \cdot x\text{H}_2\text{O}$ was used as the starting material. Sealed reaction vessels were placed in box furnaces that had been preheated to 200 °C. The reactions occurred under an air atmosphere. Cooling was accomplished by turning the furnaces off. All solid products reported in the reaction schemes were isolated as single crystals and their structures determined using single-crystal X-ray diffraction to confirm their identity.

All studies were conducted in a laboratory dedicated to studies on transuranium elements. This laboratory is located in a nuclear science facility and is equipped with HEPA-filtered hoods and gloveboxes that are ported directly into the hoods. A series of counters continually monitor radiation levels in the laboratory. The laboratory is licensed by the State of Alabama (a NRC-compliant state) and Auburn University's Radiation Safety Office. All experiments were carried out with approved safety operating procedures. All free-flowing solids are manipulated in the gloveboxes, and solid products are only examined when coated with either water or Krytox oil and water.

As a cautionary note, $\text{Np}(\text{IO}_3)_4$ is pleochroic owing to its low-dimensional structure. Different crystal growth conditions lead to changes in crystal morphology, agglomeration of crystallites, and different product coloration, depending on the angle

with which the crystallites are viewed. For $\text{Np}(\text{IO}_3)_4$, gray to green to black transitions can be observed by rotating single crystals and clusters of crystals. Crystals of $\text{Np}(\text{IO}_3)_4 \cdot n\text{H}_2\text{O} \cdot n\text{HIO}_3$ have a very pale yellow coloration. Crystals of $\text{Th}(\text{IO}_3)_4 \cdot n\text{H}_2\text{O} \cdot n\text{HIO}_3$ are colorless.

Crystallographic Studies. Single crystals of $\text{Np}(\text{IO}_3)_4$ and $\text{Np}(\text{IO}_3)_4 \cdot n\text{H}_2\text{O} \cdot n\text{HIO}_3$ were optically aligned on a Bruker SMART APEX CCD X-ray diffractometer. For each crystal, intensity measurements were performed using graphite-monochromated Mo $K\alpha$ radiation from a sealed tube and a monocapillary collimator. SMART was used for preliminary determination of the cell constants and data collection control. The intensities of the reflections of a sphere were collected by a combination of three sets of exposures (frames). Each set had a different ϕ angle for the crystal, and each exposure covered a range of 0.3° in ω . A total of 1800 frames were collected.

The determination of integrated intensities and global cell refinement was performed with the Bruker *SAINT* (v 6.02) software package using a narrow-frame integration algorithm. Numerical and semiempirical absorption corrections were applied to the data.⁸ The program suite *SHELXTL* (v 5.1) was used for space group determination, structure solution, and refinement.⁹ The final refinement included anisotropic displacement parameters for all atoms. Some crystallographic details are listed in Table 7.1 for $\text{Np}(\text{IO}_3)_4$ and $\text{Np}(\text{IO}_3)_4 \cdot n\text{H}_2\text{O} \cdot n\text{HIO}_3$; additional details can be found in Table 7.2 and Table 7.3.

Magnetic Susceptibility Measurements. Magnetism data for $\text{Np}(\text{IO}_3)_4$ were measured with a Quantum Design MPMS 7 T magnetometer/susceptometer between 2 and 300 K and in applied fields of up to 7 T. Direct-current temperature-dependent

susceptibility measurements were made under zero-field-cooled conditions with an applied field of 0.1 T. Susceptibility values were corrected for the sample diamagnetic contribution according to Pascal's constants,¹⁰ as well as for the sample holder diamagnetism. Two different single-crystal samples (0.76 and 0.44 mg) were used for the susceptibility measurement. The data shown here are from the larger sample, which gave results identical with those of the smaller sample. The sample was cooled down at zero field, and the magnetic moment was measured at fixed field. The Curie constant was obtained either from the Curie-Weiss fitting or from the slope of $(\chi - \chi_0)^{-1}$ vs temperature, which gave similar results.

Nonlinear Optical Measurements. Powder second-harmonic-generation (SHG) measurements were performed on a Kurtz-Perry nonlinear optical system,¹¹ as modified by Porter and co-workers,¹² and updated here to include laser-pulse energy normalization. A Q-switched Nd:YAG laser (Continuum Surelite I-10), operated at 10 Hz, provided the 1064 nm light used for all measurements. The SHG intensity was recorded from $\text{Th}(\text{IO}_3)_4 \cdot n\text{H}_2\text{O} \cdot n\text{HIO}_3$ and from fine-ground α -quartz. These powders were placed in separate glass tubes of the same dimensions. No index of refraction matching fluid was used in these experiments. The SHG light at 532 nm was collected in reflection, selected by a narrow band-pass interference filter (Pomfret), and detected by a photomultiplier tube (RCA 1P28). A near-normal incidence beam splitter reflected a small fraction of the laser beam onto a pyroelectric detector (Molelectron J3-05) that was used as a laser-pulse energy monitor. A digital storage oscilloscope (Tektronix TDS 640A) signal averaged and recorded both the SHG and incident laser-energy signals. The average laser power was measured separately with a calibrated Scientech volume-absorber calorimeter. The

observed SHG intensity per unit laser intensity, $I^{2\omega}$, was obtained by dividing the SHG signal by the laser-energy signal. Replicate measurements determined the value of interest for the sample compound, $I^{2\omega}(s)$, and for α -quartz, $I^{2\omega}(q)$. The ratio of these values, $I^{2\omega}(s)/I^{2\omega}(q)$, was found to be 12 at an incident laser intensity of 6.7 MW/cm².

RESULTS AND DISCUSSION

Syntheses. When $^{237}\text{NpO}_2$ is reacted with excess iodate under acidic mild hydrothermal conditions, neptunium(IV), neptunium(V), and neptunium(VI) iodates are isolated as shown in Scheme 7.1.

Scheme 7.1

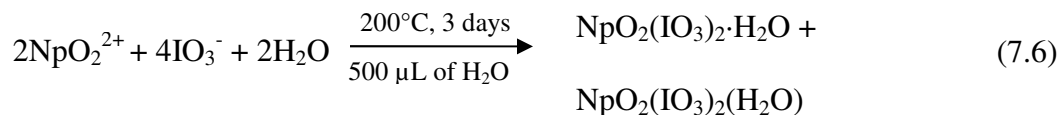
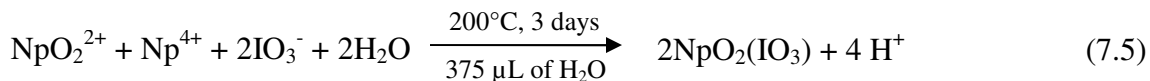
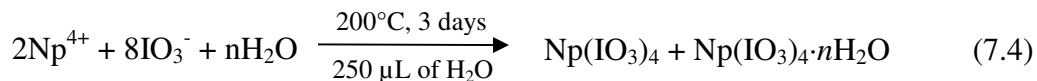
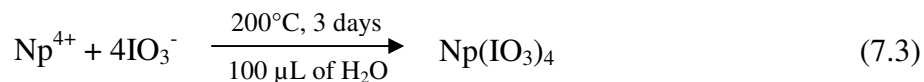
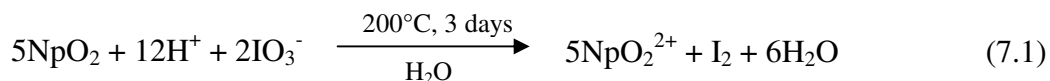


Table 7.1. Crystallographic Data for $\text{Np}(\text{IO}_3)_4$ and $\text{Np}(\text{IO}_3)_4 \cdot n\text{H}_2\text{O} \cdot n\text{HIO}_3$.

Compound	$\text{Np}(\text{IO}_3)_4$	$\text{Np}(\text{IO}_3)_4 \cdot n\text{H}_2\text{O} \cdot n\text{HIO}_3$
Formula Mass	936.60	956.41
Crystal System	Tetragonal	Rhombohedral
Space group	$P4_2/n$ (No. 86)	$R3c$ (No. 161)
a (Å)	9.8790(5)	21.868(1)
c (Å)	5.3063(4)	12.9705(8)
V (Å ³)	517.87(5)	5371.4(5)
Z	2	18
T (K)	-80	-80
λ (Å)	0.71073	0.71073
ρ_{calcd} (g cm ⁻³)	6.006	5.322
$\mu(\text{Mo } K\alpha)$ (cm ⁻¹)	220.17	191.93
$R(F)$ for $F_o^2 > 2\sigma(F_o^2)$	0.0250	0.0403
$R_w(F_o^2)^b$	0.0654	0.0880

$$^a R(F) = \frac{\sum ||F_o| - |F_c||}{\sum |F_o|}. \quad ^b R_w(F_o^2) = \left[\frac{\sum [w(F_o^2 - F_c^2)^2]}{\sum wF_o^4} \right]^{1/2}.$$

Table 7.2. Atomic Coordinates and Equivalent Isotropic Displacement Parameters for $\text{Np}(\text{IO}_3)_4$.

Atom	x	y	z	$U_{\text{eq}} (\text{\AA}^2)^a$
Np(1)	-1/4	3/4	1/4	0.0069(2)
I(1)	0.02735(4)	0.75159(4)	-0.21763(8)	0.0070(2)
O(1)	0.0560(4)	0.8294(4)	0.0496(8)	0.0098(8)
O(2)	0.1604(5)	0.8720(5)	-0.2510(9)	0.0132(9)
O(3)	-0.0944(4)	0.8223(4)	0.4411(8)	0.0112(8)

^a U_{eq} is defined as one-third of the trace of the orthogonalized \mathbf{U}_{ij} tensor.

Table 7.3. Atomic Coordinates and Equivalent Isotropic Displacement Parameters for $\text{Np}(\text{IO}_3)_4 \cdot n\text{H}_2\text{O} \cdot n\text{HIO}_3$.

Atom	<i>x</i>	<i>y</i>	<i>z</i>	$U_{\text{eq}} (\text{\AA}^2)^a$
Np(1)	0.46873(3)	0.29993(3)	0.07189(4)	0.01100(13)
I(1)	0.40628(5)	0.21498(5)	-0.18841(7)	0.0153(2)
I(2)	0.62932(5)	0.47685(5)	0.12928(8)	0.0190(2)
I(3)	0.30522(5)	0.30142(5)	-0.05064(7)	0.01257(19)
I(4)	0.49551(5)	0.45279(5)	-0.11549(7)	0.01204(19)
I(5)	0.6667(8)	0.3333(8)	0.0463(13)	0.014(6)
O(1)	0.3313(7)	0.1316(7)	-0.1544(12)	0.041(4)
O(2)	0.4555(11)	0.2302(11)	-0.0683(10)	0.070(6)
O(3)	0.4575(6)	0.1813(6)	-0.2513(9)	0.020(2)
O(4)	0.6470(7)	0.5043(6)	0.2604(9)	0.026(3)
O(5)	0.7087(6)	0.4743(7)	0.1031(9)	0.026(3)
O(6)	0.5717(6)	0.3849(6)	0.1544(9)	0.025(3)
O(7)	0.3515(6)	0.3963(6)	-0.0720(9)	0.026(3)
O(8)	0.2788(5)	0.2717(6)	-0.1823(8)	0.019(2)
O(9)	0.3823(5)	0.2908(5)	-0.0513(7)	0.0093(19)
O(10)	0.4880(6)	0.5227(6)	-0.0497(8)	0.017(2)
O(11)	0.5859(6)	0.5025(6)	-0.1530(10)	0.027(3)
O(12)	0.5086(6)	0.4135(6)	-0.0001(9)	0.022(2)
O(13)	1.5867(15)	0.3457(15)	-0.0394(17)	0.104(9)

^a U_{eq} is defined as one-third of the trace of the orthogonalized \mathbf{U}_{ij} tensor.

Table 7.4. Selected Bond Distances (Å) and Angles (°) for Np(IO₃)₄.

Distances (Å)			
Np(1)–O(1) X 4	2.329(4)	I(1)–O(1)	1.811(4)
Np(1)–O(3) X 4	2.358(4)	I(1)–O(2)	1.782(5)
		I(1)–O(3)	1.827(4)
Angles (°)			
O(1)–Np(1)–O(1)	102.04(9)	O(1)–Np(1)–O(3)	71.25(15)
O(1)–Np(1)–O(1)	125.7(2)	O(3)–Np(1)–O(3)	118.90(13)
O(1)–Np(1)–O(1)	102.04(9)	O(3)–Np(1)–O(3)	91.9(2)
O(1)–Np(1)–O(3)	163.00(16)	O(1)–I(1)–O(2)	97.4(2)
O(1)–Np(1)–O(3)	69.73(14)	O(1)–I(1)–O(3)	92.7(2)
O(1)–Np(1)–O(3)	73.24(14)	O(2)–I(1)–O(3)	99.6(2)

Table 7.5. Selected Bond Distances (Å) and Angles (°) for Np(IO₃)₄·nH₂O·nHIO₃.

Distances (Å)			
Np(1)–O(2)	2.296(13)	I(1)–O(3)	1.812(13)
Np(1)–O(3)	2.337(11)	I(2)–O(4)	1.781(12)
Np(1)–O(5)	2.358(11)	I(2)–O(5)	1.796(12)
Np(1)–O(6)	2.342(11)	I(2)–O(6)	1.790(12)
Np(1)–O(8)	2.423(10)	I(3)–O(7)	1.817(11)
Np(1)–O(9)	2.406(9)	I(3)–O(8)	1.816(10)
Np(1)–O(10)	2.391(10)	I(3)–O(9)	1.813(9)
Np(1)–O(12)	2.374(12)	I(4)–O(10)	1.827(10)
Np(1)–O(13)	2.68(2)	I(4)–O(11)	1.782(11)
I(1)–O(1)	1.794(11)	I(4)–O(12)	1.818(11)
I(1)–O(2)	1.827(11)	I(5)–O(13) X 3	2.20(3)

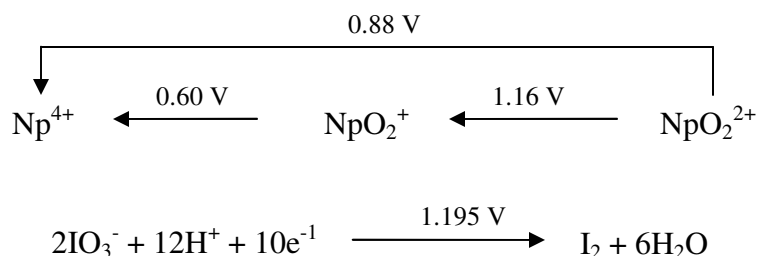
Angles (°)			
O(2)–Np(1)–O(3)	131.7(5)	O(8)–Np(1)–O(9)	70.9(3)
O(2)–Np(1)–O(5)	70.4(4)	O(8)–Np(1)–O(10)	79.7(4)
O(2)–Np(1)–O(6)	129.8(6)	O(8)–Np(1)–O(12)	75.3(4)
O(2)–Np(1)–O(8)	133.8(5)	O(8)–Np(1)–O(13)	141.7(6)
O(2)–Np(1)–O(9)	65.5(4)	O(9)–Np(1)–O(10)	77.9(3)
O(2)–Np(1)–O(10)	77.0(6)	O(9)–Np(1)–O(12)	71.8(4)
O(2)–Np(1)–O(12)	104.0(6)	O(9)–Np(1)–O(13)	104.1(6)
O(2)–Np(1)–O(13)	66.4(8)	O(10)–Np(1)–O(12)	145.6(4)
O(3)–Np(1)–O(5)	74.0(4)	O(10)–Np(1)–O(13)	137.6(6)
O(3)–Np(1)–O(6)	71.4(4)	O(12)–Np(1)–O(13)	67.4(6)

O(3)–Np(1)–O(8)	69.6(4)		
O(3)–Np(1)–O(9)	130.0(4)	O(1)–I(1)–O(2)	97.5(9)
O(3)–Np(1)–O(10)	66.0(4)	O(1)–I(1)–O(3)	97.7(6)
O(3)–Np(1)–O(12)	124.1(4)	O(2)–I(1)–O(3)	91.7(6)
O(3)–Np(1)–O(13)	126.0(7)	O(4)–I(2)–O(5)	98.1(5)
O(5)–Np(1)–O(6)	79.2(4)	O(4)–I(2)–O(6)	96.7(5)
O(5)–Np(1)–O(8)	143.2(4)	O(5)–I(2)–O(6)	98.5(5)
O(5)–Np(1)–O(9)	134.1(4)	O(7)–I(3)–O(8)	99.3(5)
O(5)–Np(1)–O(10)	80.9(4)	O(7)–I(3)–O(9)	97.0(5)
O(5)–Np(1)–O(12)	132.4(4)	O(8)–I(3)–O(9)	95.7(4)
O(5)–Np(1)–O(13)	67.5(7)	O(10)–I(4)–O(11)	98.9(5)
O(6)–Np(1)–O(8)	93.9(4)	O(10)–I(4)–O(12)	96.4(5)
O(6)–Np(1)–O(9)	104.7(4)	O(11)–I(4)–O(12)	97.1(6)
O(6)–Np(1)–O(10)	136.5(4)	O(13)–I(5)–O(13)	96.7(9)
O(6)–Np(1)–O(12)	69.2(4)		
O(6)–Np(1)–O(13)	65.5 (6)		

Reaction 7.1 describes the direct two-electron reduction of Np^{4+} to NpO_2^{2+} by iodate acidic dissolution of NpO_2 in the presence of oxygen typically yields Np(V) in the form of NpO_2^+ in solution (e.g., in 1 M HCl). Reaction 7.1 is governed by the strong oxidizing potential of iodate under acidic conditions that is sufficient to directly oxidize Np^{4+} to NpO_2^{2+} .^{6,13} The formal potentials for these reactions are given below in Scheme 7.2.

It is important to note that these E° values are given at 25 °C and 1 atm. Our reactions are occurring at 200 °C and approximately 17 atm (if H_2O exhibits the vapor pressure of pure water), and therefore, these potentials can only be used for guidance. These reactions should be thought of as taking place in steam under autogenously generated pressure. There is approximately 170 μL of liquid water present at 200 °C in a reaction that starts with 250 μL of water. In contrast, there will only be 20 μL of liquid water present at 200 °C in a reaction that begins with 100 μL of water. When the reactions occur with only a limited amount of liquid water present, as demonstrated in reactions 7.2 and 7.7, reduction of NpO_2^{2+} back to Np^{4+} takes place.

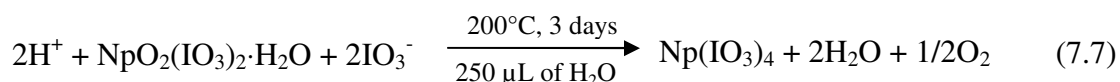
Scheme 7.2



When sufficient amounts of water are present to approximate a solution (500 μL), as in reaction 7.6, the predicted reaction between NpO_2 and iodate occurs, via reaction 7.1, and $\text{NpO}_2(\text{IO}_3)_2(\text{H}_2\text{O})$ and $\text{NpO}_2(\text{IO}_3)_2 \cdot \text{H}_2\text{O}$ form.¹⁴ Reaction 7.5 is the most

interesting of this series and represents conditions under which comproportionation of Np^{4+} and NpO_2^{2+} occurs to yield 2 equiv of NpO_2^+ . It is important to note that, even when the Np(VI) products are isolated as solids, they can be slowly converted to neptunium(IV) iodates by the application of appropriate hydrothermal conditions (250 μL of water), as shown in reaction 7.7. If the amount of water is increased to 500 μL , reduction does not take place.

Reactions 7.2-7.4 are not solely driven by the solution-phase thermodynamics of the oxidation of Np^{4+} by iodate but also by the reduction of Np(VI) to yield Np(IV) and the subsequent crystallization of the neptunium(IV) iodate products, $\text{Np(IO}_3)_4$ and $\text{Np(IO}_3)_4 \cdot n\text{H}_2\text{O} \cdot n\text{HIO}_3$. Figure 7.1 depicts the results of reaction 7.7 and shows crystals of $\text{Np(IO}_3)_4$ and $\text{Np(IO}_3)_4 \cdot n\text{H}_2\text{O} \cdot n\text{HIO}_3$ that have grown directly off the surface of the delaminating crystals of $\text{NpO}_2(\text{IO}_3)_2(\text{H}_2\text{O})$. This result supports the hypothesis that the reaction is a solid-to-solid transformation that is probably surface-mediated. The same may be true for reactions 7.2-7.5. In the presence of a large external radiation source, radiolysis products of water (e.g., H , HO_2 , and H_2O_2) might play a role in the reduction of Np(VI) to Np(IV) .¹⁵



In previous work, it was shown that the stock solution of Np^{4+} reacts with excess metaperiodate, IO_4^- , to yield products that contain the actinides in the 6+ oxidation state (e.g., $\text{NpO}_2(\text{IO}_3)_2(\text{H}_2\text{O})$ and $\text{NpO}_2(\text{IO}_3)_2 \cdot \text{H}_2\text{O}$).¹⁴ Metaperiodate contains I(VII) and is a much stronger oxidant than iodate (1.601 vs 1.195 V). Clearly, the reactions reported

herein of NpO_2 with iodate under hydrothermal conditions with limited amounts of water are dramatically different from those of aqueous actinide ions with very strong oxidants. Although these reactions are occurring at a much lower pH than natural groundwaters, this work calls into question the use of standard solution reactivity data on actinide ions to predict the behavior of snf that will start off as a reduced solid. The thermodynamic data for actinide complexation are already being reevaluated in light of the substantial changes that occur at elevated temperatures.¹⁶

The least complex of these reactions is that of UO_2 with iodate. The process proceeds in accordance with Scheme 7.3, yielding only U(VI) iodates, such as $\text{UO}_2(\text{IO}_3)_2$ and $\text{UO}_2(\text{IO}_3)_2(\text{H}_2\text{O})$.¹⁷ Given the ease of oxidation of U^{4+} to UO_2^{2+} , this result is not surprising ($E^\circ = -0.327 \text{ V}$).⁶

Scheme 7.3



Crystal Structure of $\text{Np}(\text{IO}_3)_4$. In addition to the new actinide reactivity patterns, these syntheses provide access to single crystals of $\text{Np}(\text{IO}_3)_4$ and $\text{Np}(\text{IO}_3)_4 \cdot n\text{H}_2\text{O} \cdot n\text{HIO}_3$. The crystal structure of $\text{Np}(\text{IO}_3)_4$ consists of eight-coordinate, trigonal dodecahedral $\text{Np}(\text{IV})$ centers (D_{2d}) bridged by iodate to form one-dimensional chains as shown in Figure 7.2A. These compounds are isostructural with $\text{Ce}(\text{IO}_3)_4$.¹⁸ The Np centers reside on -4 sites, yielding two independent Np-O bond distances of 2.329(4) Å ($\times 4$) and 2.358(4) Å ($\times 4$). The I-O bond distances of 1.782(5), 1.811(4), and 1.827(4)

Å are normal.¹⁹ The terminal I-O bond distance is slightly shorter than those bridging to the Np(IV) ions. These chains pack together in a pinwheel fashion (Figure 7.2B). Although the structures of neptunium(IV) iodates are expected to be similar, if not identical, with those of thorium(IV), we have yet to isolate a thorium analogue of Np(IO₃)₄, although the Ce(IV) version has been prepared, underscoring some of the problems of using early, less-radioactive actinides like Th(IV) and U(IV) as surrogates for Np(IV) and Pu(IV).²⁰ This was also observed in the An(VI) iodates, where the U(VI) compounds are not isostructural.^{14,17}

Crystal Structure of Np(IO₃)₄·nH₂O·nHIO₃. The structure of Np(IO₃)₄·nH₂O·nHIO₃ is similar to that of K₃Am₃(IO₃)₁₂·HIO₃.²² This structure type consists of a three-dimensional network constructed from nine-coordinate tricapped trigonal prismatic An(III) or An(IV) centers bridged by iodate anions to create a channel structure, as shown in Figure 7.3. The channels are partially filled by iodate anions or water molecules. Although the structure of K₃Am₃(IO₃)₁₂·HIO₃ was reported as being stoichiometric, refinement on the occupancy of the iodate units in the channels reveals that they are only partially occupied. Furthermore, there are three very long I-O bonds of ca. 1.9 Å to this partially occupied iodine atom. We have prepared the Ce analogue of K₃Am₃(IO₃)₁₂·HIO₃, and it shows partial occupancy of the iodine atoms in the channels, disorder and partial occupancy of the K⁺ sites, and mixed valency (Ce(III)/Ce(IV)). Clearly, something unusual is taking place in this series of compounds associated with iodate groups in the channels.

K₃Am₃(IO₃)₁₂·HIO₃ is reported as crystallizing in the polar rhombohedral space group *R3c*. Confirmation of the polarity of the space group via some external

measurement, e.g., second-harmonic generation, is quite challenging given the extreme radioactivity of ^{241}Am . Although ^{237}Np is substantially less radioactive than ^{241}Am , it nevertheless poses serious handling challenges. Fortunately, as the result of separate studies, the Th analogue of $\text{Np}(\text{IO}_3)_4 \cdot n\text{H}_2\text{O} \cdot n\text{HIO}_3$ was prepared, and second-harmonic-generation measurements were performed that showed a response of approximately 12 \times that of α -quartz, confirming the acentricity of the structure.

An unusual type of disorder to explain the abnormal bond distances and partial occupancy in this family of compounds is proposed here based on the following data: (1) the ninth capping position (O(13)) around the NpO_9 units appears to be fully occupied. (2) the atom lying at the center of the channels refines best as a partially occupied iodine. (3) the displacement parameters for O(13) are large (all light atoms were refined isotropically in $\text{K}_3\text{Am}_3(\text{IO}_3)_{12} \cdot \text{HIO}_3$). Taken together, a model can be proposed where the channels are occupied either by iodate or only by the capping water molecules. This would create an oxygen position (O(13)) that is an average of the water position(s) and the position(s) of the oxygen atoms from the iodate unit.

The Np-O bond distances range from 2.296(13) to 2.68(2) Å; the longest distance is to the coordinating water molecules in the channels. The four ordered iodate anions that are a part of the three-dimensional network contain regular I-O bond distances that range from 1.781(12) to 1.827(13) Å. All other aspects of the structure are also normal.

Magnetic property of $\text{Np}(\text{IO}_3)_4$. $\text{Np}(\text{IO}_3)_4$ crystallizes as single crystals that can have maximum dimensions as large as several millimeters, making this compound amenable to single-crystal magnetic susceptibility measurements. Magnetic susceptibility data for $\text{Np}(\text{IO}_3)_4$ are shown in Figure 7.4. Data were collected on two different crystals,

yielding μ_{eff} of 2.22 and 2.25 μ_{B} per Np atom for the different crystals. The observed magnetic moment for the Np^{4+} ions in $\text{Np}(\text{IO}_3)_4$ is markedly lower than that calculated for the free ions (3.62 μ_{B}).²¹ This is not a reflection of the covalency of the 5f orbitals, but rather arises from the crystal field effects in $\text{Np}(\text{IO}_3)_4$,²³ as has also been suggested recently for two Np(V) compounds.²⁴ Magnetic fields well outside of the range of a standard 7 T magnet would be needed to achieve full saturation of the magnetic moment.²² The data follow the Curie-Weiss law with $\theta = 0.0(5)$ K, indicating that the Np(IV) ions are magnetically isolated from one another. This observation is consistent with the large Np...Np distance of 5.306(1) Å within the one-dimensional chains.

CONCLUSIONS

These synthetic, structural, and magnetic data provide new avenues for addressing the reactivity, structures, and properties of transuranic compounds. The use of hydrothermal conditions with smaller amounts of water than has typically been employed gives access to pure compounds in the form of single crystals that have not been previously available from standard synthetic techniques. In a general sense, the actinide chemistry presented here can be considered as being a part of a larger synthetic methodology wherein redox reactions are used to control the introduction of ions that lead to the slow crystallization of highly insoluble products.²⁵ This gradual introduction of reactants facilitates crystal growth of compounds that normally only form microcrystalline or amorphous powders.

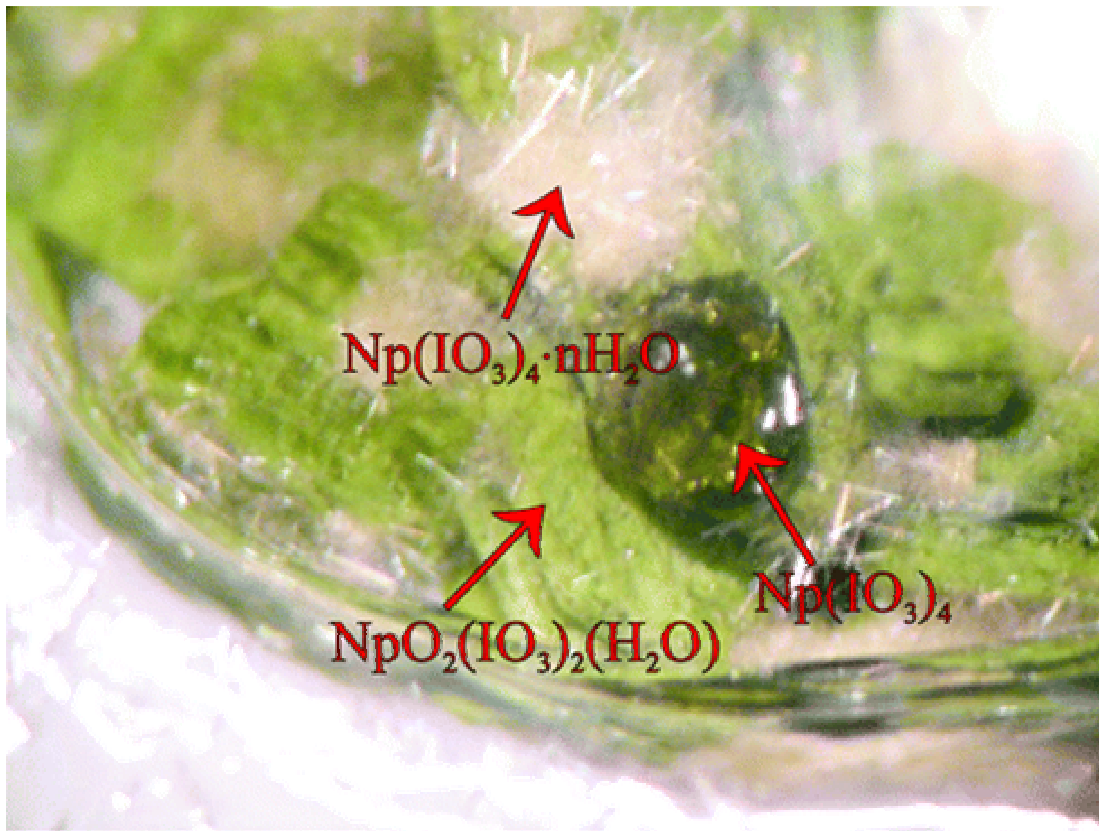


Figure 7.1. Photograph showing the hydrothermal reduction of the neptunium(VI) iodate $\text{NpO}_2(\text{IO}_3)_2(\text{H}_2\text{O})$ to the neptunium(IV) iodates $\text{Np}(\text{IO}_3)_4$ and $\text{Np}(\text{IO}_3)_4 \cdot n\text{H}_2\text{O} \cdot n\text{HIO}_3$.

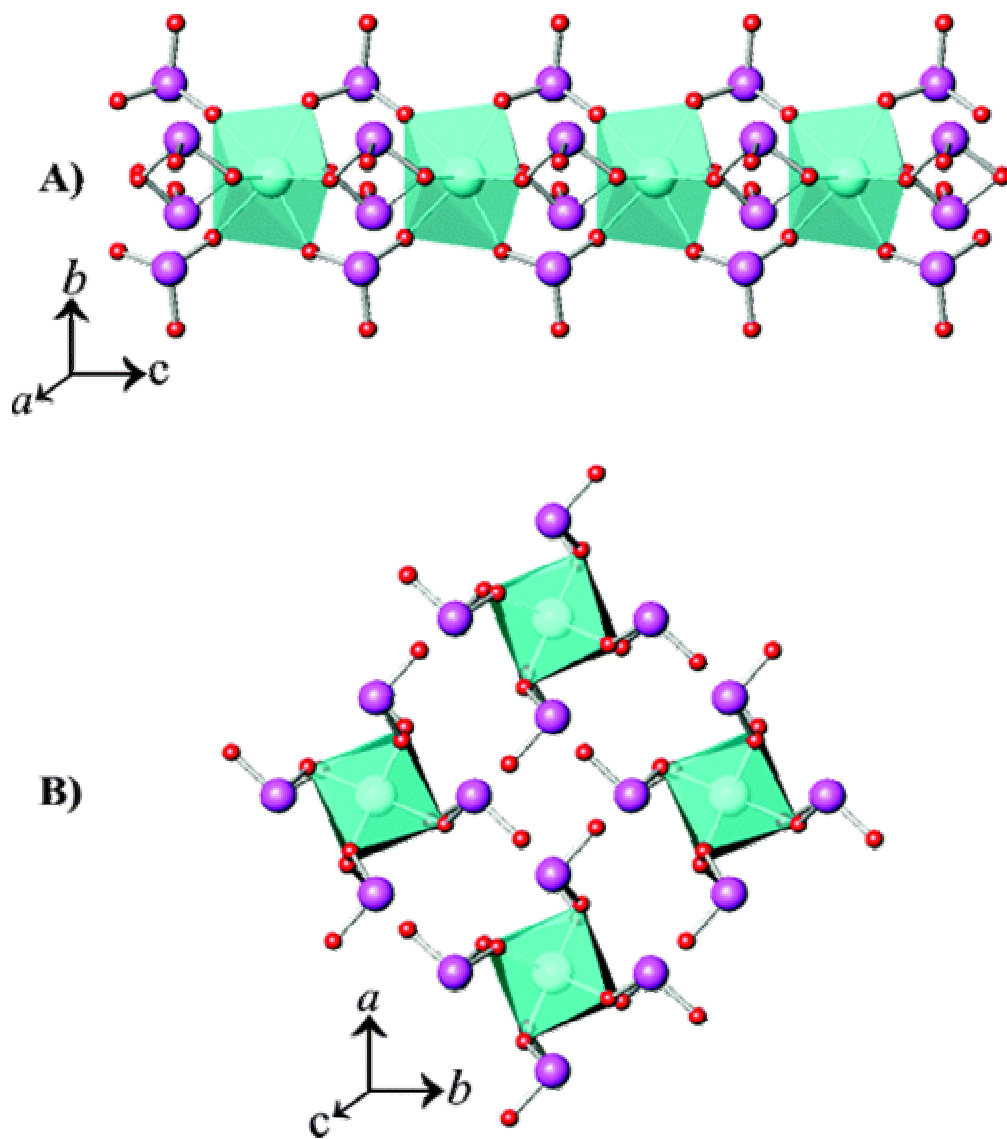


Figure 7.2. (a) View of the one-dimensional chains in $\text{Np}(\text{IO}_3)_4$ consisting of eight-coordinate, dodecahedral $\text{Np}(\text{IV})$ centers bridged by iodate. (b) Depiction of the pinwheel packing of the $\text{Np}(\text{IO}_3)_4$ chains.

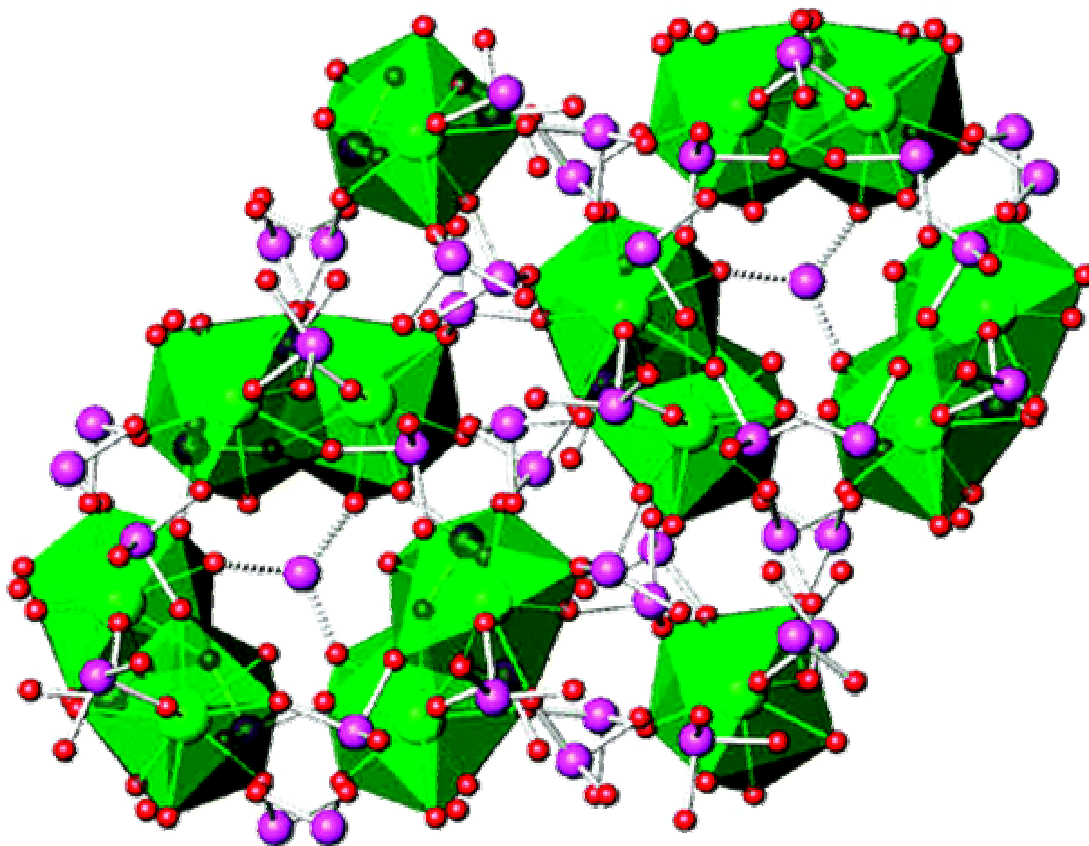


Figure 7.3. Depiction of the structure of $\text{Np}(\text{IO}_3)_4 \cdot n\text{H}_2\text{O} \cdot n\text{HIO}_3$. This structure consists of a three-dimensional network constructed from nine-coordinate tricapped trigonal prismatic $\text{Np}(\text{IV})$ that are bridged by iodate anions to create the channels that extend along the c axis. The channels are partially filled by iodate anions or water molecules.

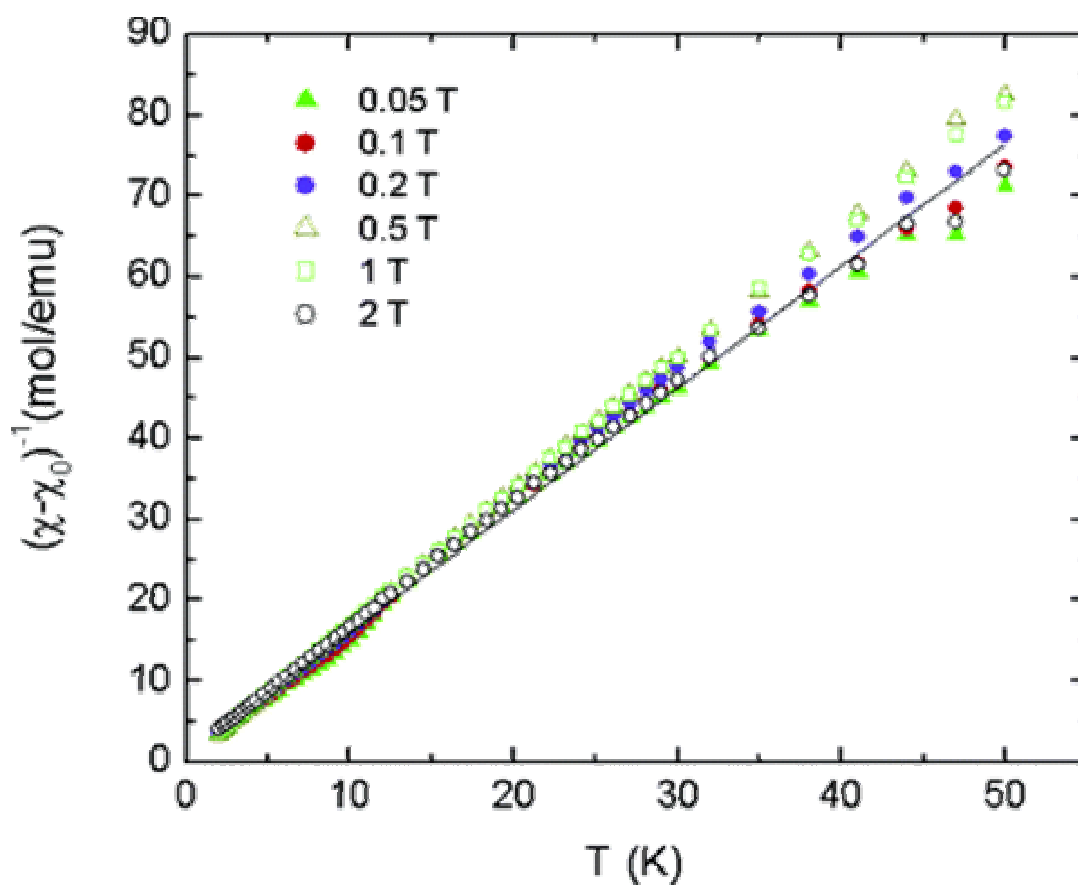


Figure 7.4. Temperature dependence of the inverse magnetic susceptibility of a $\text{Np}(\text{IO}_3)_4$ single crystal. The Curie-Weiss fitting curve is shown as a solid line.

REFERENCES

1. (a) Bruchertseifer, H.; Cripps, R.; Guentay, S.; Jaeckel, B. *Anal. Bioanal. Chem.* **2003**, *375*, 1107. (b) Huang, Z.; Ito, K.; Timerbaev, A. R.; Hirokawa, T. *Anal. Bioanal. Chem.* **2004**, *378*, 1836. (c) Bard, A. J.; Parsons, R.; Jordan, J. *Standard Potentials in Aqueous Solution*; Dekker: New York, 1985. (d) Charlot, G. *Oxidation-Reduction Potentials*; Pergamon: London, 1958. (e) Pourbaix, M. *Atlas d'equilibres electrochimiques à 25 °C*; Gautier Villars: Paris, 1963.
2. (a) Crawford, M.-J.; Ellern, A.; Karaghiosoff, K.; Mayer, P. Noth, H.; Suter, M. *Inorg. Chem.* **2004**, *43*, 7120. (b) Berthet, J.-C.; Nierlich, M.; Ephritikhine, M. *Chem. Commun.* **2004**, *7*, 870.
3. (a) Choppin, G. R.; Khalili, F. I.; Rizkalla, E. N. *J. Coord. Chem.* **1992**, *26*, 243. (b) Rao, P. R. V.; Patil, S. K. *Radiochem. Radioanal. Lett.* **1978**, *36*, 169.
4. (a) Seaborg, G. T.; Wahl, A. C. *J. Am. Chem. Soc.* **1948**, *70*, 1128. (b) Cunningham, B. B.; Werner, L. B. *J. Am. Chem. Soc.* **1949**, *71*, 1521. (c) Seaborg, G. T.; Thompson, S. G. U.S. Patent 2,950,168, 1960.
5. Kaholek, M.; Triendl, L. *React. Kinet. Catal. Lett.* **1998**, *63*, 297.
6. (a) Morss, L. R.; Edelstein, N. M.; Fuger, J. *The Chemistry of the Actinide and Transactinide Elements*; Springer: Heidelberg, 2006; Vol. 2, Chapter 6. (b) Katz, J. J.; Seaborg, G. T.; Morss, L. R. *The Chemistry of the Actinide Elements*, 2nd ed.; Chapman and Hall: New York, 1986; Vol. 1, Chapter 6.
7. Bray, T. H.; Ling, J.; Choi, E. S.; Brooks, J. S.; Beitz, J. V.; Sykora, R. E.; Haire, R. G.; Stanbury, D. M.; Albrecht-Shmitt, T. E. *Inorg. Chem.* **2007**, *46*, 3663.

8. Sheldrick, G. M. *SADABS* 2001, Program for Absorption Correction Using SMART CCD Based on the Method of Blessing; Blessing, R. H. *Acta Crystallogr.* **1995**, *A51*, 33.
9. Sheldrick, G. M. *SHELXTL PC*, version 6.12, An Integrated System for Solving, Refining, and Displaying Crystal Structures from Diffraction Data; Siemens Analytical X-ray Instruments, Inc.: Madison, WI, 2001.
10. Mulay, L. N.; Boudreaux, E. A. *Theory and Applications of Molecular Diamagnetism*; Wiley-Interscience: New York, 1976.
11. Kurtz, S. K.; Perry, T. T. *J. Appl. Phys.* **1968**, *39*, 3798.
12. Porter, Y.; Ok, K. M.; Bhuvanesh, N. S. P.; Halasyamani, P. S. *Chem. Mater.* **2001**, *13* 1910.
13. Lide, D. R. *CRC Handbook of Chemistry and Physics*, 71st ed.; CRC Press: Boston, 1990; 8.
14. Bean, A. C.; Scott, B. L.; Albrecht-Schmitt, T. E.; Runde, W. *Inorg. Chem.* **2003**, *42*, 5632.
15. Vladimirova, M. V. *Radiochemistry* **1997**, *39*, 250.
16. Rao, L.; Srinivasan, T. G.; Garnov, A. Y.; Zanonato, P. L.; Di Bernardo, P.; Bismondo, A. *Geochim. Cosmochim. Acta* **2004**, *68*, 4821.
17. (a) Weigel, F.; Engelhardt, L. W. H. *J. Less-Common Met.* **1983**, *91*, 339. (b) Bean, A. C.; Peper, S. M.; Albrecht-Schmitt, T. E. *Chem. Mater.* **2001**, *13*, 1266.
18. (a) Staritsky, E.; Cromer, D. T. *Anal. Chem.* **1956**, *28*, 913. (b) Cromer, T.; Larson, A. C. *Acta Crystallogr.* **1956**, *9*, 1015.

19. (a) Sullens, T. A.; Almond, P. M.; Albrecht-Schmitt, T. E. *Mater. Res. Soc.* **2006**, 893, 283. (b) Gorden, A. E. V.; Shuh, D. K.; Tiedemann, B. E. F.; Wilson, R. E.; Xu, J.; Raymond, K. N. *Chem.-Eur. J.* **2005**, 11, 2842.
20. A historical footnote is worthwhile here: The microscale precipitation of $\text{Pu}(\text{IO}_3)_4$ was used by B. B. Cunningham and L. B. Werner to show, for the first time, that Pu has a stable 4+ oxidation state in 1942 (4b). Since this time, $\text{Pu}(\text{IO}_3)_4$ has been used as a benchmark compound because of its remarkable insolubility in low pH media. The structure, precise elemental analyses, and spectroscopic data for plutonium(IV) iodates have never been reported in the primary literature.
21. Runde, W.; Bean, A. C.; Scott, B. L. *Chem. Commun.* **2003**, 15, 1848.
22. Kittel, C. *Introduction to Solid State Physics*, 6th ed.; Wiley: New York, 1986.
23. (a) Morss, L. R.; Edelstein, N. M.; Fuger, J. *The Chemistry of the Actinide and Transactinide Elements*; Springer: Heidelberg, 2006; Vol. 4, Chapter 20.
24. Forbes, T. Z.; Burns, P. C.; Soderholm, L.; Skanthakumar, S. *Chem. Mater.* **2006**, 18, 1643.
25. See, for example: Grohol, D.; Matan, K.; Cho, J.-H.; Lee, S.-H.; Lynn, J. W.; Nocera, D. G.; Lee, Y. S. *Nat. Mater.* **2005**, 4, 323.

CHAPTER 8

SUMMARY

As a summary of the data in the previous chapters, this chapter was written on the purpose of recalling the highlights in this research.

All of the reported compounds, except $\text{Lu}(\text{IO}_3)_3$, were generated under hydrothermal conditions in the temperatures range from 180 °C and 200 °C. The $\text{Lu}(\text{IO}_3)_3$, as mentioned in Chapter 5, was synthesized by applying supercritical reaction conditions¹ at the temperature of 425 °C. The structures were determined using single crystal X-ray diffraction. The possible elements in the compounds were investigated using EDX. Powder X-ray diffractometer was used to check their purity. Vibrational spectroscopy (IR and Raman), UV-Vis diffuse reflectance spectrum,² second-harmonic generation of light,³ thermal analysis, and magnetic susceptibility were employed in order to characterize these materials. As a summary, some crystallographic, SHG, and physical properties of all reported compounds are listed in Table 8.1.

Chapter 2 introduced the syntheses, structures and properties of five new noble metal iodates – $\text{M}^{\text{I}}\text{Au}(\text{IO}_3)_4$ ($\text{M}^{\text{I}} = \text{Na}, \text{K}, \text{Rb}$), $\text{K}_{2.5}\text{Pd}(\text{IO}_3)_4 \cdot \text{H}_{0.5}\text{IO}_3$ and $\text{Pd}(\text{IO}_3)_2$. As a highlight in the syntheses of the gold iodates, concentrated H_2SeO_4 was selected to dissolve gold metal. Then periodate, which can be reduced slowly into iodate under hydrothermal conditions, was added as the source of iodate to crystallize dissolved gold

cation from selenic acid solution as yellow gold iodate compounds. The synthesis of $\text{K}_{2.5}\text{Pd}(\text{IO}_3)_4 \cdot \text{H}_{0.5}\text{IO}_3$ was much simpler; it could be produced by directly reacting KIO_4 and $\text{Pd}(\text{NO}_3)_2$ under hydrothermal conditions. Within the synthesis of $\text{Pd}(\text{IO}_3)_2$, H_2SeO_4 was used to increase the solubility of $\text{Pd}(\text{NO}_3)_2 \cdot 2\text{H}_2\text{O}$. Attempts of making $\text{Pd}(\text{IO}_3)_2$ by reacting $\text{Pd}(\text{NO}_3)_2 \cdot 2\text{H}_2\text{O}$ directly with iodic acid failed.

$\text{M}^{\text{I}}\text{Au}(\text{IO}_3)_4$ and $\text{K}_{2.5}\text{Pd}(\text{IO}_3)_4 \cdot \text{H}_{0.5}\text{IO}_3$ have zero-dimensional structures. $\text{M}^{\text{I}}\text{Au}(\text{IO}_3)_4$ possesses NCS structures that stem from the asymmetric $[\text{Au}(\text{IO}_3)_4]^-$ anions. Within these anions, four iodates are aligned on one side of the AuO_4 square plane. In the structure of $\text{K}_{2.5}\text{Pd}(\text{IO}_3)_4 \cdot \text{H}_{0.5}\text{IO}_3$, it has similar asymmetric $[\text{Pd}(\text{IO}_3)_4]^{2-}$ anions, but the individual anions are related through an inversion center, resulting in a centrosymmetric (CS) structure. In the structure of $\text{Pd}(\text{IO}_3)_2$, although Pd^{2+} also has a square planar geometry coordinated with four iodates through bridging oxygen atoms, four iodate anions sit on both sides of the $[\text{PdO}_4]$ plane. The $[\text{PdO}_4]$ units are further joined together through two bidentated iodates to form a two-dimensional layer structure.

As a potential NLO material, some correlated physical properties of $\text{KAu}(\text{IO}_3)_4$ were investigated. IR and Raman spectra proved the existence of $[\text{AuO}_4]$ and IO_3^- in this compound. UV-Vis diffuse reflectance spectrum indicated $\text{KAu}(\text{IO}_3)_4$ is transparent at the wavelengths of 1064 and 532 cm^{-1} , which represent the wavelengths of initial laser and induced SHG light, respectively.³ TGA analysis showed it is thermally stable up to 375 °C. The SHG measurement on this material is still in progress.

In Chapter 3, three new palladium selenites and selenate were synthesized under hydrothermal conditions. Like the noble metal cations in these iodate compounds discussed in Chapter 1, Pd^{2+} cations in all of these three selenites and selenate have a

square-planar coordination environment. In the structure of PdSeO₃, adjacent [PdO₄] units join together through corner-sharing to form a chain along the *b* axis. These chains are further linked together by tridentate SeO₃²⁻ anions and form a layer structure in the [*ab*] plane. In the structure of PdSe₂O₅, a one-dimensional chain structure is constructed by connecting neighboring [PdO₄] units through two Se₂O₅²⁻. Na₂Pd(SeO₄)₂ also has a one-dimensional structure; neighboring [PdO₄] units are joined together by bidentate SeO₄²⁻ and form a chain along the *a* axis.

Three new transition metal selenite compounds, Ag₄(Mo₂O₅)(SeO₄)₂(SeO₃), Ag₂(MoO₃)₃SeO₃, and AgNbO(SeO₃)₂, were reported in Chapter 4. In the synthesis of Ag₄(Mo₂O₅)(SeO₄)₂(SeO₃), some selenic acid (H₂SeO₄) was reduced to selenite by water under hydrothermal conditions resulting in the formation of the mixed-valent selenite compound.⁴ Ag₂(MoO₃)₃SeO₃ was generated by reacting AgNO₃, MoO₃, and SeO₂; HF was added into the above system as a mineralizing agent. For the synthesis of AgNbO(SeO₃)₂, pure Nb powder was utilized as the starting material, and a longer period of heating was required for the reaction.

The structure of Ag₄(Mo₂O₅)(SeO₄)₂(SeO₃) consists of *cis*-MoO₂²⁺ molybdenyl units that are bridged to neighboring molybdenyl moieties by selenate anions and by a bridging oxo anion. These dimeric units are joined by selenite anions to yield zigzag one-dimensional chains that extend down the *c*-axis. Individual chains are polar with the C₂ distortion of the Mo(VI) octahedra aligning on one side of each chain. However, the overall structure is centrosymmetric because neighboring chains have opposite alignment of the C₂ distortion. In the structure of Ag₂(MoO₃)₃SeO₃, MoO₆ units are connected to form a molybdenyl ribbon that extends along the *c*-axis. These ribbons are further

connected together through tridentate selenite anions to form two-dimensional layers in the $[bc]$ plane. In contrast to the above two compounds, $\text{AgNbO}(\text{SeO}_3)_2$ crystallizes in a polar one dimensional structure which stems from corner-sharing connection of distorted NbO_6 building blocks along the c axis. NbO_6 polyhedra are further linked by two bidentated SeO_3^{2-} anions to form a more rigid structure. Within these chains, all NbO_6 polyhedra are aligned in the same direction and cause the polarity of these chains; while for two adjacent Nb chains which are built by crystallographically different niobium atoms, they are heading in opposite directions and cancel some of the polarity in this compound.

The TGA data of $\text{Ag}_4(\text{Mo}_2\text{O}_5)(\text{SeO}_4)_2(\text{SeO}_3)$ and $\text{Ag}_2(\text{MoO}_3)_3\text{SeO}_3$ indicated they are thermally stable up to 375 °C and 350 °C, respectively. The thermal decomposition of $\text{Ag}_4(\text{Mo}_2\text{O}_5)(\text{SeO}_4)_2(\text{SeO}_3)$ follows a two-step mechanism, while $\text{Ag}_2(\text{MoO}_3)_3\text{SeO}_3$ shows a one-step weight loss over a broad range from 350 to 550 °C.

In Chapter 5, four new late lanthanide iodates were synthesized and studied. The reaction of Lu^{3+} or Yb^{3+} and H_5IO_6 in aqueous media at 180 °C leads to the formation of $\text{Yb}(\text{IO}_3)_3(\text{H}_2\text{O})$ or $\text{Lu}(\text{IO}_3)_3(\text{H}_2\text{O})$, respectively, while the reaction of Yb metal with H_5IO_6 under similar reaction conditions gives rise to the anhydrous iodate, $\text{Yb}(\text{IO}_3)_3$. Anhydrous $\text{Lu}(\text{IO}_3)_3$ was made under supercritical conditions by reacting Lu^{3+} with HIO_3 and KIO_4 .

The late lanthanide elements in all of the compounds are found in seven-coordinate environments and bridged with monodentate, bidentate, or tridentate iodate anions. Both $\text{Lu}(\text{IO}_3)_3(\text{H}_2\text{O})$ and $\text{Yb}(\text{IO}_3)_3(\text{H}_2\text{O})$ display distinctively different vibrational profiles from their respective anhydrous analogs. Hence, the Raman profile can be used

as a complementary diagnostic tool to discern the different structural motifs of the compounds.

In Chapter 6, the first example of intercalation of iodic acid molecules into an uranyl phase was reported. It is of great importance for the immobilization of ^{129}I which is a key long-lived radionuclide in spent nuclear fuel.⁵ The intercalated uranyl iodate was synthesized by reacting $\text{UO}_2(\text{NO}_3)_2 \cdot 6\text{H}_2\text{O}$ with excess iodic acid (over 30 fold) under mild hydrothermal conditions. In the structure of $\text{UO}_2(\text{IO}_3)_2(\text{H}_2\text{O}) \cdot 2\text{HIO}_3$, it has an identical $\text{UO}_2(\text{IO}_3)_2(\text{H}_2\text{O})$ layered structure to the previously reported structure of $\text{UO}_2(\text{IO}_3)_2(\text{H}_2\text{O})$ in the $[ab]$ plane. Iodic acid molecules are intercalated in to gap between the $\text{UO}_2(\text{IO}_3)_2(\text{H}_2\text{O})$ layers and results in the increase of unit cell value along the c axis. The intercalated iodic acid molecules are stabilized by weak interactions between the iodic acid molecules and iodates anions. The iodic acid molecule intercalated uranyl iodate could also be made by directly reacting $\text{UO}_2(\text{IO}_3)_2(\text{H}_2\text{O})$ with excess iodic acid.

A characteristic I-OH stretch at 1138 cm^{-1} in the IR spectrum of $\text{UO}_2(\text{IO}_3)_2(\text{H}_2\text{O}) \cdot 2\text{HIO}_3$ proved the existence of iodic acid molecules in this compound. A DSC study of $\text{UO}_2(\text{IO}_3)_2(\text{H}_2\text{O}) \cdot 2\text{HIO}_3$ reveals two endotherms at 267 and 559 °C. These features are similar to those found for the parent compound and are ascribed to the loss of water and thermal disproportionation of iodate, respectively. Water loss occurs at a lower temperature for $\text{UO}_2(\text{IO}_3)_2(\text{H}_2\text{O}) \cdot 2\text{HIO}_3$ than for $\text{UO}_2(\text{IO}_3)_2(\text{H}_2\text{O})$. The new feature in the thermogram of $\text{UO}_2(\text{IO}_3)_2(\text{H}_2\text{O}) \cdot 2\text{HIO}_3$ is an exotherm that immediately follows the loss of water at 299 °C. We suggest that this exothermic feature represents the filling of the open-coordination site previously occupied by water by an O atom from an iodic acid molecule in the interlayer space, yielding $\text{UO}_2(\text{IO}_3)_2(\text{HIO}_3) \cdot \text{HIO}_3$.

As reported in the earlier work done by A. C. Bean,⁶ $\text{NpO}_2(\text{IO}_3)_2(\text{H}_2\text{O})$ is isostructural with the corresponding uranyl phase. Therefore, we were thinking of making the iodic acid molecule intercalated neptunium iodate using the same method mentioned above. But beyond our expectation, $\text{Np}(\text{IO}_3)_4$, instead of $\text{NpO}_2(\text{IO}_3)_2(\text{H}_2\text{O}) \cdot 2\text{HIO}_3$ was produced under hydrothermal condition. What is more interesting, by changing the amount of water in the reaction, one may be able to control the oxidation states of Np in the final products. As discussed in Chapter 7, when the reactions occur with only a limited amount of liquid water present (less than 375 μL), NpO_2 will be oxidized to NpO_2^{2+} by iodate and then reduced back to Np^{4+} by water under hydrothermal condition. Np^{4+} will be precipitated by iodate to form $\text{Np}(\text{IO}_3)_4$. When sufficient amounts of water are present to approximate a solution (over 500 μL), NpO_2^{2+} will not be reduced back to Np^{4+} and $\text{NpO}_2(\text{IO}_3)_2(\text{H}_2\text{O})$ and $\text{NpO}_2(\text{IO}_3)_2 \cdot \text{H}_2\text{O}$ will form. The reaction with 375 μL of water is the most interesting of this series and represents conditions under which comproportionation of Np^{4+} and NpO_2^{2+} occurs to yield 2 equiv of NpO_2^+ . $\text{NpO}_2(\text{IO}_3)_2$ was crystallized as the only solid product.

As a conclusion, over 18 new iodate and selenite compounds were synthesized and studied in this work (in fact, more than 35 new compounds were generated during the period of pursuing my Ph.D. degree). To the purpose of making novel non-linear optical (NLO) materials, iodate and selenite anions possessing nonbonding, but stereochemically active lone pair of electrons, were selected as the building blocks to produce new compounds with noncentrosymmetric structures. A broad range of other elements, including transition metals, lanthanides and even actinides, were utilized to synthesize new compounds and new structures. Among them, gold iodates are especially interesting

owing to the highly polarized structures and the difficulties of synthesis. The iodate chemistry of actinides is also of great importance because it is very helpful for the investigation and understanding of the chemistry happening in spent nuclear fuel. The success of intercalating iodic acid molecules into an existing uranyl phase provides a great example of the immobilization of ^{129}I , which is a key long-lived radionuclide in spent nuclear fuel.

Table 8.1. A list of new compounds and some of their properties reported in this dissertation.

Formula	Chapter	Crystal System	Space Group	CS or NCS ^a	Dimension	Color/Apperance
NaAu(IO ₃) ₄	2	Triclinic	<i>P1</i>	NCS	0	Yellow/Block
KAu(IO ₃) ₄	2	Triclinic	<i>P1</i>	NCS	0	Yellow/Block
RbAu(IO ₃) ₄	2	Monoclinic	<i>C2</i>	NCS	0	Yellow/Block
K _{2.5} Pd(IO ₃) ₄ ·H _{0.5} IO ₃	2	Monoclinic	<i>C2/m</i>	CS	0	Yellow/Flake
Pd(IO ₃) ₂	2	Orthorhombic	<i>Pbcn</i>	CS	2	Orange/Block
PdSeO ₃	3	Monoclinic	<i>P2₁/m</i>	CS	2	Orange/Plate
PdSe ₂ O ₅	3	Monoclinic	<i>C2/c</i>	CS	1	Orange/Prism
Na ₂ Pd(SeO ₄) ₂	3	Triclinic	<i>P$\bar{1}$</i>	CS	1	Yellow/Block
Ag ₄ (Mo ₂ O ₅)(SeO ₄) ₂ (SeO ₃)	4	Orthorhombic	<i>Pbcm</i>	CS	1	Yellow/Block
Ag ₂ (MoO ₃) ₃ SeO ₃	4	Monoclinic	<i>P2₁/n</i>	CS	2	Orange/Block

Table 8.1. (con't) A list of new compounds and some of their properties reported in this dissertation.

Formula	Chapter	Crystal System	Space Group	CS or NCS	Dimension	Color/Apperance
AgNbO(SeO ₃) ₂	4	Orthorhombic	<i>Cmc2(1)</i>	NCS	1	Colorless/Neddle
Yb(IO ₃) ₃ (H ₂ O)	5	Monoclinic	<i>C2/c</i>	CS	2	Colorless/Plate
Lu(IO ₃) ₃ (H ₂ O)	5	Monoclinic	<i>C2/c</i>	CS	2	Colorless/Plate
Yb(IO ₃) ₃	5	Monoclinic	<i>P2₁/n</i>	CS	2	Colorless/Prism
Lu(IO ₃) ₃	5	Monoclinic	<i>P2₁/n</i>	CS	2	Colorless/Neddle
UO ₂ (IO ₃) ₂ (H ₂ O)·2HIO ₃	6	Orthorhombic	<i>Pbcn</i>	CS	2	Yellow/Prism
Np(IO ₃) ₄	7	Tetragonal	<i>P4₂/n</i>	CS	1	Pleochroic /Block
Np(IO ₃) ₄ · <i>n</i> H ₂ O· <i>n</i> HIO ₃	7	Rhombohedral	<i>R3c</i>	NCS	3	Pale Yellow/Block

^a CS and NCS represent centrosymmetric and noncentrosymmetric, respectively.

REFERENCES

1. Kolis, J. W.; Korzenski, M. B. *Chemical Synthesis Using Supercritical Fluids*, **1999**, 213. urbaix, M. *Atlas d'equilibres electrochimiques à 25 °C*; Gautier Villars: Paris, 1963.
2. Wendlandt, W. W.; Hecht, H. G.: *Reflectance Spectroscopy*. Interscience Publisher, New Yourk, 1966.
3. (a) Kurtz, S. K.; Perry, T. T. *J. Appl. Phys.* **1968**, 39,3798. (b) <http://www.chem.uh.edu/Faculty/Halasyamani/online/shg.html>.
4. Sullens, T. A.; Almond, P. M.; Byrd, J. A.; Beitz, J. V.; Bray T. H.; Albrecht-Schmitt, T. E. *J. Solid State Chem.* **2006**, 179, 1192.
5. (a) Bruchertseifer, H.; Cripps, R.; Guentary, S.; Jaeckel, B. *Anal. Bioanal. Chem.* **2003**, 375, 1107. (b) Huang, Z.; Ito, K.; Timerbaev, A. R.; Hirokawa, T. *Anal. Bioanal. Chem.* **2004**, 378, 1836.
6. (a) Bean, A. C.; Peper, S. M.; Albrecht-Schmitt, T. E. *Chem. Mater.* **2001**, 13, 1266. (b) Bean, A. C.; Scott, B. L.; Albrecht-Schmitt, T. E.; Wolfgang, R. *Inorg. Chem.* **2003**, 42, 5632.